

UNIVERSIDADE DE SANTIAGO DE COMPOSTELA

Departamento de Electrónica e Computación



Doctoral thesis

**CHARACTERIZATION, MODELLING AND OPTIMIZATION OF
INDUSTRIAL SILICON THIN FILM SOLAR CELLS**

Submitted by:

José Antonio Rodríguez González

Supervised by:

Dr. Antonio J. García Loureiro

Dr. Ing. Michael Vetter

Santiago de Compostela, September 2013

Dr. Antonio J. García Loureiro, Profesor Titular del Área de Electrónica de la Universidade de Santiago de Compostela

Dr. Ing. Michael Vetter, Director del Laboratorio de I+D de la empresa T-Solar Global S.A.

HACEN CONSTAR:

Que la memoria titulada **CHARACTERIZATION, MODELLING AND OPTIMIZATION OF INDUSTRIAL SILICON THIN FILM SOLAR CELLS** ha sido realizada por **D. José Antonio Rodríguez González** bajo nuestra dirección en el Departamento de Electrónica e Computación de la Universidade de Santiago de Compostela, y constituye la Tesis que presenta para optar al título de Doctor.

Santiago de Compostela, septiembre de 2013



Dr. Antonio J. García Loureiro
Codirector de la tesis



Dr. Ing. Michael Vetter
Codirector de la tesis



José Antonio Rodríguez González
Autor de la tesis

A mis padres

No podemos resolver problemas pensando de la misma manera que cuando los creamos.

Albert Einstein

Casi todo lo que realice será insignificante, pero es muy importante que lo haga.

Mahatma Gandhi

Acknowledgments

Fist of all, I want to kindly thank my PhD supervisors, Michael Vetter and Antonio García Loureiro, for their constant help, support and encouragement, which have allowed me to carry out this PhD. As well, for their ability to successfully manage their respective teams and their motivation and passion showed at work. I would also thank Jordi Andreu for his confidence.

To my T-Solar workmates from all the departments but especially from the Laboratory: Carlos, Jacinto, Florent, José Manuel, Miguel, Óscar, Boris, Teresa and Luis. The working environment was really nice and to work with you a rewarding experience. I want to also thank you for the good moments in Ourense playing football, tennis, going to the swimming pool or making party at "Vinos". Particularly, I want to thank to Eva, Montse and Amaury, to work in group with you has been very easy and your motivation a pleasure.

To my CITIUS workmates, where I have performed the simulations and wrote this memory, especially to Enrique for his help with the simulations and computer problems.

I cannot forget Pablo, which has been my "brother" in Ourense during the last four years. We form a nice "tandem" and I hope it is going to continue in the future with our jump to the business world.

To my parents and my brother Santi for their constant support, help and their sacrifice to let me study whatever I wanted and to let me participate in the Erasmus internship program. To my friends for being always there and for so many unforgettable moments.

Finally, I acknowledge the funding of the Spanish Ministry of Economics and Competitiveness in the frame of the program "Torres Quevedo" (Contract No. PTQ-10-03524) and under project TEC2010-17320. This work was supported by the FP7 European Project HELATHIS (Grant Agreement No. 241378) and the regional government of Galicia (Projects No. IN841D-2010/14 and IN841C 2011/231).

Santiago de Compostela, September 2013

Contents

List of Figures	xv
List of Tables	xxiii
List of Acronyms	xxvii
Introduction	1
1 Photovoltaics status and T-Solar's thin film silicon factory	5
1.1 Photovoltaic technologies	6
1.1.1 First generation PV technologies: Crystalline silicon solar cells	6
1.1.2 Second generation PV technologies: Thin film solar cells	7
1.1.3 Third generation PV technologies	8
1.1.4 Thin film silicon (a-Si:H) vs. crystalline silicon (c-Si)	11
1.2 Photovoltaic applications	13
1.3 Evolution of photovoltaic production and installed capacity	14
1.3.1 Photovoltaic market: Installations	14
1.3.2 Photovoltaic industry	18
1.3.3 Outlook	20
1.4 Group T-Solar Global S.A.	22
1.5 T-Solar production line: Fabrication process and process control	24
1.6 Technology and R&D Department	38
1.7 FP7 European Project HELATHIS	40
2 Theory and simulation models of a-Si:H solar cells	43

2.1	Electrical model	44
2.2	Physical model	47
2.2.1	Density of states models for amorphous silicon	50
2.2.2	Recombination-generation statistics in amorphous silicon	54
2.2.3	Graded layers	61
2.2.4	Band structure	61
2.2.5	Light-induced degradation. Staebler-Wronski effect	63
2.2.6	Baseline input parameters applied in the simulation	65
2.3	Optical model	66
2.3.1	Optical generation	67
2.3.2	Improvement of light trapping and scattering through textured interfaces	69
2.3.3	Spectral irradiance	72
2.3.4	Simulation of the illumination	73
2.4	Numerical methods and solvers	74
2.4.1	Introduction into numerical methods	74
2.4.2	Equations	74
2.4.3	Boundary conditions	79
2.4.4	Discretization	81
2.4.5	Linearization of the discretised system	82
2.4.6	Numerical resolution of the non-linear equations	82
3	Industrial production process and basic equipment set-ups of a-Si:H solar cells	85
3.1	Plasma enhanced chemical vapour deposition	85
3.2	Production process to obtain mini cells and mini modules: laser scribe processes, shunt busting and annealing	88
3.3	Conventional spectral response equipment	96
3.3.1	Components for the conventional spectral response system	96
3.3.2	Spectral response and quantum efficiency	100
3.3.3	Differential spectral response method	101
3.3.4	Determination of the calibration factor, the spectral response and the integrated short circuit current density	101
3.3.5	Experimental set-up	102
3.3.6	Software developed for the conventional spectral response equipment	105

3.3.7	Calibration procedure and control plan for the conventional spectral response equipment	106
3.4	Very fast spectral response equipment	107
3.4.1	Light emitting diodes: Characterization and selection	109
3.4.2	Sinusoidal generators	113
3.4.3	Fast Fourier transform concept	113
3.4.4	Measurement procedure for the very fast spectral response equipment	114
3.4.5	Software developed for the very fast spectral response equipment . .	115
3.5	Measurements of illuminated and dark current-voltage curves	119
3.5.1	Equipment	119
3.5.2	Current-voltage curves under illumination	121
3.5.3	Dark current-voltage curves	124
3.5.4	Calibration procedure and control plan for the class A solar simulator	125
3.5.5	Software developed for current-voltage curve measurements	128
3.5.6	Measurement procedure for illuminated current-voltage curves	129
4	Modelling, characterization and optimization of a-Si:H solar cells	131
4.1	Evolution of the fabrication of highly efficient and reliable a-Si:H test solar cells in the industrial environment of T-Solar	132
4.1.1	Solar cell production method (shadow mask vs. laser scribe)	132
4.1.2	Influence of shunt busting and annealing	134
4.1.3	Industrial solar cells produced with laboratory TCO-glasses	137
4.2	Preparation of samples with solar cells for shipments to project partners . . .	139
4.2.1	First shipments to Research Centre Jülich	139
4.2.2	Oxidation study	142
4.3	Front TCO layer and glass developments	146
4.3.1	Front TCO layer developments	146
4.3.2	New generation TCO glasses	151
4.3.3	Anti-reflection coating or interface layer	154
4.3.4	Study for new materials in the front TCO-layer (ZnO-TCO)	158
4.4	p-i-n structure developments	164
4.4.1	Uniformity of thin film properties along the panel	164
4.4.2	Electrical parameters variation with i-layer thickness	167
4.4.3	p-i-n structure evolution	169

4.5	Back contact developments	174
4.6	Experimental results with the very fast spectral response equipment	176
4.7	Simulation results	179
4.7.1	Study on theoretical electrical performance of the p-i-n structure	180
4.7.2	Study on the front TCO layer texture	183
4.8	Improvements in the industrial production line of T-Solar	188
	Conclusions	191
	Resumen de la tesis	197
	Bibliography	205

List of Figures

Fig. 1.1	Crystalline silicon module production chain	6
Fig. 1.2	Reported timeline of solar cell energy conversion efficiencies	11
Fig. 1.3	Energy payback times for different technologies in function of the installation site in Europe	12
Fig. 1.4	Two examples of BIPV	13
Fig. 1.5	Annual PV installations from 2000 to 2012	15
Fig. 1.6	Cumulative PV installations from 2000 to 2012	16
Fig. 1.7	New installed or decommissioned electricity generation capacity in Europe in 2012	16
Fig. 1.8	Annual PV market scenarios until 2017 - Bussiness-as-usual and Policy-driven	17
Fig. 1.9	Cumulative PV market scenarios until 2017 - Bussiness-as-usual and Policy-driven	18
Fig. 1.10	World PV cell/module production capacity from 2009 to 2012 and annual forecast until 2017	19
Fig. 1.11	Price learning curve by technology from 1980 to 2011	22
Fig. 1.12	T-Solar Global S.A.'s a-Si:H PV module factory	23
Fig. 1.13	Basic steps of the manufacture process of T-Solar a-Si:H modules	25
Fig. 1.14	Kuka robot charging a front TCO-glass at the beginning of the production line	26
Fig. 1.15	Operator seaming the front glass sheet with TCO-layer	27
Fig. 1.16	Laser tool picture. Panels are placed onto an air table	27
Fig. 1.17	TCO layer laser scribing step, P1	28
Fig. 1.18	PECVD deposition cluster tool. It has an octogonal shape due to the fact that the seven deposition chambers and the load lock chamber, are all placed around a central transfer chamber	29

Fig. 1.19	PECVD tool chamber usage for the p-i-n deposition	29
Fig. 1.20	a-Si:H laser scribing step, P2	30
Fig. 1.21	PVD sputtering tool	31
Fig. 1.22	a-Si:H and back contact laser scribing step, P3	31
Fig. 1.23	P1, P2 and P3 scribes (microscope view)	32
Fig. 1.24	Final module structure which allows the current to flow among the cells	32
Fig. 1.25	T-Solar production line is ready to produce modules of four different sizes	33
Fig. 1.26	Buss tool picture and clean room to handle the PVB	34
Fig. 1.27	Lamination tool and autoclave tool overall view	35
Fig. 1.28	Junction box tool and in-line solar simulator tool	35
Fig. 1.29	Finished full and quarter size modules	36
Fig. 1.30	Control plan scheme with all the controls made in-line and off-line	38
Fig. 2.1	Generation of electron-hole pairs due to the photon incidence in a p-n junction	45
Fig. 2.2	Solar cell IV curve as result of the diode IV curve minus the I_{ph}	46
Fig. 2.3	Equivalent circuit of an a-Si:H solar cell	47
Fig. 2.4	p-i-n structure	48
Fig. 2.5	Amorphous silicon structure (random network) showing a bond with a hydrogen atom	48
Fig. 2.6	DOS distribution model for intrinsic a-Si:H layer on a linear scale	51
Fig. 2.7	DOS distribution model for intrinsic a-Si:H layer on a logarithmic scale	51
Fig. 2.8	Different types of localized states in the band gap of a-Si:H and models that are used to calculate the recombination rate and charge occupation	55
Fig. 2.9	Electronic transitions in the recombination process between a single energy level in the band gap of a semiconductor and the energy bands	56
Fig. 2.10	Possible electronic transitions in the recombination process between the energy bands and an amphoteric R-G center represented by two energy levels in the band gap	59
Fig. 2.11	Band diagram for the a-Si:H p-i-n layers under 1 sun illumination and without polarization ($V = 0$ V)	63
Fig. 2.12	Structure of the simulated a-Si:H solar cell	65
Fig. 2.13	Photon flux into a semiconductor	67
Fig. 2.14	Optical absorption coefficient for different PV materials	68
Fig. 2.15	Complex refractive index for our a-Si:H layers	69

Fig. 2.16 SEM picture of an industrial TCO sample AN10 from AGC showing fine surface roughness of the crystal grains	71
Fig. 2.17 AFM picture of an industrial TCO sample AN10 from AGC	71
Fig. 2.18 Solar spectrum AM0, AM1.5G and AM1.5D	73
Fig. 2.19 Simplified flow chart of the method used for the numerical resolution	75
Fig. 2.20 Energy band diagram of a typical single junction a-Si:H solar cell under equilibrium conditions	77
Fig. 3.1 Schematic representation of the glow-discharge deposition process	87
Fig. 3.2 PECVD chamber diagram	88
Fig. 3.3 Former T-Solar coupon with 1 cm ² solar cells and sample holder for MCs measurements of IV curves and SR with the switch box to choose the solar cell to be measured	90
Fig. 3.4 Scratch mask, scratch pencils and Combi mask with their four pieces	92
Fig. 3.5 Back contact side and glass side of a coupon produced at FZJ with a magnetized mask (Combi mask)	92
Fig. 3.6 Position of the coupons with MCs along the full size panel	93
Fig. 3.7 Back contact side and glass side of a coupon produced at TS through laser scribe	94
Fig. 3.8 Position of the MMs along the full size panel	95
Fig. 3.9 10 cm x 10 cm total area MM produced at TS through LSR scribe	95
Fig. 3.10 Arc lamp and monochromator	97
Fig. 3.11 Incoming beam divided by the beam-splitter	98
Fig. 3.12 Two lock-in amplifiers and cold light source with its illumination system	99
Fig. 3.13 SR equipment and links between the different devices	103
Fig. 3.14 Configuration of a Czerny-Turner monochromator	104
Fig. 3.15 The beam-splitter with the two arms	104
Fig. 3.16 Optical path of the light through the system	105
Fig. 3.17 Relationship between hardware and software for the CSR equipment	106
Fig. 3.18 Comparison of the EQE provided by the manufacturer and the average EQE measured in the T-Solar equipment for the reference solar cell WPVS Cell 06-2008	107
Fig. 3.19 Experimental IV curve and DC bias point for 4 representative LEDs	111

Fig. 3.20	Peak wavelength and FWHM for a LED with narrow band width and for a LED with wide band width	112
Fig. 3.21	Experimental spectral irradiance for 23 selected LEDs in the range 370 nm - 1000 nm	112
Fig. 3.22	Decomposition of a periodic signal in its different harmonics	113
Fig. 3.23	Sine wave in the time-domain and, after FFT analysis, sine wave in the frequency-domain	114
Fig. 3.24	MM with every cell connected individually with a conducting adhesive side buss	115
Fig. 3.25	Diagram of the VFSR measurement system	116
Fig. 3.26	Time dependent current density curve	117
Fig. 3.27	Current density curve in the frequency-domain as resulting from FFT analysis	117
Fig. 3.28	EQE measured in a CSR equipment with monochromator and in a VFSR equipment	118
Fig. 3.29	Solar simulator and the other parts of IV curve measurement devices	120
Fig. 3.30	Equivalent circuit of an a-Si:H PV solar cell	122
Fig. 3.31	Typical illuminated IV curve and PV curve of a photovoltaic solar cell	124
Fig. 3.32	Typical dark IV curve of a photovoltaic solar cell	125
Fig. 3.33	Spatial mapping result of the calibration done on 29/11/2011	127
Fig. 3.34	LabVIEW front panel for the IV curve tracer	129
Fig. 4.1	Design for the former T-Solar solar cells produced with shadow mask	133
Fig. 4.2	JV curves for solar cells on Asahi U TCO-glass	138
Fig. 4.3	Illuminated JV curve for three cells before and after performing shunt busting for a coupon sent to FZJ without back contact (first shipment)	141
Fig. 4.4	Dark JV curve for the best cell (C17) before and after performing shunt busting for a coupon sent to FZJ without back contact (first shipment)	141
Fig. 4.5	JV curve comparison for the best cells between the samples produced on 04/02/10 only with p-i-n, with back contact layers added on 18/03/10: p-i-n without any treatment, p-i-n treated with HF etching and p-i-n + AZO	144
Fig. 4.6	Dark JV curves for two solar cells sent with and without back contact	144
Fig. 4.7	EQE comparison between the samples produced on 04/02/10 with back contact layers deposited on 18/03/10: p-i-n without any treatment, p-i-n treated with HF etching, p-i-n + AZO	145

Fig. 4.8	Total transmission for five TCO types with different carrier mobility, thickness and resistivity	148
Fig. 4.9	Correlation between J_{sc} measured in the SS and TCO-glass absorbance for five TCO-glass types with different carrier mobility, thickness and resistivity	148
Fig. 4.10	JV curve for five TCO types with different carrier mobility, thickness and resistivity	150
Fig. 4.11	EQE curve for five TCO types with different carrier mobility, thickness and resistivity	150
Fig. 4.12	Total transmission for three industrial TCO-glasses and one laboratory TCO-glass (Asahi U)	152
Fig. 4.13	JV curve for two TCO-glass types with different total transmission, carrier mobility and thickness	153
Fig. 4.14	EQE curve for two TCO-glass types with different total transmission, carrier mobility and thickness	154
Fig. 4.15	Structure of an a-Si:H solar cell including the placement of two ARC at interfaces air/glass and TCO/p-layer	155
Fig. 4.16	JV curve for four solar cells with NTO interface layer with different thickness and doping concentration deposited on Asahi U TCO-glass	157
Fig. 4.17	EQE curve for four solar cells with NTO interface layer with different thickness and doping concentration deposited on Asahi U TCO-glass	157
Fig. 4.18	Reflection for four solar cells with NTO interface layer with different thickness and doping concentration deposited on Asahi U TCO-glass	158
Fig. 4.19	Total and diffuse transmission for a SnO_2 TCO deposited on float glass of 3.2 mm and a ZnO TCO deposited on Corning glass of 1.0 mm	159
Fig. 4.20	Haze for a SnO_2 TCO deposited on float glass of 3.2 mm and a ZnO TCO deposited on Corning glass of 1.0 mm	160
Fig. 4.21	JV curve for three solar cells with ZnO front TCO produced at FZJ with different doping concentration and deposition process	161
Fig. 4.22	EQE curve for three solar cells with ZnO front TCO produced at FZJ with different doping concentration and deposition process	162
Fig. 4.23	JV curve for two solar cells with ZnO front TCO produced at FZJ and Asahi U (SnO_2) front TCO. Both samples have $\mu\text{c-Si}$ p-layer	163

Fig. 4.24	EQE curve for two solar cells with ZnO front TCO produced at FZJ and with Asahi U (SnO ₂) front TCO. Both samples have $\mu\text{c-Si}$ p-layer and are compared with a solar cell with ZnO front TCO with a-Si:H p-layer	163
Fig. 4.25	Typical thickness mapping of a n-type a-Si:H control layer	165
Fig. 4.26	Variation of the main electrical parameters for four coupons placed along the diagonal F-I of the panel	165
Fig. 4.27	EQE curve for two coupons of the same panel, one placed in the centre and the other one in a corner	166
Fig. 4.28	Degradation factors of Jsc for solar cells prepared with different i-layer thicknesses in different laboratories	168
Fig. 4.29	Degradation factors of Voc and FF for solar cells prepared with different i-layer thicknesses in different laboratories	168
Fig. 4.30	Efficiency of quarter size modules in the initial and stabilized state and η degradation factors	169
Fig. 4.31	Relation between i-layer thickness reduction and throughput increase of the PECVD machine and extrapolation to the annual production capacity	169
Fig. 4.32	JV curve for three solar cells which represent the main three evolutions performed at T-Solar during the three years of the HELATHIS project	172
Fig. 4.33	EQE curve for three coupons which represent the main three evolutions performed at T-Solar during the three years of the HELATHIS project. The EQE for the world record solar cell of Oerlikon Solar-Lab is also presented	173
Fig. 4.34	Gain of the main electrical parameters (in stabilized state) respect to evolution No. 4 for the main four evolutions performed at T-Solar during the three years of the HELATHIS project	173
Fig. 4.35	EQE curve for two solar cells, one with Al back contact and another one with Ag back contact, both deposited by sputtering at UU	175
Fig. 4.36	Reflectance for five different Ag and/or Al back reflectors	175
Fig. 4.37	EQE of two SJ solar cells with different i-layer thickness, both measured with our CSR equipment and the new VFSR equipment	176
Fig. 4.38	EQE of two SJ solar cells with different BKM evolutions (No.4 vs. No.8), both measured with the CSR and VFSR equipment	178
Fig. 4.39	Jsc spatial mapping along a 10 x 10 cm ² size mini module measured with the VFSR equipment	179

Fig. 4.40 Variation of short circuit current density and open circuit voltage with the i-layer thickness for three different p-layer thicknesses 180

Fig. 4.41 Variation of efficiency and fill factor with the i-layer thickness for three different p-layer thicknesses 181

Fig. 4.42 Variation of short circuit current density and open circuit voltage with the i-layer thickness for three different p-layer doping concentrations 181

Fig. 4.43 Variation of efficiency and fill factor with the i-layer thickness for three different p-layer doping concentrations 182

Fig. 4.44 Light trapping in the active layer (i-layer) of an a-Si:H solar cell 183

Fig. 4.45 Representation of the texture interface parameters 184

Fig. 4.46 Simulated JV curves for flat and textured interfaces with different heights . . . 185

Fig. 4.47 Simulated EQE for flat and textured interfaces with different heights 186

Fig. 4.48 Experimental and simulated JV curve in the initial and degraded state 187

Fig. 4.49 Experimental and simulated EQE in the initial and degraded state 187

Fig. 4.50 Efficiency evolution in modules in the last four years 188

Fig. 4.51 Efficiency histogram for similar production periods of 5.72 m² a-Si:H modules from 2009 to 2012 189

Fig. 4.52 Evolution of the T-Solar production capacity and throughput during the period 2009 - 2012 190

List of Tables

Tabla 1.1	An overview of major PV technologies	10
Tabla 1.2	Evolution of the cumulative solar electrical capacities until 2035	21
Tabla 2.1	Time rates of change in the carrier concentrations for transitions involving VB and CB tail states at an arbitrary energy level E_T in the band gap	56
Tabla 2.2	Transition rates of change in the carrier concentrations for recombination processes involving DB states.	59
Tabla 2.3	Baseline input parameters used in the simulation	66
Tabla 3.1	IV curve parameters of the calibrated solar cell (4 cm ²) from FHG-ISE measured under STC	99
Tabla 3.2	Comparison of the technical data sheet values with the experimental data obtained at our lab for the 24 selected LEDs	110
Tabla 3.3	Results of all the calibration controls done for the three lamps used until the moment in the solar simulator	128
Tabla 4.1	Electrical parameters comparison for the old (shadow mask) and new (laser scribe) T-Solar solar cell design	134
Tabla 4.2	Electrical parameters comparison for three different types of annealing performed in three coupons which were located side by side in the same panel. Top: Results before and after annealing and after 300 kWh/m ² of light soaking. Middle: Variation for the three coupons before and after performing annealing. Bottom: LID for the three coupons	135

Tabla 4.3	Electrical parameters average for the best 5 cells of a coupon without treatment, after shunt busting and after shunt busting and annealing (top). Variation respect to values without treatment (middle). Number of good cells in four different coupons without treatment, after annealing, after shunt busting or after shunt busting and annealing (bottom)	136
Tabla 4.4	Electrical parameters comparison for 1 cm ² solar cells and 5.72 m ² full size modules produced on 16/06/2011	137
Tabla 4.5	Electrical parameters for solar cells on Asahi U TCO-glass produced with different production methods and treatments	139
Tabla 4.6	Average electrical parameter values before and after performing shunt busting for a coupon sent to FZJ without back contact (first shipment) . . .	140
Tabla 4.7	Average electrical parameter values for the measured solar cells in each experiment (p-i-n: 8 cells, p-i-n + HF: 12 cells, p-i-n + AZO: 8 cells) . . .	143
Tabla 4.8	Electrical parameter values of the best cell for the three experiments and average values for 1 cm ² cells produced (with mask) with the T-Solar standard process	143
Tabla 4.9	Summary of the main characteristics of the different TCO types	146
Tabla 4.10	Transmission, absorption and sheet resistance for five TCO-glass types with different carrier mobility, thickness and resistivity	147
Tabla 4.11	Electrical parameters for five TCO types with different carrier mobility, thickness and resistivity	149
Tabla 4.12	Integrated total transmission in the range 400 nm - 800 nm for three industrial TCO-glasses and one laboratory TCO-glass (Asahi U) and their gain with respect to AN10	151
Tabla 4.13	Electrical parameters for two TCO-glass types with different total transmission, carrier mobility and thickness	153
Tabla 4.14	Thickness and doping conditions for four different interface layers of NTO deposited on Asahi U	155
Tabla 4.15	Electrical parameters (initial state) for two references and four solar cells with NTO interface layer with different thickness and doping concentration deposited on Asahi U TCO-glass	156
Tabla 4.16	Material properties of a SnO ₂ TCO deposited on float glass of 3.2 mm and a ZnO TCO deposited on Corning glass of 1.0 mm	158

Tabla 4.17	Electrical parameters (initial state) for three solar cells with ZnO front TCO produced at FZJ with different doping concentration and deposition process	160
Tabla 4.18	Electrical parameters (initial state) for two solar cells with ZnO front TCO produced at FZJ and Asahi U (SnO ₂) front TCO. Both samples have μ c-Si p-layer	162
Tabla 4.19	Electrical parameters statistics for four coupons of the same panel placed along the diagonal	166
Tabla 4.20	LID for thirteen coupons produced at different laboratories (2 at UU, 3 at FZJ and 8 at TS) with different i-layer thicknesses	167
Tabla 4.21	Main BKM evolution related to the PECVD process since the T-Solar production start	170
Tabla 4.22	Electrical parameters for five coupons with solar cells which represent the main five evolutions performed at T-Solar during the three years of the HELATHIS project	171
Tabla 4.23	Gain in the stabilized state respect to evolution No. 4	174
Tabla 4.24	Electrical parameters for the stabilized record T-Solar solar cell and world record solar cell of Oerlikon Solar-Lab	174
Tabla 4.25	Jsc determined from SR with the VFSR and CSR equipment for solar cells with i-layer thickness (d_i) of 260 nm and 200 nm	177
Tabla 4.26	Jsc determined from SR with the VFSR and CSR equipment for solar cells with different BKM evolution steps (No.4 vs. No.8)	177
Tabla 4.27	Statistical parameters obtained from the mapping in Fig. 4.39 (VFSR equipment) and the same mapping obtained with the CSR equipment	179
Tabla 4.28	Simulated electrical parameters depending on the β angle in the degraded state	185
Tabla 4.29	Electrical parameters for an experimental and simulated solar cell in the initial and degraded state	186

List of Acronyms

a-Si:H hydrogenated amorphous silicon

a-Si:H/ μ c-Si:H hydrogenated amorphous silicon/micro-crystalline silicon

AC alternating current

ACL autoclave

AFM atomic force microscopy

Ag silver

AGC AGC Flat Glass Europe S.A.

AIMEN "Asociación de Investigación Metalúrgica del Noroeste"

Al aluminium

AM air mass

AMAT Applied Materials Inc.

APAC Asia Pacific

APCVD atmospheric pressure chemical vapour deposition

Ar Argon

ARC anti-reflection coating

AZO aluminium-doped zinc oxide, $ZnO : Al$

- B** boron
- BC** back contact
- BC** best cell
- BEOL** back end of line
- BIPV** building integrated photovoltaics
- BKM** best known method
- BOS** balance of system
- c-Si** crystalline silicon
- CAGR** compound annual growth rate
- CB** conduction band
- CBT** conduction band tail
- CdTe** cadmium telluride
- CIGS** copper, indium, gallium, selenium
- CPV** concentration photovoltaic
- CSR** conventional spectral response
- CVD** chemical vapour deposition
- DB** dangling bond
- DC** direct current
- DNI** direct normal irradiation
- DOS** density of states
- DSP** digital signal processing
- DSR** differential spectral response

e electron

EPIA European Photovoltaic Industry Association

EQE external quantum efficiency

EREC European Renewable Energy Council

EU European Union

F calibration factor

F fluorine

FAS factory automation software

FC front contact

FEOL front end of line

FF fill factor

FFT fast Fourier transform

FWHM full width at half maximum

FZJ Research Centre Jülich GmbH

G_{irrad} irradiance

η efficiency

h hole

H₂ hydrogen

HCl hydrogen chloride

HELATHIS High Efficient very LArge area THIn film Silicon photovoltaic modules

HF hydrogen fluoride

i-layer intrinsic layer

- I₀** reverse saturation current
- IEA** International Energy Agency
- IFL** interface layer
- I_{mpp}** current at maximum power point
- IPP** independent power producer
- IQE** internal quantum efficiency
- IR** infrared
- I_{sc}** short circuit current
- ISS** in-line solar simulator
- IV** current-voltage
- J₀** reverse saturation current density
- JRC** Joint Research Centre
- J_{sc}** short circuit current density
- JV** current density-voltage
- k** extinction coefficient
- LDR** low deposition rate
- LED** light emitting diode
- LID** light-induced degradation
- LOMG** "Laboratorio Oficial de Metrología de Galicia"
- LSR** laser
- LSS** light soaking station
- MC** mini cell

- $\mu\text{c-Si:H}$** micro-crystalline silicon
- ME** mobility enhanced
- MEA** Middle East and Africa
- MHS** material handling system
- MM** mini module
- n** refractive index
- n** ideality factor of the diode
- n- μcSi** microcrystalline n-layer
- Nd:YVO₄** Neodymium-doped yttrium orthovanadate
- NF₃** nitrogen trifluoride
- NIR** near infrared
- NiV** nickel vanadium
- NREL** National Renewable Energy Laboratory
- NTO** Niobium pentoxide-doped titanium oxide, $TiO_2 : Nb_2O_5$
- Oerlikon Solar-Lab** Oerlikon Solar-Lab S.A.
- OPV** organic photovoltaic
- P** phosphorus
- PECVD** plasma enhanced chemical vapour deposition
- PH₃** phosphine
- pib** p/i buffer
- P_{mp}** maximum power
- PV** photovoltaic

PV power-voltage

PVB polyvinyl butyral

PVD physical vapour deposition

QASR quality assurance and shunt removal

QE quantum efficiency

r reflection

R-G recombination-generation

RF radiofrequency

ROW rest of the World

R_s series resistance

R_{sh} shunt resistance

R_{sq} sheet resistance

SB shunt busting

SCPI standard commands for programmable instruments

SEM scanning electron microscopy

Si silicon

SiF₄ silicon tetrafluoride

SIGMA "SIstema de Gestión y Monitorización Avanzado"

SiH₄ silane

SiO₂ silicon oxide

SJ single junction

SnO₂ tin oxide

SnO₂:F fluorine-doped tin oxide

SR spectral response

SRH Shockley Read Hall

SS solar simulator

STC standard test conditions (1000 W/m², 25 °C and AM1.5G spectral distribution)

SWE Staebler-Wronski effect

T temperature

T-Solar T-Solar Global S.A.

TCO transparent conductive oxide

TCS thermal conditioning station

TiO₂ titanium oxide

TJ tandem junction

TMM transfer matrix method

TS T-Solar Global S.A.

UB University de Barcelona

USC University of Santiago de Compostela

UU University Utrecht

UV ultraviolet

UVI University of Vigo

VB valence band

VBT valence band tail

VFSR very fast spectral response

VI virtual instrument

V_{mpp} voltage at maximum power point

V_{oc} open circuit voltage

WP work packages

ZnO zinc oxide

Introduction

Nowadays the most of the energy consumption is provided from fossil fuels as oil, natural gas or coal. Nevertheless, in the last years, the world-wide energetic policies are changing and renewable energies are increasing rapidly their quota in the energy mix. The main reasons for this modification are, on one hand, that fossil fuel prices are raising due to the decreasing availability of this sources. On the other hand, the consumer countries are dependent of the producer countries. In addition, the massive use of them is producing the climate change.

The European Union (EU) climate and energy targets, known as the "20-20-20" targets, set three key objectives for 2020 [1]: A 20% reduction in EU greenhouse gas emissions from 1990 levels (to come back to 450 ppm - 550 ppm range), to raise the share of EU energy consumption produced from renewable resources to 20% and a 20% improvement in the EU's energy efficiency.

During the last years the investments into renewable energy and energy efficiency sectors has been increasing. In 2011, world-wide new investments into these sectors increased to a new record of € 202 billion, including € 19.8 billion research and development spending. More than 85% (€ 173 billion) of these investments were non-governmental, non-research clean energy investments [2]. This resulted in a record of 83.5 GW of new clean energy generation capacity, bringing the total to more than 565 GW (50% more than the installed nuclear generating capacity world-wide).

Specifically for solar energy, in 2011 (for the second year in a row) attracted the largest amount of new investments into renewable energies [2]. There was a 44% increase (respectively to 2010) in solar energy investments to € 98.5 billion [2].

Nowadays, electricity production from photovoltaic (PV) solar systems has shown that it can be cheaper than peak prices in the electricity exchange. The electricity generation costs

are already at the level of residential electricity prices in several countries, depending on the actual electricity price and the local solar irradiance level.

Photovoltaic solar energy will continue to grow at high rates in the coming years accelerating its consolidation because it is considered to be the most powerful energy source in the future since it joins optimal conditions such as solar energy is an unlimited resource (the sun supplies 1000 times more energy than the world energy consumption) or it is a clean energy. Furthermore, the current solar module technologies are well established and provide a reliable product, with sufficient efficiency and energy output for at least 25 years lifetime.

The development and recent fast growth of the PV industry has resulted in module oversupply and a fast decrease of module prices in the last years, demanding now on all actors in the PV sector an important increase in R&D activities to be competitive in the future. The investigations of this PhD thesis were performed in that frame. It was financed by the High Efficient very LArge area THIn film Silicon photovoltaic modules (HELATHIS) project and the "Torres Quevedo" program. The activity involved the Technology and R&D Department of the T-Solar Global S.A. (T-Solar) company and the Department of Electronics and Computer Science of the University of Santiago de Compostela.

This PhD thesis is structured in four chapters and is based on the optical and electrical characterization of solar cells with different materials and deposition process conditions, the optimization and modelling of these cells and the development of metrology equipments. The first chapter presents a general view on the photovoltaic status analysing the different photovoltaic technologies and its applications, as well we will take a glance on the evolution of the world-wide photovoltaic production capacity and installed capacity since 2000 and the forecast until 2017. Next, we will focus in T-Solar and its hydrogenated amorphous silicon (a-Si:H) photovoltaic module factory. Finally, the main aims for the optimization of a-Si:H solar cells in the frame of the FP7 European Project HELATHIS are exposed.

In the second chapter the electrical model that governs the a-Si:H solar cells is presented, as well as their equivalent circuit, both obtained from the ideal diode model and deduced from the crystalline silicon (c-Si) solar cell model. Then, the physical model is explained emphasising in the differences between the properties of a-Si:H and c-Si. The most important changes result from the density of states (DOS), the recombination-generation statistics, the graded layers and the light induced degradation produced in a-Si:H due to the Staebler-Wronski effect (SWE). Next, it is explained how the optical generation is produced in a-Si:H solar cells, how the spectral irradiance is considered and how the optical transmission,

reflection and absorption works in the different solar cell layers. As well, we point out the different methods adopted in the here used Sentaurus (Synopsys) simulation tool to simulate both models, with flat or textured layers. Finally, a summary is presented about how the semiconductor equations are solved. That section introduces the equations and boundary conditions that the Sentaurus software solves to get, e.g., the current-voltage (IV) curves or external quantum efficiency (EQE) curves. The simulated device is meshed forming thousands of nodes and the respective equations describing the device and the boundary conditions are discretised in every of these nodes, then, the resulting system of equations is linearised and solved with the Gummel or Newton-Raphson methods.

The third chapter presents how the plasma enhanced chemical vapour deposition (PECVD) production process works, as well as how we fabricate R&D solar cells of 1 cm^2 (or 4 cm^2) or mini modules in the industrial production line. Later, the equipment installed in the laboratory are shown. Concerning this thesis, the most important ones are a conventional spectral response (CSR) and a very fast spectral response (VFSR) equipment, which are used to determine the EQE curves, and a solar simulator (SS) equipment with its IV tracer to measure the illuminated or dark IV curves. The three equipment were developed in our laboratory. The development to produce R&D solar cells and mini modules in the T-Solar production line as well as the development of the measurement equipment have been crucial to improve the production module efficiency.

In the fourth chapter we mainly present work performed in the frame of the European project HELATHIS. One of its objectives is the optimization of the solar cell structure implemented in T-Solar's industrial production process for very large area ($2.6\text{ m} \times 2.2\text{ m}$) a-Si:H PV modules. In the optimization not only the achievement of the physical efficiency limit of the solar cells has to be taken into account, but also aspects like solar cell fabrication time (impacting on factory throughput), the material and energy consumption (impacting on production cost), etc. In reference to this we report here, firstly, on the evolution to fabricate highly efficient and reliable a-Si:H test solar cells in the industrial environment of T-Solar and the preparation of samples with solar cells for shipments to project partners. Next, we investigate the cell structure developments, reporting on the front transparent conductive oxide (TCO) layer and glass developments, p-i-n structure developments and back contact developments. Next, we analyse the results obtained with the VFSR equipment and simulation studies on the p-i-n structure and the front TCO layer texture. To conclude this chapter, the

improvements in the industrial production line of T-Solar since the beginning in the year 2008 are shown.

Finally, the conclusions and the main advances achieved during this PhD thesis are indicated.

CHAPTER 1

PHOTOVOLTAICS STATUS AND T-SOLAR'S THIN FILM SILICON FACTORY

Photovoltaic (PV) solar energy is expected to be the most powerful energy source in the future since it gathers the optimal conditions for this. For instance, solar energy is an unlimited resource (the sun supplies 1000 times more energy than the world energy consumption) and furthermore, it is a clean energy. In fact, the current solar module technologies are well established and provide a reliable product, with sufficient efficiency and energy output to have at least a 25-year-long lifetime. In addition, the increasing amount of electricity interruptions (due to grid overloads), together with the continuous price rise of electricity coming from conventional energy sources, add attractiveness to the PV systems.

This chapter presents a general overview of the status of photovoltaics, analysing the different photovoltaic technologies and their applications. Likewise, we will take a glance on the evolution of the world-wide photovoltaic production capacity and the installed capacity from year 2000 to the present, and the forecast until year 2017. Next, we will focus on the company T-Solar Global S.A. and its hydrogenated amorphous silicon (a-Si:H) photovoltaic module factory. Finally, the main aims for the optimization of a-Si:H solar cells in the frame of the FP7 European Project HELATHIS are exposed.

1.1 Photovoltaic technologies

There are a wide range of PV cell technologies on the market today, using different types of materials, and even a larger number will be available in the future. PV cell technologies are usually classified into three generations, depending on the material on which they are based and on their level of commercial maturity [3].

1.1.1 First generation PV technologies: Crystalline silicon solar cells

Silicon is one of the most abundant elements in the earth's crust. Crystalline silicon is the material most commonly used in the PV industry, therefore wafer-based crystalline silicon (c-Si) PV cells and modules dominate the current market. This is a mature technology that employs the accumulated knowledge basis developed in the electronic industry. This type of solar cell is produced in mass, individual companies produce them at a rate of several hundred MW per year, reaching in some cases the GW-scale. In Fig. 1.1 the manufacturing process of wafer-based silicon PV modules is presented. It comprises four main steps: poly-silicon production, ingot/wafer production, cell production and module assembly.

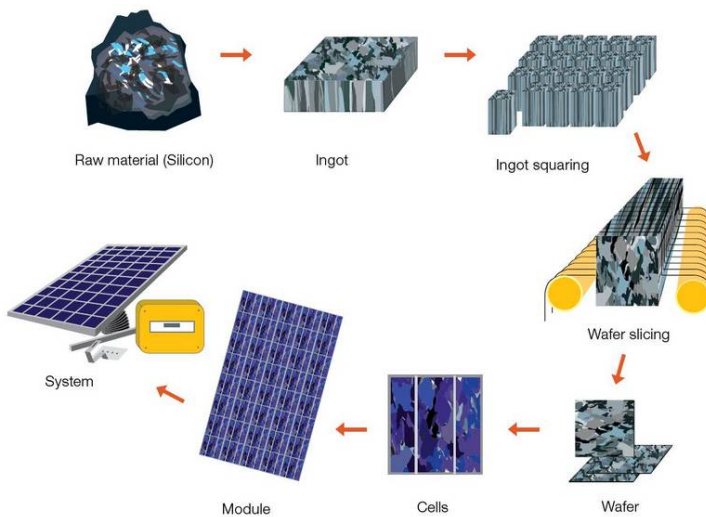


Figure 1.1: Crystalline silicon module production chain [4].

Crystalline silicon solar cells are classified into three main types depending on how the Si wafers are made [3]. They are:

- Mono-crystalline (c-Si).
- Multi-crystalline (mc-Si).
- Edge-defined film-fed growth (EFG) ribbon silicon.

Crystalline silicon technologies accounted about 85% of the global PV sales in 2012 [5]. The efficiency of crystalline silicon modules ranges from 15% to 21% [6]. Since it is a mature technology, continued cost reductions are possible through improvements in materials and manufacturing processes. From the economies of scale, one can predict that when the market continues to grow, more high-volume manufacturers will emerge.

1.1.2 Second generation PV technologies: Thin film solar cells

Thin film solar cells could potentially provide lower cost electricity than c-Si wafer-based solar cells. However, this is not certain. The lower capital costs (due to lower production and materials costs) are offset, to some extent, by the lower efficiencies of this technology. Besides, the reduction of c-Si modules' costs will make the economics even more challenging.

Thin film solar cells do not use wafers to produce the semiconductor, in contrast, they consist of successive thin layers (of about 1 μm to 4 μm thick) deposited on a large inexpensive substrate, such as: glass, polymer, or metal. As a consequence, they require a lot less semiconductor material to absorb the same amount of sunlight (up to 99% less material than crystalline solar cells). In addition, thin films can be packaged into flexible and lightweight structures which can be easily integrated into building components, such as roofs or facades (building integrated photovoltaics (BIPV)). The three primary commercially developed technologies employed in thin film solar cells are: amorphous silicon; cadmium telluride (CdTe); and copper, indium, gallium, selenium (CIGS)[3]. They are thoroughly explained in the following paragraphs:

- **Amorphous silicon solar cells (a-Si:H and a-Si:H/ $\mu\text{c-Si:H}$):** Amorphous silicon can be deposited on cheap and very large substrates (up to 5.7 m^2 of glass) based on continuous deposition techniques, thus considerably reducing manufacturing costs. Currently, amorphous silicon PV module efficiencies are in the range from 5%

to 8%. The main disadvantage of a-Si:H solar cells is that they suffer from a significant reduction in power output over time (11% to 35%), as the sun degrades their performance during the first hundreds hours of operation (degradation coefficients). Thinner layers could increase the electric field strength across the material and provide better stability and less reduction in power output, but this reduces light absorption and hence cell efficiency. Further developments must be carried out.

A notable variant of amorphous silicon solar cells is the multi-junction thin film silicon a-Si:H/ μ c-Si:H which consists of a-Si:H cell with additional layers of micro-crystalline silicon (μ c-Si:H) applied onto the substrate. The main advantages of the μ c-Si:H layer is that it absorbs more light from the red and near infrared part of the light spectrum (wavelength range 450 nm - 1100 nm for μ c-Si:H whereas 300 nm - 800 nm for a-Si:H) and it allows to deposit very thin a-Si:H layers resulting in very low degradation coefficients. Thus, the efficiency goes up to about 12%.

- **CdTe technology:** It has lower production costs and higher efficiencies, up to 18.3% in solar cells (GE Global Research) and 15.3% in modules (First Solar) [6] than other thin film technologies. This combination makes CdTe thin films economically very competitive. First Solar is largely the most important company producing this technology. The two main raw materials are cadmium and tellurium. A potential problem is that tellurium is produced in far lower quantities than cadmium and availability in the long-term may depend on whether the copper industry can optimise extraction, refining and recycling yields. Cadmium also has issues around its toxicity that may limit its use.
- **CIGS technology:** CIGS cells offer the highest efficiencies of all thin film PV technologies. CIGS solar cell production has been successfully commercialised by several firms in conjunction with universities. Current module efficiencies are in the range from 7% to 16%, but efficiencies up to 20.3% [7] have been achieved in laboratory scale, close to that of c-Si cells [8]. The race is now on to increase the efficiency of commercial modules. In long-term, indium could present supplied issues.

1.1.3 Third generation PV technologies

Third generation PV technologies are at the precommercial stage and vary from technologies under demonstration (e.g. multi-junction concentrating PV) to novel concepts

still in need of basic R&D (e.g. quantum-structured PV cells). Some third generation PV technologies are beginning to be commercialised, but it remains to be seen how successful they will be in taking market share from existing technologies. There are basically four types of third-generation PV technologies [3]:

- **Concentration PV (CPV) solar cells:** These systems utilise optical devices, such as lenses or mirrors, to concentrate direct solar radiation onto very small, highly efficient multi-junction solar cells made of a semiconductor material. The sunlight concentration factor ranges from 2 to 100 suns (low- to medium-concentration) up to 1000 suns (high concentration). To be effective, the lenses require high direct normal irradiation (DNI), to be permanently oriented towards the sun, which is gotten by using a single- or double-axis tracking system for low and high concentrations, respectively. In addition, the technology has a limit geographical range, the "Sun Belt" of the Earth and need clear skies. Cooling systems (active or passive) are a must for some concentrating PV designs.

Commercial CPV modules with silicon-based cells offer efficiency in the range of 20% to 25%. CPV based on multi-junction solar cells using III-V semiconductors have achieved laboratory efficiency of more than 40% [9]. Commercial multi-junction devices manufactured by Sharp and others [3] have efficiencies of near 35% (significantly higher than conventional single-junction c-Si solar cells). Nevertheless this technology is nowadays too expensive since multijunction solar cells, along with sun-tracking systems, result in expensive CPV modules in comparison with conventional PV.

- **Dye-sensitized solar cells (DSSC):** This technology uses photo-electrochemical solar cells, which are based on semiconductor structures formed between a photo-sensitised anode and an electrolyte. These cells are attractive because they use low-cost materials and they are easy to manufacture. However, their performance can degrade over time with exposure to ultraviolet (UV) light and the use of a liquid electrolyte can be problematic when there is a risk of freezing. Laboratory efficiencies of around 12% [6] have been achieved however, commercial efficiencies are low, typically under 4% to 5%. The main reason why efficiencies of DSSC are low is because there are very few dyes that can absorb a broad spectral range but new developments will allow higher power conversion efficiencies for DSSCs.

- **Organic solar cells:** They are composed of organic or polymer materials. They are inexpensive, but not very efficient. They are emerging as a niche technology, but their future development is not clear. Organic PV module efficiencies are now in the range 4% to 5% for commercial systems [10] and about 11% in laboratory. In addition to low efficiency, a major challenge for organic solar cells is their instability over time.

Organic solar cells production uses high-speed and low temperature roll-to-roll manufacturing processes and standard printing technologies. They are lightweight and flexible, being ideal for mobile applications such as battery charger for mobile phones, laptops, radios, etc. They can also be rolled up or folded for storage when not in use. These properties will make organic PV modules attractive for building-integrated applications.

- **Novel and emerging solar cell concepts:** There are a number of novel solar cell technologies under development that rely on using quantum dots/wires, quantum wells, or super lattice technologies [11] and [12]. These cells are likely to be used in concentrating PV technologies where they could achieve very high efficiencies by overcoming the thermodynamic limitations of conventional (crystalline) cells. However, these high efficiency approaches are in the fundamental materials research phase.

To summarize, in Table 1.1 an overview of major PV technologies looking at the efficiencies achieved not only in laboratory scale but also in commercial modules is presented. As well the module cost per W_p in June 2012 is shown. Fig. 1.2 plots the best research cell efficiencies since 1976 until June 2013 for the different PV technologies.

Table 1.1: An overview of major PV technologies [3], [6].

Technology	Units	1st Generation PV		2nd Generation PV			3rd Generation PV		
		c-Si	mc-Si	a-Si:H	CIGS	CdTe	III-V CPV	DSSC	Organic
Best research solar cell efficiency at STC	%	25.0	20.4	10.4 SJ 13.4 TJ	20.3	18.3	44.0	11.9	11.1
Commercial PV module efficiency at STC	%	15-21	13-19	5-8	7-16	8-15	25-33	1-5	1-5
June 2012 PV module cost	USD/W	< 1.4	< 1.4	≈ 0.8	≈ 0.9	≈ 0.9	-	-	-

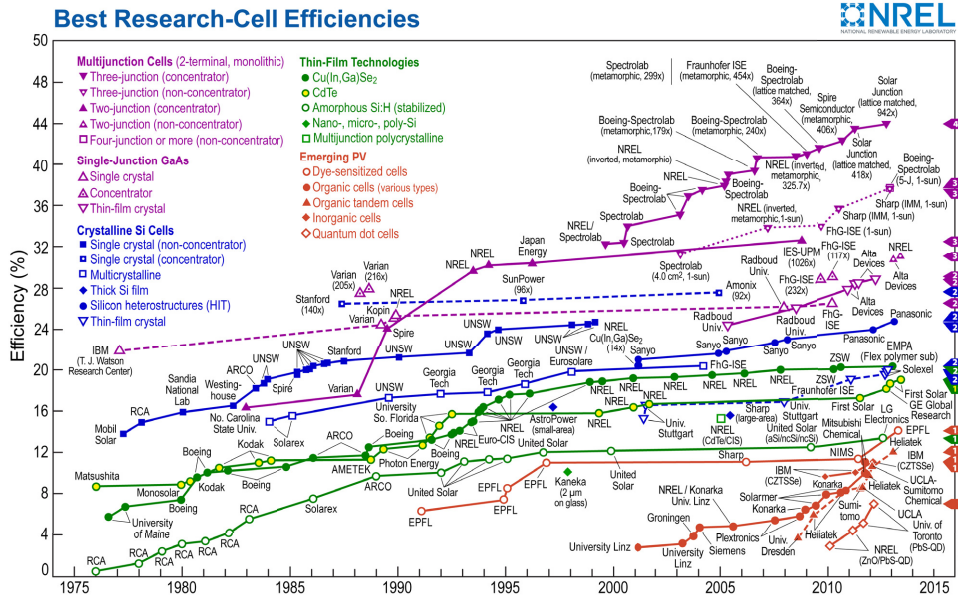


Figure 1.2: Reported timeline of solar cell energy conversion efficiencies. NREL, revised in June 2013.

1.1.4 Thin film silicon (a-Si:H) vs. crystalline silicon (c-Si)

Next, we compare the main differences between thin film silicon (a-Si:H) and crystalline silicon (c-Si) technologies:

- **Module cost:** a-Si:H costs between 0.47-0.75 €/W_p approximately whereas c-Si costs about 0.90-1.35 €/W_p. The main reasons are that a-Si:H uses less energy for modules production as well as for silicon purity processes and less raw material. Moreover, due to the a-Si:H modules size (usually four times bigger than c-Si) has less logistic cost and less labour cost.
- **Energetic payback:** It is the time required by a solar module to generate the same amount of energy that the one employed during the module life cycle (which includes the energy requirement for manufacturing, installation, etc.). The energetic payback depends on the region where the modules are installed as well as the fabrication process of the modules, etc (see Fig. 1.3). In the south of Europe the energetic payback is less

than 1 year for a-Si:H and about 2 years for c-Si. This is due to the fact that a lot of energy is needed to purify the crystalline material and a-Si:H deposition process is done at low temperature (about 200 °C).

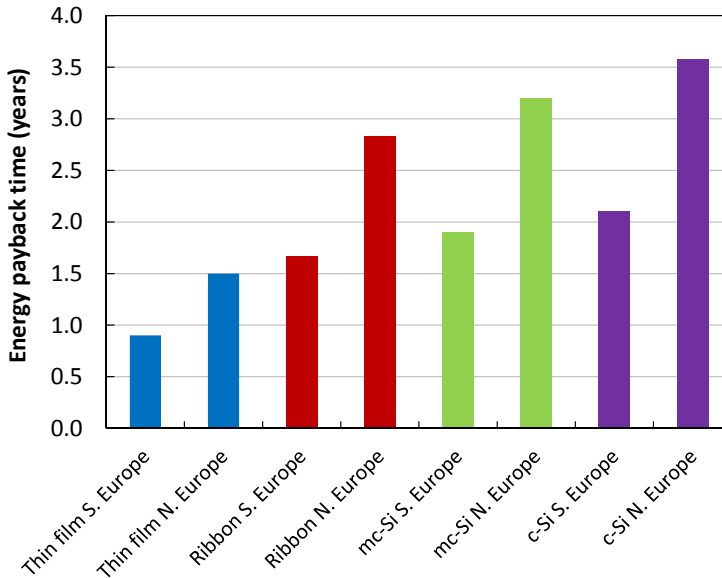


Figure 1.3: Energy payback times for different technologies in function of the installation site in Europe (Northern, N or Southern, S) [13].

- Energetic yield: a-Si:H gets between 5% and 10% more kWh per kW_p in normal use conditions. This is a consequence of the thin film silicon semiconductor characteristics, especially for the power reduction with the temperature increase of the cell (about 50% less compared with the best crystallines silicon) and the better behaviour under diffuse radiation.
- Higher reliability of a-Si:H modules since there are no soldering joints between cells and the lamination process is stronger, so there is no need to place a polymer between the front glass and the solar cell.
- Building integrated photovoltaics (BIPV): The employment of PV modules as structural elements in buildings will probably become a big market in the near future. These modules generate electricity, act as tail or façade avoiding the water penetration,

reduce the temperature increase of the building in summer through the ventilated façade and reduce the heating consumption in winter by preheating the air of ventilation.

a-Si:H modules are better for BIPV since they are more aesthetic, have less orientation impact and have less price per m^2 . In Fig. 1.4 we see two examples with both technologies (c-Si in the left and a-Si:H in the right).



Figure 1.4: Two examples of BIPV (left c-Si [14], right a-Si:H [15] technology).

- a-Si:H needs more surface per W_p than c-Si technology since it has less efficiency (about 7.5% vs. about 15%). It is needed the double of surface for an equivalent power. Nevertheless, this is not crucial in many applications since, e.g. the land cost is less than 1% of the inversion of a PV solar farm.

1.2 Photovoltaic applications

Solar PV systems can be installed on rooftops, integrated in a building's envelope, or ground-mounted. PV applications include residential systems, larger industrial/commercial systems and utility-scale power plants, but also consumer goods. A solar PV system can be either connected to the grid or off-grid (also called "island systems") [4].

- **Grid-connected residential systems:** Can be rooftop, integrated in the building's envelope (used as a building component for insulation, roofing tile, shading, etc.) or mounted directly on the ground (e.g. in the garden). Connection to the local electricity network allows any excess power produced to feed into the electricity grid and to sell it to the utility. Electricity is imported from the network when there is no sun.

- **Grid-connected power plants:** Can be ground-mounted, or located on large industrial/commercial buildings such as shopping malls, airport terminals or railway stations. These produce a large quantity of PV electricity at a single point.
- **Off-grid systems for rural electrification:** Can be a small solar PV system covering the basic electricity needs of a household, or a larger solar mini-plant, providing enough power for several homes. These systems bring access to electricity to remote areas (mountain huts, villages in developing countries or small islands).
- **Off-grid industrial applications:** Very frequent in the telecommunications and transport fields. For example for repeater stations for mobile phones, traffic signals, marine navigation aids, security phones, remote lighting, highway signs, etc. These bring cost-effective power to areas far away from the electricity grid, avoiding the high cost of installing cabled networks.
- **Consumer goods:** Many everyday electrical appliances use PV solar cells: watches, calculators, toys, battery chargers, water sprinklers, lighting, etc.

1.3 Evolution of photovoltaic production and installed capacity

The data presented in this section is mainly obtained from the reports "Global market outlook for photovoltaics 2013 - 2017" of the European Photovoltaic Industry Association (EPIA) [5] and "PV status report 2012" of the Joint Research Centre (JRC) [2].

1.3.1 Photovoltaic market: Installations

The installed PV power here presented includes only systems connected to the grid and not those that have been installed but not yet connected.

In Fig. 1.5 the annual PV installations from 2000 to 2012 are presented. PV technology has grown over the past decade at a remarkable rate and is on the way to becoming a major source of power generation for the world. The annual PV installations in 2012 were about 31 GW. After the world-wide PV market more than doubled in 2010, the growth in 2011 was 80% compared to 2010, nevertheless, in 2012 the PV market stabilized. The 2012 market volume was mainly led by Germany (7.6 GW installed in 2012 / 32.4 GW cumulative installed capacity), China (5.0 GW / 8.3 GW), Italy (3.4 GW / 16.4 GW), the USA (3.3 GW / 7.8 GW) and Japan (2.0 GW / 6.9 GW).

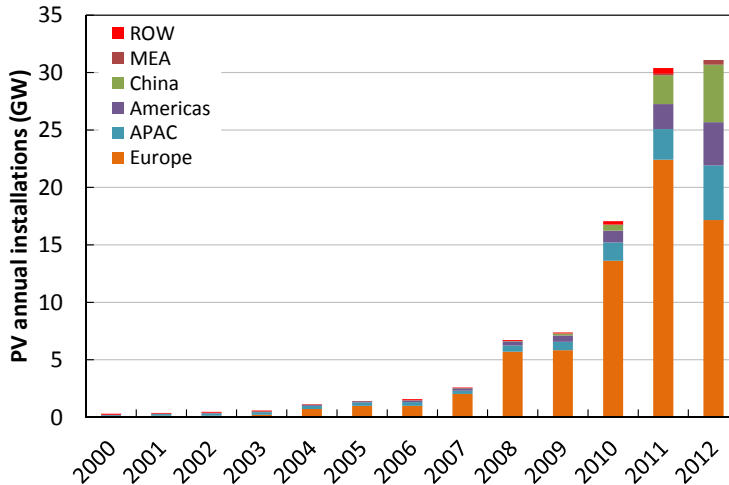


Figure 1.5: Annual PV installations from 2000 to 2012 [5]. ROW: Rest of the World, MEA: Middle East and Africa, APAC: Asia Pacific.

The results in 2012 and the forecast for the coming years indicate that Europe's leading role in the PV market is coming to an end. In 2011, Europe accounted for 74% of the world's new PV installations (22.4 GW); in 2012 this number was around 55% (17.2 GW) [5]. In 2013 it is almost certain that the majority of new PV capacity in the world will be installed outside of Europe. Therefore, in the next years the PV growth in Europe will occur at a more stable – and sustainable – rate than it has in the last few years. In the future the driving forces will be countries like China, the USA, Japan and India. The PV market is becoming truly global.

As shown in Fig. 1.6, at the end of 2012 the total cumulative PV installations world-wide were 102 GW. The 69% of the world-wide installed capacity (70 GW from the 102 GW) are installed in the European Union (EU). Moreover, Germany counts on 32 GW. In the period 2000 - 2012, Europe has increased 540 times (from 129 MW to 70 GW) its installed capacity [5], [16].

In 2012, for the second year in a row, PV was the number-one new source of electricity generation installed in Europe. PV covers 2.6% of the electricity demand in Europe [5]. The development of PV electricity in Europe is occurring at a faster rate than almost anyone had expected. As shown in Fig. 1.7, in 2012 a total of 44.9 GW of new power capacity was connected in the EU while 15.8 GW were decommissioned. This resulted in 29.1 GW of new

net capacity in the EU. From this figure, 16.7 GW (or 57%) of the new net capacity came from PV and 30.8 GW (or 106%) corresponded to renewable energies. The net capacity from non-renewable energies was negative [5].

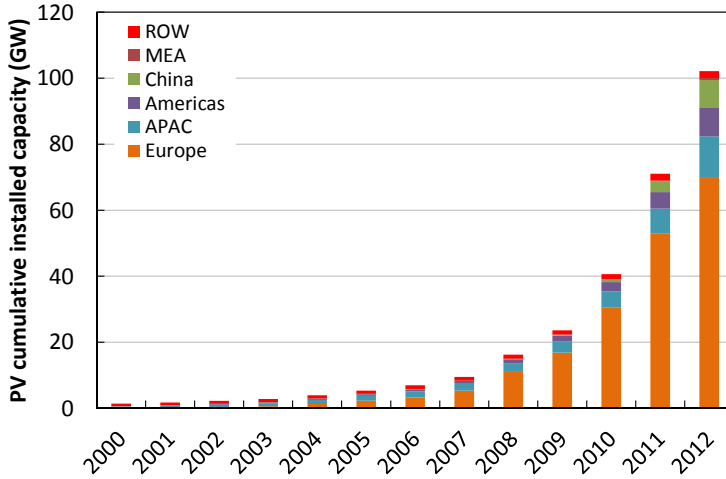


Figure 1.6: Cumulative PV installations from 2000 to 2012 [5].

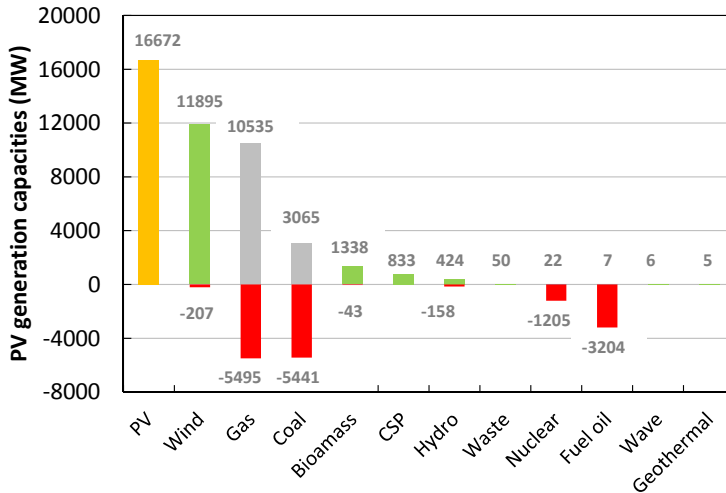


Figure 1.7: New installed or decommissioned electricity generation capacity in Europe in 2012 [5].

Regarding the future PV development, EPIA considers two scenarios for PV markets. The Business-as-usual scenario assumes rather pessimistic market behaviour. The Policy-driven scenario assumes a positive market behaviour, considering PV as a major power source in the coming years [5].

For the first time in the last 12 years, the PV market in Europe decreased in 2012 in terms of new connected capacity, as shown in Fig. 1.5. The future of the European market is uncertain for the coming years and the short-term prospects are stable in the best case or declining.

In the Business-as-usual scenario, the expected growth of markets outside Europe is not likely to compensate fast enough for the slowdown of the market in Europe in the two coming years. But even in this scenario, the global market could be as high as 48 GW in 2017 as indicated in Fig. 1.8 [5].

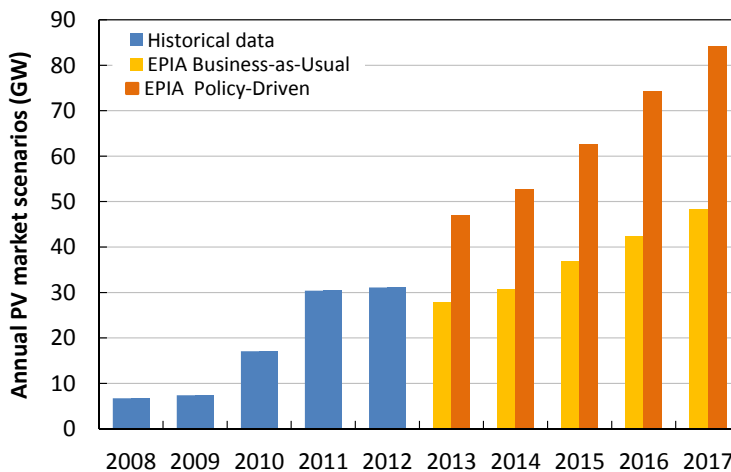


Figure 1.8: Annual PV market scenarios until 2017 - Business-as-usual and Policy-driven [5].

In the Policy-Driven scenario, the European market would stabilise first around 16 GW - 17 GW in 2013 before growing slowly again to around 25 GW - 28 GW five years from now. In that case, the global market could top more than 84 GW in 2017 (see Fig. 1.8), with two-thirds of this coming from new markets outside Europe [5]. EPIA expects the Asia Pacific (APAC) region (without China) to represent between 10 GW and 20 GW each year until 2017. China alone could add 10 GW of PV installations each year [5].

As shown in Fig. 1.9, in the Business-as-Usual scenario, the 200 GW mark could be reached in between 2014 and 2016, while in the Policy-Driven scenario, more than 420 GW of PV systems could be connected to the grid over the next five years [5].

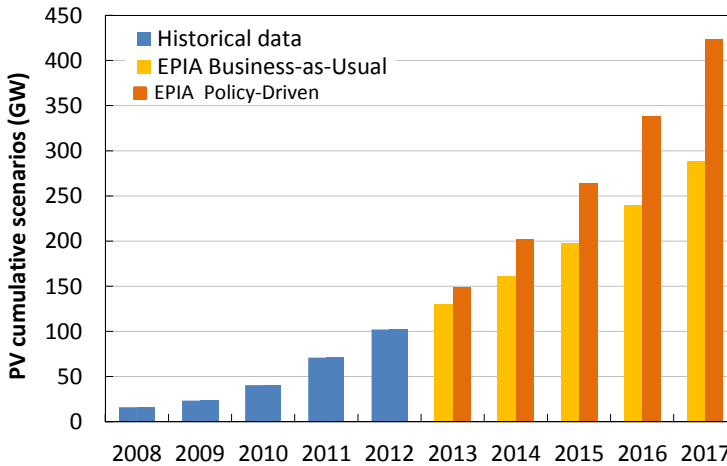


Figure 1.9: Cumulative PV market scenarios until 2017 - Business-as-usual and Policy-driven [5].

1.3.2 Photovoltaic industry

In 2012, the PV industry went again through a challenging period, with political, market and industry factors affecting business along the whole value chain. Important manufacturers disappeared, were acquired or had to adapt their business plan, decrease the utilisation rate and consequently reduce significantly their production. The tough market environment in Europe has forced many important players out of the PV business.

The PV global market capacity has evolved mainly in a context of production overcapacity. In the last three years, module production capacity was in between 150% - 230% higher than annual global installations [5]. This, resulted in continuous price pressure in PV systems market. However, the aggressive reduction of prices also opened new markets getting higher growth of the industry than hoped. This scenario benefits some PV companies and damages others.

In Fig. 1.10 world PV cell/module production from 2009 to 2012, as well as the forecast from 2013 to 2017 is presented (bar graph). In the period from 2000 to 2011, total PV

production increased almost by two orders of magnitude with annual growth rates between 40% and 90% [2]. According to IHS Solar, the world PV production capacity in 2012 reached 56.5 GW, increasing 24% compared to 2011. Those capacities are likely to grow continuously, with a growth rate of around 6% until 2017, reaching a production capacity up to 75 GW in 2017 [5].

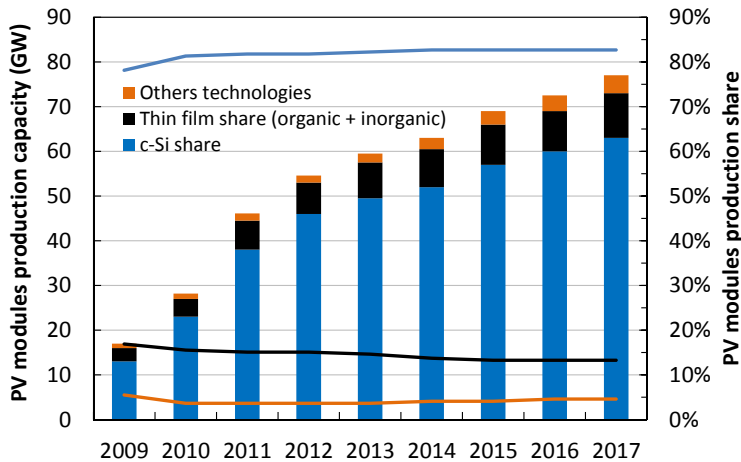


Figure 1.10: World PV cell/module production capacity from 2009 to 2012 and annual forecast until 2017 [5].

Since 2011, European industry represents only about 8% - 13% of the global market in terms of actual module production. China and APAC countries supply about 70% of the global PV demand [2], [5], since this region has experienced the most rapid growth in annual production over the last years.

Regarding the representation per technology, the predominant c-Si technology is expected to maintain its market share at levels slightly higher than 80% (blue line in Fig. 1.10). The main advantage of c-Si technology is that complete production lines can be bought, installed and producing within a relatively short time-frame. However, the temporary shortage in silicon feedstock and the market entry of companies offering turn-key production lines for thin film solar cells, led to a massive expansion of investments into thin film capacities between 2005 and 2009 (more than 200 companies are involved) [2].

In 2005 the production of thin film solar modules reached more than 100 MW/year. In the period 2005 - 2009, compound annual growth rate (CAGR) of thin film solar module production was beyond that of the overall industry increasing the market share of thin film

products: 6% in 2005, 10% in 2007 and between 16% - 20% in 2009. Since then, the thin film share (black line in Fig. 1.10) is decreasing slowly as their ramp up of new production lines did not follow that of wafer-based silicon due to the competing market price of c-Si technology. Anyway, the forecast for thin film is to grow at a lower rate, and therefore, their market share will stabilise over the next five years. If the forecast presented in Fig. 1.10 is fulfilled, thin film production capacity could be 10 GW or 13% of the total 75 GW in 2017.

The growth rate of a-Si:H technologies might be reduced by around 3% until 2017 [5]. The reason for this negative CAGR is the lower module efficiency of a-Si:H in comparison with the rapid evolution of CdTe and CIGS, limiting the market for thin film modules with efficiencies below 10% on module level.

Among emerging technologies, organic photovoltaic (OPV) technologies and especially concentration photovoltaic (CPV) technologies are expected to enjoy around 1% of the market share by 2017. The development of these technologies is accelerated by the positive development of the PV market.

The existing PV technology mix is a solid foundation for future growth of the sector as a whole. No single technology can satisfy all the different consumer needs.

1.3.3 Outlook

In 1996, the Directorate-General for Energy of the European Commission published the study "Photovoltaics in 2010" [17]. The medium scenario forecast a cumulative installed capacity of 3 GW in the EU by 2010. The most aggressive scenario in this report predicted a cumulative installed PV capacity of 27.3 GW world-wide and 8.7 GW in EU for 2010. The reality check reveals that even the most aggressive scenario is lower than what we expect from the current developments. At the end of 2010, PV systems with a cumulative capacity of over 41 GW world-wide and over 30 GW in Europe were generating electricity (the installations increased further to about 102 GW world-wide and 70 GW in Europe at the end of 2012).

Turnkey system prices as low as 1.0 €/W_p have been reported for projects to be finished in 2013 [18]. After the massive cost reductions for the technical components of PV systems like modules and other components (Balance Of System, BOS) the next challenge is to lower the soft costs of PV system installations, like the permission or financing costs [2].

The different PV industry associations, as well as Greenpeace, the European Renewable Energy Council (EREC) and the International Energy Agency (IEA), have developed new scenarios for the future growth of PV. Table 1.2 shows the different scenarios of the

Greenpeace / EREC study, as well as the different 2011 IEA World Energy Outlook scenarios and the IEA PV Technology Roadmap. It is interesting to note that the 2015 capacity values of four of the six scenarios presented in the table (in red) have already been reached or exceeded in 2012. With forecast cumulative PV installations (according to 2013 EPIA scenarios in Fig. 1.9) between 198 GW to 264 GW in 2015, even the Greenpeace revolution scenario is no longer fictional thinking [18].

Table 1.2: Evolution of the cumulative solar electrical capacities until 2035. In red, capacity values already reached or exceeded. Source: [2], [9], [19].

Cumulative PV power capacity (GW)	2012	2015	2020	2030	2035
Actual installations	102				
Greenpeace - Reference scenario*		88	124	234	290
Greenpeace - [r]evolution scenario*		234	674	1764	2420
IEA - Current policy scenario**		60	161	268	314
IEA - New policy scenario**		112	184	385	499
IEA - 450 ppm scenario**		70	220	625	901
IEA - PV technology roadmap***		76	210	872	1330

* 2035 values are extrapolated, as only 2030 and 2040 values are given

** 2015 values are extrapolated, as only 2009 and 2020 values are given

*** 2015 & 2035 values are extrapolated, as only 2010, 2020, 2030 & 2040 values are given

The IEA's Energy Technology Perspectives 2010 stated that for their current Baseline Scenario, the overall investments in energy supply and use, for the period between 2010 and 2050, totals € 208 trillion [20]. The BLUE-Map scenario, which would limit the concentration of Greenhouse Gases at 450 ppm, has an additional financing need of € 35.4 trillion, but at the same time the cumulative fuel savings of this scenario compared to the Baseline would be € 86.2 trillion, or more than twice the investment cost. This clearly indicates the huge societal benefit of a more aggressive climate change approach.

The photovoltaic industry has changed from a MW size industry into a mass-producing industry, aiming for multi GW production on the long term. The development to economy of scale that comes with large production volumes, allows new large solar cell companies to use their cost advantages to offer lower-priced products accelerating the growth rate. On the contrary, this development will influence negatively the small and medium companies. To survive they have to specialise in niche markets with high added value in their products.

Renewable energies are, contrary to conventional energy sources, the only ones to offer a reduction of prices rather than an increase in the future. We see a continuous decrease in production costs for renewable energy technologies, as a result of steep learning curves (see Fig. 1.11). Despite of this, renewable energies and photovoltaics are still perceived as being more expensive in the market than conventional energy sources. This is due to the fact that external energy costs, subsidies in conventional energies and price volatility risks are generally not yet taken into consideration. Nevertheless, electricity production from photovoltaic solar systems has already proved to be cheaper than residential consumer prices in a wide range of countries.

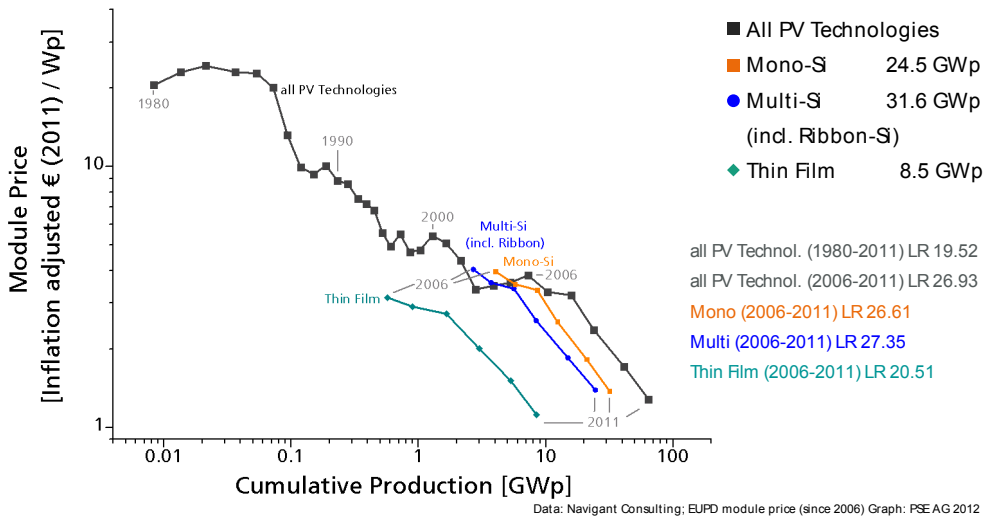


Figure 1.11: Price learning curve by technology from 1980 to 2011 [21].

1.4 Group T-Solar Global S.A.

T-Solar Global S.A. (T-Solar) is a company dedicated to hydrogenated amorphous silicon (a-Si:H) PV module manufacture. It was founded in October 2006 and is part of T-Solar Group which itself is a subsidiary of the multinational company Isolux. Its first PV modules were fabricated in July 2008.

T-Solar has implemented in its production line, which is fully automated and integrated, the SunFab factory technology from the American company Applied Materials Inc. (AMAT). T-Solar was the second customer of AMAT and its factory the first constructed in Europe. Its thin film module fabrication process was an innovative project on world-wide level, due to the low cost of the production process and the enormous size of the modules with dimensions of 2.2 m x 2.6 m and a maximum power of about 430 W_p (efficiency of 7.52%) [22]. The factory has an annual production capacity of about 72 MW_p, equivalent to about 900.000 m² of PV modules.

The factory is located in the "Parque Tecnológico de Galicia", part of the San Cibrao das Viñas industrial area, in Ourense, Spain. The production plant and the offices take up a plot of 29.000 m² (see Fig. 1.12). The laboratories are placed in the technical annex, the orange painted part of the building in the lower right side of Fig. 1.12.



Figure 1.12: T-Solar Global S.A.'s a-Si:H PV module factory.

Apart from fabrication and commercialization of PV modules, T-Solar Group has also built large PV power plants. It stands currently as one of the largest producers of PV electricity in Spain. In fact, it is one of the leading independent power producers (IPPs) of solar PV energy worldwide. The group has an installed capacity of 284 MW_p throughout Spain, Italy, India, Peru, Puerto Rico and California.

1.5 T-Solar production line: Fabrication process and process control

The manufacturing process for the T-Solar modules basically consists of the deposition of different thin films on 2.6 m x 2.2 m glass substrates covered with a transparent conductive oxide (TCO) layer and laser scribing process of the thin films to get separate cells and a monolithic cell interconnection to collect the current. By sequential deposition and laser scribing one achieves a series connection of 216 cells of 1 cm x 257 cm. The semiconductor structure is a-Si:H p-i-n junction which absorbs the light and generates an electron flux from the incident photon energy. The positive electrode (which contacts the first cell of the series connection) and the negative electrode (connected to the last cell) are both connected by means of metal strips to a junction box located in the back part of the module. Semiconductor layers are protected from moisture and mechanical friction using another glass substrate and a polyvinylbutyral (PVB) foil for encapsulation. The use of laser marking to define the monolithic connection between the cells contrasts with the technology employed on crystalline silicon PV panels, where cells are connected in series by welding conductive strips between them.

In Fig. 1.13 we see the basic steps of the module manufacturing process previously summarized. These steps are divided in two parts:

- Front end of line (FEOL). In this sector of the line, all the layers of the solar cell are deposited, therefore it covers the electrical part of the modules' production.
- Back end of line (BEOL) where basically the module is finished adding the buss connection to pick up the current, a back glass is laminated and the junction box is fixed.

Next, it is described in detail every step followed in the production of T-Solar a-Si:H thin film modules.

1. **Sheet glass panel and TCO:** In the manufacturing process, float glass panels with a size of 2.6 m x 2.2 m are used. Later, different thin films will be deposited on it. Nowadays, the glass arrives to the factory with the first layer already deposited on its top face, which is a TCO layer (see Fig. 1.14). The TCO is a transparent and conductive material, in this case its composition is fluorine-doped tin oxide ($\text{SnO}_2\text{:F}$). It carries

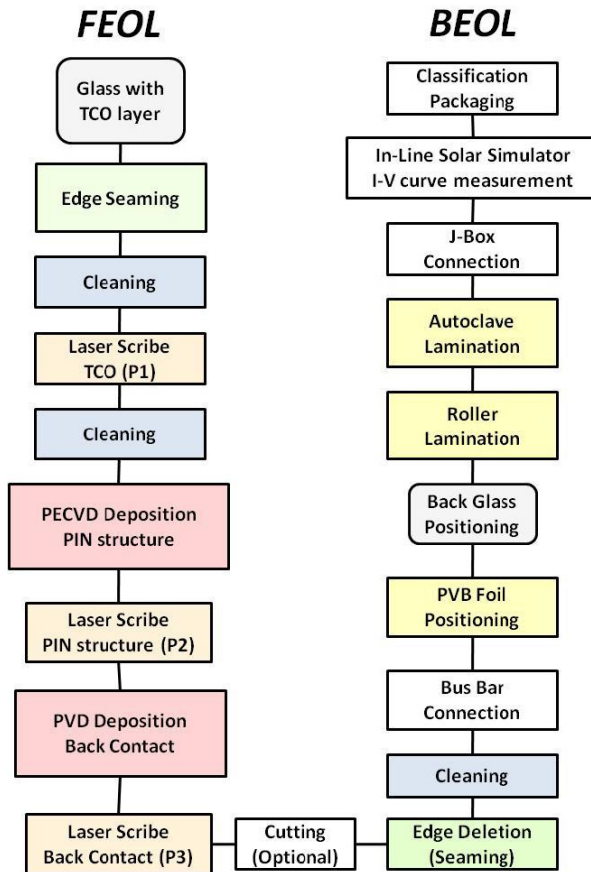


Figure 1.13: Basic steps of the manufacture process of T-Solar a-Si:H modules (FEOL = Front End Of Line, BEOL = Back End Of Line).

out two main functions, on the one hand, it allows the light to pass through it (with a high transmission coefficient) to absorb the maximum light in the silicon layer (p-i-n structure). Furthermore, the TCO layer has a high surface roughness that induces a dispersion effect increasing the light path in the a-Si:H film. And, on the other hand, the TCO acts like an electrical contact to transport the photogenerated charge carriers away from the p-i-n junction to the metal contact. Therefore it is a transparent front electrode.



Figure 1.14: Kuka robot charging a front TCO-glass at the beginning of the production line.

- Manual seaming and washing:** In the production line the first step is to take the TCO covered glass sheet (TCO-glass) with the front glass loader (Kuka robot) which places it on a conveyor. Then, in several process steps, a visual inspection of glass is done and edges are seamed (see Fig. 1.15) to eliminate any cracks, shavings or flakes that can damage both the glass itself and the process equipments as the glass advances through the production line. Later, the TCO-glass is washed.
- First laser (LSR) scribing, LSR1:** Once the panel is seamed and washed it passes to the first laser scribe, the first of three in total. For the three laser scribing operation the panel is previously set into a thermal conditioning station (TCS) to ensure that there are no changes in glass temperatures which would change the extension of the glass sheet. Any changes of the temperature could cause dilatation or contraction of the glass and consequently defective scribing, which needs precision in the μm range. Then, the panel goes to a clean room as the one in Fig. 1.16 and is placed onto an air table where it is fixed and then, the laser scribe is done.

LSR1 is used to burn or ablate in a line the TCO layer (which crosses the panel from up to down) about $30\ \mu\text{m}$ of width and with a distance between lines of 1 cm. Therefore, it creates the isolation along all the module (260 cm) for the 216 solar cells in series



Figure 1.15: Operator seaming the front glass sheet with TCO layer.



Figure 1.16: Laser tool picture. Panels are placed onto an air table.

(see Fig. 1.17). LSR1 applies a Neodymium-doped yttrium orthovanadate (Nd:YVO_4) light emission, working in Q-switch pulse mode with a maximum power of 16 W and

uses a wavelength of 1064 nm (infrared wavelength range). Consequently, the glass is transparent to it while it is absorbed by the TCO, vaporizing the film at high laser power.



Figure 1.17: TCO layer laser scribing step, P1 (cross section view) where is indicated the 1 cm width of one solar cell.

Furthermore, there is a second laser that marks a barcode in the TCO layer, this not only identifies the panel along the production line, but also enables a control over its lifetime. This step provides panel tracking and traceability. After this scribe, the glass sheet is washed again.

4. Silicon deposition in a plasma enhanced chemical vapour deposition (PECVD)

5.72 m² cluster tool: This step is the keystone of the silicon thin film PV module manufacture. It consists in the amorphous silicon layers deposition, the p-i-n structure.

The process is based on the deposition of a-Si:H layers by PECVD in a 7 chamber cluster tool on a 2.2 m x 2.6 m substrate (Fig. 1.18). The thin films are deposited from a gas (vapour) to a solid state on the substrate. The layers deposition on each module is done in two of the seven chambers available in the PECVD machine. One is used to deposit the p-layer (doped with trimethyl borane (TMB, $B(CH_3)_3$)) and the other one is used to deposit the intrinsic layer (i-layer) (non-doped) and the n-layer (doped with phosphine (PH_3)) (see Fig. 1.19). Detailed information about this process is given in section 4.4.

5. Second laser scribing, LSR2:

In the second laser scribing process the a-Si:H layers are ablated just beside the TCO scribe line. LSR2 applies a Nd:YVO₄ light emission, works in Q-switch pulse mode with a maximum power of 16 W and uses a wavelength of 532 nm (green). The glass and TCO layers are transparent to this laser light, whereas it is absorbed by the a-Si:H layers which are ablated at high laser power. This laser line (P2) later provides the interconnection between cells, allowing to transport the current from one cell to another through the area in contact with the front TCO as shown in



Figure 1.18: PECVD deposition cluster tool. It has an octagonal shape due to the fact that the seven deposition chambers and the load lock chamber, are all placed around a central transfer chamber.

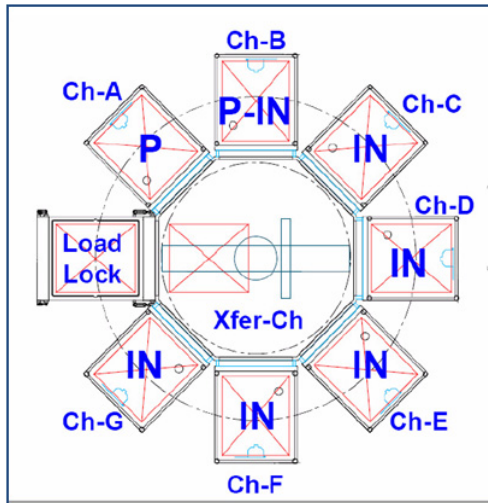


Figure 1.19: PECVD tool chamber usage for the p-i-n deposition.

Fig. 1.20. The width of the laser line is approximately $35 \mu\text{m}$ and it is separated about $105 \mu\text{m}$ from the first laser line.



Figure 1.20: a-Si:H laser scribing step, P2 (cross section view).

6. Back contact deposition in physical vapour deposition (PVD) 5.72 m² in-line sputter tool:

This last thin film deposition on the glass panel creates the back contact that consists of three layers which are obtained by PVD technique (Fig. 1.21). In our case this is a plasma process with pulsed direct current (DC) sputtering from ceramic and metallic targets in Argon (Ar)-atmosphere. The sputter compartment has a cathode (target) that is bombarded by the plasma atoms (Ar) to deposit metal on the glass. The chamber is evacuated with turbo pumps to achieve low base pressure (in the range of 1×10^{-6} mbar - 10×10^{-6} mbar), the deposition process is carried out at around 5×10^{-3} mbar of pressure. The following layers are implemented:

- Aluminium-doped zinc oxide (ZnO:Al or AZO): Acts as transparent back contact to improve the light reflection at the back metal layer and, thus, to improve the optical confinement. Layer thickness is about 90 nm, deposited with a planar target.
- Aluminium (Al): Reflective and conductive layer. Its thickness is about 200 nm, deposited simultaneously with dual rotatable targets.
- Nickel vanadium (NiV): Protective and solder layer. Its thickness is about 50 nm, deposited with a single rotatable target.

7. Third laser scribing, LSR3: The function of this last laser scribing is, together with LSR1, to isolate one cell from another at the back contact. LSR3 applies a Nd:YVO₄ light emission, works in Q-switch pulse mode with a maximum power of 16 W and uses a wavelength of 532 nm (green). It removes the a-Si:H layer and with it, the back contact by ablating them as presented in Fig. 1.22. The thickness of the laser line is approximately 40 μm and it is separated about 110 μm from the second laser line. The death area between outside extremes of the P1 and P3 laser scribes is about 250 μm . In Fig. 1.23 a microscope view of the three laser scribes with the separation between them and the diameter of each one is presented.



Figure 1.21: PVD sputtering tool.



Figure 1.22: a-Si:H and back contact laser scribing step, P3 (cross section view).

8. **Tests. Quality assurance and shunt removal:** Once the module is electrically finished, some basic electrical tests are done on each module in the quality assurance and shunt removal (QASR) tool. First, a shunt removal step is applied to eliminate shunts by reverse biasing the cells with a high current for a very short time. Then, the quality assurance checks the performance of every single solar cell on the panel by measuring the shunt resistance (R_{sh}) and open circuit voltage (V_{oc}) under low illumination.

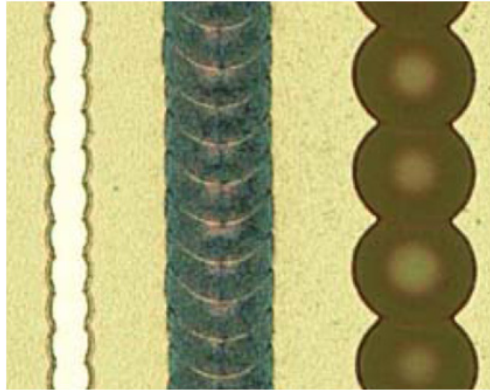


Figure 1.23: P1 (left), P2 (middle) and P3 (right) scribes (microscope view).

9. **Final cell structure:** The final structure of each solar cell is shown in Fig. 1.24. The generated current in the p-i-n junction passes vertically to the front TCO layer and it flows laterally from one cell to another through the P2 laser scribe area (LSR2 scribe) contacting the front TCO to the back contact and allowing the series connection between cells. Laser scribes 1 and 3 separate and isolate consecutive cells.

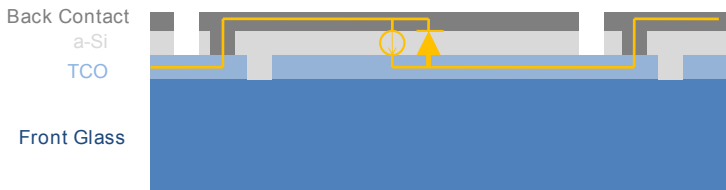


Figure 1.24: Final module structure which allows the current to flow among the cells (cross section view).

10. **Panel cutout (optional):** The cutting table is used only when other sizes, rather than the full size modules, are required (quarter size or half size). Fig. 1.25 presents the four different sizes available.
11. **Edge deletion by an automatic seaming:** In the next fabrication step, the layers at the glass edge are removed for a width of about 12 mm from the glass border. The goal is to get a module electrically well isolated and more resistant to meteorological

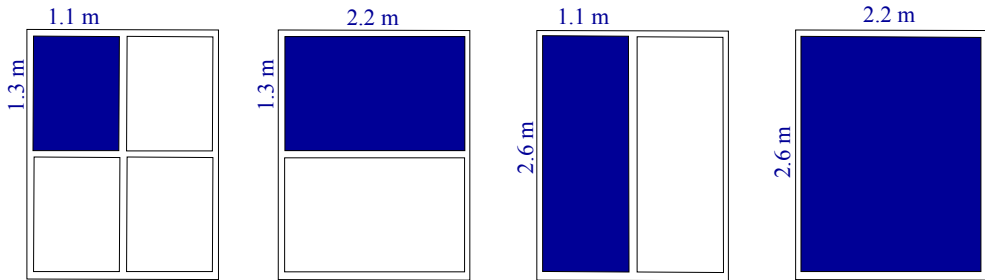


Figure 1.25: T-Solar production line is ready to produce modules of four different sizes.

inclemency. Humidity penetration caused by atmospheric exposure is prevented, as well as the current leaks at the borders and edges that can induce electric shock (the modules operate at about 200 V and 3 A). After this seaming process the module is washed again.

12. **Wiring:** The buss line attachment tool (see the left side of Fig. 1.26) places buss wires on the panel to retrieve the current from the module. The side buss wires are soldered on the first and last cell of the panel collecting the current of the whole panel (due to the series connection of the cells through the laser scribe). The cross buss wires are used to connect each side buss to the junction box.
13. **Polyvinyl butyral (PVB) foil and front glass positioning:** A PVB sheet is placed on the front panel to ensure the merge between the front and the back glass. The PVB is a hygroscopic material, thus it must be stored at low temperature (cold room) and handled under controlled temperature and humidity conditions (clean room as the one shown in the right side of Fig. 1.26). Next, the back glass is placed over the PVB.
14. **Module lamination.** This process consists of two stages:
 - Preheating at about 140 °C with the subsequent pressure roller laminator. This step deals the air removal.
 - Heating at about 230 °C with the subsequent pressure roller. This step seals the edges.

It is important to separate these two steps considering that, to obtain a good air removal you cannot apply high temperatures, otherwise the sealing of edges would start too



Figure 1.26: Buss tool picture (left) and clean room to handle the PVB (right).

early, enclosing inside some of the air. Lamination tool is shown in the left side of Fig. 1.27.

15. **Autoclave (ACL):** This process occurs at high pressure and temperature to ensure the complete elimination of the remaining air in the glass/PVB/glass sandwich. The process lasts about 3 h and reaches a pressure of about 12 bar - 13 bar and a temperature of 145 °C. The operation is done in a ramp of three steps: Heating, stabilization and cooling. ACL tool is shown in the right side of Fig. 1.27.
16. **Junction box attachment:** The junction box is an electrical connector to extract the current generated by the module (see left side of Fig. 1.28). The box contains two connectors that are soldered to the cross buss wires and a bypass diode to prevent the array from failing under partial shadow conditions since the panels are usually connected in series. Its placement consists of three phases:
 - Adhesion of the box to the rear glass.
 - Welding the pins of the junction box to the module wires.
 - Sealing and insulation the connections using a polymer (pottant).

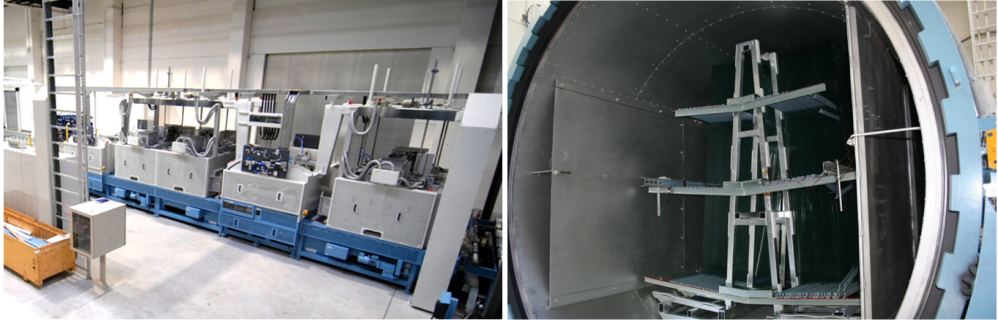


Figure 1.27: Lamination tool (left) and autoclave tool (right) overall view.

17. **In-line solar simulator:** When the module is finished it passes through the solar simulator in order to be electrically tested (see right side of Fig. 1.28). Modules are illuminated with a xenon lamp under standard test conditions (STC, 1000 W/m^2 light power, AM1.5G spectrum and $25 \text{ }^\circ\text{C}$ temperature) and then, their electrical parameters are measured (η , I_{sc} , V_{oc} , FF, R_s , R_{sh} , V_{mpp} , I_{mpp} and P_{mpp}). The data is stored for each module and is printed on a label (together with the series number and a bar code) which is glued on the backside of the module.

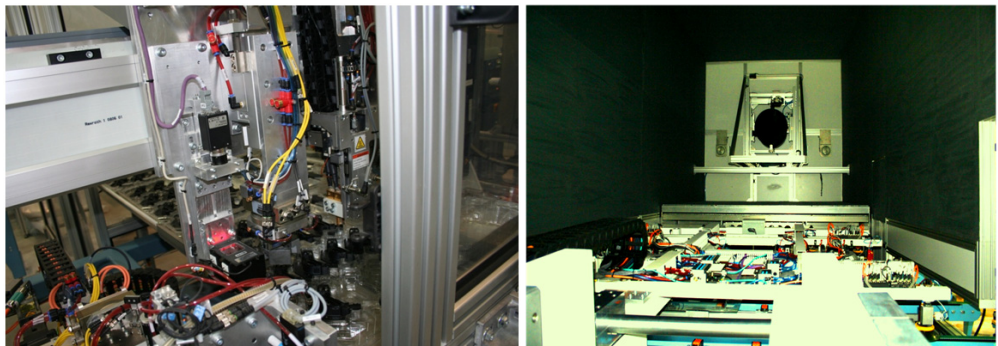


Figure 1.28: Junction box tool (left) and in-line solar simulator tool (right).

18. **Rail bonding:** Four (two) rails are placed in the full size modules (quarter size modules) on the back side of the module to fix it on the support structures when they are installed in the field.

19. **Sorting and packaging the PV modules:** The modules pass the last quality control, where is checked visually if they have any imperfection. Then, they are classified and packaged depending on their power. The power class achieved in the last generation of 5.72 m² full size modules is TS410, whose maximum power is 410 + 20 W. Fig. 1.29 shows a full and quarter size module as example.

The modules have been certified according to European standards IEC 61646 and IEC 61730. In addition, the plant where they are manufactured fulfils the standards ISO 9001, ISO 14001, OHSAS 28001 and EMAS.



Figure 1.29: Finished full and quarter size modules (lower left).

Since the very beginning of the production line, 100% of modules are handled in automatic mode by the material handling system (MHS). The MHS is controlled by the factory automation software (FAS) system, developed by AMAT. Another important tool to automate the production line is the "Sistema de Gestión y Monitorización Avanzado" (SIGMA) tool (advanced management and monitoring tool), which is a powerful in-home

developed interface for data collection and data mining. SIGMA software tool uploads in-line and on real time data (from tools, inspection metrology, etc) to be further studied and used for panel tracking and traceability. The information provided by SIGMA is commonly used by several departments such as management, R&D, quality, engineering, production, maintenance, logistics, etc. We divide the most important tasks of SIGMA into three fields:

- **Line management:** SIGMA offers detailed information about the actual and previous status of all the production line, e.g. tool status, tool specifications, material availability, panel location within the production line, panel history, or current and previous recipes used in each panel.
- **Product quality and process control:** They are done in-line and off-line. The electrical part is checked in the in-line solar simulator (ISS) (illuminated current-voltage (IV) curve), QASR (voltage measurement when the panel is electrically finished) and Brightview (PECVD layer properties). The optical properties control is mostly performed off-line in the laboratory. The visual control is done in-line by the quality operators which avoid that scrap panels with defects to go forward in the production line. In Fig. 1.30 a schematic control plan with all the controls made in-line and off-line is presented.
- **Tool control:** The different tools are also monitored and controlled with SIGMA. Therefore, all data of sensors available at the tools is stored.

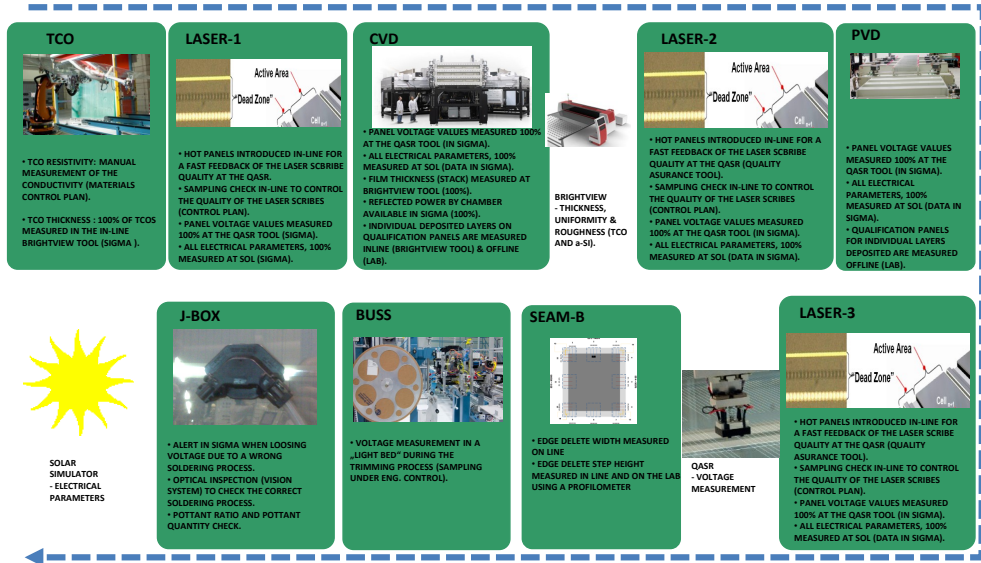


Figure 1.30: Control plan scheme with all the controls made in-line and off-line.

1.6 Technology and R&D Department

In order to improve the efficiency and quality of the modules and to develop the technology in the factory, T-Solar has installed a scientific laboratory. With the purpose of implementing in a fast and efficient way its research activity, this department operates directly beside the production line. In the organizational structure of T-Solar, the laboratory, where the here reported PhD activity was carried out, is located within the Technology and R&D Department. Some objectives of the Department are:

- To improve the process for each machine as well as for each process step of the production line.
- To optimize the optical and electrical properties of the modules, in order to increase their efficiency.
- To minimize the a-Si:H degradation due to illumination (Staebler-Wronski effect (SWE)).

- To develop and to implement production control techniques, such as new metrology systems, with the objective of verifying that modules meet the design specifications.

The tasks carried out by the laboratory staff are divided in two fields, control plan and R&D activities. The control plan activities are, on one hand, the control of the process parameters. This includes different measurements such as thickness, resistivity or optical properties of TCO, PECVD and PVD individual layers deposited on control panels. On the other hand, it consists on the implementation of the automation of the control plan by, e.g. developing in-line metrology equipments.

Concerning the R&D activities, T-Solar is collaborating with different institutions like the University of Santiago de Compostela (USC), the University of Vigo (UVI) and Galician research centers such as "Laboratorio Oficial de Metrología de Galicia" (LOMG) and "Asociación de Investigación Metalúrgica del Noroeste" (AIMEN).

Besides this, the most important research activity during the last three years, 2010-2012, was performed in the frame of the European Project HELATHIS, which is the acronym of "High Efficient very LARge area THIn film Silicon photovoltaic modules". This project was created in the program call "FP7 - ENERGY 2009.2.1.1: Efficiency and material issues for thin film photovoltaics". T-Solar was the coordinator, the other partners of the project were the Belgian subsidiary of the multinational glass producer AGC, AGC Flat Glass Europe S.A. (AGC); the photovoltaic department of the Research Centre Jülich GmbH (FZJ); the Debye Institute of the University Utrecht (UU); and the Department of Applied Physics and Optics of the University de Barcelona (UB). The participants cover the whole fabrication chain from the TCO-glass (AGC) to the final a-Si:H solar cells or small modules (UU, UB and FZJ) and of the very large area (5.72 m²) a-Si:H modules (T-Solar). In fact, T-Solar was the first company in Europe fabricating modules with size larger than 5 m². Covering the whole fabrication process allowed the consortium to implement fast optimization cycles for the *TCO-glass/p-i-n/back reflector* system. In the next section, more about the main aims of this project in the points related with this thesis will be explained.

T-Solar also participated in other national and regional projects such as the "Torres Quevedo" program from the Spanish Ministry of Economics and Competitiveness. The investigations of this PhD thesis were performed in the frame of the HELATHIS project and the "Torres Quevedo" program.

Finally, it is noteworthy to mention that a sophisticated Outdoor test station was developed over the years by the laboratory staff. It allows monitoring and measuring a large number

of modules under ambient conditions. Thus, we perform continuously studies to determine which R&D developments in modules present lower degradation coefficients and higher power in the stabilized state. The Outdoor test station includes a complete meteorological station placed next to the modules, which collects every 5 s data of irradiance, air temperature, wind and relative humidity providing additional information about the modules performance under different climate conditions.

1.7 FP7 European Project HELATHIS

The HELATHIS project identifies optical light confinement as a key point to increase our module efficiency. The optimization of the properties of the TCO layers at the front contact and the back reflector must be achieved for large area deposition. Additionally, methods for the reduction of reflection losses at the front glass shall be developed. This optimization has to be done, on one hand, for a-Si:H single junction (SJ) solar cells and modules and, on the other hand, for hydrogenated amorphous silicon/micro-crystalline silicon (a-Si:H/ μ c-Si:H) tandem junction (TJ) solar cells and modules. On the present work, only SJ solar cells will be analysed.

The project has developed innovative schemes for application in large area industrial modules. This includes most of the optical confinement strategies that are presently state-of-the-art in highest efficiency a-Si:H laboratory cells. The objective of the project has been to push the implementation of optical layers as part of adapted thin film silicon solar cells into large scale production facilities. In the time frame of 3 years (since beginning 2010) a stabilized large scale module (5.72 m^2) efficiency of 8% for very large area SJ and 11% for very large area TJ modules should be achieved.

The quantum efficiency in conventional superstrate cells is always $< 80\%$. About 10% is accounted for by reflection losses, the rest is lost by absorption in the glass, front TCO and p-layer. A reduction of the reflection and absorption losses shall therefore, increase considerably the output power. In addition, to increase the light absorbed in the active layer (i-layer), to improve the light trapping is crucial since in a-Si:H SJ solar cells the current is limited by weak absorption in the red part of the solar spectrum. To improve the optical light confinement the main targets are:

- Development of anti-reflection coating (ARC) on front glass surface.
- Optimization of TCO at the front and back contact.

- Implementation of optimized solar cell structures.

Keeping in mind the basic structure of a solar module (see Fig. 1.24), three interfaces are relevant for the optimization of light confinement: 1) the front glass surface, 2) the glass/solar cell interface and 3) the solar cell back side. The project has four technical work packages (WP) in reference to these interfaces and investigated in this thesis:

- **Front glass surface:** To achieve higher module efficiencies, it is necessary to apply anti-reflection concepts on the exterior front glass surface. These could include structuring or texturing of the glass front side and/or the deposition of an ARC. Small scale industrial processes exist for ARC's. But the growing demand of low cost coated glass for PV applications requires a new process that can be integrated or combined with a float glass production line. Tasks in this context have been:
 - Development of ARC on front glass surface.
 - Implementation of ARC on large area solar modules.
 - Implementation of low iron content glasses which presents higher integrated transmission.
- **Glass/TCO interface:** Nowadays large-scale TCO coatings for PV applications have been developed by glass producers and are being used by solar cell manufacturers. These large scale TCOs made by chemical vapour deposition (CVD) on a float line do not reach the performance of the reference TCO made by off-line CVD on a smaller scale. Due to the separated development of TCO and solar cell, they do not yet fulfil the requirements for an optimized solar module. Therefore, the solar cell processes and back reflector design had to be adapted to the TCO available on the market. A major problem is that the interactions of the properties of these TCOs with the solar cell are still poorly understood. Tasks in this context have been:
 - Benchmarking of commercial and laboratory TCO substrates newly developed.
 - Development and improvement of new front TCOs by in-line and off-line atmospheric pressure chemical vapour deposition (APCVD).
 - Characterization of newly developed TCOs.
 - Application of newly developed TCOs on very large area.

– Back reflector:

- Accelerated feedback from laboratories to improve the efficiency of industrial modules.
- Development of back reflectors on the laboratory scale with potential for up-scaling to large area modules.
- Evaluation and application of the optimized back reflectors to industrial large area modules.

– Advanced characterization methods:

- Analysis of the surface structure and identification of optimized profiles for light trapping.
- Development of advanced electrical and optical characterization of material properties.
- Identification of the best stabilized ARC under light soaking and environmental conditions.

Several development cycles have been made to improve the previously industrially available large area float glass/TCO layer structure. The fabrication of coated glass samples was made in the float line equipment of AGC (APCVD SnO_2). The optical and electrical properties of the different glass/TCO structures and the rest of layers have been investigated by the different participants. The most promising glass/TCO structures have been identified in laboratory solar cells and small modules in which the p-i-n/back reflector system has been optimized. Once the development cycle was finished, the TCO-glasses with the best characteristics were tested in T-Solar industrial modules. After optimizing and adopting the process performance of the industrial fabrication process, the TCO-glass was implemented in T-Solar module's production line as standard substrate.

The results and advances achieved in the different layers and interfaces during the project, as well as the further potential of improvement, will be presented in chapter 4.

CHAPTER 2

THEORY AND SIMULATION MODELS OF A-Si:H SOLAR CELLS

The development and recent fast growth of the PV industry has resulted in modules oversupply and a fast decrease of module prices in the last years, demanding now on all actors in the PV sector an important increase in R&D activities to be competitive in the future. Performing experimental work in a production line to achieve efficiency improvements is very expensive, reason why we consider device simulation as one of the best tools to achieve a faster development. Therefore, we have performed two dimensional simulations of a-Si:H solar cell structures with the objective to find the best performance of the solar cell under given material properties.

First of all, in this chapter, the electrical model that governs the a-Si:H solar cells is presented, as well as their equivalent circuit, both obtained from the ideal diode model and deduced from the c-Si solar cell model. Then, the physical model is explained emphasising the differences between the properties of a-Si:H and c-Si. The most important changes result from the density of states (DOS), the recombination-generation statistics, the graded layers and the light induced degradation produced in a-Si:H due to the Staebler-Wronski effect (SWE). Next, it is explained how the optical generation is produced in a-Si:H solar cells; how the spectral irradiance is considered and how the optical transmission, reflection and absorption works in the different solar cell layers. As well, we point out the different methods adopted in the here used Sentaurus (Synopsys) simulation tool to study both models, with flat or textured layers. Finally, a summary is presented about how the semiconductor equations are solved. That

section introduces the equations and boundary conditions that the Sentaurus software solves to get, e.g., the IV curves or external quantum efficiency (EQE) curves. The simulated device is meshed forming thousands of nodes. The respective equations describing the device are discretised in every of these nodes. Then, the resulting system of equations is linearised and solved with the Gummel or Newton-Raphson methods.

2.1 Electrical model

The photovoltaic effect is the direct conversion of the light in electricity without any mechanical movement. This effect consists in the photon-semiconductor interaction when the material is illuminated. The energy of a photon with energy higher than the semiconductor's electronic band gap is absorbed by the electrons giving them the possibility to jump over the gap between the valence band and the conduction band and therefore, electron-hole ($e-h$) pairs are generated (see Fig. 2.1). The implementation of a p-n or p-i-n junction (as used in a-Si:H technology) induces an electric field which separates the electrons and holes and thus an electric current is produced. Under dark conditions the behaviour of solar cells is the same as diodes. So, the electrical model of solar cells is governed by the equation of the ideal diode:

$$I = I_0 \left[\exp\left(\frac{qV}{nkT}\right) - 1 \right] \quad (2.1)$$

where:

$$I_0 = S \left(\frac{qD_e n_i^2}{L_e N_A} + \frac{qD_h n_i^2}{L_h N_D} \right) \quad (2.2)$$

and where S (cm²) is the surface of our device; q is the electron charge, $q = 1.602 \times 10^{-19}$ C; D_e (cm²/s) is the diffusion constant of electrons (e), D_h (cm²/s) is the diffusion constant of holes (h); n_i (cm⁻³) is the intrinsic free carrier concentration; L_e (cm) is the electron diffusion length; L_h (cm) is the hole diffusion length; N_A (cm⁻³) is the acceptor doping concentration; N_D (cm⁻³) is the donor doping concentration; I_0 (A) is the reverse saturated current under dark conditions; n is the ideality factor of the diode, $1 \leq n \leq 2$; k is the Boltzman constant, $k = 1.38 \times 10^{-23}$ (J/K); T (K) is the device temperature; V (V) is the voltage across the device; I (A) is the device current.

Equations 2.1 and 2.2 consider a p-n junction with constant doping, carrier diffusion of quasi-neutral regions, negligible current unbalance and approximation of carrier injection at zero bias ($n_{p0} \approx n_i^2/N_A$, $p_{n0} \approx n_i^2/N_D$). Where n_{p0} (cm⁻³) is the minority electron

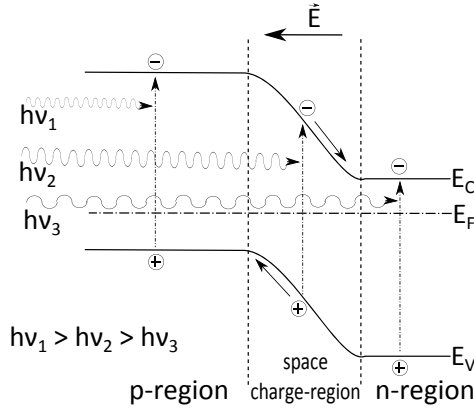


Figure 2.1: Generation of electron-hole pairs due to the photon incidence in a p-n junction. The photons with larger wavelengths ($h\nu_3$) are absorbed most deeply in the semiconductor than the photons with shorter wavelengths ($h\nu_1$ and $h\nu_2$).

concentration in equilibrium in the neutral p-region and p_{n0} (cm^{-3}) is the minority hole concentration in equilibrium in the neutral n-region.

Introducing the current generated by irradiance (I_{ph}) in Eq. 2.1, we get the simplified illuminated IV curve for c-Si solar cells (Eq. 2.3):

$$I = I_0 \left[\exp \left(\frac{qV}{nkT} \right) - 1 \right] - I_{ph} \quad (2.3)$$

where:

$$I_{ph} = qSG(L_e + W + L_h) \quad (2.4)$$

and where G ($\text{cm}^{-3} \text{ s}^{-1}$) is the generation rate, W (cm) is the thickness of the space charge-region and I_{ph} (A) is the illuminated current generated in the solar cell.

As presented in Fig. 2.2, the typical IV curve of a solar cell is like the one of a diode shifted in the negative current axis by a quantity I_{ph} . The important part of the curve is in the fourth quadrant. To have a more intuitive view, the current is usually changed in sign, presenting the curve in the first quadrant.

Eq. 2.3 represents an electrical circuit with a diode and an illumination source. To obtain a more accurate model to present the illuminated IV curves of solar cells we have to introduce a series resistance (R_s) and a parallel or shunt resistance (R_{sh}) into the equivalent circuit (see

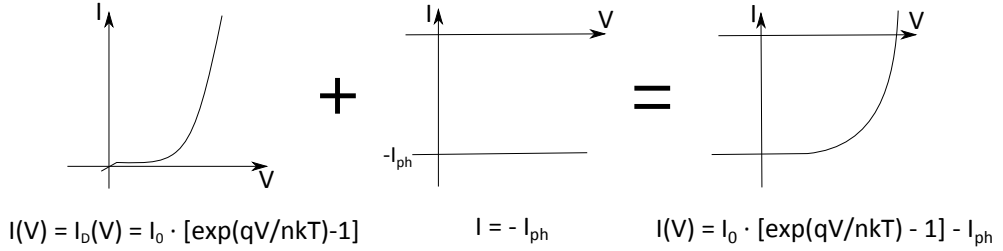


Figure 2.2: Solar cell IV curve as result of the diode IV curve minus the I_{ph} .

Fig. 2.3). Hence, in eq. 2.3, we have to substitute the voltage drop at the diode, V , by $V - IR_s$ and to add the term $(V - IR_s)/R_{sh}$ as a sum in the second part of the equality.

To get the illuminated IV curve for a-Si:H p-i-n junction solar cells we have to add a term due to current loss by recombination within the i-layer, thus we obtain [23]:

$$I = -I_{ph} + I_{ph} \frac{d_i^2}{(\mu\tau)_{eff}[V_{bi} - (V - IR_s)]} + I_0 \left(\exp\left(\frac{q(V - IR_s)}{nkT}\right) - 1 \right) + \frac{V - IR_s}{R_{sh}} \quad (2.5)$$

where V_{bi} (V) is the built-in voltage, which is the difference between the electron and hole quasi-Fermi levels under illuminated conditions, its value depends on the illumination level; d_i (cm) is the p-i-n junction thickness for the solar cell; $(\mu\tau)_{eff}$ (cm^2/V), where μ ($\text{cm}^2/(\text{V}\cdot\text{s})$) is the effective carrier mobility in the intrinsic region and τ (s) the effective carrier lifetime in the intrinsic region. The equivalent circuit is shown in Fig. 2.3.

With this equation we obtain the typical IV curve of an a-Si:H solar cell. The term $I_{rec} = I_{ph} \frac{d_i^2}{(\mu\tau)_{eff}[V_{bi} - (V - IR_s)]}$ describes the recombination in the intrinsic region. It is important to consider this term in the a-Si:H technology due to the SWE (see subsection 2.2.5). This term expresses a decrease in the carriers mobility and lifetime with illumination time.

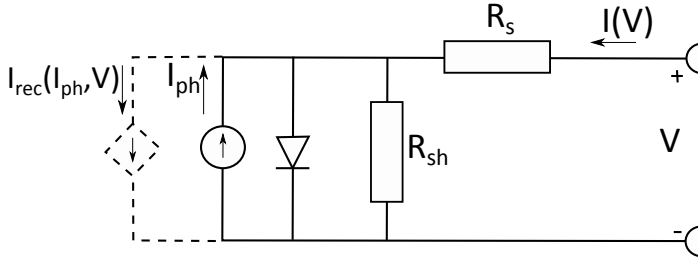


Figure 2.3: Equivalent circuit of an a-Si:H solar cell. The current sink (I_{rec} , dashed lines) takes into account the current losses due to recombination in the i-layer of the device [23].

2.2 Physical model

Silicon (Si) belongs to IV group of the periodic element table and has four electrons in its valence band that form a tetrahedral structure through covalent bonds when it forms a crystal or an amorphous structure. When doped with a V group element, such as phosphorus (P), there is an excess of electrons and provides a n-type semiconductor material (donor). On the other hand, if III group impurities are introduced, e.g. boron (B), holes are created in the network of atoms, resulting in a p-type semiconductor material (acceptor).

Crystalline semiconductors are materials with a very low concentration of contaminants and a crystalline structure with a very low density of structural defects. The effort to industrialize solar cells at lower costs has led to the development of thin film semiconductor devices such as a-Si:H solar cells. The properties of a-Si:H are different from the ones of c-Si, as a consequence, solar cells based on this material, need an special device structure. Next, we present the main differences in material properties in terms of device features:

- **Carrier mobility:** Doped a-Si:H films present a very short carrier lifetime due to its high defect density and the resulting fast recombination processes. Therefore, one uses an intrinsic (non-doped) material with low defect density as absorber layer that allows the generated carriers (electrons or holes) to have larger lifetime. The carriers are separated due to the electric field created by very thin p and n-layers deposited on top and bottom of the intrinsic layer (see Fig. 2.4). The drift length produced by the electric field is longer than the width of the intrinsic region. Therefore, the solar cell structure of amorphous silicon (a-Si:H) modules is generally p-i-n or n-i-p type.



Figure 2.4: p-i-n structure.

- **Structure:** Amorphous silicon molecules have a local tetrahedral bonding structure similar to c-Si, but the amorphous structure has an important amount of sites with a lower electronic coordination, in these sites a non-saturated bond (or dangling bond) appears. These non-saturated bonds produce electronic states with energies close to the middle of the gap (recombination centres). Therefore, the amorphous silicon films are deposited in a plasma containing a silane (SiH_4)/hydrogen (H_2) atmosphere. Due to the high amount of hydrogen in the plasma, hydrogen is bonded to the silicon (Si) atoms in the sites with lower electronic coordination, saturating the dangling bonds (see Fig. 2.5). This is an important process to achieve amorphous silicon with electronic device quality with a low defect density and carrier recombination rate.

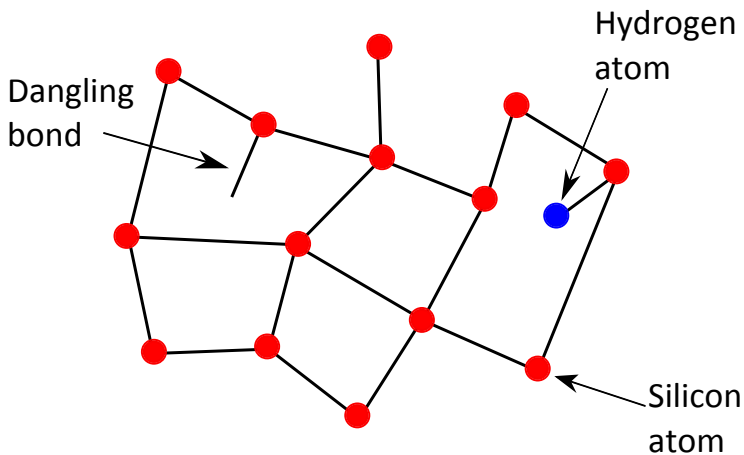


Figure 2.5: Amorphous silicon structure (random network) showing a bond with a hydrogen atom.

- **Electronic states:** Even without long range order, a-Si:H presents band states similar to the ones of c-Si. The valence band can be understood as a product of the bonding sp^3

orbital and the conduction band as a product of the antibonding sp^3 . The unsaturated bonds produce electronic states with energies close to the middle of the gap. For non-hydrogenated silicon the density of these defects is about 10^{20} cm^{-3} , hydrogen introduction decreases this density to about 10^{16} cm^{-3} . The disorder also produces exponential tails of localized states near the edges of the conduction and valence bands. The energy limit between extended and localized states is called the mobility edge.

- **Doping:** Although a-Si:H can be doped with several atoms, the doping efficiency is much lower than that in c-Si. For n-type doping the minimum separation between Fermi level and conduction band is 0.25 eV. For p-type doping the minimum distance between valence band and Fermi level is 0.40 eV. The reason of lower Fermi level shift in comparison to c-Si is because most of the electrons released by the donors in n-type a-Si:H go to a defect and do not contribute to fill the conduction band. In the same way, most of the acceptors take the electron from a deep defect state in p-type a-Si:H and do not come from the valence band.

Regarding the simulations, there are different software packages available for electronic device simulation in the market. Sentaurus TCAD software (Synopsys Inc.) is one of the most advanced tools. We have chosen this tool to simulate complex 2D a-Si:H solar cell structures. Sentaurus is basically designed for simulation of electronic devices. Therefore, it can be used for the simulation of a-Si:H devices since it is based on using physical models to describe the semiconductor material properties and solving the semiconductor equations. However, to simulate a-Si:H devices a lot of basic configuration work must be done. Besides the standard models and equations used for c-Si, the main features to include in an a-Si:H solar cell simulation are [24]:

- Theoretical models to describe a continuous DOS distribution in the band gap of a-Si:H.
- Model for recombination-generation (R-G) rate and occupation involving the localized states in the mobility gap of a-Si:H.
- Modelling of graded layers.
- Introduction of textured layers (front TCO). Optical modelling including scattering at the rough interfaces.

In the next sections the description of the models of a-Si:H for the DOS distribution, R-G statistics, graded layers and textured layers is introduced.

2.2.1 Density of states models for amorphous silicon

The standard model of the DOS distribution consists in a parabolic conduction band (CB) and valence band (VB) as in c-Si. In addition, in a-Si:H, the continuous distribution of the DOS in the band gap strongly affects the trapping and recombination processes and therefore, the trapped charge in the localized states cannot be ignored. The localized states are formed by:

- **Tail states:** They are modelled by an exponential distribution in the energy gap which are called conduction band tail (CBT) and valence band tail (VBT). They behave like ordinary acceptor-like states (CB tail states) or donor-like states (VB tail states).
- **Dangling bond states** ($DB^{+/0}$ and $DB^{0/-}$): They are simulated by adding two equal Gaussian distributions separated by an energy U . The dangling bond (DB) are amphoteric states so they can act both as acceptor-like and donor-like states and are represented by two energy levels.

The different nature of the localized states in comparison to the extended states requires that different models are applied to calculate R-G statistics through localized states. It is assumed that within the mobility gap the mobility of charge carriers is zero.

Next, we show the standard model of the DOS distribution in a-Si:H on a linear scale in Fig. 2.6 and on a logarithmic scale in Fig. 2.7. It is assumed that the mobility edges of conduction and valence band (E_C^{mob} and E_V^{mob}) are equal to the connection points (E_C^{tail} and E_V^{tail}), thus $E_C^{mob} = E_C^{tail}$, $E_V^{mob} = E_V^{tail}$. The values of DOS at the mobility edges E_C^{mob} and E_V^{mob} are denoted N_C^{mob} and N_V^{mob} , respectively.

The energy levels E_C and E_V , in eV, define the band gap. In the case of a-Si:H it corresponds to the so-called optical band gap, E_{gap}^{opt} (eV) (see Fig. 2.6):

$$E_{gap}^{opt} = E_C - E_V \quad (2.6)$$

When considering the transport properties of carriers in a-Si:H we have to differentiate between the extended states and the localized states in the DOS distribution. The energy levels E_C^{mob} and E_V^{mob} , define the mobility gap, E_{gap}^{mob} (eV) (see Fig. 2.7):

$$E_{gap}^{mob} = E_C^{mob} - E_V^{mob} \quad (2.7)$$

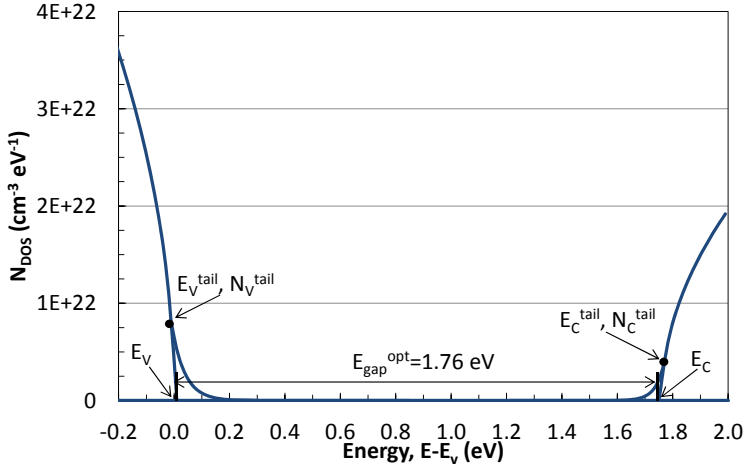


Figure 2.6: DOS distribution model for intrinsic a-Si:H layer on a linear scale. The density in the conduction band is lower than in the valence band resulting in a non-symmetric DOS distribution. The points (E_C^{tail}, N_C^{tail}) and (E_V^{tail}, N_V^{tail}) are the connection between the parabolic distribution of extended states and the exponential distribution of tails.

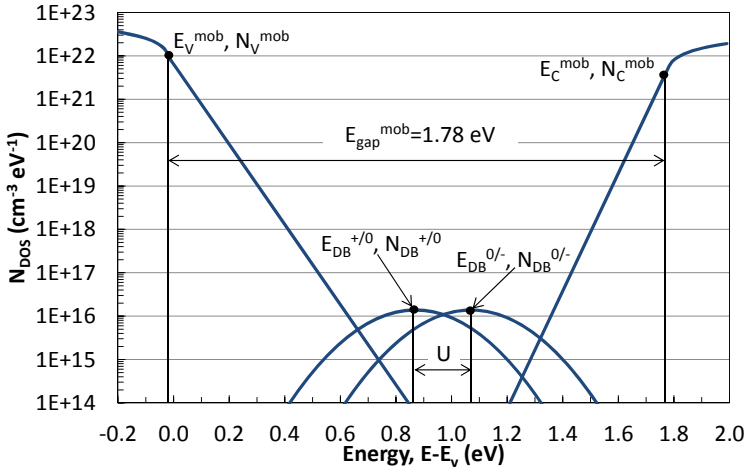


Figure 2.7: DOS distribution model for intrinsic a-Si:H layer on a logarithmic scale. It is assumed that the mobility edges are equal to the connection points $(E_C^{mob} = E_C^{tail}, E_V^{mob} = E_V^{tail})$.

The mathematical description of the DOS distribution in a-Si:H is given by the equations presented in the following subsections [25].

Conduction and valence band states

The DOS distribution of the conduction band is given by:

$$N_{CB+CBT}(E) = \begin{cases} N_{CB}(E) & \text{for } E \geq E_C^{tail} \\ N_{CBT}(E) & \text{for } E \leq E_C^{tail} \end{cases} \quad (2.8)$$

$$N_{CB}(E) = N_C^0(E - E_C)^{(1/2)} \quad (2.9)$$

$$N_{CBT}(E) = N_C^{tail} \exp \left[-\left(\frac{E_C^{tail} - E}{E_{C0}^{tail}} \right) \right] \quad (2.10)$$

The DOS distribution of the valence band is given by:

$$N_{VB+VBT}(E) = \begin{cases} N_{VB}(E) & \text{for } E \leq E_V^{tail} \\ N_{VBT}(E) & \text{for } E \geq E_V^{tail} \end{cases} \quad (2.11)$$

$$N_{VB}(E) = N_V^0(E_V - E)^{(1/2)} \quad (2.12)$$

$$N_{VBT}(E) = N_V^{tail} \exp \left[-\left(\frac{E - E_V^{tail}}{E_{V0}^{tail}} \right) \right] \quad (2.13)$$

where N_C^0 and N_V^0 , in cm^{-3} , are the parameters which describes the parabolic distribution of states in the conduction and valence band respectively; E_{C0}^{tail} and E_{V0}^{tail} , in eV, are the characteristic energies describing the decay of the CB and VB tails respectively and $(E_C^{tail}$, $N_C^{tail})$ and $(E_V^{tail}$, $N_V^{tail})$ are the connection points of the parabolic and exponential part of the conduction and valence band, respectively.

Dangling bond states

To describe the continuous distribution of the DB states in the band gap, a Gaussian distribution is used. A DB can be in three charge states: positive (D^+), neutral (D^0) and negative (D^-). A defect with three possible charge states acts in good approximation like a group of two defects consisting of a donor-like state ($DB^{+/0}$) and an acceptor-like state ($DB^{0/-}$) and is therefore represented by two energy levels $E^{+/0}$ and $E^{0/-}$ in the band diagram, respectively. These energy levels are called the transition energy levels, they are separated from each other by a correlation energy, U (eV), which is the energy needed to add the second electron to a singly occupied (neutral) DB. U is assumed to be constant and positive. Under these assumptions the DB are represented by two equal Gaussian distributions in the band

diagram separated from each other by a distance U . The equations to represent the density of DB states are the following:

$$N_{DB^{+/0}}(E) = \frac{N_{DB}^{tot}}{\sigma_{DB}\sqrt{2\pi}} \exp\left[-\frac{(E - E_{DB}^{+/0})^2}{2\sigma_{DB}^2}\right] \quad (2.14a)$$

$$N_{DB^{0/-}}(E) = \frac{N_{DB}^{tot}}{\sigma_{DB}\sqrt{2\pi}} \exp\left[-\frac{(E - E_{DB}^{0/-})^2}{2\sigma_{DB}^2}\right] \quad (2.14b)$$

where N_{DB}^{tot} (cm^{-3}) is the total density of defects, $E_{DB}^{+/0}$ and $E_{DB}^{0/-}$, in eV, are the energies of the peaks of Gaussian distributions for the donor-like states $DB^{+/0}$ and the acceptor-like states $DB^{0/-}$, respectively and σ_{DB} (eV) is the standard deviation of the distribution.

To correlate $N_{DB^{+/0}}$ and $N_{DB^{0/-}}$ and $E_{DB}^{+/0}$ and $E_{DB}^{0/-}$ one uses the next relations:

$$N_{DB^{0/-}}(E) = N_{DB^{+/0}}(E + U) \quad (2.15)$$

$$E_{DB}^{0/-} = E_{DB}^{+/0} + U \quad (2.16)$$

Concentration of charge carriers

The states in the conduction band above the mobility edge E_C^{mob} are extended states. They are populated with electrons that are characterized by the concentration n and the extended-state mobility $\mu_n > 0$. The states in the valence band below the mobility edge E_V^{mob} are also extended states. They are populated with holes that are characterized by the concentration p and the extended-state mobility $\mu_p > 0$.

In the operational range of a-Si:H solar cells the dominant electric transport mechanism is multiple trapping and release. The transport is then characterized by the concentration of carriers in the extended states (n , p) and the extended-state mobilities (μ_n , μ_p). Furthermore, it is assumed that the mobilities are the same in thermal equilibrium and in steady state illumination conditions. For the concentration of charge carriers we can write [25]:

$$n = N_{C_{mob}}^{eff} \exp\left(\frac{E_{FN} - E_C^{mob}}{kT}\right) \quad (2.17a)$$

$$p = N_{V_{mob}}^{eff} \exp\left(\frac{E_V^{mob} - E_{FP}}{kT}\right) \quad (2.17b)$$

where $N_{C_{mob}}^{eff}$ and $N_{V_{mob}}^{eff}$, in cm^{-3} , are the effective density of states at the CB and VB mobility edge. In case of a-Si:H the effective density of states N_C and N_V are equal to $N_{C_{mob}}^{eff}$ and $N_{V_{mob}}^{eff}$, respectively.

2.2.2 Recombination-generation statistics in amorphous silicon

The recombination process in crystalline semiconductors is typically dominated by a single energy level of a recombination center in the band gap. However, in the band gap of a-Si:H there is a continuous density of allowed states which contribute to the net R-G rate. Hence, one needs to integrate the recombination rate contributions from the gap states over the whole band gap. Under the assumption that the recombination centres are non-interacting, the net R-G rate, R_{net} ($\text{cm}^{-3} \text{s}^{-1}$), can be calculated from:

$$R_{net} = \int_{E_V^{mob}}^{E_C^{mob}} N(E) \eta_R(E) dE \quad (2.18)$$

where $\eta_R(E)$ is the recombination rate contribution of a state at energy E and $N(E)$ is the DOS as function of energy in the band gap.

The trapped charge in tail states is calculated using the following equations for ordinary donor-like and acceptor-like states, respectively:

$$\rho_D = q \int_{E_C^{mob}}^{E_V^{mob}} N_D(E) [1 - f(E)] dE \quad (2.19)$$

$$\rho_A = -q \int_{E_C^{mob}}^{E_V^{mob}} N_A(E) f(E) dE \quad (2.20)$$

where $f(E)$ is the occupation function [26] [27]. In case of the amphoteric DB states the space charge is given by:

$$\rho_{DB} = q \int_{E_C^{mob}}^{E_V^{mob}} N_{DB}(E) [F^+(E) - F^-(E)] dE \quad (2.21)$$

In this equation $F^+(E)$ and $F^-(E)$ are the occupation functions of empty and doubly occupied DB, respectively.

The assumption of non-interacting centres means that the localized states in the band gap can only interact with carriers in the extended states of the conduction and valence bands. This assumption allows to use the Shockley Read Hall (SRH) R-G statistics [28] to model the recombination process through the single-level states and the Sah and Shockley [29] multi-level R-G statistics for the amphoteric DB states. The different types of the localized states in the band gap of a-Si:H and the models that are used to calculate the recombination rate through these states and their charge occupation are schematized in Fig. 2.8.

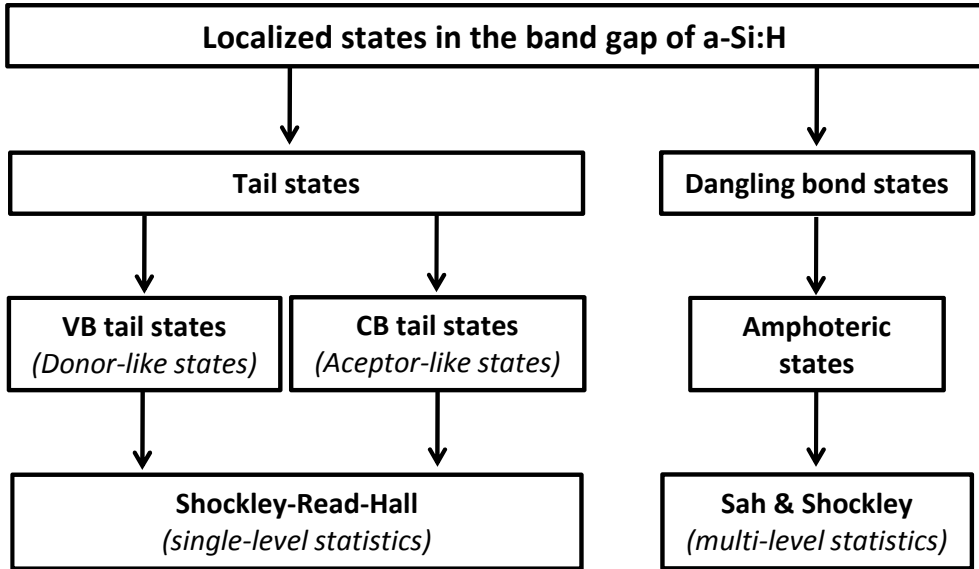


Figure 2.8: Different types of localized states in the band gap of a-Si:H and models that are used to calculate the recombination rate and charge occupation [25].

R-G statistics of CB and VB tail states

In the energy band diagram, the donor and acceptor R-G center is represented by a single energy level. The CB tail states behave like ordinary acceptor states and are neutral (T_A^0) or negative (T_A^-). The VB tail states behave like ordinary donor states and are neutral (T_D^0) or positive (T_D^+). The theory that describes the recombination process involving a single energy level in the band gap of a semiconductor was developed by Shockley and Read [28] and Hall [30], [31].

The SRH theory is based on four possible transitions between an energy level E_T in the band gap and the extended states of the CB and VB:

1. Electron capture at an R-G center.
2. Electron thermal emission from an R-G center.
3. Hole capture at an R-G center.
4. Hole thermal emission from an R-G center.

These processes are schematically shown in Fig. 2.9 and their corresponding rates of change in the carrier concentrations are listed in Table 2.1.

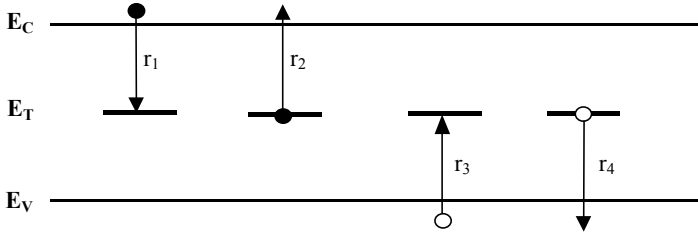


Figure 2.9: Electronic transitions in the recombination process between a single energy level in the band gap of a semiconductor and the energy bands [25].

The recombination rate of the VB and CB tail states are presented next:

– **VB tail states:**

The resulting expression for the recombination rate of the VB tail states, R_{VB} ($\text{cm}^{-3} \text{s}^{-1}$), at energy E_T is:

$$R_{VB} = N_D \frac{C_p^0 C_n^+ (np - n_i^2)}{C_p^0 n + e_p^+ + C_n^+ p + e_n^0} \quad (2.22)$$

in this equation, N_D (cm^{-3}) is the total number of donor-like states at energy E_T (eV); C_p^0 and C_n^+ , in cm^3/s , are the capture coefficients for holes and electrons and e_p^+ and e_n^0 , in s^{-1} , are the emission coefficients for holes and electrons, respectively. These

Table 2.1: Time rates of change in the carrier concentrations for transitions involving VB and CB tail states at an arbitrary energy level E_T in the band gap [25].

Process	VB tail states (donor-like R-G centers)		CB tail states (acceptor-like R-G centers)	
	Transition	Rate ($\text{cm}^{-3}\text{s}^{-1}$)	Transition	Rate ($\text{cm}^{-3}\text{s}^{-1}$)
r ₁ Electron capture	$T_D^+ + e \rightarrow T_D^0$	$n \cdot C_n^+ \cdot N_D \cdot (1 - f^0)$	$T_A^0 + e \rightarrow T_A^-$	$n \cdot C_n^0 \cdot N_A \cdot (1 - f^-)$
r ₂ Electron emission	$T_D^0 \rightarrow T_D^+ + e$	$e_n^0 \cdot N_D \cdot f^0$	$T_A^- \rightarrow T_A^0 + e$	$e_n^- \cdot N_A \cdot f^-$
r ₃ Hole capture	$T_D^0 + h \rightarrow T_D^+$	$p \cdot C_p^0 \cdot N_D \cdot f^0$	$T_A^- + h \rightarrow T_A^0$	$p \cdot C_p^- \cdot N_A \cdot f^-$
r ₄ Hole emission	$T_D^+ \rightarrow T_D^0 + h$	$e_p^+ \cdot N_D \cdot (1 - f^0)$	$T_A^0 \rightarrow T_A^- + h$	$e_p^0 \cdot N_A \cdot (1 - f^-)$

emission coefficients are determined from the principle of detailed balance [26]. This principle states that, under equilibrium conditions, each fundamental process and its inverse must self-balance independently of any other process that may be occurring inside the material. Under the assumption that the emission and capture coefficients under non-equilibrium conditions remain approximately equal to their equilibrium values, the emission coefficients for electrons and holes can be expressed as:

$$e_n^0 = C_n^+ N_C \exp[(E_T - E_C)/kT] \quad (2.23a)$$

$$e_p^+ = C_p^0 N_V \exp[(E_V - E_T)/kT] \quad (2.23b)$$

In thermal equilibrium, the occupation function of states at energy E_T is described by the Fermi-Dirac distribution function. The steady-state occupation function of donor-like states (f^0) is given by:

$$f^0 = \frac{C_n^+ n + e_p^+}{C_p^0 p + e_p^+ + C_n^+ n + e_n^0} \quad (2.24)$$

Since the density of VB tail states continuously decays within the band gap, the total R-G rate and concentration of localized holes including all VB tail states is calculated by integrating over the band gap the equations 2.18 and 2.19, respectively. In praxis, the integrals from these equations are replaced in Sentaurus by a summation over a set of m discrete energy levels on which the continuous density of VB tail states is applied:

$$R_{VB}^{tot} = \sum_m R_{VB} \quad (2.25)$$

$$p_{VB}^{tot} = \sum_m N_D (1 - f^0) \quad (2.26)$$

– CB tail states:

The derivation of the recombination rate (R_{CB}) and steady state occupation function of the CB tail states (f^-) is analogous to the one of VB tail states. The resulting equations are:

$$R_{CB} = N_A \frac{C_p^- C_n^0 (np - n_i^2)}{C_p^- n + e_p^0 + C_n^0 p + e_n^-} \quad (2.27)$$

$$e_n^- = C_n^0 N_C \exp[(E_T - E_C)/kT] \quad (2.28a)$$

$$e_p^0 = C_p^- N_V \exp[(E_V - E_T)/kT] \quad (2.28b)$$

$$f^- = \frac{C_n^0 n + e_p^0}{C_p^- p + e_p^0 + C_n^0 n + e_n^-} \quad (2.29)$$

where N_A (cm^{-3}) is the total number of acceptor-like states at energy E_T ; C_p^- and C_n^0 , in cm^3/s , are the capture coefficient for holes and electrons and e_p^0 and e_n^- , in s^{-1} , are the emission coefficient for holes and electrons, respectively.

The total R-G rate and concentration of localized electrons including all CB tail states is calculated from Eqs. 2.18 and 2.20, respectively, replacing the integrals by a summation:

$$R_{CB}^{tot} = \sum_m R_{CB} \quad (2.30)$$

$$n_{CB}^{tot} = \sum_m N_A f^- \quad (2.31)$$

R-G statistics of DB states

As explained previously, a dangling bond can be in three charge states: positive (D^+), neutral (D^0) and negative (D^-). In the band diagram a dangling bond is represented by the two transition energy levels ($E^{+/0}$ and $E^{0/-}$). The recombination process involving these amphoteric DB states is described by the Sah and Shockley multi-level R-G statistics. Possible electronic transitions between an amphoteric R-G center and the extended states are illustrated in Fig. 2.10, as well, the rates of change in carrier concentrations due to these transitions are listed in Table 2.2.

The probability whether a dangling bond is in positive, neutral or negative charge state is given by the occupation functions F^+ , F^0 and F^- , respectively. The sum of the occupation functions has to be the unity:

$$F^+ + F^0 + F^- = 1 \quad (2.32)$$

The emission coefficients are determined from the principle of detailed balance using the thermal equilibrium occupation functions [32], capture coefficients, and electron and hole concentrations:

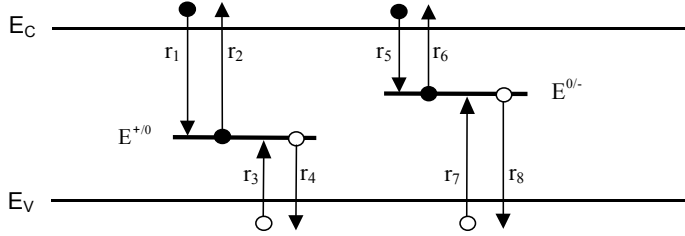


Figure 2.10: Possible electronic transitions in the recombination process between the energy bands and an amphoteric R-G center represented by two energy levels in the band gap [25].

$$e_n^0 = C_n^+ N_C \exp \left[\frac{(E - kT \ln 2) - E_C}{kT} \right] \quad (2.33a)$$

$$e_p^+ = C_p^0 N_V \exp \left[\frac{E_V - (E - kT \ln 2)}{kT} \right] \quad (2.33b)$$

$$e_n^- = C_n^0 N_C \exp \left[\frac{(E + U + kT \ln 2) - E_C}{kT} \right] \quad (2.33c)$$

$$e_p^0 = C_p^- N_V \exp \left[\frac{E_V - (E + U + kT \ln 2)}{kT} \right] \quad (2.33d)$$

Under steady state conditions the charge occupation of the DB states does not change with time, which leads to the following equations:

$$0 = N_{DB} (-C_n^+ n F^+ + e_n^0 F^0 + C_p^0 p F^0 - e_p^+ F^+) \quad (2.34a)$$

$$0 = N_{DB} (-C_n^0 n F^0 + e_n^- F^- + C_p^- p F^- - e_p^0 F^0) \quad (2.34b)$$

Table 2.2: Transition rates of change in the carrier concentrations for recombination processes involving DB states [25].

Process	DB ⁺⁰ states		DB ⁰⁻ states	
	Transition	Rate (cm ⁻³ s ⁻¹)	Transition	Rate (cm ⁻³ s ⁻¹)
Electron capture	r₁ $D^+ + e^- \rightarrow D^0$	$n \cdot C_n^+ \cdot N_{DB} \cdot F^+$	r₅ $D^0 + e^- \rightarrow D^-$	$n \cdot C_n^0 \cdot N_{DB} \cdot F^0$
Electron emission	r₂ $D^0 \rightarrow D^+ + e^-$	$e_n^0 \cdot N_{DB} \cdot F^0$	r₆ $D^- \rightarrow D^0 + e^-$	$e_n^- \cdot N_{DB} \cdot F^-$
Hole capture	r₃ $D^0 + h^- \rightarrow D^+$	$p \cdot C_p^0 \cdot N_{DB} \cdot F^0$	r₇ $D^- + h^- \rightarrow D^0$	$p \cdot C_p^- \cdot N_{DB} \cdot F^-$
Hole emission	r₄ $D^+ \rightarrow D^0 + h^-$	$e_p^+ \cdot N_{DB} \cdot F^+$	r₈ $D^0 \rightarrow D^- + h^-$	$e_p^0 \cdot N_{DB} \cdot F^0$

where N_{DB} (cm^{-3}) is the concentration of DB states represented by transitions between $E^{+}/0$ and $E^{0}/-$ transition levels.

After a bit of manipulation one can rewrite the equations 2.34 as:

$$F^+N^+ = F^0P^0 \quad (2.35a)$$

$$F^0N^0 = F^-P^- \quad (2.35b)$$

where we have considered:

$$N^+ = C_n^+n + e_p^+ \quad (2.36a)$$

$$P^0 = C_p^0p + e_n^0 \quad (2.36b)$$

$$N^0 = C_n^0n + e_p^0 \quad (2.36c)$$

$$P^- = C_p^-p + e_n^- \quad (2.36d)$$

Taking into account that the sum of the occupation functions is the unity, the steady-state occupation functions can be described as follows:

$$F^+ = \frac{P^-P^0}{N^+P^- + P^0P^- + N^+N^0} \quad (2.37a)$$

$$F^0 = \frac{P^-N^+}{N^+P^- + P^0P^- + N^+N^0} \quad (2.37b)$$

$$F^- = \frac{N^0N^+}{N^+P^- + P^0P^- + N^+N^0} \quad (2.37c)$$

The R-G rate involving the DB states represented by a pair of energy levels $E^{+}/0$ and $E^{0}/-$ in the band gap is:

$$R_{DB} = N_{DB}(np - n_i^2) \frac{C_n^+C_p^0P^- + C_n^0C_p^-N^+}{N^+P^- + P^0P^- + N^+N^0} \quad (2.38)$$

The net contribution of all DB states to the R-G is calculated using equation 2.18. The integral in this equation is replaced in Sentaurus by summation over a set of m discrete energy levels on which the continuous density of DB states is applied:

$$R_{DB}^{tot} = \sum_m R_{DB} \quad (2.39)$$

The total concentration of localized holes and electrons in DB states is calculated using the following expressions, respectively:

$$p_{DB}^{tot} = \sum_m N_{DB} F^+ \quad (2.40a)$$

$$n_{DB}^{tot} = \sum_m N_{DB} F^- \quad (2.40b)$$

Total R-G rate and space charge in the localized states of the band gap

The net R-G rate including all states in the band gap is calculated as a sum of the net R-G rates of VB and CB tail states and DB states:

$$R_{net} = R_{VB}^{tot} + R_{CB}^{tot} + R_{DB}^{tot} \quad (2.41)$$

On the other hand, the total space charge (C/cm^3) in the localized states in the band gap is:

$$\rho_{loc}^{tot} = q(p_{VB}^{tot} - n_{CB}^{tot} + p_{DB}^{tot} - n_{DB}^{tot}) \quad (2.42)$$

2.2.3 Graded layers

In a-Si:H p-i-n solar cells, the first 10 nm - 20 nm have a dominant influence on the overall performance of the device [25]. A major improvement in the efficiency was obtained by incorporating a carbonated (a-SiC:H) p-layer which has a wider band gap than pure a-Si:H [33]. Another important change to enhance the performance in the blue wavelength region of the spectrum was the introduction of a buffer layer with graded doping concentration at the p/i interface (piB-layer) [34].

In general, the improved quantum efficiency (QE) in the blue region and a higher V_{oc} and fill factor (FF) have usually been attributed to a reduced interface density of recombination centres near the junction [34], [35].

The properties of the n-layer and the i/n interface are much less critical to the cell performance because the local generation rate is much smaller than at the p/i interface.

To simulate the graded piB-layer we introduce a doping profile, to pass from the doping in the p-layer to the non-doped intrinsic layer.

2.2.4 Band structure

For device simulation, the most fundamental property of a semiconductor is its band structure. In Sentaurus [36], the band structure is simplified to four quantities: band gap, electron affinity and effective masses for electrons and holes.

- **Electron and hole effective masses:** The electron and hole effective masses are defined with the next formula [36]:

$$\frac{m_e}{m_0} = \left(\frac{N_{C,300}}{2.540 \times 10^{19}} \right)^{2/3} \quad (2.43a)$$

$$\frac{m_h}{m_0} = \left(\frac{N_{V,300}}{2.540 \times 10^{19}} \right)^{2/3} \quad (2.43b)$$

where we set $N_{C,300} = N_{V,300} = 1.0 \times 10^{20} \text{ (cm}^{-3}\text{)}$ which are the effective DOS in the CB and VB, respectively at a temperature of 300 K. To know the effective DOS at any temperature we apply the next equation:

$$N_C(T) = N_{C,300} \cdot (T/300)^{3/2} \quad (2.44a)$$

$$N_V(T) = N_{V,300} \cdot (T/300)^{3/2} \quad (2.44b)$$

- **Band gap and electron affinity:** In crystalline semiconductors, the band gap (E_G) is the difference between the lowest energy in the CB and the highest energy in the VB (E_G^{opt} in Fig. 2.6). In a-Si:H based material the E_G represents the mobility gap (E_G^{mob} in Fig. 2.7). The electron affinity (χ) is the difference between the lowest energy in the CB and the vacuum level (E_0).

Sentaurus models the lattice temperature–dependence of the band gap as [37]:

$$E_G(T) = E_G(0) - \frac{\alpha T^2}{T + \beta} \quad (2.45)$$

where we have chosen $\beta = 0$ and $\alpha = 0.0004 \text{ eV/K}$ [38].

The effective band gap results from the reduction caused by the temperature and doping concentration. It is presented in the next equation:

$$E_{G,eff}(T) = E_G(T) - E_{BGN} \quad (2.46)$$

Another parameter that can be obtained from the previous ones is the intrinsic density:

$$n_i(T) = \sqrt{N_C(T)N_V(T)} \cdot \exp\left(-\frac{E_G(T)}{2kT}\right) \quad (2.47)$$

The effective intrinsic density (including doping-dependent band gap narrowing) is:

$$n_{i,eff} = n_i \cdot \exp\left(-\frac{E_{BGN}}{2kT}\right) \quad (2.48)$$

where E_{BGN} (eV) is the energy reduction in the band gap due to high doping level.

Fig. 2.11 shows the band diagram for the a-Si:H p-i-n layers under illumination and without polarization. One can appreciate that the doped layers are much thinner than the intrinsic layer which has sloped energy bands as consequence of the electric field created by the doped layers. One also sees a larger energy gap for the p-layer due to its carbon content (a-SiC:H) which increases the energy band gap with the objective to absorb less photons in this region.

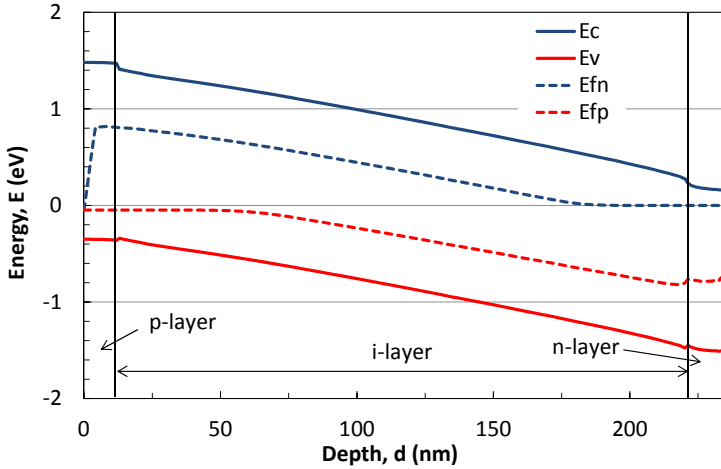


Figure 2.11: Band diagram for the a-Si:H p-i-n layers under 1 sun illumination and without polarization ($V = 0$ V). The drop in E_{FN} at the beginning of the p-layer is because the anode is placed at the TCO/p interface.

2.2.5 Light-induced degradation. Staebler-Wronski effect

The a-Si:H presents a light-induced metastability of its electronic properties (also known as Staebler-Wronski effect, SWE) [39], [40]. It causes a reduction of the conversion efficiency of a-Si:H solar cells due to light exposure. The rate of degradation during continuous illumination at 1 sun (1000 W/m^2) intensity is high during the first tens of hours, but decreases over time. Finally, the cell performance stabilizes after several hundreds of hours.

The initial efficiency can be completely recovered by annealing of the device at about 150 °C for several hours. The reversibility of the device performance shows that the initial loss is not due to diffusion of ions or dopants, nor to other irreversible processes, but it is due to the increase of DB defects created in the i-layer which act as recombination centres for the photogenerated carriers. The metastable DBs have an energetic and spatial distribution, which determines their charge state. The space charge distribution of the charged states then, modifies the internal electric field profile which in turn has an effect on the carrier collection in the device [25].

The main material properties that could play a role in the SWE are the concentration of impurities, the hydrogen concentration and its complex bonding structure and the disorder of the Si network.

The most commonly observed effects in the electrical parameters of p-i-n a-Si:H solar cells are:

- The biggest relative changes occur in the fill factor (FF), the relative changes in short circuit current density (J_{sc}) and open circuit voltage (V_{oc}) are significantly smaller.
- Solar cells with a thick intrinsic layer degrade more than those with a thin intrinsic layer.
- Solar cells with a high impurity concentration (above 10^{18} cm^{-3}) in the i-layer degrade stronger than those with high purity i-layer.
- Solar cells operated at elevated temperatures (60 °C - 90 °C) stabilize at a higher efficiency than those operated at room temperature or below.
- Cyclic exposure results into a higher efficiency stabilization than continuous exposure.
- Exposure at high intensity illumination causes stronger degradation than 1 sun. Illumination levels less than 1000 W/m^2 lead to reduced degradation.

In order to reduce the SWE related degradation of a-Si:H solar cells several methods have been investigated, e.g.:

- To make the i-layer as thin as possible in order to maintain a high electric field after degradation. At the same time, the absorbed fraction of the incident light is maximized by using optical light confinement techniques made possible by textured electrodes and enhanced multilayer back reflectors.

- To assist the transport of the minority carriers (holes) in the low field region by band gap profiling [41].
- To redistribute the field by using graded low-level impurity doping [42].
- To stack layers with different carrier mobilities, making a mobility grading [43].

2.2.6 Baseline input parameters applied in the simulation

The here simulated structure is $TCO/a-SiC:H/a-Si:H/a-Si:H/AZO/Al$ implemented in the T-Solar module fabrication. In the simulation we assume an ideal tunnel contact at the front contact and an ideal ohmic contact at the back one. To implement this, we fix the front contact at the TCO/p-layer interface and the back contact at the end of the Al layer. Hence, the electrical features of the TCO are not considered, only its optical characteristics are taken into account. The p-i-n single junction solar cell is shown in Fig. 2.12.

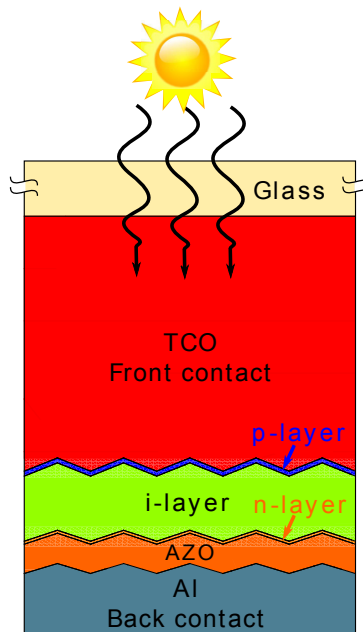


Figure 2.12: Structure of the simulated a-Si:H solar cell.

Table 2.3 shows the baseline input parameters for the initial state used in the simulation. The values are adjusted to fit the electrical parameters and the spectral response of our typical 1 cm² laboratory a-Si:H solar cells produced in the T-Solar production line. To simulate the stabilized state (light-soaked state) we only need to increase the maximum density of dangling bonds (N_{DB}) in the i-layer [44].

Table 2.3: Baseline input parameters used in the simulation. Some parameters were taken from [25]

	p-layer	i-layer	n-layer
MATERIAL PARAMETERS			
d (nm)	10-30	200-300	10-20
Doping (cm ⁻³)	3×10^{18}	1×10^{15}	8×10^{18}
ϵ_r	7.2	11.9	11.9
χ (eV)	3.90	4.00	3.99
E_{gap}^{mob} (eV)	1.95	1.78	1.80
μ_n (cm ² /(V·s))	20	20	20
μ_p (cm ² /(V·s))	5	5	5
N_C (cm ⁻³)	1×10^{20}	1×10^{20}	1×10^{20}
N_V (cm ⁻³)	1×10^{20}	1×10^{20}	1×10^{20}
TAIL STATES PARAMETERS			
N_C^{tail} (cm ⁻³ /eV)	2×10^{21}	8×10^{21}	1×10^{21}
N_V^{tail} (cm ⁻³ /eV)	1×10^{21}	4×10^{21}	2×10^{21}
E_{C0}^{tail} (eV)	0.180	0.032	0.070
E_{V0}^{tail} (eV)	0.090	0.047	0.160
C_p^-, C_n^+ (cm ³ /s)	1×10^{-8}	1×10^{-8}	1×10^{-8}
C_p^0, C_n^0 (cm ³ /s)	1×10^{-10}	1×10^{-10}	1×10^{-10}
DANGLING BOND STATES PARAMETERS			
σ (eV)	0.144	0.144	0.144
N_{DB}^{tot} (cm ⁻³)	8×10^{18}	5×10^{15}	2×10^{19}
$E_{DB}^{+/0}$ (eV) (from CB)	-0.70	-0.89	-1.40
U (eV)	0.20	0.20	0.20
C_p^-, C_n^+ (cm ³ /s)	4×10^{-8}	8×10^{-9}	4×10^{-8}
C_p^0, C_n^0 (cm ³ /s)	4×10^{-9}	8×10^{-10}	4×10^{-9}

2.3 Optical model

The optical model is based on the optical generation in the solar cell which depends on the transmission and reflection coefficients of the different layers of the solar cell, the light

scattering and light trapping properties of the device and the spectral irradiance of the sun or an equivalent light source.

2.3.1 Optical generation

The optical generation in a solar cell is expressed by the number of electrons and holes generated by the incident photons per cm^3 and second in a concrete position inside the device. The amount of photons penetrating the absorber material decay exponentially when going deeper into the semiconductor as we see in Fig. 2.13.

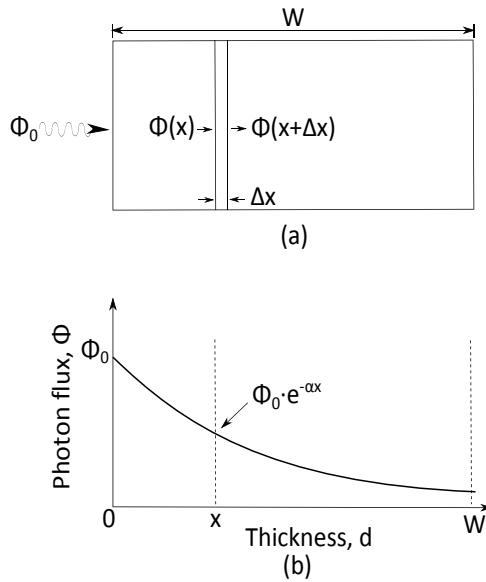


Figure 2.13: Photon flux into a semiconductor.

The photon flux, $\phi \left(\frac{\text{photons}}{\text{cm}^2 \cdot \text{s}} \right)$, is given by the Lambert law as shown in the next equation:

$$\phi(x, \lambda) = \phi(0, \lambda) \exp^{-\alpha(\lambda)x} \quad (2.49)$$

where $\alpha \text{ (cm}^{-1}\text{)}$ is the absorption coefficient which is different for every semiconductor (see Fig. 2.14). The effective range of absorption of a-Si:H is from about 300 nm to 800 nm.

The optical generation, $G_{opt} \left(\frac{1}{cm^3s} \right)$, of a semiconductor, depending on the position and the wavelength, results in:

$$G_{opt}(x, \lambda) = -\frac{d\phi(x, \lambda)}{dx} = \alpha(\lambda)\phi(0, \lambda)\exp^{-\alpha(\lambda)x} \quad (2.50)$$

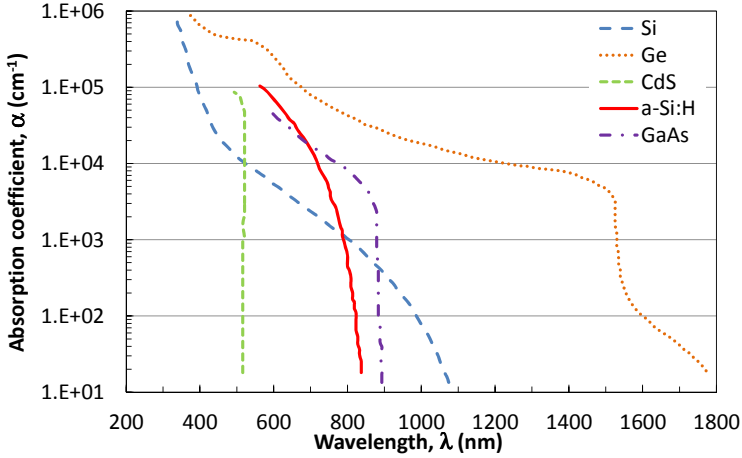


Figure 2.14: Optical absorption coefficient for different PV materials.

Concerning the complex refractive index (\vec{n}), it is used to describe the propagation and absorption of light in a media:

$$\vec{n} = n - ik \quad (2.51)$$

The refractive index (n) relates the speed of light in vacuum (c) and in the media (v):

$$n = \frac{c}{v} \quad (2.52)$$

The extinction coefficient (k) describes the absorption of the light in the media:

$$k = \frac{\alpha\lambda}{4\pi} \quad (2.53)$$

We have added in the material library of every layer in Sentaurus a table with the complex refractive index in the a-Si:H wavelength range of interest (300 nm - 800 nm). In Fig. 2.15 we see the refractive index and the extinction coefficient for the three p-i-n layers. We cannot measure the coefficients in the range 300 nm - 400 nm therefore, we extrapolate the trend of each one to get the data.

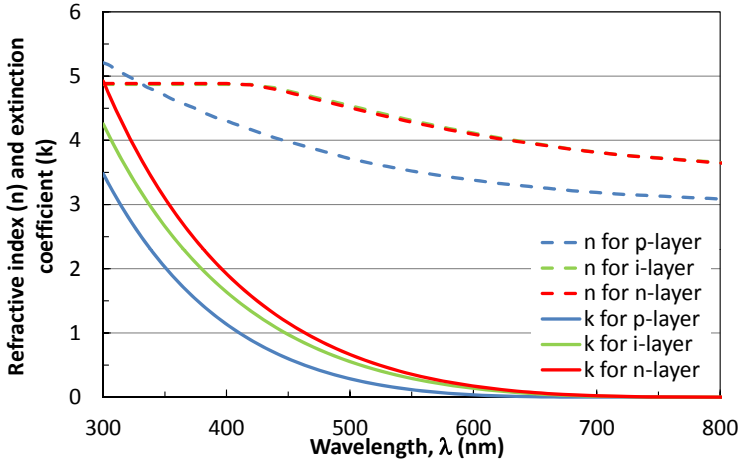


Figure 2.15: Complex refractive index for our a-Si:H layers.

2.3.2 Improvement of light trapping and scattering through textured interfaces

A crucial aspect to improve the current generation in the solar cell having thin intrinsic layers is the high dispersion at the front TCO, which is described by the haze factor. The haze is the ratio between the diffuse transmission (T_{dif}) and the total transmission (T), as indicated in Eq. 2.54. Thus, a front TCO with high haze will lead to more scattered light in the device and longer absorption, increasing the probabilities of photons to be absorbed in the solar cell. This is achieved by texturing the front TCO layer which results in textured interfaces as shown in Fig. 2.12. Apart of good scattering, to increase the current generation in the 550 nm - 800 nm wavelength range, we need a highly reflective back reflector to take advantage of the non-absorbed photons in the i-layer which could be absorbed after rebounding in the back reflector. This improvement would not be possible in the long wavelength range without both the textured front TCO and the back reflector.

$$Haze = \frac{T_{dif}}{T} \quad (2.54)$$

To simulate the texture we have used two options: the Hegedus model (assuming a light enhancement factor, which is an approximation) and to build a regular triangular structure (which is a more precise method).

- **Hegedus model:** To simulate the light trapping effect we use a method to calculate an optical path enhancement factor $m(\lambda)$ depending on the wavelength range using the model developed by Hegedus et al. [45]. Thus, the absorption of the i-layer (A_i) changes from Eq. 2.55a to 2.55b. This provides an adjustment of the spectral response to the respective experimental data in the long wavelength range.

$$A_i(\lambda) = 1 - \exp[-\alpha(\lambda) \cdot d_i] \quad (2.55a)$$

$$A_i(\lambda) = 1 - \exp[-\alpha(\lambda) \cdot m(\lambda) \cdot d_i] \quad (2.55b)$$

The use of non-textured surfaces/interfaces implies the formation of interferences in the spectral response depending mainly on the TCO and i-layer thickness. Therefore, to suppress the interference effects coming from the TCO, we implement a very thin TCO layer ($d = 75$ nm, when usually $d \approx 700$ nm - 1000 nm). We also applied a respectively enhanced extinction coefficient (k) to approximate the real absorption properties of the TCO in the device.

- **Geometry with texture:** We took the front TCO AGC AN10 as experimental texture reference. This TCO type is not any more the standard TCO at T-Solar, which now is ANS10ME. However, the texture of both can be considered nearly identical. Scanning electron microscopy (SEM) and atomic force microscopy (AFM) pictures of the AN10 TCO texture have been studied [46]. One example of these measurements is presented in Figs. 2.16 and 2.17. They show how the texture is irregular having, in general, pyramidal shape. To simulate the texture in 2D we have employed, for the interface TCO/p-layer, a regular triangular structure with height and base using the average parameters obtained from the AFM data. In the interfaces i-layer/n-layer and AZO/Al we have applied a scaled coefficient to slightly reduce the height of the texture [47], [48], [49], [50].

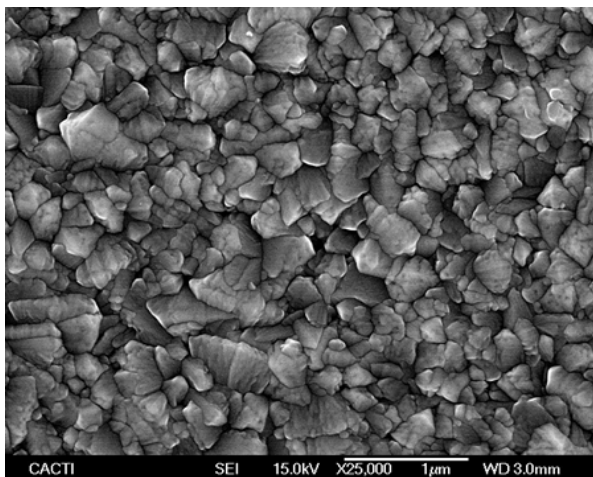


Figure 2.16: SEM picture of an industrial TCO sample AN10 from AGC showing fine surface roughness of the crystal grains [46].

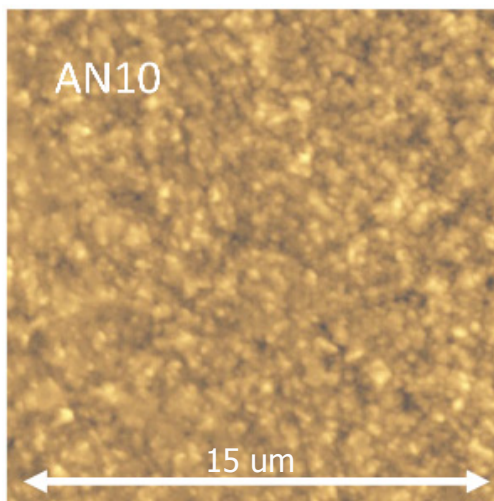


Figure 2.17: AFM picture of an industrial TCO sample AN10 from AGC [46].

2.3.3 Spectral irradiance

The spectral irradiance (G_{irrad}), as a function of photon wavelength (or energy), is the most common way to characterise a light source as, e.g., the sun. It gives the power density at a particular wavelength. The units of spectral irradiance are $\text{Wm}^{-2}\text{nm}^{-1}$. The Wm^{-2} term is the power density at the wavelength λ (nm). Therefore, the m^{-2} refers to the surface area of the light emitter and the nm^{-1} refers to the wavelength of interest. The spectral irradiance, $G_{irrad} \left(\frac{\text{W}}{\text{cm}^2\text{nm}} \right)$, can be determined from the photon flux, $\phi(\lambda)$ as shown in Eq. 2.56.

$$G_{irrad}(\lambda) = hc \frac{\phi(\lambda)}{\lambda \cdot \Delta\lambda} = q \cdot 1240 \frac{\phi(\lambda)}{\lambda \cdot \Delta\lambda} \quad (2.56)$$

where h is the Planck's constant ($h = 6.626 \times 10^{-34}$ J·s), c is the speed of light in vacuum ($c = 3 \times 10^{17}$ nm/s), $1240 \left(\frac{\text{W}\cdot\text{s}\cdot\text{nm}}{\text{C}} \right)$ is the result of the product $\frac{hc}{q}$ and λ (nm) is the wavelength of the incident photons.

Fig. 2.18 shows the solar spectrum of the AM0, AM1.5G and AM1.5D. AM stands for air mass. The number indicates the optical path travelled by the sun photons within the Earth's atmosphere, normalized to the position when the sun is at zenith. Finally, the G stands for global and includes both direct (normal, specular component) and diffuse radiation. The D is only referred to direct radiation. We see that the maximum of this spectrum corresponds with the range of absorption of a-Si:H solar cells. The AM0 is the spectrum outside the atmosphere, the meaning is zero atmospheres. The AM1 is the spectrum after travelling through the atmosphere to sea level with the sun directly overhead. Nevertheless, the solar panels do not generally operate under exactly one atmosphere's thickness. If the sun is at an angle to the Earth's surface, the effective thickness will be greater. Many of the world's major population centres, and hence solar installations and industry, lie in temperate latitudes. That is why the solar spectrum used for all the standardised testing of terrestrial solar panels is the AM1.5 spectrum (red line in Fig. 2.18). AM1.5 (it means 1.5 atmosphere thickness) corresponds to a solar zenith angle of $z = 48.2^\circ$. While the summertime AM number for mid-latitudes during the middle parts of the day is less than 1.5, higher values apply in the morning and evening and at other times of the year. Therefore, AM1.5 is useful to represent the overall yearly average for mid-latitudes [51], [52]. When AM1.5 is written we are referring to AM1.5G spectrum.

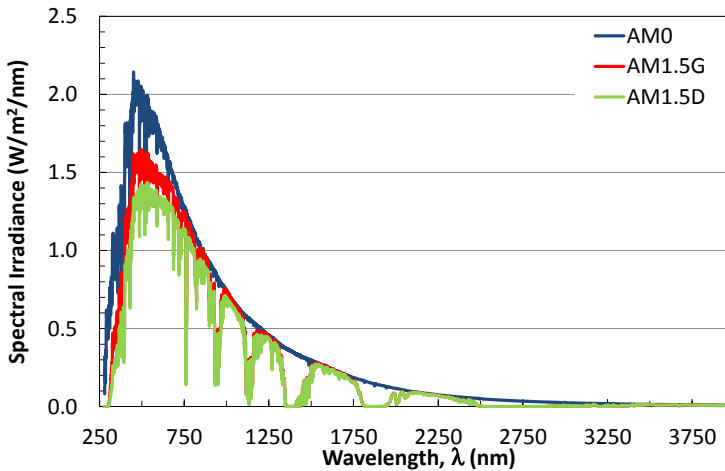


Figure 2.18: Solar spectrum AM0, AM1.5G and AM1.5D [51].

2.3.4 Simulation of the illumination

The simulation of the illumination is done by taking the AM1.5 irradiance spectrum data from a file and using two different methods available in Sentaurus [36]:

- **The transfer matrix method (TMM):** The optical carrier generation rate is modelled by monochromatic plane waves penetrating a number of planar and parallel layers (each layer must be homogeneous, isotropic and optically linear). The TMM is used when no texture is included and we take into account this effect through the Hegedus approximation as explained in section 2.3.
- **The Monte Carlo ray tracing method:** The simulation of photogeneration by Monte Carlo ray tracing in 2D is used for rough surfaces where rays are randomly scattered. Therefore, the Monte Carlo ray tracing is used when textured layers are included. The calculation of refraction, transmission, and reflection follows geometric optics, and special boundary conditions can be defined. The concept of Monte Carlo ray tracing follows that of the Monte Carlo method for carrier transport simulation. Suppose a ray impinges an interface. In the deterministic framework, the ray would split into a reflected part and a transmitted part at a material interface. In the Monte Carlo framework, you track only one ray path and take the reflectivity as a probability

constraint to decide if the ray is to be reflected or transmitted. As more rays impinge this material interface, the aggregate number of reflected rays will recover information about the reflectivity. This is the crux of the Monte Carlo method.

2.4 Numerical methods and solvers

Sentaurus solves the Poisson, and electrons and holes continuity equations by using the continuous density of state model, which includes the DOS distribution of the localized states (DOS distributed in the band gap) and their recombination mechanisms; and computes the generation profile of electron (e)-hole (h) pairs from the optical parameters (refractive index and extinction coefficient as function of the wavelength) of each layer [53].

2.4.1 Introduction into numerical methods

The numerical solution of a system of equations requires device geometry divided in a discrete number of regions. The semiconductor differential equations are approximated in each region by a group of differential equations. This process is known as discretization and it results in a high number of non-linear equations [54]. There are several methods to discretise the equations. The most important ones are based in finite differences [55] and finite elements [56], [57] which are especially useful in semiconductor devices with irregular geometry, since they ease the introduction of elements with different shape and size.

Concerning the discretization of the equations, the most relevant are the choice of the number of nodes to divide the device, the distribution of the resulting cells and their shapes in the device. Another important part as for simulation algorithms is to improve the convergence of the system by extending the discretization or by changing variables or basic functions [58]. In Fig. 2.19 a simplified flow chart of the method used for the numerical resolution is presented.

2.4.2 Equations

The set of basic equations are complemented by other equations to describe the device properties. One obtains these equations mainly from three models: The band diagram, the carrier statistics and the current transport.

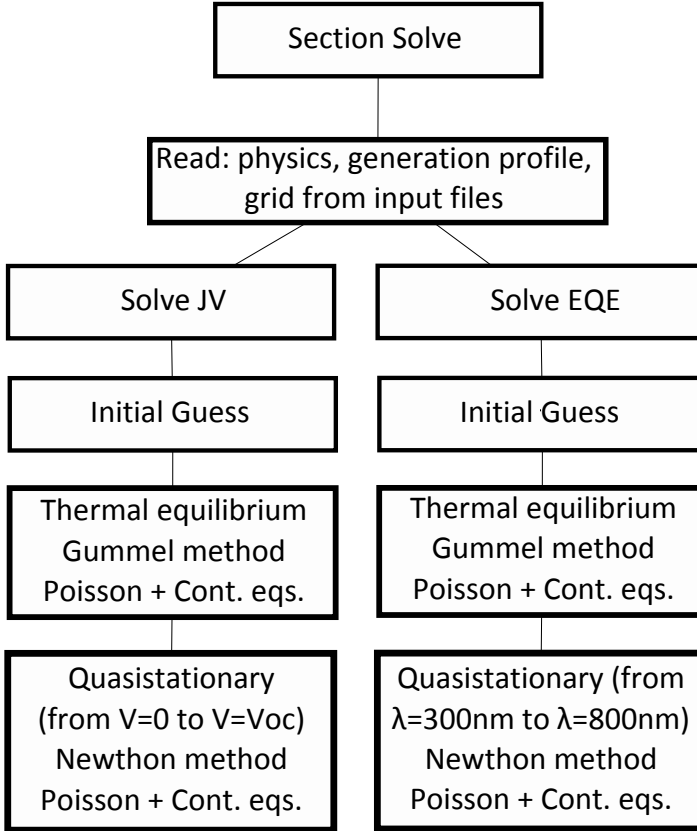


Figure 2.19: Simplified flow chart of the method used for the numerical resolution.

Basic equations of semiconductor devices

Solar cells and semiconductor devices using the drift-diffusion model are governed by three basic equations: Poisson, and electron and hole continuity equations.

$$\nabla(\varepsilon\nabla\psi) = -\rho \quad (2.57)$$

$$\frac{1}{q}\nabla\vec{J}_n = R_{net} - G_{opt} + \frac{\partial n}{\partial t} \quad (2.58)$$

$$-\frac{1}{q}\nabla\vec{J}_p = R_{net} - G_{opt} + \frac{\partial p}{\partial t} \quad (2.59)$$

in these equations ϵ (F/cm) is the permittivity of the semiconductor, ψ (eV) is the electrostatic potential with reference to the vacuum level E_0 , ρ (C/cm³) is the space charge density, J_n and J_p , in A/cm², are the electron and hole current densities, G_{opt} (cm⁻³ s⁻¹) is the optical generation rate, R_{net} (cm⁻³ s⁻¹) is the net recombination-generation rate of electrons and holes and $\frac{\partial n}{\partial t}$ and $\frac{\partial p}{\partial t}$, in cm⁻³ s⁻¹, are the changes in the electron and hole concentrations with time.

For a-Si:H p-i-n devices the space charge density is defined as:

$$\rho = q(p - n + N_D - N_A) + \rho_{trap} \quad (2.60a)$$

$$\rho_{trap} = q(p_{loc} - n_{loc}) \quad (2.60b)$$

where n and p , in cm⁻³, are the free electron and hole concentrations, ρ_{trap} is the space charge density contributed by traps and fixed charges in the localized states, n_{loc} and p_{loc} , in cm⁻³, are the localized electron and hole concentrations, N_D and N_A , in cm⁻³, are the concentrations of ionized (active) dopant atoms (not the total concentration of dopant atoms). We have to take into account that, in a-Si:H, not all incorporated dopant atoms are electronically active at room temperature as it is assumed in the case of c-Si [25].

To obtain the current density in the device from the continuity equations of electrons and holes, we use their current transport equations:

$$\vec{J}_n = n\mu_n \nabla E_{Fn} \quad (2.61a)$$

$$\vec{J}_p = -p\mu_p \nabla E_{Fp} \quad (2.61b)$$

where μ_n and μ_p , in cm²/(V·s), are the electron and hole mobilities and E_{Fn} and E_{Fp} , in eV, are the electron and hole quasi-Fermi energy levels.

In addition, power conversion in solar cells is considered to be a steady state operation, therefore:

$$\frac{\partial n}{\partial t} = \frac{\partial p}{\partial t} = 0 \quad (2.62)$$

Finally, G_{opt} is obtained from Eq. 2.50 (Lambert law) and R_{net} from Eq. 2.41.

Band diagram

Fig. 2.20 shows the energy band diagram under equilibrium conditions for a typical single junction a-Si:H solar cell. In crystalline semiconductors, E_C represents the minimum energy

of the CB and E_V the maximum energy level of the VB. In a-Si:H based material these energies are related to the mobility edge of the CB and VB, respectively. Both energy levels are related to the vacuum energy level E_0 by:

$$E_C = E_0 - q\psi - \chi \quad (2.63a)$$

$$E_V = E_0 - q\psi - \chi - E_G \quad (2.63b)$$

where χ is the electron affinity and E_G is the band gap energy. In the case of a-Si:H based material, E_G represents the mobility gap E_{gap}^{mob} .

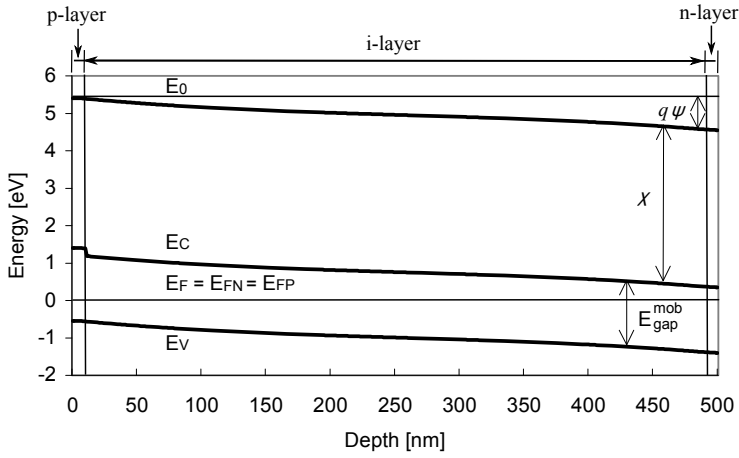


Figure 2.20: Energy band diagram of a typical single junction a-Si:H solar cell under equilibrium conditions. The E_C energy level in the p-layer is higher due to the higher energy gap of this region.

Carrier statistics

The electron and hole concentrations are calculated from the Fermi-Dirac distribution for degenerated semiconductors assuming parabolic DOS [26] [27]:

$$n = N_C \cdot F_{1/2}(\eta_n) \quad (2.64a)$$

$$p = N_V \cdot F_{1/2}(\eta_p) \quad (2.64b)$$

where:

$$F_{1/2}(\eta) = \frac{2}{\sqrt{\pi}} \int_0^{\infty} \frac{\xi^{1/2}}{1 + \exp(\xi - \eta)} d\xi \quad (2.65)$$

$$\eta_n = \frac{E_{Fn} - E_C}{kT} \quad (2.66a)$$

$$\eta_p = \frac{E_V - E_{Fp}}{kT} \quad (2.66b)$$

in the equations above N_C and N_V , in cm^{-3} , are the effective DOS in the CB and VB. Their values are given by Eq. 2.44; $F_{1/2}$ is the Fermi integral of order 1/2; $E_{Fn} = q\phi_n$ and $E_{Fp} = q\phi_p$ are the quasi-Fermi energies for electron and holes, and ϕ_n and ϕ_p , in V, are the quasi-Fermi potentials for electron and holes.

Alternatively, one can write the equations 2.64 as:

$$n = \gamma_n \cdot N_C \cdot \exp\left(\frac{E_{Fn} - E_C}{kT}\right) = \gamma_n \cdot N_C \cdot \exp\left(\frac{E_{Fn} - E_0 + q\psi + \chi}{kT}\right) \quad (2.67a)$$

$$p = \gamma_p \cdot N_V \cdot \exp\left(\frac{E_V - E_{Fp}}{kT}\right) = \gamma_p \cdot N_V \cdot \exp\left(\frac{E_0 - q\psi - \chi - E_G - E_{Fp}}{kT}\right) \quad (2.67b)$$

where γ_n and γ_p are function of η_n and η_p :

$$\gamma_n = \frac{F_{1/2}(\eta_n)}{\exp(\eta_n)} \quad (2.68a)$$

$$\gamma_p = \frac{F_{1/2}(\eta_p)}{\exp(\eta_p)} \quad (2.68b)$$

Working out the value of E_{Fn} and E_{Fp} , respectively, we obtain:

$$E_{Fn} = E_C + kT \ln\left(\frac{n}{\gamma_n N_C}\right) = E_0 - q\psi - \chi + kT \ln\left(\frac{n}{\gamma_n N_C}\right) \quad (2.69a)$$

$$E_{Fp} = E_V - kT \ln\left(\frac{p}{\gamma_p N_V}\right) = E_0 - q\psi - \chi - E_G - kT \ln\left(\frac{p}{\gamma_p N_V}\right) \quad (2.69b)$$

Current transport. Drift-Diffusion model

Using equations 2.69a and 2.69b in equations 2.61a and 2.61b, respectively, and after a manipulation which makes use of the Einstein relations for the diffusion coefficient for electrons and holes:

$$D_n = \frac{kT}{q} \mu_n \quad (2.70a)$$

$$D_p = \frac{kT}{q} \mu_p \quad (2.70b)$$

and the fact that $\frac{dE_0}{dx} = 0$, we find:

$$J_n = \underbrace{qD_n \frac{dn}{dx}}_{\text{Electron diffusion current}} + \underbrace{\mu_{nn} \left[-q \frac{d\psi}{dx} - \frac{d\chi}{dx} - \frac{kT}{N_C} \frac{dN_C}{dx} \right]}_{\text{Electron drift current}} \quad (2.71a)$$

$$J_p = \underbrace{-qD_p \frac{dp}{dx}}_{\text{Hole diffusion current}} + \underbrace{\mu_{pp} \left[-q \frac{d\psi}{dx} - \frac{d\chi}{dx} - \frac{dE_G}{dx} + \frac{kT}{N_V} \frac{dN_V}{dx} \right]}_{\text{Hole drift current}} \quad (2.71b)$$

In Equations 2.71 the first term represents the current due to diffusion of the carriers and the second term represents drift transport. The terms in the square brackets are considered to be the effective drift fields. In the case that the device is made of spatially uniform material (homojunction device), we obtain:

$$\frac{d\chi}{dx} = \frac{dE_G}{dx} = \frac{dN_C}{dx} = \frac{dN_V}{dx} = 0 \quad (2.72)$$

Therefore, the Eqs. 2.71 result in the classical current density expressions for electron and hole, which are used in c-Si homojunction non-degenerated devices analysed with Maxwell-Boltzmann statistics.

2.4.3 Boundary conditions

There are two boundaries in the device, the front and the back contact. The implied conditions at the contacts fix the values of the independent model variables at these points. The boundary conditions depend on how the contacts of a device are modelled. Generally, two types of contacts are distinguished: Ohmic contacts and Schottky contacts.

Our device is modelled with Ohmic contacts where the electrostatic potential and electron and hole concentrations at the boundaries of the device ($x = 0$, anode and $x = L$, cathode, where L is the device thickness) are fixed, or the minority carrier concentrations are determined by surface recombination. It is assumed that the majority carrier concentration is independent of the injection level. In case of ideal Ohmic contacts infinite surface recombination, equilibrium and charge neutrality at the contacts is assumed:

$$\rho(0, y) = 0 \quad \Rightarrow \quad n_0(0, y) - p_0(0, y) = p_{loc} - n_{loc} + N_D - N_A \quad (2.73a)$$

$$\rho(L, y) = 0 \quad \Rightarrow \quad n_0(L, y) - p_0(L, y) = p_{loc} - n_{loc} + N_D - N_A \quad (2.73b)$$

$$n_0(0, y) \cdot p_0(0, y) = n_{i,eff}^2 \quad (2.74a)$$

$$n_0(L, y) \cdot p_0(L, y) = n_{i,eff}^2 \quad (2.74b)$$

The space charge density $\rho(x)$ is given by Eq. 2.60. The following conditions are introduced for the electrostatic potential ψ and quasi-Fermi potentials ϕ_{Fn} and ϕ_{Fp} at the boundaries:

$$\psi(0, y) = \psi_0(0, y) + V_{app} \quad (2.75a)$$

$$\psi(L, y) = \psi_0(L, y) \quad (2.75b)$$

$$\phi_{Fn}(0, y) = \phi_{Fp}(0, y) = V_{app} \quad (2.76a)$$

$$\phi_{Fn}(L, y) = \phi_{Fp}(L, y) = 0 \quad (2.76b)$$

where $\psi_0(0, y)$ and $\psi_0(L, y)$ are the solutions of equations 2.73 and V_{app} is the applied external voltage.

For Boltzmann statistics, these conditions can be expressed analytically. For Fermi statistics this is not possible, hence, Sentaurus Device computes the equilibrium solution numerically.

Furthermore, for Ohmic contacts the surface recombination velocities for electrons, v_n and holes, v_p , in cm/s, determine the carrier concentrations at the boundaries. If they are specified, Sentaurus Device uses the following current density boundary conditions:

$$\vec{J}_n \cdot \hat{n} = qv_n \cdot (n - n_0) \quad (2.77a)$$

$$\vec{J}_p \cdot \hat{n} = qv_p \cdot (p - p_0) \quad (2.77b)$$

where n and p are the electron and hole concentrations at the front and back contacts, n_0 and p_0 are the electron and hole concentrations in thermodynamic equilibrium at the front and back contacts and \hat{n} is the normal vector to the contact.

Replacing the general point x by $x = 0$ and $x = L$, we find:

$$\vec{J}_n(0, y) \cdot \hat{n} = q \cdot v_{n0} \cdot [n(0, y) - n_0(0, y)] \quad (2.78a)$$

$$\vec{J}_n(L, y) \cdot \hat{n} = q \cdot v_{nL} \cdot [n(L, y) - n_0(L, y)] \quad (2.78b)$$

$$\vec{J}_p(0, y) \cdot \hat{n} = q \cdot v_{p0} \cdot [p(0, y) - p_0(0, y)] \quad (2.79a)$$

$$\vec{J}_p(L, y) \cdot \hat{n} = q \cdot v_{pL} \cdot [p(L, y) - p_0(L, y)] \quad (2.79b)$$

where v_{n0} and v_{nL} are the surface recombination velocities for electrons at the front and back contact, respectively, and v_{p0} and v_{pL} are the surface recombination velocities for holes at the front and back contact, respectively. By default, $n = n_0$ and $p = p_0$ are applied for concentrations at the Ohmic contacts since $\vec{J}_{n,p} = 0$ at the boundaries.

2.4.4 Discretization

The model described previously is formed by the differential equations which model the behaviour of the corresponding semiconductor. To solve the model we need to look for a numerical solution of the system of equations together with their boundary conditions. This, results in a non-linear system of partial differential equations. The procedure used to solve this system of a simulated semiconductor device is the following [59]:

- To discretise the system of non-linear equations. Hence, the continuous problem is replaced by a discrete non-linear system of equations.
- To apply any linearization method to the non-linear problem.
- To solve a system of linear and disperse equations in order to get the wished solution.

To solve the non-linear system of $3N$ (where N is the number of nodes) differential equations formed by the Poisson and the continuity carrier equations (2.57, 2.58 and 2.59) one needs to discretise the system of equations. In spite that our simulation is in 2D, we are going to simplify in the following the discretization to 1D since the resolution methods are not the aim of this thesis, they are presented just to clarify how the simulations steps are.

The discretization starts dividing the device in cells. In every cell there are two kinds of points: the cell edges which are called i or $x(i)$ and the central points $i + 1/2$ or $x(i + 1/2)$. The anode (positive electrode) or front contact is placed at the point 0 and the cathode (negative electrode) or back contact is placed at the point $N - 1$.

The equations relate three variables at the point i : $\psi(i)$, $n(i)$ and $p(i)$. Therefore, there are $3N$ variables with $3N$ equations in total. In addition, the three equations at each i position depend not only on the three variable values at this location but also on the variable values at the adjacent points $i - 1$ and $i + 1$.

To obtain the discretised equations at a point i (which is not a contact) of the cited equations 2.57, 2.58 and 2.59 we have to integrate them with limits $i - 1/2$ and $i + 1/2$, considering $h_i = x(i + 1) - x(i)$ and $h_{i-1} = x(i) - x(i - 1)$, we get:

$$\varepsilon_{i+1/2} \frac{\psi_{i+1} - \psi_i}{h_i} - \varepsilon_{i-1/2} \frac{\psi_i - \psi_{i-1}}{h_{i-1}} = \frac{h_i + h_{i-1}}{2} (n - p + N_A - N_D)|_i \quad (2.80)$$

$$J_n(i + 1/2) - J_n(i - 1/2) = IR(i) \quad (2.81)$$

$$J_p(i + 1/2) - J_p(i - 1/2) = -IR(i) \quad (2.82)$$

where $IR(i)$ is the integral of the net recombination (R_{net}) which was obtained in Eq. 2.41, resulting in:

$$IR(i) = \int_{i-1/2}^{i+1/2} (R_{CB}^{tot} + R_{VB}^{tot} + R_{DB}^{tot}) dx \quad (2.83)$$

2.4.5 Linearization of the discretised system

The coupled non-linear system of $3N$ equations, discretised in the previous section, is solved using the Newton method [60].

To obtain the linear system we have to take into account that in every point i there are 3 discretised equations (Poisson and continuity carrier equations). They can be written equalling them to zero: $G_1^i = 0$, $G_2^i = 0$ and $G_3^i = 0$. Due to the discretization, the equations only depend on three variables (ψ , n and p) in three points ($i-1$, i and $i+1$). We name W^i the vector whose components are the variables in this point ($W_i = (\psi_i, n_i, p_i)$) and dW_i its differential vector. Then, we apply the Taylor series development of the functions G_1^i , G_2^i and G_3^i for a range of values of the variables together with the Newton method. It leads in each iteration to three linear equations which can be represented in matrix as follow:

$$\begin{pmatrix} \frac{\partial G_1^i}{\partial W^{i-1}} & \frac{\partial G_1^i}{\partial W^i} & \frac{\partial G_1^i}{\partial W^{i+1}} \\ \frac{\partial G_2^i}{\partial W^{i-1}} & \frac{\partial G_2^i}{\partial W^i} & \frac{\partial G_2^i}{\partial W^{i+1}} \\ \frac{\partial G_3^i}{\partial W^{i-1}} & \frac{\partial G_3^i}{\partial W^i} & \frac{\partial G_3^i}{\partial W^{i+1}} \end{pmatrix} \cdot \begin{pmatrix} dW^{i-1} \\ dW^i \\ dW^{i+1} \end{pmatrix} = \begin{pmatrix} -G_1^i \\ -G_2^i \\ -G_3^i \end{pmatrix} \quad (2.84)$$

2.4.6 Numerical resolution of the non-linear equations

To solve the system 2.84, coming from the drift-diffusion model, two approximation methods are usually employed [61] [59] [62], the Newton-Raphson method (coupled) and the Gummel method (uncoupled). To choose between both methods, one has to consider the operation characteristics of the device, the algorithms used to solve the linearised system of equations or the amount of memory of the computational system where the simulations are run.

Newton-Raphson method

The Newton-Raphson method consists in solving the complete system of $3N$ equations simultaneously by applying any iterative method of type Newton [63]. This method is very robust and provides a very accurate solution. However, it may need a lot of time and memory

resources since it solves a non-linear and non-symmetric system of equations with high number of dimensions.

Gummel method

The Gummel method [59] [64] uses an iteration type Gauss-Seidel/Jacobi which uncouples the equations G_1 , G_2 and G_3 , so that it is only necessary to solve three systems of equations of dimension N . Hence, the Poisson equation and the continuity equations of electron and holes are solved separately. This method is very useful since it is possible to reach the convergence even starting with poor initial conditions and it is a fast method.

Nevertheless, for some applications such as very high injection level in the semiconductor or high recombination, the method could have convergence problems. In addition, in some cases the Gummel method converges very fast in the first iterations but later the convergence turns slower. In this case, one can combine the Gummel and Newton-Raphson methods. Thus one can approximate the solution by using the Gummel method and later change to the Newton-Raphson method in order to take advantage of its quadratic convergence properties near the solution.

CHAPTER 3

INDUSTRIAL PRODUCTION PROCESS AND BASIC EQUIPMENT SET-UPS OF A-Si:H SOLAR CELLS

This chapter presents how the PECVD production process works, as well as how we fabricate R&D solar cells of 1 cm^2 (or 4 cm^2) or mini modules in the industrial production line. Later, the equipment installed in the laboratory are shown. Concerning this thesis, the most important ones are the conventional spectral response and the very fast spectral response equipment, which are used to determine the external quantum efficiency (EQE) curves; and the solar simulator equipment with its current-voltage (IV) tracer to measure the illuminated or dark IV curves. The three equipment were developed in our laboratory. The development of R&D solar cells and mini modules in the T-Solar production line as well as the measurement equipment have been crucial to improve the production modules' efficiency.

3.1 Plasma enhanced chemical vapour deposition

As explained in section 1.5, the solar cell fabrication process is based on the deposition of a-Si:H layers by PECVD in a 7 chamber cluster tool on a $2.2\text{ m} \times 2.6\text{ m}$ substrate. The first layer deposition is a p-type layer doped with trimethyl borane (TMB, $B(CH_3)_3$), the second one is an intrinsic layer and, at last, a n-type layer doped with PH_3 . The p-layer is deposited in one chamber while the other two are deposited together in another chamber to prevent

cross contamination. The a-Si:H layers are formed through deposition of SiH_4 and H_2 . This deposition of a p-i-n structure allows the generation of the current in the cell when the module is exposed to the light.

The thin film deposition process results from the decomposition of SiH_4 , H_2 and other gases creating a plasma at moderate substrate (glass film) temperatures, around 200 °C (PECVD). In this process the silicon forms an amorphous layer mixed with hydrogen in a random bond net (random network, see Fig. 2.5). PECVD uses electrical power coupled into the plasma at a radiofrequency (RF) of 13.56 MHz to create radicals and ions of incoming gases, so that they can react to form silicon layers on the substrate glass. The whole system is kept in vacuum by a mechanical roughing system. The chambers are cleaned by dissociating nitrogen trifluoride (NF_3) which removes Si remaining in the chamber. The fluorine (F) atoms formed in the plasma react with Si to a volatile molecule, silicon tetrafluoride (SiF_4), which then, are pumped out of the chamber.

The deposition process by an RF discharge can be described as a four step process [25], it is schematically represented in Fig. 3.1 [65]:

- The primary reactions in the gas phase are electron-impact excitation, dissociation and ionization of SiH_4 molecules. The plasma thus, consists of neutral radicals and molecules, positive and negative ions and electrons.
- Secondary reactions, between molecules and ions or radicals, are very important as they predominantly control the electronic and structural film properties. Reactive neutral species move to the substrate by diffusion, positive ions bombard the growing film and negative ions are trapped within the sheaths [66] of the counter electrode and may eventually form small particles or dust.
- The third step consists of surface reactions, such as hydrogen abstraction, radical diffusion and chemical bonding.
- The fourth step is the subsurface release of hydrogen molecules and relaxation of the silicon matrix.

The deposition process is a very complicated matter as the physical and chemical interactions in the plasma and at the growing film surface are dependent on the RF power and frequency, the substrate temperature, the gas pressure and composition, the magnitude and the pattern of the gas flow, the electrode geometry, etc.

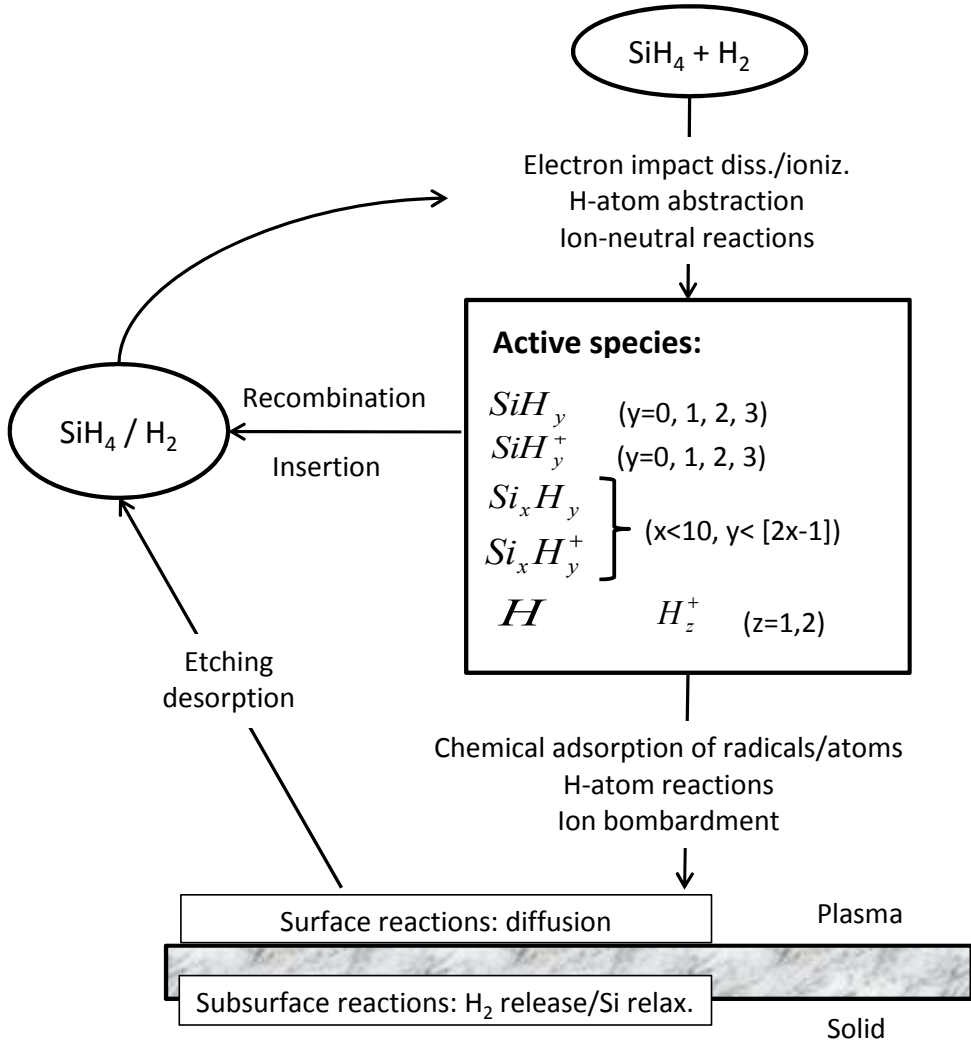


Figure 3.1: Schematic representation of the glow-discharge deposition process [25].

In Fig. 3.2 we see the main parts of a PECVD chamber as well as their distribution and the place of the substrate.

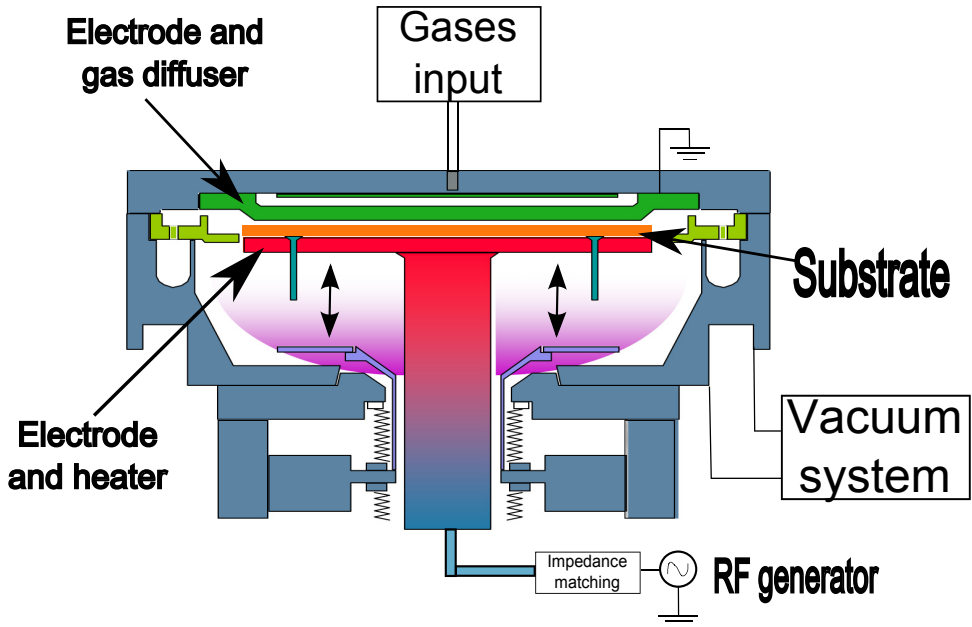


Figure 3.2: PECVD chamber diagram.

3.2 Production process to obtain mini cells and mini modules: laser scribe processes, shunt busting and annealing

As explained in section 1.5, in the T-Solar factory, the production process is based on a-Si:H p-i-n structure deposition on float glass with a TCO layer; also known as superstrate configuration because following the direction of incident light, the substrate is above the actual device structure. The back contact of the device consists of a zinc oxide (ZnO) TCO and Al/NiV metal coatings which act as reflectors for the light non-absorbed in the first path through the p-i-n structure (see Fig. 2.12) [67].

The front electrode is a textured F-doped tin oxide ($\text{SnO}_2:\text{F}$) layer and has the functions of transmitting and scattering the light and conducting the current generated in the p-i-n structure. The doped and intrinsic a-Si:H layers are deposited by PECVD. The doped layers (p and n) have the function to create an electrical field over the intrinsic layer (i-layer, the one that generates the current) and to provide an electrical contact to the end terminals.

The i-layer has the functions of absorbing the light and transporting the photogenerated carriers. The back TCO is an aluminium-doped zinc oxide, $ZnO : Al$ (AZO) layer that acts as reflection-enhancing dielectric layer and contact layer. The metal coating is Al and is used as reflector [24].

The production of mini cells (MCs) and mini modules (MMs) is based in manufacturing periodically special panels, with basically the process parameters used for full size standard modules. In this manufacture we create several coupons distributed over the surface of the full size panel. The main aim to produce them is to be able to measure the spectral response (SR), which cannot be done in modules, and gives important information about how to improve the solar cell efficiency. Therefore, MCs and MMs are useful to perform different experiments to know, e.g. the influence of process changes on the SR and IV curves. With them, we can also observe the effects of the non-uniformity in the p-i-n layers within the same module (according to the position of these samples) or the differences existing between modules produced in different PECVD chambers. They also present a time-saving advantage for light-induced degradation (LID) in comparison to full size modules. Full size modules, due to their big size, must degrade under outdoor conditions, needing between one and a half and three months depending on the season to reach 300 kWh/m^2 of illumination. On the contrary, MCs and MMs can be degraded indoor in the light soaking station (LSS) where they only need about three weeks to reach the same radiation value. So, we get degradation results faster with MCs and MMs. Therefore, we can advance some experiments and extrapolate the trend of electrical parameters to full size modules. Moreover, MCs and MMs allow us to compare SR and/or IV curves results with MCs and MMs from other research centres as FZJ, UU or UB.

The production process of these special panels has been changed and continuously improved since the beginning of the module production. The main development steps are presented next:

- **Initial design of mini cells: production with shadow masks.** The production process of these panels had no laser scribe and before entry in the PVD for deposition of the back contact (BC), the panels went out of the line for the placement of shadow masks with sixteen 1 cm^2 circular holes spread around the entire panel. Later, the panels went back to the production line and the three back contact layers ($ZnO/Al/NiV$) were deposited. So, we created sixteen solar cells per coupon (pads) which were isolated one to another but had a common grid or front contact (FC). Then, we took the full size panel out of the line and cut out the coupons. Finally we scratched manually the a-Si:H

layers in the shadowed area to give access to the FC TCO. In the left part of Fig. 3.3 one sees the former T-Solar coupon with sixteen 1 cm^2 solar cells.

To measure the IV curves and spectral response the coupons are placed in the sample holder shown in the right part of Fig. 3.3. The contact areas of the coupon are oriented downsides to measure them, so illumination is done from the top. Flexible contact pins (Pogo pins, ECT) are placed in the base plate of the sample holder to contact the FC and BC of the coupon. There are two pins to contact each cell (BC) and two pins for the common FC (four point probe measurement principle). There is a switch device to select the cell that we want to measure.

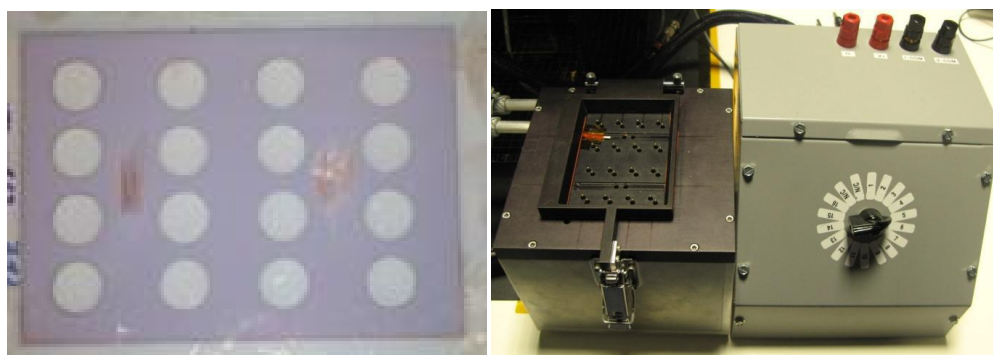


Figure 3.3: Former T-Solar coupon with 1 cm^2 solar cells (left) and sample holder for MCs measurements of IV curves and SR with the switch box to choose the solar cell to be measured (right).

The production process can be summarized as:

Glass → *TCO (SnO₂)* → *a-Si:H* → *Shadow mask (round cells)* →
ZnO → *Al* → *NiV* → *Manual scratch for FC*

This first design presented several problems and its data was not very reliable. We found out that there was an error due to the current generation at the solar cell border, obtaining an effective cell area of more than 1 cm^2 . Therefore, we had to measure the illuminated IV curves with the shadow mask put upon the coupon. Although we tried to solve that problem by putting the shadow mask, there was still illumination at the border of the solar cells due to light scattering in the 3.2 mm thick substrate glass. Furthermore, the solar cell area was not properly defined, having slight differences in the area of the

cells. In addition, the manually scratched front contact caused that not all the pads were at the same distance of the grid. Resulting from this, a series resistance (R_s) higher than in modules was obtained, and fill factor (FF) and efficiency (η) were reduced. We can see in the left side of Fig. 3.3 that the scratch area is only in the centre between the rows of cells. Additionally, these solar cells often presented problems in the annealing process and turned out to be damaged (the reason for this is still not known), thus the initial state was not reached.

- **Mini cells designed at FZJ:** During a 3 months intership of the author at FZJ, the knowledge about an improved production process and MCs design was transferred to T-Solar. In this design FZJ can choose reliably between MC production with both, mask or laser scribe process. In the mask process, the layers are deposited on a glass with size of 10 cm x 10 cm. The substrate can be Corning Glass (1.0 mm thickness) or Float Glass (3.2 mm). Next, the front TCO, a-Si:H and BC ZnO layers are deposited. Then, a scratch mask and a scratch pencil (Fig. 3.4, left) are used to produce the FC scratching a line (which removes the BC ZnO layer and the a-Si:H layers) from one border of the sample to the opposite (see Fig. 3.5). By this, we will always have the same separation between pads and grids. Next, we place the samples into a new mask holder, in the most common case (which is silver evaporation) a magnetized mask (called Combi mask), that fixes the sample putting it in the middle of two metallic plates, is used (see Fig. 3.4, right). With this magnetic mask, very well defined solar cell areas are achieved. The next step is silver evaporation on the cells to finish the BC. Afterwards, one has to etch the sample with hydrogen chloride (HCl) to remove the ZnO layer and to get isolated solar cells. Finally, an annealing is done to bring the cells into a well-defined initial state. With the Combi mask eighteen square solar cells of 1 cm² surface and another eighteen with different smaller surfaces are obtained.

The FZJ production process with shadow mask can be summarized as:

Glass → *TCO* → *a-Si:H* → *ZnO BC* → *Scratch mask* → *Scratch* →
Deposition shadow mask → *Ag dep.* → *HCl etch* → *Annealing*

Nevertheless, this mask concept is not applicable in the T-Solar production line. Therefore, a process including the laser scribe process was developed to fabricate well isolated solar cells with well-defined area.

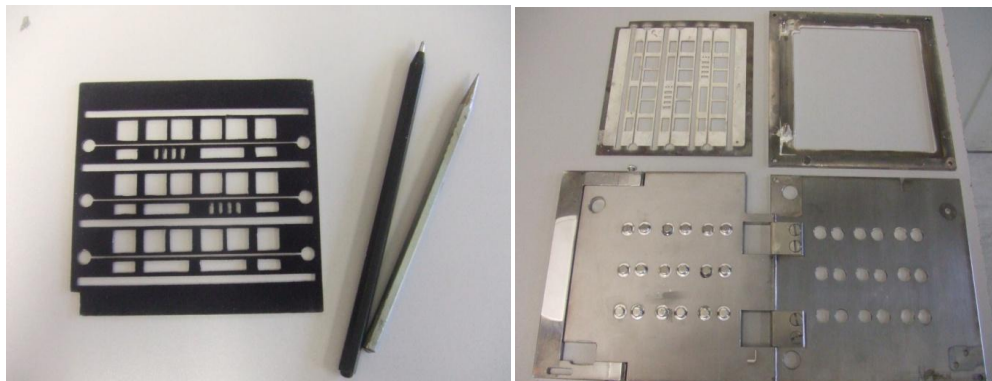


Figure 3.4: Scratch mask (side in contact with the sample) and scratch pencils (left) and Combi mask with their four pieces (right).

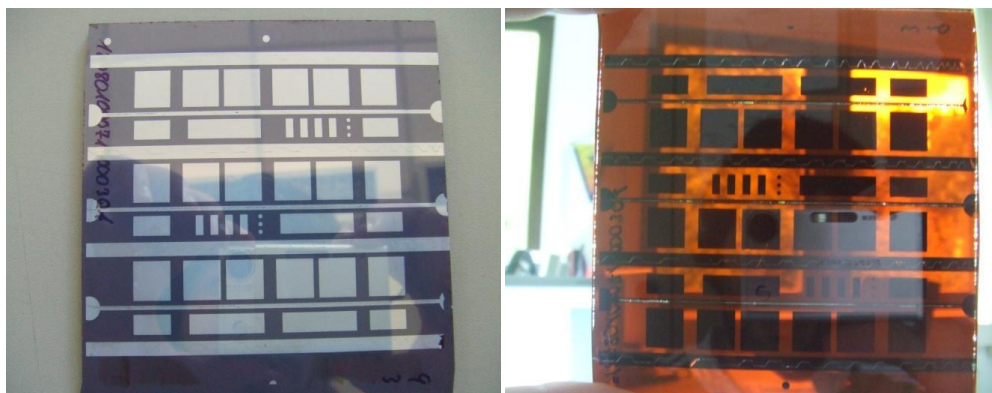


Figure 3.5: Back contact side (left) and glass side (right) of a coupon produced at FZJ with a magnetized mask (Combi mask).

- **Current design of mini cells: production through laser scribe.** The current MCs recipe has basically the same process parameters as used for full size modules, the only change is the LSR design which is adapted to get eight coupons 10 cm x 10 cm distributed over the surface of the full size panel as shown in Fig. 3.6. As one sees in the figure, the coupons are named through a hexadecimal nomenclature. The notation system for the coupons is based in separate the full size panel in quarter size panels which have assigned a letter (F, G, H, I) and applying for each quarter of 1.1 m x 1.3 m a matrix of 11 coupons x 13 coupons.

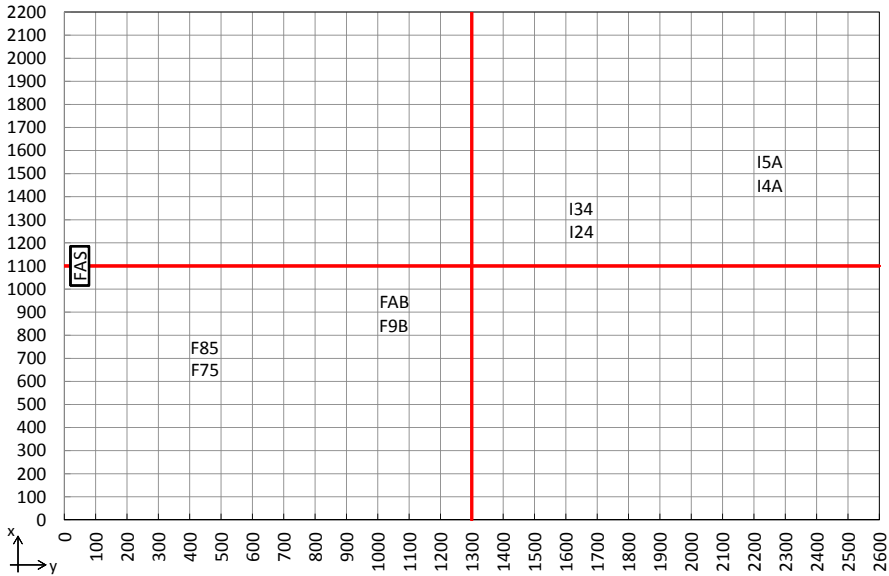


Figure 3.6: Position of the coupons with MCs along the full size panel (distance in mm).

The P1 LSR scribe writes the barcode and ID (serial number) of the panel and makes the reference crosses. The P2 LSR scribe marks the edge of the coupons and the grids (front contact lines). The P3 LSR scribe defines the lines for the pads (cell area) isolating the cells. Cells are isolated one to another sharing a common FC using the same P2 scribe method as applied in modules. These coupons have ten solar cells, eight with 1 cm^2 and two with 4 cm^2 area (see Fig. 3.7). After the P3 LSR scribe the panel is taken out of the line to cut the coupons out with a glass cutting table.

Once the coupons are fabricated, they still have two process steps. First, we apply the so-called shunt busting (SB), which is also performed in the production line for the standard modules and which consist in the application of 6 V in reverse condition of every cell during 100 ms with a current density limit of 20 mA/cm^2 . This, results in an improvement of efficiency and increases of solar cell yield of each coupon. In the second process step, we put the samples in an oven at around $145 \text{ }^\circ\text{C}$ during 30 min performing a heating cycle like in the autoclave process in the production line. Annealing the coupons we bring the solar cells to their so-called initial state. Experiments showed that performance of only the annealing without SB results in

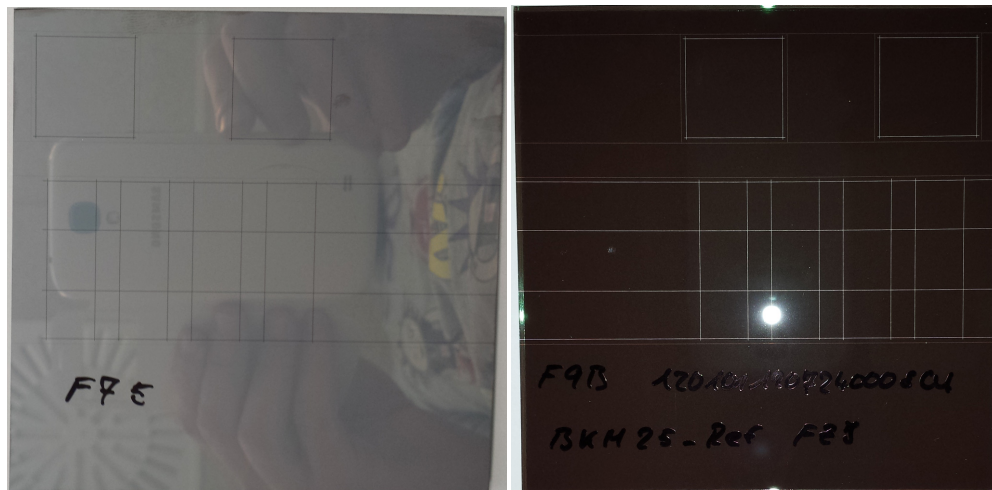


Figure 3.7: Back contact side (left) and glass side (right) of a coupon produced at TS through laser scribe.

high efficiency but often in bad cell yield. However, combining SB and annealing we achieve high efficiency, high yield and low dispersion in electrical parameters. Together with the very accurate cell area definition on coupons, MCs produced with LSR scribe method return very reliable data.

The production process can be summarized as:

Glass → *TCO (SnO₂)* → *a-Si:H* → *LSR scribe (P2) for grids* → *ZnO*
 → *Al* → *NiV* → *LSR scribe (P3) for pads* → *SB* → *Annealing*

The design through LSR scribe allows a flexible design, which finally has permitted the fabrication of MC sizes with 1 cm² and 4 cm², as well as MMs of several sizes (usually 10 x 10 cm² and 20 x 20 cm² of total or active surface). As an example, Fig. 3.8 presents the location of 18 MMs 20 x 20 cm² and 18 MMs 10 x 10 cm² in the full size panel. The overall design of these MMs is the same as the one of full size modules having the same measurements for the edge delete area and the contact cells at the module border. An example of a 10 x 10 cm² MM design is presented in Fig. 3.9.

To measure the MMs we do not use a sample holder. We solder side buss on the contact cells to make the connection and then we perform the SB. Previously to these two steps,

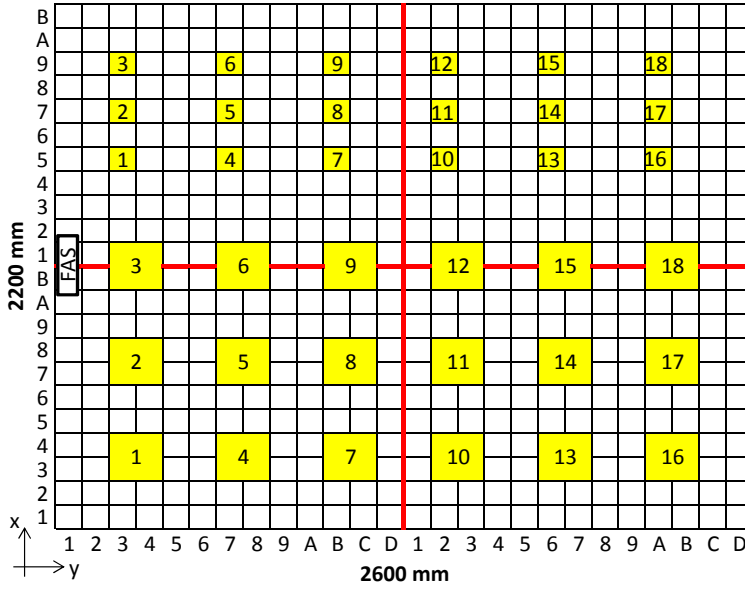


Figure 3.8: Position of the MMs along the full size panel.

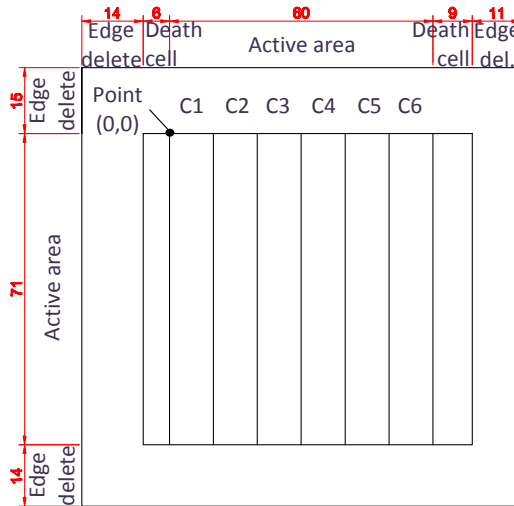


Figure 3.9: 10 cm x 10 cm total area MM produced at TS through LSR scribe. Distances in mm.

we delete the edges by manual grinding. Most of the times, we laminate them following a process similar to the one performed in-line and we make the annealing placing the MMs in the ACL.

3.3 Conventional spectral response equipment

With the SR equipment we measure the generated current in the solar cells for a determined wavelength and for the wavelength range where the solar cell is sensitive to light. This range depends on the kind of semiconductor used and on the solar cell structure. For SJ a-Si:H p-i-n structures, the interesting wavelength range goes from 300 nm to 800 nm.

3.3.1 Components for the conventional spectral response system

The conventional spectral response (CSR) equipment is made up of the following devices:

- Arc lamp: This lamp is a Newport 300 W Xenon Ozone free lamp supplied by a power controller to have stable illumination conditions (see left side of Fig. 3.10). This kind of lamp delivers stable radiation, from UV to near infrared (NIR) radiation with a variable intensity. However its output spectrum presents some peaks that could affect the accuracy of the final measurement.
- Chopper wheel: It converts continuous light (provided by the arc lamp) into pulsed light with a constant frequency that we set.
- Filter wheel: This filter wheel allows to use and to change automatically different filters when measuring over the wavelength spectrum. These filters are used to avoid illumination effects at second order wavelengths caused by the diffraction grating in the monochromator. For example, if the diffraction grating is in the position to transmit light at 800 nm wavelength, the monochromator will also transmit a small 400 nm component where our solar cell is also sensitive. This would induce a current higher than the true current generated at 800 nm. The filters eliminate second order light by just transmitting above the wavelength range of interest. As an example, if we want to scan from 400 nm to 900 nm, we will use a filter from 800 nm on, that will transmit only from wavelengths greater than 400 nm.

- Monochromator: It is shown in the right side of Fig. 3.10, it is the main component of the CSR equipment. It supplies the system with monochromatic light. The monochromator receives a large band spectrum light of the arc lamp which is focused on a grating which only transmits a certain wavelength to the monochromator output depending on the incidence angle of the grating. Changing the incidence angle and changing to different gratings, a wide range of wavelengths can be selected. All the mechanical manipulations in the monochromator used to select the wavelength, are operated by a computer program developed in the laboratory (to be explained in section 3.3.6).

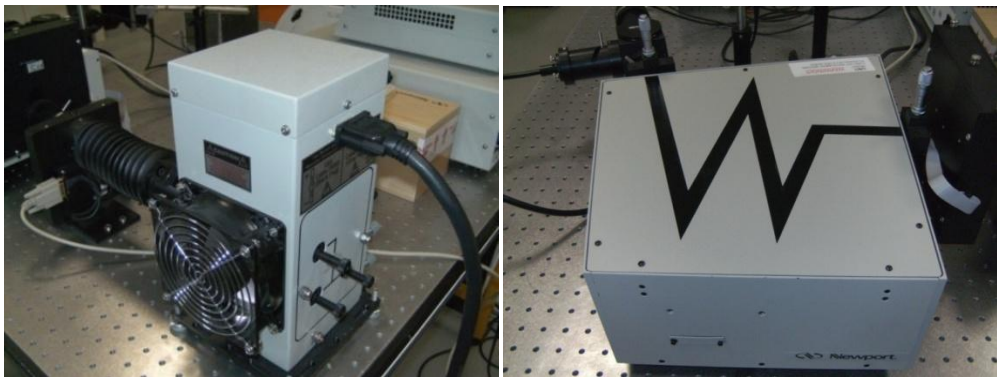


Figure 3.10: Arc lamp (left) and monochromator (right).

- Beam-splitter: It is used to divide the main incoming beam into two beams of light with an angle of 90° . One is called *fibre optic output* (where the solar cell under test is placed) and the other one is the *reference output* (where the reference photodiode is placed). By using different semitransparent materials, e.g. partially covered glasses or mirrors, a beam-splitter has different transmissions properties and therefore different light intensities for the two output beams. It is important to optimize the light division to have adequate light intensities in both, the reference photodiode and the solar cell under test.
- Reference photodiode and calibrated photodiode: Two photodiodes are used in the spectral response measurement principle. In the calibration procedure a calibrated photodiode, with known SR, is located at the fibre optic output (replacing the solar cell

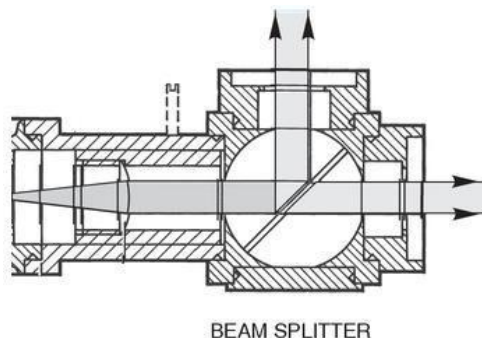


Figure 3.11: Incoming beam divided by the beam-splitter.

under test) and the signal is measured at the same time with the reference photodiode (whose SR is also known). From this measurement we obtain the calibration factor (F) for each wavelength of the optical assembly. The F is used later to calculate the SR of the solar cell under test comparing its intensity with the one of the reference photodiode which stays always at the reference output of the beam splitter.

- Optical fibre: This optical fibre bundle transports the light from the beam-splitter to the solar cell under test. We use a fibre bundle to have more flexibility to illuminate easily different parts of the coupon.
- Lock-in amplifiers: The small currents generated by the solar cell and the photodiode are measured with two lock-in amplifiers (see left side of Fig. 3.12). A lock-in amplifier uses a reference frequency provided by the chopper wheel to stimulate the test sample and phase locked loop technology. It is able to detect very small signals (at the same frequency as that of the reference frequency) in a noisy signal background. The two lock-in amplifiers are used to simultaneously measure the small currents generated by the monochromatic light of the reference photodiode and the solar cell under test.
- Cold light: This light source, used as a bias light, illuminates the test cell with a white light during the measurement (see right side of Fig. 3.12). This illumination adjusts the cell to operating conditions similar to standard test conditions (1000 W/m^2 , $25 \text{ }^\circ\text{C}$ and AM1.5G spectral distribution) (STC). It is called cold light because the lamp filters the

infrared (IR) light so that it does not create heat during the illumination and, therefore, does not transmit heat to the illuminated solar cell.



Figure 3.12: Two lock-in amplifiers (left) and cold light source with its illumination system (right).

Other devices/equipments linked to the CSR equipment are:

- Reference solar cell: The calibrated filtered solar cell (fabricated and calibrated by the FHG-ISE Callab Freiburg, Germany) is used to check if we are working under an irradiance of 1000 W/m^2 with the solar simulator (SS) and to know the error of our SR equipment. We know its SR and EQE in 10 nm steps for a spectrum from 280 nm to 930 nm, as well as its IV curve in the first quadrant under STC. The main electrical parameters are exposed in Table 3.1:

Table 3.1: IV curve parameters of the calibrated solar cell (4 cm^2) from FHG-ISE measured under STC [68].

Electrical parameters	
η (%)	7.6 ± 0.2
I_{sc} (mA)	61.0 ± 1.5
J_{sc} (mA/cm ²)	15.23 ± 0.38
V_{oc} (mV)	624.2 ± 3.1
FF (%)	80.1 ± 0.8
I_{mpp} (mA)	57.0
V_{mpp} (mV)	532.9
P_{mpp} (mW)	31.0

- Spectrophotometre: The Perkin Elmer LAMBDA 950 spectrophotometre is an instrument operating from the UV to the NIR spectral range. It is made up of two monochromators, two radiation sources (a deuterium lamp and a halogen lamp) and a detector compartment. In the laboratory, this equipment allows measuring the diffuse and total transmission and reflection of thin films and thus, it can calculate the direct transmission and absorption. Related to the SR, we determine the internal quantum efficiency (IQE) by measuring the solar cell reflection (as explained in the next section).

3.3.2 Spectral response and quantum efficiency

The spectral response (SR, expressed in A/W) represents the intensity of the photovoltaic effect depending on the incoming light for a given wavelength in a solar cell. It allows to determine how much current is generated by a solar cell for a specific irradiance and for each wavelength of the whole spectrum. The SR is also associated to the external quantum efficiency (EQE, dimensionless), which represents the number of electron/hole pairs generated in the cell by the incident photon flux at each wavelength [69]. Both parameters are linked by Eq. 3.1:

$$EQE(\lambda) = \frac{SR(\lambda) hc}{q \lambda} = 1240 \frac{SR(\lambda)}{\lambda} \quad (3.1)$$

where q is the electric charge of one electron ($q = 1.602 \times 10^{-19}$ C), h is the Planck's constant ($h = 6.626 \times 10^{-34}$ J·s), c is the speed of light in vacuum ($c = 3 \times 10^{17}$ nm/s) and λ (nm) is the wavelength of the incident light.

The SR is usually used to extract information about recombination at front and rear contacts, diffusion or drift lengths of carriers, width of the depletion region and light trapping properties among the most important [70] [71]. In addition, it gives detailed information about which wavelengths have more carrier generation in the solar cell and therefore, it is essential to optimize the modules.

There is another parameter related to the QE, the internal quantum efficiency (IQE) which considers the reflection loss at the solar cell's surface. It represents the number of carriers generated in the solar cell per absorbed photon. Knowing the EQE and the reflection (r) of the device we calculate the IQE through the Eq. 3.2:

$$IQE(\lambda) = \frac{EQE(\lambda)}{1 - r(\lambda)} \quad (3.2)$$

3.3.3 Differential spectral response method

Traditionally, the differential spectral response (DSR) method is based on the detection by a lock-in amplifier of the solar cell's response (solar cell's current). The illumination source is a modulated (AC) monochromatic test light. The cell is simultaneously exposed to a white bias (DC) light of irradiance in the range of 1 sun illumination. Another variation of this method is to use an incandescent lamp, filtered with a set of spectral filters, to obtain the monochromatic light source. In this version, a solar simulator is used as the bias light source [72].

The principle of the DSR method [52] is to compare the current of a reference photodiode and the current of the solar cell under test illuminated simultaneously by the same light source under STC [73]. Monitoring simultaneously these two currents for each wavelength, and knowing the calibration factor ($F(\lambda)$) for the reference cell, we can calculate the SR of the solar cell under test and, thus, the EQE and the short circuit current (I_{sc}) (see below).

3.3.4 Determination of the calibration factor, the spectral response and the integrated short circuit current density

Before measuring the solar cell in the SR equipment, we have to know a calibration factor ($F(\lambda)$) for the calculations of the solar cell SR. In the case of the CSR equipment, the F is determined by the transmission and reflection characteristics of the beam splitter and by the losses in the fibre optic. This factor takes into consideration the difference of light intensity in the two arms of the beam splitter. To determine it, we use a second photodiode (calibrated photodiode) with a known SR. In the calibration measurement the calibrated photodiode is in the position of the solar cell under test. Consequently, we will measure simultaneously the signals of the reference and calibrated photodiodes to obtain the ratio between them for each wavelength. One has to put special attention in the quantity of incident light reaching the calibrated photodiode, so it is very important to concentrate all the light in the active area of the photodiode (the same holds for the solar cells). Therefore, the beam is focused by placing a lens in the fibre optic output.

Taking into account the definition of the EQE, we get the following equation:

$$EQE(\lambda) = \frac{I_{ph}(\lambda)}{q \cdot \phi_{tot}(\lambda)} \quad (3.3)$$

where I_{ph} (A) is the generated current of a solar cell and ϕ_{tot} (photons/s) is the incident photon flux.

Applying Eq. 3.3 for the calibrated photodiode (cal), the reference photodiode (ref) and the solar cell under test (cell), we get:

$$EQE_{cal}(\lambda) = \frac{I_{ph}^{cal}(\lambda)}{q \cdot \phi_{tot}(\lambda) \cdot t(\lambda)} \quad (\text{at fibre optic output}) \quad (3.4a)$$

$$EQE_{ref}(\lambda) = \frac{I_{ph}^{ref}(\lambda)}{q \cdot \phi_{tot}(\lambda) \cdot r(\lambda)} \quad (\text{at direct output}) \quad (3.4b)$$

$$EQE_{cell}(\lambda) = \frac{I_{ph}^{cell}(\lambda)}{q \cdot \phi_{tot}(\lambda) \cdot t(\lambda)} \quad (\text{at fibre optic output}) \quad (3.4c)$$

where ϕ_{tot} (photons/s) is the incident photon flux on the beam-splitter, t is the transmittance of the beam splitter and r is the reflection of the beam-splitter.

Combining the equations 3.4 and changing EQE for SR following the Eq. 3.1 we obtain the SR of the solar cell under test:

$$SR_{cell}(\lambda) = \frac{I_{ph}^{cell}(\lambda)}{I_{ph}^{ref}(\lambda)} \cdot F(\lambda) \cdot SR_{cal}(\lambda) \quad (3.5)$$

where the F is:

$$F(\lambda) = \frac{I_{ph}^{ref}(\lambda)}{I_{ph}^{cal}(\lambda)} \quad (3.6)$$

The SR equipment is configured to measure the samples in short circuit conditions. So, to calculate the I_{sc} of the solar cell from the spectral response measurement one only has to integrate over the spectrum of interest the product of the measured $SR(\lambda)$, the irradiance ($G(\lambda)$) of the AM1.5 spectrum and the surface of the solar cell under test as shown in the following equation:

$$I_{sc} = \int_{\lambda_0}^{\lambda_f} G_{irrad}(\lambda) \cdot SR(\lambda) \cdot S \cdot d\lambda \quad (3.7)$$

where G_{irrad} (W/cm²/nm) is the irradiance provided by the solar spectrum AM1.5 by unit of surface and wavelength and S (cm²) is the surface of the solar cell.

3.3.5 Experimental set-up

In Fig. 3.13 the scheme of the experimental set-up of the CSR measurement equipment is presented. The operation is based in the conversion of continuous light provided by

the arc lamp to pulsed light employing the chopper wheel. Then, the beam arrives to the monochromator which converts the pulsed light in monochromatic light depending on its wavelength. This beam of monochromatic light is separated into two by the beam splitter. One beam goes directly to the reference photodiode and the other one goes through a flexible optical fibre whose output illuminates just above the solar cell. A sample holder is used to establish the electrical contact with the solar cell (see Fig. 3.3, right). Lastly, the two lock-in amplifiers detect and measure the small current generated per wavelength.

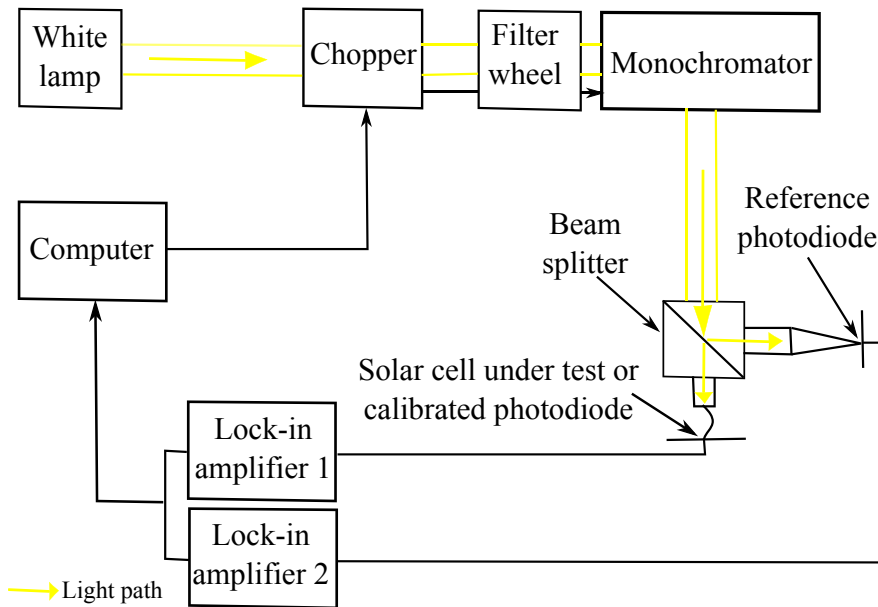


Figure 3.13: SR equipment and links between the different devices.

The optical tuning during the installation of the equipment is a challenge. The optical components of the equipment must be installed step by step by optimizing the beam at each transition point, beginning at the arc lamp and finishing in the reference photodiode and the solar cell. One of the most important steps is to properly focus the collimated beam provided by the arc lamp on the input slit of the monochromator. This point is vital to use the maximum area of the diffraction grating and to have the maximum amount of light at the output slit of

the monochromator (see scheme of the monochromator in Fig. 3.14). Another critical point is the size of the two monochromator slits (input and output) [69]. Both must be adjusted to the same width, its dimension will directly affect the dispersion of the monochromator in each wavelength. After the monochromator, the beam must be collimated again to pass through the beam splitter (see Fig. 3.15). Then, the beams are separated in two parts and both of them are refocused by lenses. In Fig. 3.16 we can see all the lenses that make up the system.

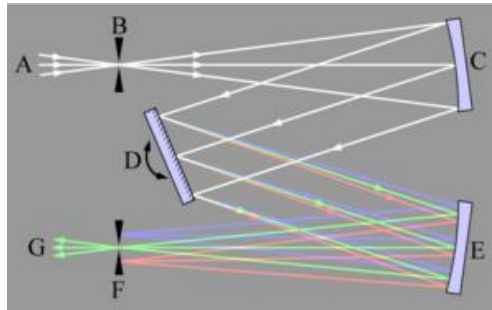


Figure 3.14: Configuration of a Czerny-Turner monochromator.

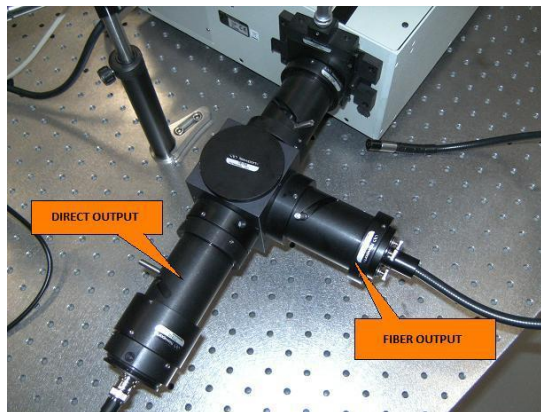


Figure 3.15: The beam splitter with the two arms.

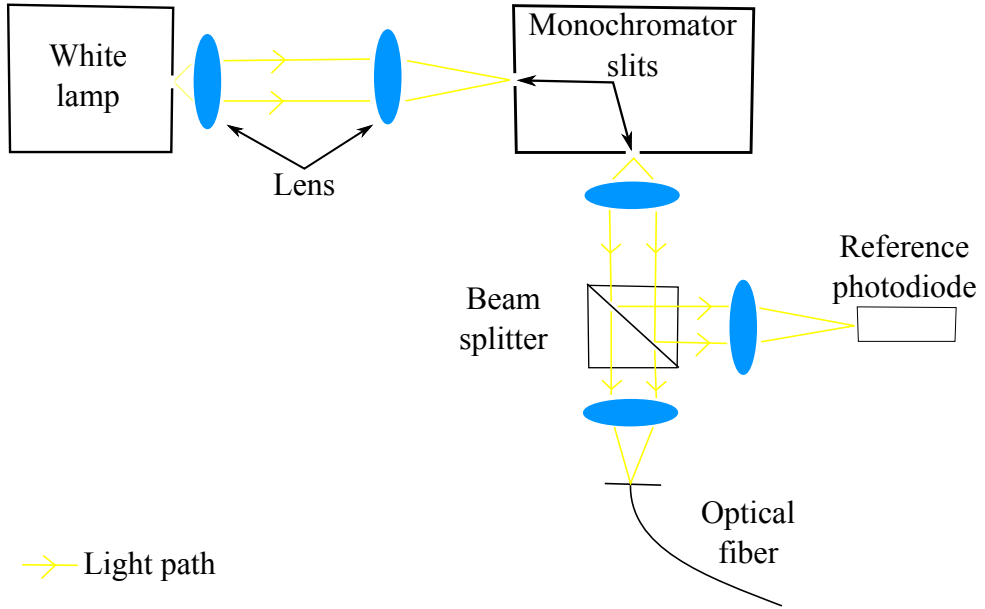


Figure 3.16: Optical path of the light through the system.

3.3.6 Software developed for the conventional spectral response equipment

The control and acquisition of the different signals are done automatically through a program developed in the LabVIEW 8.5 visual platform (virtual instrument (VI)). The goal of this programming work was to create a VI able to control and measure automatically the SR of a solar cell. This program handles all the scan parameters of the monochromator (e.g. for SJ a-Si:H solar cell measurements we cover the spectrum from 300 nm to 800 nm in 5 nm steps), as well as the main parameters of the two lock-in amplifiers (sensitivity, time constant or data storage rate). In addition, it reads and stores the two measured signals for each wavelength (currents of the reference photodiode and the solar cell under test) and calculates and records the SR and J_{sc} of the solar cell under investigation. The schema of the relationship between software and hardware for this equipment is shown in Fig. 3.17.

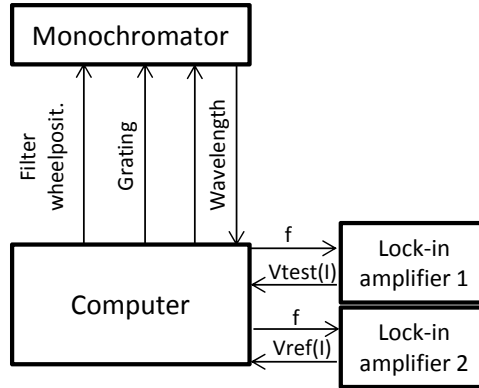


Figure 3.17: Relationship between hardware and software for the CSR equipment.

3.3.7 Calibration procedure and control plan for the conventional spectral response equipment

The calibration procedure consists of the measurement of the SR with a calibrated reference solar cell. For this purpose we use a WPVS Cell (SN: 06-2008) from ISE Fraunhofer, which is a micro-crystalline silicon solar cell of 4.008 cm² area. It has a KG5-filter to absorb only in the a-Si:H wavelength range. We use as well a Hamamatsu S2281-04 photodiode. The calibration procedure is as follows:

1. Set the chopper frequency to 397 Hz. Verify that the two lock-in amplifiers are set to the following parameters. Time constant: 100 ms, 24 dB. Signal input: A, AC, Ground. Reserve: Low noise. Channel one: X. Channel two: θ . Reference: POS EDGE.
2. Place the reference solar cell in the fibre optic output, where usually the solar cell under test is placed.
3. Perform five times the SR measurement in the wavelength range 300 nm - 800 nm with a step width of 5 nm. The EQE of the reference solar cell provided by the manufacturer and an example of the average EQE measured five times with the T-Solar equipment is presented in Fig. 3.18.

4. Calculate the integrated J_{sc} over the spectrum using the SR and the irradiance spectrum AM1.5G. We calculate the integrated J_{sc} for each one of the five measurements. To fill the five J_{sc} values, the average and the standard deviation into the SR calibration file.
5. Check the equipment until the J_{sc} deviation is lower than 0.1 mA/cm^2 (0.7% of the J_{sc} of the WPVS cell).

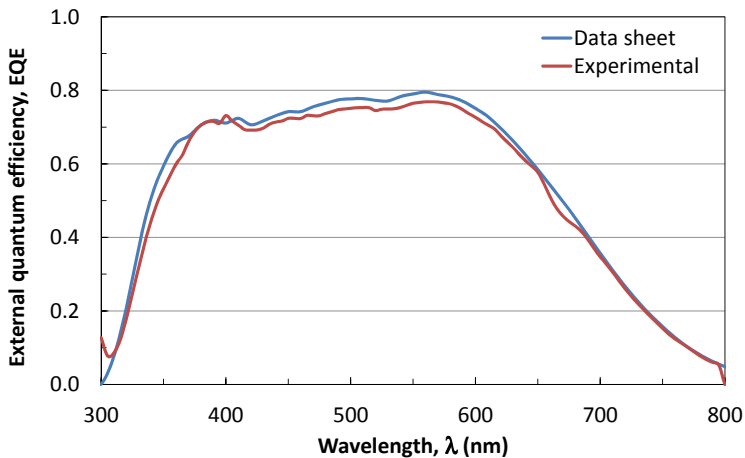


Figure 3.18: Comparison of the EQE provided by the manufacturer (blue) and the average EQE measured in the T-Solar equipment (red) for the reference solar cell WPVS Cell 06-2008 [68].

3.4 Very fast spectral response equipment

The actual design of the T-Solar very large modules consists of various parallel strings of 216 solar cells with a width of 1 cm connected in series. The homogeneous deposition of all the different layers implemented in the p–i–n structure of the solar cell is a challenge and, e.g. high uniformity of film thickness is necessary to assure high module efficiency. Since a large number of solar cells are connected in series, a very uniform current generation is desired along the module. The locally generated current, i.e. the J_{sc} , in the solar cell can be calculated from the SR measurement of a small illuminated area. However, this kind of SR measurements are usually performed on laboratory scale using a monochromator as light source and lock-in amplifier technology to measure the small solar cell current (as explained

in section 3.3), which is a time consuming method (about 15 min per SR in the wavelength range from 300 nm to 800 nm in our lab) and therefore is not suitable for the creation of spatial mappings of J_{sc} values with a resolution of a few cm on a very large area module as fabricated in T-Solar.

We have developed a very fast spectral response (VFSR) measurement system to obtain the SR in about 1 s using simultaneous light generation of high power light emitting diodes (LEDs) operating at different frequencies as already presented in [74], [75], [76]. Applying a fast Fourier transform (FFT) analysis to the generated solar cell current, we extract the SR at a small area (approx. 0.5 cm diameter).

Other research groups have investigated this kind of rapid measurement technique, mainly focusing on light coupling by fibre optics and applying lock-in amplifying technology for the signal (solar cell current) detection [75], [76], [77], [78], [79]. Especially in earlier work, LEDs with very high light intensity were not available for the whole wavelength range between UV and NIR (300 nm – 1100 nm), so lock-in technology was still needed to be applied to detect the small solar cell currents resulting in complex programming work to achieve fast reliable measurements. In addition, the application of optical fibres results in poor utilization of the LED light and consequently, measurements systems are expensive and not very compact. In the last few years, high intensive compact and cheap LEDs have become available in the commercial market for the whole UV/Visible (VIS)/NIR wavelength range. This has made possible the implementation of another type of light coupling technique, avoiding the need of lock-in amplifiers, resulting in a very compact and low cost measurement equipment.

The measurement system can be designed to generate spatial SR mappings with a resolution in the range of centimetres, allowing the location of low current generation areas in modules. Then, deposition process optimization can be performed to increase the overall module current. In addition, we also intend to use this equipment to perform in-line diagnostics to identify possible process errors once the solar cell fabrication is completed (after P3 laser scribe process) and the module is still not laminated e.g. contacting the solar cells at the panel back side with point probes.

In the following paragraphs a novel DSR experimental set-up using LED illumination is presented. The light source is changed but not the basic procedure of the method. Therefore, the concepts (simultaneous measurement of the solar cell under test and reference photodiode) and equations presented in sections 3.3.3 and 3.3.4 will be applied.

3.4.1 Light emitting diodes: Characterization and selection

To build up the VFSR measurement system we use coloured LEDs of different wavelengths as light source (replacing the Xenon lamp and monochromator used in the CSR equipment). A coloured LED is not monochromatic, but has a spectral bandwidth of tens of nanometres in the visible range. However, the use of LEDs provides several important advantages compared to the conventional monochromator-based light-source: First of all, LEDs can be used without optical components for spectral filtering, resulting in already high uniformity irradiance on the test solar cell when adequately configured. In addition, LEDs can be modulated fast and reliably via the feeding current, which also makes modulation with a specific waveform or function possible. Therefore, the measurement set-up can be designed in a compact and efficient way by using LEDs.

With the objective of covering the wavelength range of the SR of a-Si:H solar cells (300 nm - 800 nm) we have investigated a large number of high power LEDs and determined their electrical and optical performance such as their IV curve, peak wavelength, spectral band width, etc. We have also characterized LEDs into the IR region (until 1100 nm) to upgrade the VFSR equipment in the future and use it on a-Si:H/ μ c-Si:H TJ solar cells. Data from the investigation is summarized in Table 3.2 containing the main operation parameters of the selected LEDs. In some cases, deviation from the technical data provided by the manufacturers was found. All the used LEDs are standard commercial available models and therefore, are easily exchangeable in the experimental set-up. All of them have the same size (5 mm diameter) in order to ease their mounting. We also looked for LEDs with a similar current consume (around 20 mA) and emission angle (around 15°) to get their characteristics as similar as possible. Thirty seven different LED models were purchased and characterized to evaluate if they suited this application. From them we chose eighteen in the range 300 nm - 800 nm and six in the range 800 nm - 1100 nm. The step width in wavelength is between 25 nm and 33 nm.

The main characterization results are detailed next:

- **IV curve:** The number of photons emitted by a LED is proportional to the amount of current which flows through the diode. In the VFSR equipment we supply the LEDs with a sinusoidal voltage source instead of a current source. Therefore, operating the LED in an almost linear range (where current and voltage are proportional to each

Table 3.2: Comparison of the technical data sheet values with the experimental data obtained at our lab for the 24 selected LEDs.

LED code	Data sheet peak wavelength	Experimental peak wavelength	FWHM (exp.) (nm)	Data sheet DC bias		Experimental DC bias		Experimental AC amplitude		Structure
	(nm)	(nm)		V (V)	I (mA)	V (V)	I (mA)	V (V)	I (mA)	
L1	355	-	-	3.60	25	3.70	34.0	0.3	56	-
L2	370	376	11	3.90	10	3.50	30.5	0.3	23	AlGaIn
L3	385	383	11	3.50	20	3.55	47.0	0.3	35	InGaIn
L4	400	395	12	3.70	20	3.50	18.5	0.4	26	InGaIn
L5	415	412	14	3.70	30	3.35	24.0	0.3	21	InGaIn
L6	470	470	31	3.20	30	3.40	18.0	0.4	20	InGaIn
L7	510	501	23	3.40	20	3.25	18.0	0.5	25	InGaIn
L8	525	524	38	3.20	20	3.00	37.0	0.3	33	InGaIn
L9	565	562	23	2.00	20	3.50	18.0	0.5	34	GaP
L10	596	593	15	2.10	20	2.00	14.0	0.3	25	AlGaInP
L11	625	641	16	2.20	20	2.45	35.0	0.5	41	AlGaInP
L12	660	653	21	1.90	20	2.05	32.0	0.5	40	GaAlAs
L13	670	672	25	1.80	20	1.80	22.0	0.2	31	GaAlAs/GaAlAs
L14	680	683	21	1.90	20	2.20	47.0	0.3	33	GaAlAs
L15	720	721	24	2.00	50	1.80	34.0	0.2	37	AlGaAs/AlGaAs
L16	760	755	25	1.20	20	1.65	26.0	0.3	57	AlGaAs/AlGaAs
L17	780	772	27	1.70	50	2.00	43.0	0.3	33	AlGaAs/AlGaAs
L18	800	795	30	1.80	50	1.65	66.0	0.3	67	AlGaAs
L19	820	819	30	1.60	100	1.55	42.5	0.1	43	AlGaAs
L20	840	827	31	1.60	100	1.60	47.5	0.4	74	AlGaAs
L21	870	859	49	1.50	100	1.45	58.5	0.1	49	AlGaAs
L22	910	914	57	1.40	100	1.40	47.0	0.2	44	AlGaAs
L23	950	941	44	1.40	100	1.35	80.0	0.1	100	AlGaAs/GaAs
L24	985	982	43	1.25	100	1.25	54.5	0.1	63	GaAs

other) is crucial [74]. To identify this region we measured the IV curve of each LED by introducing voltage to it and measuring (in series) the current that crossed.

In order to automate the analysis, a program was developed in the visual platform LabVIEW. The source-multimeter used for this purpose was a Keithley 2420. Fig. 3.19 shows the IV curves of four representative LEDs. The range of operation is indicated as well as their experimental direct current (DC) operating point (chosen to be in the middle of the experimental quasi linear range). Each LED is supplied with a sinusoidal voltage. It oscillates in its linear range, therefore the operating point is the DC bias and the amplitude of the sine wave is defined by the extension of the linear range.

- **Peak wavelength and spectral bandwidth:** To minimize the measurement error in our equipment we need to determine very well the peak wavelength (λ_{peak}) of emission and to select LEDs with narrow band width. Fig. 3.20 shows the spectra of two LEDs measured under 25 °C presenting a large difference in the band width. The figure illustrates as well that we found some differences between the measured peak wavelengths and the ones provided by the manufacturer. We have discarded LEDs with

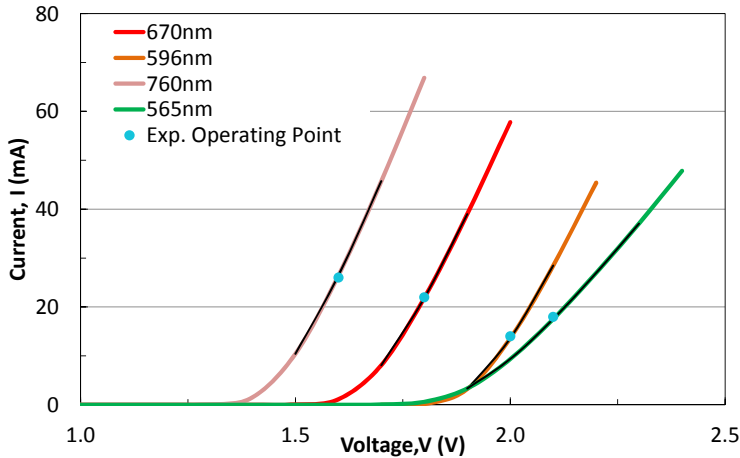


Figure 3.19: Experimental IV curve and DC bias point for 4 representative LEDs. Black lines indicate the AC amplitude.

full width at half maximum (FWHM) greater than 40 nm, in addition it is important to know the exact peak wavelength, especially for LEDs illuminating in the wavelength range at the flanges of the SR curve, to prevent large errors [74].

The peak wavelengths were determined using an Ocean's Optics USB2000+ spectrometre and supplying the LEDs with DC voltage using an Agilent N5771A. The current traversing the LED was measured connecting in series a Fluke 287 multimeter. Since the sensitivity of the mentioned spectrometre is limited from 360 nm to 1010 nm, we experienced certain restrictions while measuring the λ_{peak} of some UV and IR LEDs. In addition, the λ_{peak} and the FWHM were found to be independent from the current at which the LED works under our operation conditions. However, the emission of photons is proportional to the LEDs supply current [27].

The variation among the spectra of LEDs of the same model was also measured, observing a small deviation between the peak wavelengths (less than 2 nm). Since these results were not significant we continued evaluating one LED per model.

Fig. 3.21 presents the individual spectra of the twenty-three selected LEDs for the VFSR measurement system. L1 at 355 nm cannot be measured with our spectrometre, in this case we use the data of the LED manufacturer. The spectral irradiance values

were obtained with LEDs operating near to the recommended working point of the provider.

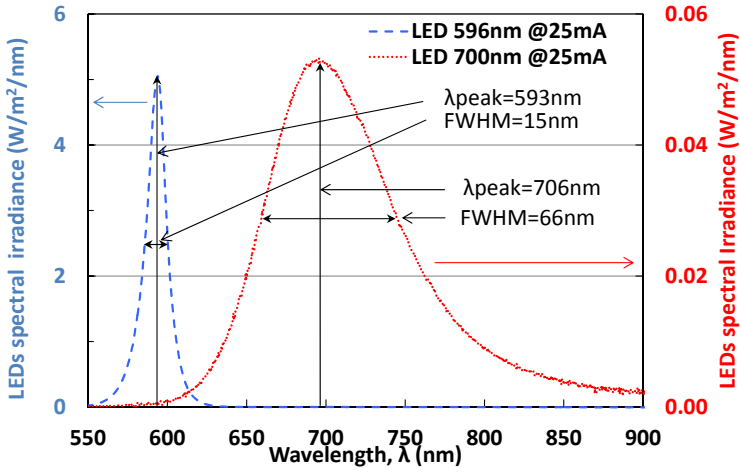


Figure 3.20: Peak wavelength (λ_{peak}) and FWHM for a LED with narrow band width (22 nm, blue dashed curve) and for a LED with wide band width (66 nm, red dotted curve).

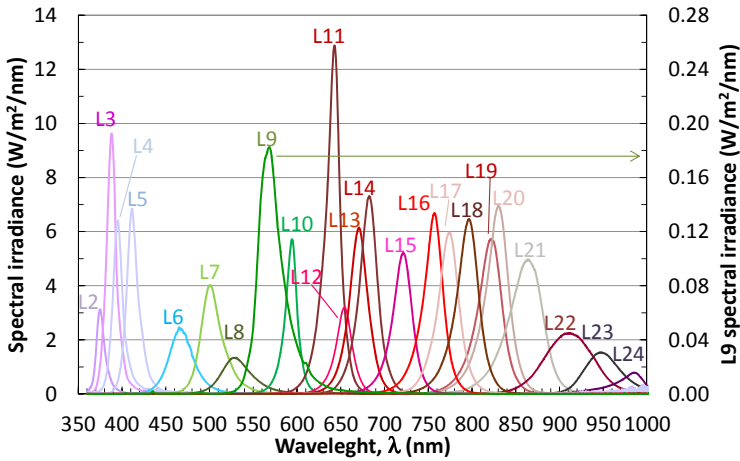


Figure 3.21: Experimental spectral irradiance for 23 selected LEDs in the range 370 nm - 1000 nm.

3.4.2 Sinusoidal generators

In order to reduce significantly the measurement time, in the VFSR system all LEDs work simultaneously and, to identify them, their light is modulated at different frequencies. Later, the current generated by each LED in the solar cell is determined by a FFT of the total generated current.

Nowadays, we use eighteen/twenty-four sine-wave generators for SJ/TJ solar cell measurements. The sine-wave generators exit simultaneously 24 individual voltage waves of ± 4.5 V of amplitude. They produce an individually optimized wave for each LED (frequency, DC bias and AC amplitude) according to their corresponding IV curve. This illumination generates sinusoidal current in the solar cell.

Concerning the excitation frequencies of these signals, they were chosen to sweep between 100 Hz and 200 Hz with a step width of 4 Hz (avoiding multiples of frequencies for the LEDs and for the 50 Hz frequency of the electricity grid). The selection of the frequency applied to each LED is important to reach a proper equipment operation. The overlap of the harmonics with the main current peaks must be avoided.

3.4.3 Fast Fourier transform concept

The fundamental tool used in the VFSR equipment is the FFT. This is widely utilized in digital signal processing (DSP). When signals are expressed in time-domain some information such as frequency and amplitude are coded. This data becomes evident in frequency-domain. Analytically, Fourier analysis provides the connection between time-domain and frequency-domain. Using the Fourier Transform a time dependent periodic function $f(t)$ can be expressed as the sum of different sinusoidal functions with different frequencies $w_n = (n + 1) \cdot w_0$ (see Fig. 3.22). For $n = 0$ we say that it is the fundamental frequency. While, for $n = 1, 2, 3, 4 \dots$ we say that it is the n^{th} harmonic.

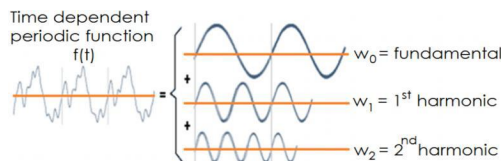


Figure 3.22: Decomposition of a periodic signal in its different harmonics.

Fast Fourier transformation is a method that allows saving calculations to find the Fourier transform of a sampled signal. We can say that for a sinusoidal wave in the time-domain the FFT is a delta function placed in the frequency-domain of this signal (see Fig. 3.23). It has no harmonics, just the fundamental component.

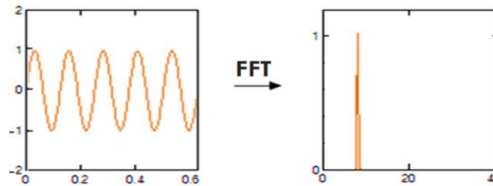


Figure 3.23: Sine wave in the time-domain (left) and, after FFT analysis, sine wave in the frequency-domain (right).

The virtual platform LabVIEW has implemented a tool for FFT calculation, using different algorithms. The FFT tool allows us to determine the spectrum for the measured periodical current and display the results in terms of peak amplitude. This means that, a sine tone of amplitude A yields a spectral value (magnitude) of A at the sine tone frequency.

3.4.4 Measurement procedure for the very fast spectral response equipment

The VFSR equipment allows the measurement of MCs, MMs or full size modules. In the case of MCs, we establish the electrical contact with the solar cells by means of the sample holder and its switch, both presented in section 3.2. The terminals of this sample holder are connected to a digital multimeter for sampling. As for MMs, we fabricated special test modules where every cell is connected individually with a side buss. This enables to perform the measurements connecting each cell directly or connecting the extremes of the mini module, as is the usual way to electrically connect a module (see Fig. 3.24). In this last case, the side buss is not soldered as usual to prevent damaging the solar cells. The used buss has a conducting adhesive that can be pasted onto the solar cells' back contact without losing conductivity. The illumination is done placing the optical coupling element directly above the respective solar cell illuminating a small area (0.5 mm of diameter). Simultaneously, the reference photodiode is lit. We use a fast and sensitive current metre, an Agilent 34410A, to directly measure the generated current in both devices ($I_{cell}(t)$ and $I_{ref}(t)$). We use shielded

cables in the connections to minimize the noise. The next steps consist in processing this data and are explained in the following section.



Figure 3.24: MM with every cell connected individually with a conducting adhesive side buss.

To measure the generated current properly, one has to take in account that to analyse an analogue (time continuous) signal it is necessary to digitalise and sample it. When this is done, a phenomenon known as aliasing can appear. This effect causes different continuous signals to become indistinguishable once sampled. To avoid it, the Nyquist theorem establishes that the sampling rate (number of samples (S) taken by unit of time) must be at least the double of the frequency of the sampled signal [80]. The frequencies at which the LEDs are driven are between 100 Hz and 200 Hz. This means that according to that theorem, the sampling rate must be at least 400 S/s. In our case, the sample frequency at which the Agilent 34410A works is 1000 S/s, taking 5000 measurements (samples).

The schematic diagram of the operation of the whole system is shown in Fig. 3.25.

3.4.5 Software developed for the very fast spectral response equipment

As mentioned, we have implemented the VFSR program using the platform LabVIEW. For this purpose, we use standard commands for programmable instruments (SCPI) instructions in order to control the digital multimeter. We measure voltage in the front and

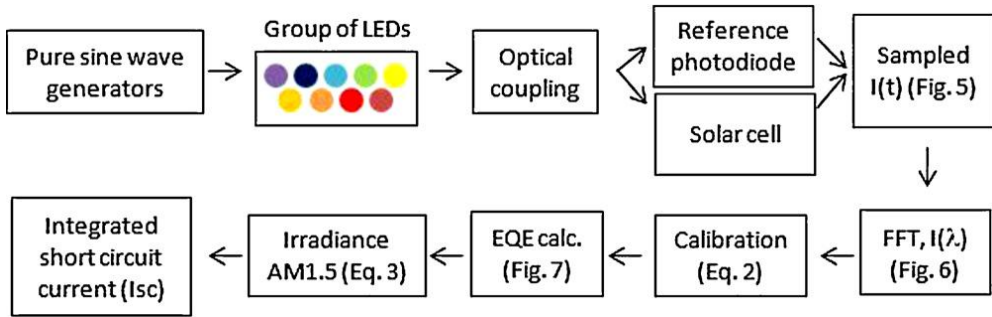


Figure 3.25: Diagram of the VFSR measurement system.

rear terminals, taking for each one 5000 samples (S) at a rate of 1000 S/s. The transduction of voltage to current is done digitally knowing the value of a resistance placed parallel to the solar cell or photodiodes.

If we are doing a calibration of the equipment, a calibrated photodiode is located in the place of the solar cell under test. The reference photodiode and calibrated photodiode currents ($I_{cal}(t)$ and $I_{ref}(t)$) are measured as explained in the previous section. Then, the FFT analysis will be performed over both current signals (obtaining frequency-domain signals $I_{cal}(v)$ and $I_{ref}(v)$). Subsequently, as the excitation frequencies of the LEDs are known, we can assign a current value to each wavelength ($I_{cal}(\lambda)$ and $I_{ref}(\lambda)$). Next, the $F(\lambda)$ factor will be calculated using Eq. 3.6. Finally, the $F(\lambda)$ factor will be saved in a .txt file, together with the $I_{ref}(\lambda)$ values during this calibration ($I_{ref,cal}(\lambda)$), the data sheet $EQE(\lambda)$ of both photodiodes and the spectrum $AM1.5(\lambda)$ for the given wavelengths. This file is used as input file when measuring a solar cell or module.

In the case of the SR measurement of a solar cell, the reference photodiode and solar cell currents ($I_{cell}(t)$ and $I_{ref}(t)$) are measured in the time-domain as explained in the previous section, resulting in Fig. 3.26. Then, with the FFT analysis we obtain the frequency-domain current signals ($I_{cell}(v)$ and $I_{ref}(v)$) as presented in Fig. 3.27. In the figure it is shown that the signal to noise ratio is about 2 – 4 orders of magnitude which is sufficient to determine the SR of an individual solar cell. Apart from the peaks corresponding to the LEDs, peaks resulting from the noise produced by the electricity grid are indicated.

Once the current is determined in the frequency-domain (resolution 0.2 Hz) we analyse the peak by searching the maximum in ± 1.6 Hz of the reference frequency of each LED and we integrate the generated current in ± 0.4 Hz from the maximum to include small deviations

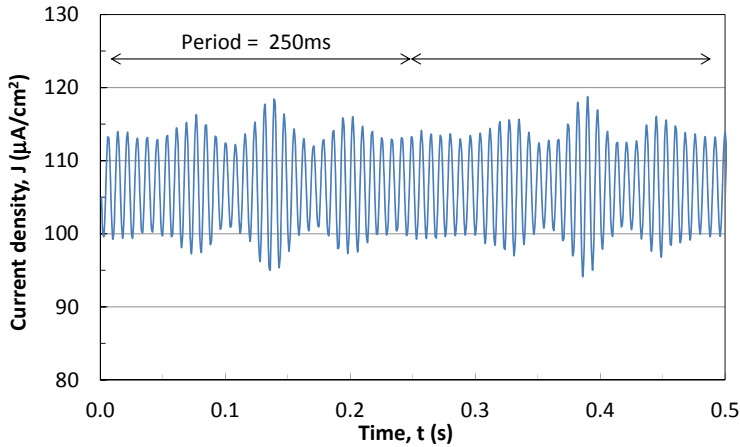


Figure 3.26: Time dependent current density curve presents repetition period of 250 ms due to the selected frequencies with highest common divisor of 4.

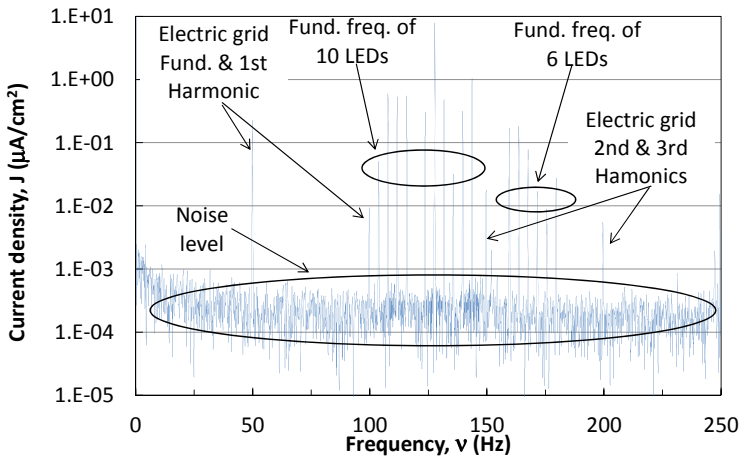


Figure 3.27: Current density curve in the frequency-domain as resulting from FFT analysis.

in frequency of the generated signal [81]. Subsequently, as the excitation frequencies of the LEDs are known, we can assign a current value to each wavelength ($I_{cell}(\lambda)$ and $I_{ref}(\lambda)$). Next, the program accesses to the input file which contains the data of the reference photodiode current determined during the last calibration ($I_{ref,cal}(\lambda)$). A comparison is done between $I_{ref,cal}(\lambda)$ and $I_{ref}(\lambda)$, the difference must not exceed $\pm 5\%$. Otherwise, the

program will be stopped, since the device needs calibration. If the actual current of the reference photodiode ($I_{ref}(\lambda)$) is within the tolerance range, the calculation of the EQE will be performed using the EQE of the calibrated photodiode and the calibration factor of the last calibration (through Eqs. 3.1 and 3.5). Additionally, if the EQE data measured with the CSR equipment is available, a comparison of the results can be done. Finally, the I_{sc} is calculated following Eq. 3.7 and the results are saved in a .txt file.

In Fig. 3.28 the comparison of the EQE measured with the CSR and VFSR equipment is presented. The red measurement points represent the average data of ten repetitive measurements at each wavelength, for the point at 593 nm (the one with higher standard deviation) an error bar (standard deviation) is indicated.

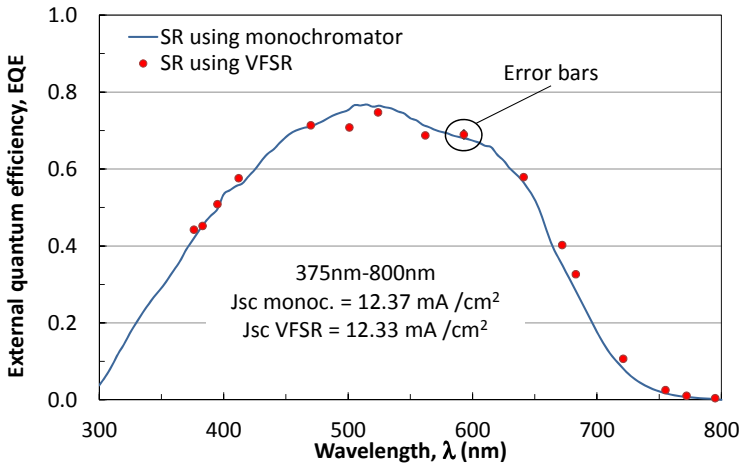


Figure 3.28: The blue curve presents the EQE measured in a CSR equipment with monochromator (5 nm wavelength step). Red dots (the point at 593 nm has an error bar indicating its standard deviation) represent the average of ten EQE measurements with the VFSR measurement system. In this case, the difference between the J_{sc} determined with the CSR equipment and the VFSR is 0.26%.

We have found that the standard deviation in repetitive measurements is less than 2% for every wavelength. For most of the points the deviation from the traditional method is small, a larger deviation is found for the LEDs at 501 nm and 562 nm wavelengths. The reason for the larger deviation at 562 nm most probably is due to the small intensity of the LED illumination at that wavelength which is under investigation, also the larger deviation at 501 nm is under investigation but no reason has been identified so far. As shown in the insert of Fig. 3.28, the short circuit current calculated in the wavelength range from 375 nm to 800 nm is very similar

for both methods with a deviation of less than 1%, and comparable to values found by other researchers [75], [76].

3.5 Measurements of illuminated and dark current-voltage curves

With the measurement of illuminated and dark IV curves we are going to characterise electrically the solar cells and mini modules. Next, we present the main electrical parameters to be considered and the equipments and procedures needed to obtain them.

3.5.1 Equipment

- Solar simulator: It is installed in the optical laboratory. It simulates the solar light in a 20 cm x 20 cm area specifically, it provides a wide beam of collimated and uniform light with an irradiance almost like the sun. The solar simulator (SS) equipment consists mainly in a 1300 W external electric power source, an arc lamp compounded by high pressure noble gases, an ellipsoid mirror around the lamp for collimation, a flat mirror to direct the light to the sample through a lens and an AM1.5 spectrum filter. It provides class AAA (the highest precision) illumination for a 20 cm x 20 cm area. Since we have a variable power supply by the external source, we could regulate the irradiance in our device changing the power, however, that could change the spectrum. Therefore, the illumination level is usually fine adjusted by the lamp position in respect to the ellipsoid, even if this could affect slightly the overall uniformity. To measure the IV curves under STC we set the SS output irradiance to 1000 W/m² following the steps described in section 3.5.4. In addition, the irradiance level is controlled every time we use the SS by measuring the I_{sc} with a reference solar cell. With this equipment we measure the illuminated IV curves for small samples as our 1 cm² and 4 cm² solar cells and our 10 x 10 cm² and 20 x 20 cm² MMs.
- Keithley 2400 source metre/multimetre: We use this source to inject current or to apply voltage to the samples in which we measure IV curves under illumination or dark conditions. The maximum power, voltage and current parameters for this source are: $P_{max} = 22$ W, $V_{max} = 200$ V, $I_{max} = 1$ A. Consequently, if we work with the maximum

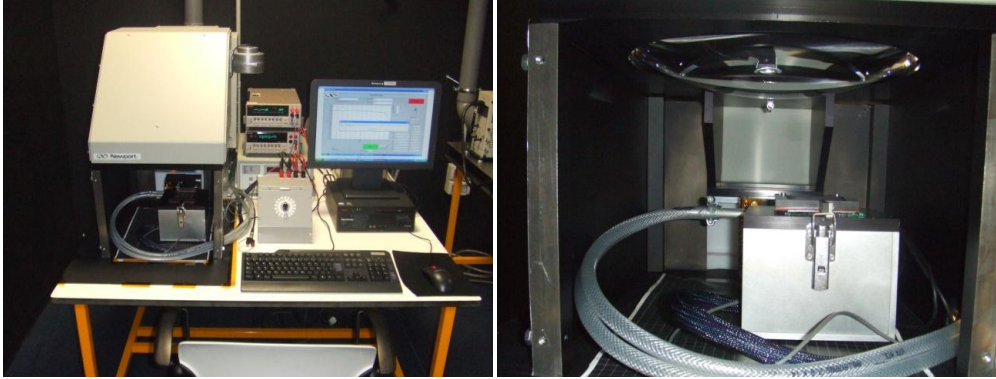


Figure 3.29: Solar simulator and the other parts of IV curve measurement devices (left) and measurement compartment where we can see at the top the solar simulator lens that illuminates the samples (right).

voltage we cannot exceed 110 mA and if we work with the maximum current we cannot overpass 22 V.

- Keithley multimeter and temperature sensor Pt 100: Both parts are used to measure the sample temperature in each moment. The Pt 100 is a probe made of platinum wire which has 100 Ω resistance at 0 $^{\circ}\text{C}$ and whose resistance increase with the temperature. We measure IV curves when the sample temperature is at 25 $^{\circ}\text{C}$ (STC). To measure MCs, the Pt 100 is installed in the probing station, with the temperature sensible surface in contact with the coupon. In the case of MMs we paste the Pt 100 in the edge delete area of the MM. With the Pt 100 and the multimeter we measure the Pt 100 resistances. Next, we calculate the temperature through the Eq. 3.8 that converts the resistance value R (in Ω) to the temperature, T (in $^{\circ}\text{C}$):

$$T = \frac{R - 100}{0.385} \quad (3.8)$$

This multimeter is also used to measure periodically the short circuit current of the reference solar cell to know the level of irradiance and to assure that this value is near to 1000 W/m^2 .

- Cooling system: It is connected to the probing station to avoid the increase in temperature due to the illumination by the SS. The system is based in two close and independent water circuits for the heat exchange of water from the factory cooling water

circuit. The second circuit goes to the probing station, to cool the coupon to 25 °C. There are two different water speeds for cooling, however, due to the slow reaction time of the system it is not able to maintain the temperature constant to 25 °C when the SS shutter is opened. Consequently we have set the water temperature to the minimum, around 15 °C, and we only switch on the SS during the measurement time (between 7 s and 30 s). The procedure consists of switching on the SS and waiting until the solar cell is at about 25 °C. Next, we switch off the SS and we wait until the temperature has decreased. Subsequently, we switch on again and measure the second cell and so on. During the measurement, time the temperature only changes about 0.5 °C to 1 °C.

- Agilent N5771A source: We can also measure the dark IV curves of entire modules to have a complete analysis of the modules manufactured in the production line. It implies to measure in a wide range of current and voltage and so, it needs a connection of two different electrical sources to cover the full range. The Keithley 2400 source does not have enough power to measure quarter or full size modules, consequently, we combine this source and the Agilent N5771A one. We use the Keithley 2400 for low currents and voltages because of its higher precision. The maximum power, voltage and current parameters for the source metre Agilent N5771A are: $P_{max} = 1500$ W, $V_{max} = 300$ V, $I_{max} = 5$ A.

3.5.2 Current-voltage curves under illumination

The equivalent circuit of an a-Si:H solar cell was introduced in section 2.1 and it is presented here again in Fig. 3.30. The figure includes as well the resulting equation for the dependence of the cell current on the external voltage under illumination [23]. This is shown to explain the basic parameters usually used to describe the electrical properties of the solar cell.

$$I = -I_{ph} + I_{ph} \frac{d_i^2}{(\mu\tau)_{eff}[V_{bi} - (V - IR_s)]} + I_0 \left(\exp\left(\frac{q(V - IR_s)}{nkT}\right) - 1 \right) + \frac{V - IR_s}{R_{sh}} \quad (3.9)$$

The main electrical parameters obtained from the measurement of illuminated IV curves and related to this equation are explained next together with their main dependencies:

- **Open circuit voltage (V_{oc}) (V)**: It is the maximum voltage that can be obtained under illumination. This happens when the cell is not connected to a load, there is no external

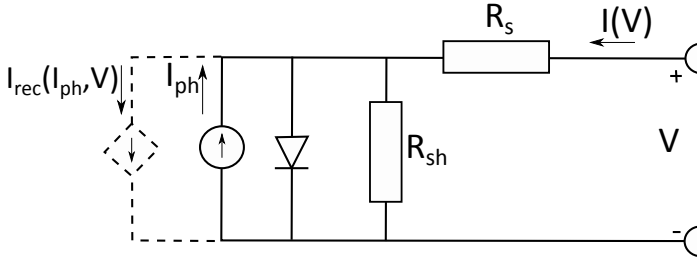


Figure 3.30: Equivalent circuit of an a-Si:H PV solar cell. The current sink (I_{rec} , dashed lines) takes into account the current losses due to recombination in the i-layer of the device [23].

consumption and the current goes to zero [82]. For a first approximation, we do not take into consideration the recombination term (e.g. we are going to work with non-degraded cells), in addition R_{sh} usually has a big value, so we neglect as well $\frac{V-IR_s}{R_{sh}}$. Therefore, when:

$$V = V_{oc} \Rightarrow I = 0 \Rightarrow V_{oc} = \frac{nkT}{q} \cdot \ln\left(\frac{I_{ph}}{I_0} - 1\right) \quad (3.10)$$

Thus, the V_{oc} depends in a logarithmic scale on the reverse saturation current (I_0), being inversely proportional. In addition, V_{oc} also depends on the thickness and doping concentration of the p and n layers. If one or both increase, the difference in the Fermi level increases and therefore, more voltage will be generated in the solar cell. The V_{oc} is also related linearly to the temperature and logarithmically to the irradiance.

- **Short circuit current (I_{sc}) and current at maximum power point (I_{mpp}) (A):** They depend basically on the i-layer thickness in the p-i-n junction where the current is generated. The I_{sc} is the maximum value of current flowing in a solar cell, this occurs when the external loads decreases to zero and the cell is short circuited. For an ideal solar cell the I_{sc} and the light net generated current are identical. Consequently, the largest current which may be drained from the solar cell is the I_{sc} (Eq. 3.11) [82].

$$I_{sc} = I_{ph} \quad (3.11)$$

The current depends among other factors on:

- The solar cell area. To remove this dependence, it is more common to use the short circuit current density (J_{sc})(usually in mA/cm²) rather than the I_{sc} .
 - The number of photons (i.e. irradiance). More incident photons correspond to more generated electrons and higher current.
 - The spectrum of the incident light. For most solar cell measurements, the spectrum is standardized to the AM1.5G. (see section 2.3).
 - The optical properties (absorption and reflection) of the solar cell.
- **Voltage at maximum power point (V_{mpp}) (V):** It is determined by the quality of the diode (given by the ideality factor of the diode (n)) and the FF.
 - **Fill factor (FF) (dimensionless):** The FF gives us the relation between the product of V_{oc} and I_{sc} (ideal power) and the maximum real power, it is defined by:

$$FF = \frac{V_{mpp} \cdot I_{mpp}}{V_{oc} \cdot I_{sc}} \quad (3.12)$$

- **Maximum power (P_{mpp}) (W):** It is the maximum power at which the solar cell operates, it is given by:

$$P_{mpp} = V_{mpp} \cdot I_{mpp} = V_{oc} \cdot I_{sc} \cdot FF \quad (3.13)$$

- **Efficiency (η) (dimensionless):** The maximum power and the efficiency are directly proportional, its expression is:

$$\eta = \frac{P_{mpp}}{G_{irrad} \cdot S} \quad (3.14)$$

Where G_{irrad} is the irradiance (W/m²) and S the surface of the device (m²).

- **Series resistance (R_s) (Ω):** The main factors that cause an increase in the value of the series resistance in our device are the interconnections between the cells (P2 contact) and the resistance between the metallic contact and the front TCO layer.
- **Shunt resistance (R_{sh}) (Ω):** The causes that induce a decrease in R_{sh} are the non-ideality of the p-i-n junction and the impurities or shunts in the junction that lead to a short circuit between the front contact and the back contact.

Both the R_s and the R_{sh} reduce the FF [83]. In the region close to V_{oc} we can fit the illuminated IV curve to a straight line $\left(I = \frac{V}{R_s}\right)$ which will give us the slope $\left(\frac{1}{R_s}\right)$ of the IV curve in the V_{oc} region. In the same way, in the region close to I_{sc} we also do a linear fit of the curve $\left(I = \frac{V}{R_{sh}}\right)$, by this we know the slope $\left(\frac{1}{R_{sh}}\right)$ of the IV curve in the I_{sc} region. These two slopes impact on the FF of our solar cell. To achieve the maximum FF we look for a R_s as small as possible and a R_{sh} as high as possible.

Fig. 3.31 shows an IV curve of a 1 cm^2 T-Solar solar cell, indicating where the electrical parameters are situated in the curve.

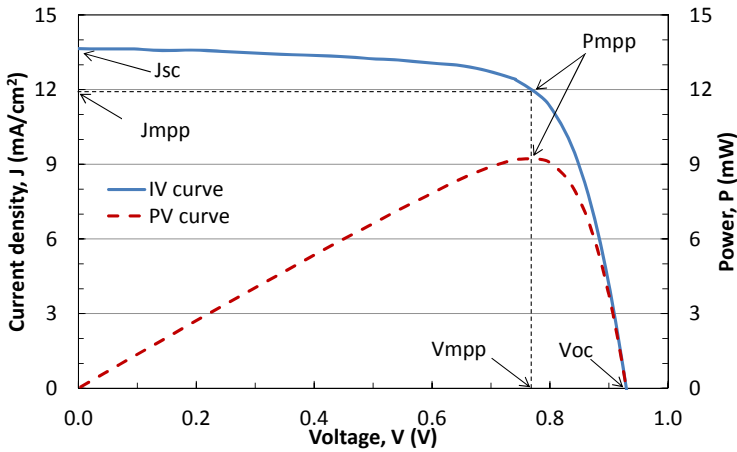


Figure 3.31: Typical illuminated IV curve (continuous blue line) and PV curve (dashed red line) of a photovoltaic solar cell.

3.5.3 Dark current-voltage curves

In this case the solar cell is not illuminated, so the term I_{ph} is cancelled in eq. 3.9, then the equation reduces to:

$$I = I_0 \left(\exp \left(\frac{q(V - IR_s)}{nkT} \right) - 1 \right) + \frac{V - IR_s}{R_{sh}} \quad (3.15)$$

In a logarithmic presentation the IV curve in the forward region at intermediate voltages results in a straight line until it turns to saturate at high voltage due to the series resistance.

Making a linear fit ($y = a + bx$) of the curve at these intermediate voltages, we can estimate the I_0 and n values:

$$\ln I = \ln I_0 + \frac{qV}{nkT} \quad (3.16)$$

where $I_0 = e^a$ and $n = \frac{q}{bkT}$

On the other hand, we can calculate R_s making a linear fit in the high voltage region. Usually this region starts when the current is higher than I_{sc} . In the same way, we can calculate R_{sh} making a linear fit in the low voltage region. Fig. 3.32 shows a dark IV curve of a 1 cm^2 T-Solar solar cell.

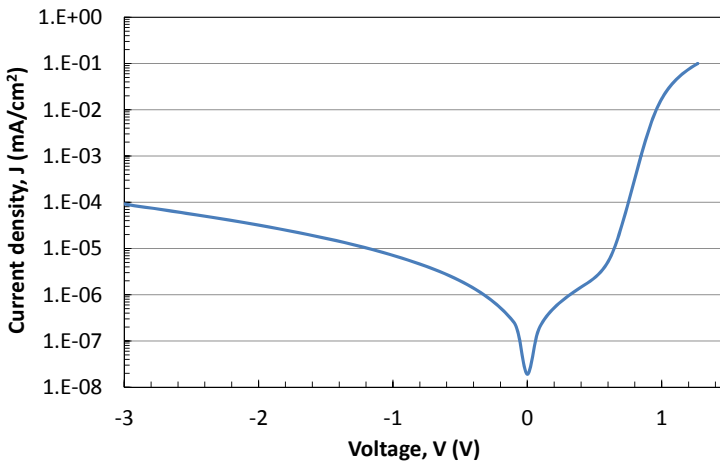


Figure 3.32: Typical dark IV curve of a photovoltaic solar cell.

3.5.4 Calibration procedure and control plan for the class A solar simulator

The calibration procedure consists in the verification of the emitted irradiance (G_{irrad}) (≈ 1 sun) in the Newport Oriel 93194A solar simulator under STC. For this purpose we use a reference solar cell WPVS Cell (SN:06-2008) and reference photodiode Hamamatsu (S1337-1010BR). The calibration procedure is made up of two parts since we check not only the temporal fluctuation but also the spatial fluctuation. The temporal fluctuation procedure is as follows:

1. One places the reference solar cell in the optical center of the SS (usually coincides with the geometric center in the scale of the table) and measures its I_{sc} during 45 min with a step of 30 s. The reference photodiode stays always fixed. The relationship between the I_{sc} and the G_{irrad} is linear. Therefore, measuring the I_{sc} is a direct measurement of the G_{irrad} of the lamp. The average and standard deviation of the G_{irrad} during the measurement for both, the reference solar cell and the reference photodiode, are stored in an Excel file sheet. Their calculated non-uniformities (see Eq. 3.17) together with other complementary data are also added, as we see in the top of Table 3.3.
2. The temporal fluctuation of the solar simulator fulfil the specifications if the average irradiance incident on the reference solar cell is in the range $1000 \pm 50 \text{ W/m}^2$ and the non-uniformity is lower than 2%.
3. If G_{irrad} is out of the range we must change the lamp power or the lamp position until reaching $\approx 1000 \text{ W/m}^2$.

Once the temporal fluctuation measurement is finished we do the spatial fluctuation measurement. The procedure is as follows:

1. In this procedure a spatial mapping of the irradiance level is performed. The mapping has 36 points in a 10 cm x 10 cm area, the step width is 2 cm. An example is shown in Fig. 3.33. The software made in LabVIEW (see section 3.5.5) indicates the position where we must locate the reference solar cell in each measurement point. The reference photodiode stays always fixed.

The average value, standard deviation and spatial non-uniformity of G_{irrad} over the spatial mapping measured with the reference solar cell are stored in an Excel file sheet, as well as the average value, standard deviation and non-uniformity of the I_{sc} temporal fluctuation of the reference photodiode during the measurement of the mapping (see bottom part of Table 3.3).

2. If the spatial non-uniformity is lower than 2%, the spatial fluctuation is in the specified range and, therefore, the calibration ends. Otherwise, one must perform the next steps:
3. One has to adjust the x, y, z lamp positions (in this order) in the SS housing to optimise the irradiance level in the optical centre and at the corners to obtain the irradiance level

within 2%. One has to move separately each axis looking for a trade-off between high irradiance level and low non-uniformity.

4. One has to repeat the spatial mapping procedure and to check if the specifications are fulfilled. This could result into a new optical centre.
5. One has to repeat the calibration of the temporal fluctuation (section above) placing the reference solar cell in the new optical centre.

The non-uniformity is calculated through the next equation:

$$\text{Non-uniformity}(x) = \frac{\text{Max}(x) - \text{min}(x)}{\text{Max}(x) + \text{min}(x)} \quad (3.17)$$

where x represents a vector or matrix of different values of a given parameter, like e.g. the irradiance.

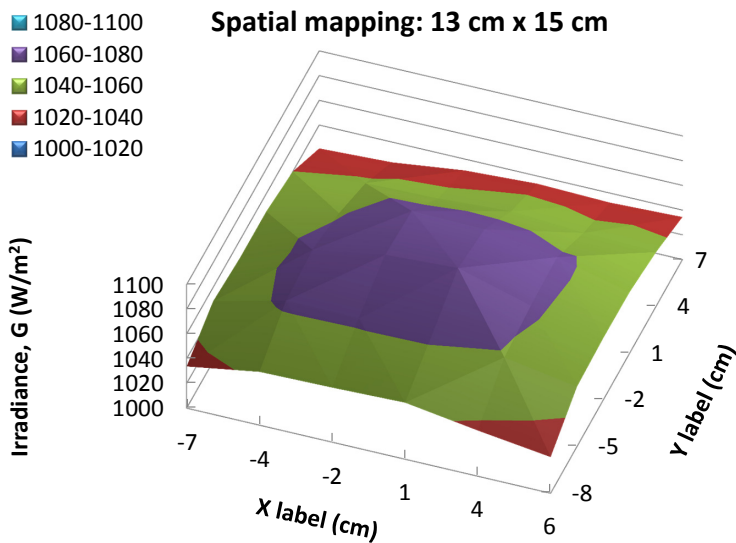


Figure 3.33: Spatial mapping result of the calibration done on 29/11/2011. It was the initial calibration (29h) for the third lamp used in the T-Solar SS.

Table 3.3: Results of all the calibration controls done for the three lamps used until the moment in the solar simulator. Top: Temporary fluctuation. Bottom: Spatial fluctuation.

Lamp number	Lamp Hours (h)	Date	Power Supply (W)	TEMPORARY FLUCTUATION				
				G solar cell (W/m ²)	Uniformity sc	I ph (mA)	Uniformity ph	
Lamp n°1	70.0	12/18/2008	1300	-	-	-	-	-
Lamp n°2	507.0	2/11/2010	1400	973.3 ± 4.1	0.77%	7.021 ± 0.010	0.27%	
Lamp n°2	834.4	3/23/2010	1500	1010.0 ± 1.9	0.49%	7.520 ± 0.009	0.29%	
Lamp n°2	1075.0	2/11/2011	1500	860.8 ± 1.7	0.52%	6.44 ± 0.03	0.78%	
Lamp n°3	23.6	11/29/2011	1100	1080.1 ± 2.0	0.44%	6.70 ± 0.00	0.12%	

Lamp number	Lamp Hours (h)	Date	Power Supply (W)	SPATIAL FLUCTUATION				
				G solar cell (W/m ²)	Rel.Error, σ	Uniformity sc	Uniformity ph	Area (cm ²)
Lamp n°1	70.0	12/18/2008	1300	969.0 ± 8.0	0.83%	1.61%	0.76%	8 x 8
Lamp n°2	507.0	2/11/2010	1400	970.0 ± 7.7	0.79%	1.50%	0.44%	10 x 10
Lamp n°2	834.4	3/23/2010	1500	993.6 ± 6.7	0.67%	1.40%	1.04%	10 x 10
Lamp n°2	1075.0	2/11/2011	1500	847.3 ± 11.2	1.32%	2.46%	-	10 x 10
Lamp n°3	23.6	11/29/2011	1100	1049.0 ± 14.8	1.41%	2.76%	0.22%	13 x 15

3.5.5 Software developed for current-voltage curve measurements

The automated IV curve measurement of cells and mini modules has been developed through LabVIEW software. To control the source metre and multimeter SCPI instructions are used. The programming is adapted to measure both illuminated and dark IV curves. We work with cells of several sizes (at T-Solar, we usually produce 1 cm² and 4 cm² solar cells), as well as MMs of several sizes (usually 10 x 10 cm² and 20 x 20 cm²). In the case of dark curves, also modules (quarter size modules of 1.3 x 1.1 m² and full size modules of 2.6 x 2.2 m²) can be measured. Additionally, the curves can be traced in both, forward and reverse direction. Furthermore, it presents the advantage that part of the IV curve uses the source in voltage mode to measure current and another part uses the source in current mode to measure voltage. This is an important point because IV curves are exponential and it is difficult to have a reliable curve with the measurement points well distributed over several decades of current. Besides the IV curves, one can also perform shunt busting of the solar cells and MMs by applying 6 V in reverse during about 100 ms.

Once the illuminated or dark IV curve is measured it is represented on the monitor and the program starts the corresponding fittings and calculations of the electrical parameters of interest of the corresponding solar cell or PV module. Then, all the required data is saved into a text (.txt) file which is stored on a database in a folder with its date. The file name is composed by the date, time and the barcode of the corresponding coupon or module. The content of these files change depending on the measurement mode but it will mainly provide the electrical parameters, the IV and PV curves and other parameters of interest like

the duration, date and time of the measurement; source metre information; the irradiance immediately previous and after the IV curve measurement or the device temperature. The LabVIEW front panel for the IV curve tracer is shown in Fig. 3.34.

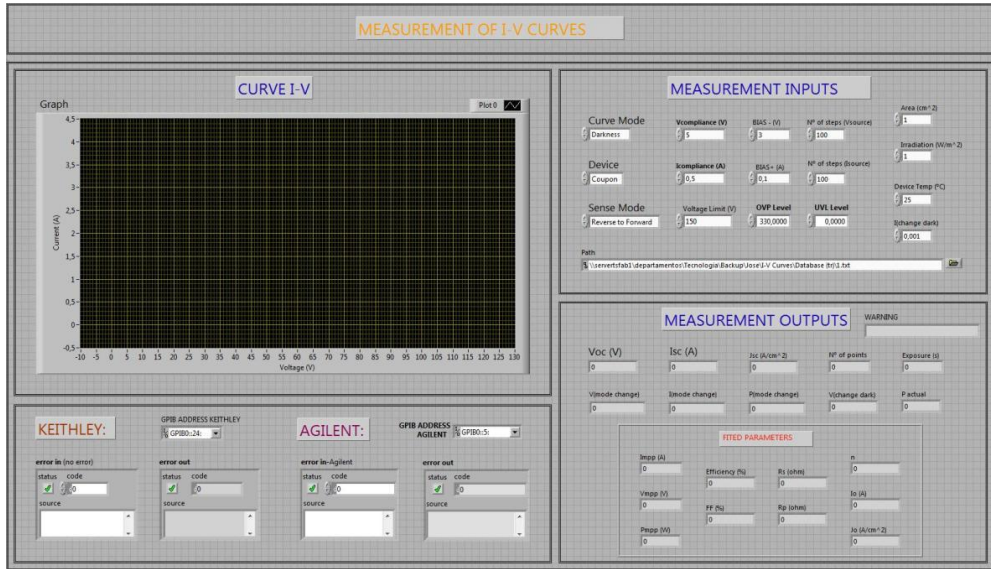


Figure 3.34: LabVIEW front panel for the IV curve tracer, where the input parameters are introduced and the main output parameters are shown.

3.5.6 Measurement procedure for illuminated current-voltage curves

The dimensions of the coupons that contain ten solar cells are 10 cm x 10 cm. To reduce the effect of the non-uniformity of the SS illumination we measure only groups of four solar cells for each coupon, placing the centre of the four cells in the SS optical centre. This way, we measure the solar cells with the centre of each cell only in a distance of 1.415 cm from the SS centre point. Therefore, we obtain a negligible spatial non-uniformity variation achieving highly reliable data. To place easily the sample holder, the mini modules or the reference solar cell we have a base gridded in cm.

The IV curves are measured as explained in 3.5.5. The resulting .txt file is introduced in a dynamic table of an Excel file which acts as database. In the case of illuminated curves, the average of the irradiance value (obtained measuring the reference solar cell before and after

the solar cell/mini module measurements), as well as the device temperature, are introduced. The voltage and current are automatically recalculated applying the next equations:

$$V_{STC}(1000W/m^2, 25^\circ C) = V_{meas}(G, T) + \frac{nkT}{q} \ln\left(\frac{1000}{G}\right) \quad (3.18)$$

$$I_{STC}(1000W/m^2, 25^\circ C) = I_{meas}(G, T) \cdot \frac{1000}{G} \quad (3.19)$$

where $n_{initial} \approx 1.5$ and $n_{degraded} \approx 1.8$.

Once we have the STC values of V_{oc} , I_{sc} , V_{mpp} and I_{mpp} , we recalculate the rest of the main electrical parameters, which are FF, P_{mpp} and η , through the equations 3.12, 3.13 and 3.14 respectively. R_s and R_{sh} are considered invariable to the small variation of illumination and are not corrected to the STC values.

CHAPTER 4

MODELLING, CHARACTERIZATION AND OPTIMIZATION OF A-Si:H SOLAR CELLS

In this chapter we mainly present work developed in the frame of the European project HELATHIS [84], [46], [85], [86], [87], [74], [81] related with this PhD thesis. One of its objectives is the optimization of the solar cell structure implemented in T-Solar's industrial production process for very large area (2.6 m x 2.2 m) a-Si:H PV modules. In the optimization, not only the achievement of the solar cells' physical limit efficiency must be taken into account, but also aspects like the solar cell's fabrication time (impacting on factory throughput), the material and the energy consumption (including its impacting on the production cost), among others. In reference to this, we report here, firstly, on the evolution to fabricate highly efficient and reliable a-Si:H test solar cells in the industrial environment of T-Solar and the preparation of samples with solar cells for shipments to project partners. Next, we investigate the cell structure developments, reporting on the front TCO layer and glass progresses, p-i-n structure improvements and back contact evolution. Next, we analyse the results obtained with the VFSR equipment and simulation studies on the p-i-n structure and the front TCO layer texture. Finally, the improvements in the industrial production line of T-Solar since the beginning in the year 2008 are shown.

4.1 Evolution of the fabrication of highly efficient and reliable a-Si:H test solar cells in the industrial environment of T-Solar

We presented in Section 3.2 how we produce the research solar cells or mini cells (MCs). The first type of cells (see Fig. 3.3) was done through shadow mask. The T-Solar solar cells produced with shadow mask could be improved focusing on two fields. On one hand, to change the solar cell's production method in order to get the front contact very close to them and always at the same distance, and a well defined solar cell area. On the other hand, to treat the solar cells performing shunt busting and annealing, to bring them into the so-called initial state. Next, we present the influence of these changes.

4.1.1 Solar cell production method (shadow mask vs. laser scribe)

To produce highly efficient and reliable solar cells we need to use different masks or to produce the solar cells through laser scribe. We are going to analyse the effect of this change, comparing the results obtained in solar cells produced with shadow mask and the ones coming from a laser scribe process.

The former T-Solar solar cells design had several problems. The most significant ones were:

- The front contact (grid) was achieved scratching by hand, which implied having different distances to the solar cells (pads). In addition, the distance was too long, resulting in high R_s and low FF values (see Fig. 4.1).
- A non well defined area for the pads, since we need a precision of $\pm 50 \mu\text{m}$ in diameter to define the cell area with an error in the range of 1%. In the T-Solar production line this is only possible using laser scribe.

In summer 2009 we started the tests for a better design by using laser scribe to define pads and grids. The laser scribe allows:

- To place the front contact closer to the cells, which results in lower R_s and higher FF, and to place it at the same distance to every cell which gives more reliable data.
- To get a well defined area and well isolated pads. When comparing the J_{sc} calculated through the EQE (J_{sc_SR}) with the J_{sc} measured in the current density-voltage (JV)

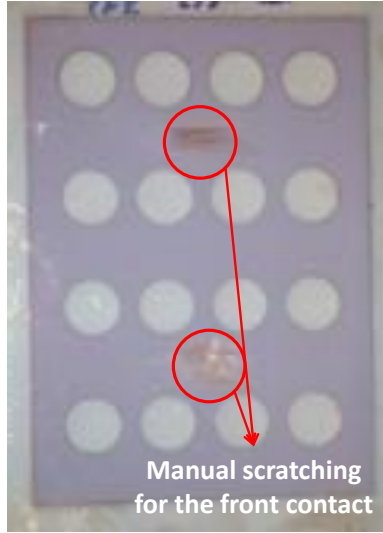


Figure 4.1: Design for the former T-Solar solar cells (1 cm²) produced with shadow mask.

curve (J_{sc_SS}), as shown in Eq. 4.1, we get a difference (Δ) of about 17% with the former coupons produced with round shadow mask whereas it was reduced to about 7% when using laser scribe. Hence, the laser scribe design is much more reliable.

$$\Delta(J_{sc}) = \frac{J_{sc_SS} - J_{sc_SR}}{J_{sc_SR}} \quad (4.1)$$

Electrical parameters for the average of the best 5 cells/coupon of a sample produced with shadow mask and another one produced through laser scribe are presented in Table 4.1. We see that the results for the solar cells produced through laser scribe are better, presenting an efficiency improvement of 2.8% in average. The most affected parameters are the R_s and J_{sc_SS} . We only appreciate a small reduction in the V_{oc} . Despite this improvement, the electrical parameters are still slightly worse than the ones in modules. This is solved performing shunt busting and annealing as presented in next section.

As previously commented we can determine the J_{sc} from two different measurements. By measuring the JV curve with the solar simulator (J_{sc_SS}) or measuring the SR and integrating the J_{sc} in the 300 nm - 800 nm wavelength range (J_{sc_SR}) (see Table 4.1). From now on, we will always present both currents in the electrical parameter tables. With shadow mask the

Table 4.1: Electrical parameters comparison for the old (shadow mask) and new (laser scribe) T-Solar solar cell design. Results are the average of the best 5 cells/coupon. J_{sc_SR} : measured with CSR, J_{sc_SS} : measured with solar simulator.

Production Method	η	Jsc (mA/cm ²)_SR	Jsc (mA/cm ²)_SS	Voc (mV)	FF	Rs (Ω cm ²)	Rsh (Ω cm ²)
Initial State							
Shadow Mask	7.97%	11.91	12.72	906.9	69.1%	7.87	1462
Laser Scribe	8.19%	12.07	13.02	896.1	70.2%	6.55	1519
Δ	2.8%	1.3%	2.4%	-1.2%	1.6%	-16.7%	3.9%

difference for both J_{sc} was about 17% in average. When using laser scribe the difference was reduced to 7%. Despite we have obtained an important reduction in the difference, we should minimise it. The main reason for the difference between both currents when using laser scribe could be due to the size of the measured solar cell. The spot of the collimated beam in the CSR equipment covers almost all the area of the solar cell. Therefore, due to the thickness of the glass (3.2 mm), part of the light could be dispersed out of the cell before reaching the deposited layers. To check this, we produced some 2 cm x 2 cm solar cells. The result was that differences of J_{sc} between solar simulator measurements and spectral response measurements were reduced about 2% in absolute value. For that reason, we produced coupons with 8 solar cells of 1 cm² and 2 solar cells of 4 cm². Nevertheless, the production of 4 cm² solar cells started at the middle of this work. Therefore, to correctly compare results of different generations of solar cells, we will only present J_{sc_SR} values of 1 cm² cells.

4.1.2 Influence of shunt busting and annealing

Next, we study the influence of the shunt busting and annealing to bring the solar cells into the so-called initial state. We analyse the changes in the electrical parameters followed for both processes.

- **Annealing:** We investigated the first test of annealing with coupons produced by shadow masks. For these cells, we did not find any improvement in the solar cells' efficiency, probably due to process not clean enough with shadow mask. Therefore, we do not show any of this results. In the case of solar cells produced through laser scribe we always get an improvement performing annealing. When we started to use solar cells produced through laser scribe we designed a test with four different annealing conditions: 120 °C, 30 min; 145 °C, 30 min; 160 °C, 30 min and 160 °C, 50 min.

In Table 4.2 the data of the three best conditions is presented. In the top, we see the electrical parameters before and after the annealing and after light-soaking in the stabilized state. In the middle part of the table, the variation for the three coupons before and after performing annealing is shown and, in the bottom part, the light-induced degradation (LID) coefficients for the three conditions.

Table 4.2: Electrical parameters comparison for three different types of annealing performed in three coupons which were located side by side in the same panel. Top: Results before and after annealing and after 300 kWh/m² of light soaking. Middle: Variation for the three coupons before and after performing annealing. Bottom: LID for the three coupons. Results are the average of the best 5 cells per coupon for JV curves and the best cell for spectral response.

Anneal. Conditions	η	Jsc (mA/cm ²) _{SR}	Jsc (mA/cm ²) _{SS}	Voc (mV)	FF	Rs (Ω cm ²)	Rsh (Ω cm ²)
Before Annealing							
120°C, 30min	7.77%	12.28	12.95	882.8	68.0%	7.26	1578
145°C,30min	7.73%	12.32	12.94	880.4	67.9%	7.30	1379
160°C, 50min	7.71%	12.22	12.87	883.1	67.8%	7.27	1523
After Annealing							
120°C, 30min	8.64%	12.34	13.35	911.2	71.1%	5.89	1697
145°C,30min	8.80%	12.37	13.36	917.5	71.8%	5.77	1824
160°C, 50min	8.85%	12.35	13.38	919.4	72.0%	5.61	1897
Stabilized State (After 300 kWh/m² of light soaking)							
120°C, 30min	7.43%	-	12.86	889.7	64.9%	7.57	1161
145°C,30min	7.53%	-	12.83	892.9	65.7%	7.39	1418
160°C, 50min	7.40%	-	12.98	886.2	64.4%	7.38	984
Δ (Variation after Annealing)							
Anneal. Conditions	$\Delta \eta$	Δ Jsc _{SR}	Δ Jsc _{SS}	Δ Voc	Δ FF	Δ Rs	Δ Rsh
120°C, 30min	10.1%	0.5%	2.9%	3.1%	4.4%	-23.2%	7.0%
145°C,30min	12.1%	0.4%	3.1%	4.0%	5.5%	-26.5%	24.4%
160°C, 50min	12.9%	1.1%	3.8%	3.9%	5.8%	-29.5%	19.7%
Δ (LID Coefficients)							
Anneal. Conditions	$\Delta \eta$	Δ Jsc _{SR}	Δ Jsc _{SS}	Δ Voc	Δ FF	Δ Rs	Δ Rsh
120°C, 30min	14.1%	-	3.7%	2.4%	8.7%	-28.5%	31.6%
145°C,30min	14.4%	-	3.9%	2.7%	8.5%	-27.9%	22.3%
160°C, 50min	16.4%	-	2.9%	3.6%	10.6%	-31.5%	48.1%

The efficiency improvement with the annealing is between 10% - 13%. The parameter on which the annealing has a much positive impact is the FF followed by the V_{oc} . The improvement in the efficiency is approximately the sum of the improvements in J_{sc} , V_{oc} and FF (see Eq. 3.13 and 3.14).

After annealing, the sample with highest average efficiency is the one with 160 °C, 50 min. However, this coupon has suffered more degradation than others. So, in

the degraded state, the best coupon is the one with 145 °C, 30 min which represents the autoclave conditions (145 °C). It shows an efficiency degradation of about 14%, which corresponds with the modules degradation coefficients at this time. Therefore, the condition 145 °C, 30 min is chosen as the standard procedure.

- **Combination of shunt busting and annealing:** In reference to this experiment, at the top of Table 4.3 one can find the electrical parameters of cells of the same coupon without treatment, after shunt busting and after shunt busting and annealing. The variation of these parameters respect to values without treatment is presented in the middle. Finally, the number of good cells in four different coupons without treatment, after annealing, after shunt busting and after shunt busting+annealing are shown in the bottom of the table. If we do not apply any treatment to the coupons with solar cells we often find low η , high dispersion of electrical data and low yield (number of good cells/coupon). Performing only annealing we get high η but sometimes low cell yield. With shunt busting we improve the efficiency and especially the solar cell yield. Finally, combining shunt busting and annealing, we achieve highly efficient cells, low dispersion and high yield.

Table 4.3: Electrical parameters average for the best 5 cells of a coupon without treatment, after shunt busting and after shunt busting and annealing (top). Variation respect to values without treatment (middle). Number of good cells in four different coupons without treatment, after annealing, after shunt busting or after shunt busting and annealing (bottom). The criteria to consider a cell as good is $\eta \geq 0.95\eta_{max}$.

Treatment	η	Jsc (mA/cm ²) _{SR}	Jsc (mA/cm ²) _{SS}	Voc (mV)	FF	Rs (Ωcm ²)	Rsh (Ωcm ²)
No treatment	7.44%	-	12.83	885.4	65.5%	6.58	858
Shunt Busting	8.13%	-	13.08	894.9	69.4%	6.14	1500
Shunt Bust.+Anneal.	8.50%	12.29	12.97	911.8	71.9%	5.48	1724

Treatment	$\Delta \eta$	ΔJsc_{SR}	ΔJsc_{SS}	ΔVoc	ΔFF	ΔRs	ΔRsh
Shunt Busting	9.2%	-	1.9%	1.1%	6.0%	-6.7%	74.9%
Shunt Bust.+Anneal.	14.2%	-	1.1%	3.0%	9.7%	-16.7%	100.9%

Treatment	Coupon 1	Coupon 2	Coupon 3	Coupon 4
No treatment	2	8	7	4
Annealing	-	4	-	2
Shunt Busting	8	-	8	-
Shunt Busting+Anneal	7	-	6	-

We conclude that the production of 1 cm² test solar cells through laser scribe has solved the problems that we had with masks. With laser scribe process we obtain good values for FF and for R_s. We also get reliable data for J_{sc} measured in the solar simulator due to the high precision in the cells' area and better electrical edge isolation. In addition, we have automated the production of test panels, so we know exactly where the cells are placed in the full size panel and we spend less time for their production.

For the final treatment, we obtained the best results for shunt busting in combination with annealing (145 °C, 30 min). With this procedure, we achieve highly efficient cells, low dispersion and high yield.

It is worth to note that the efficiency for a solar cell produced through laser scribe with shunt busting and annealing is about 3.5% better than the efficiency of a module taking into account the effective area (see Table 4.4). This variation is mainly due to the difference in J_{sc} and FF.

Table 4.4: Electrical parameters comparison for 1 cm² solar cells and 5.72 m² full size modules produced on 16/06/2011. Results for 1 cm² cells are the average of the best 5 cells/coupon and for modules are the average of the modules produced just before and after the mini cells fabrication.

Device size	Eff	Jsc (mA/cm ²)	Voc (mV)	FF	Rs (Ω cm ²)	Rsh (Ω cm ²)
1cm ² solar cell	8.77%	13.35	913.1	72.0%	5.82	1872
5.72m ² full module	8.46%	13.18	911.5	70.3%	5.96	3568
Δ	3.5%	1.3%	0.2%	2.2%	-2.5%	-90.6%

In the following, we will always present solar cells with the next characteristics (excepting the cases where a deviation from the process is indicated):

- Cells are produced through laser scribe.
- When referring to "initial state" we mean with shunt busting and annealing.
- In the electrical parameters tables we will present the average values of the 5 best cells/coupon.

4.1.3 Industrial solar cells produced with laboratory TCO-glasses

Nowadays, T-Solar can also produce solar cells with laboratory TCO-glasses (e.g. Asahi U TCO-glass) or with TCO layers deposited on Corning substrates by placing them onto

industrial TCO-glass substrate and using laser scribe technique, shunt busting and annealing. With Asahi U TCO-glass we have achieved a slightly better efficiency in comparison to our reference ANS10ME substrate (9.03% vs. 8.98%) due to the gain in J_{sc} caused by different glass absorption.

Fig. 4.2 shows four JV curves of solar cells on Asahi U TCO-glass, one produced with shadow mask (without shunt busting and annealing) and three produced through laser scribe (one without shunt busting and annealing, another one with annealing and the third one with both, shunt busting and annealing). Changing shadow mask for laser scribe process, the parameter that improves the most is the FF due to a high reduction in R_s . Performing SB and annealing there is a significant increase in the V_{oc} and the FF. Table 4.5 presents the electrical parameters' summary of the graph.

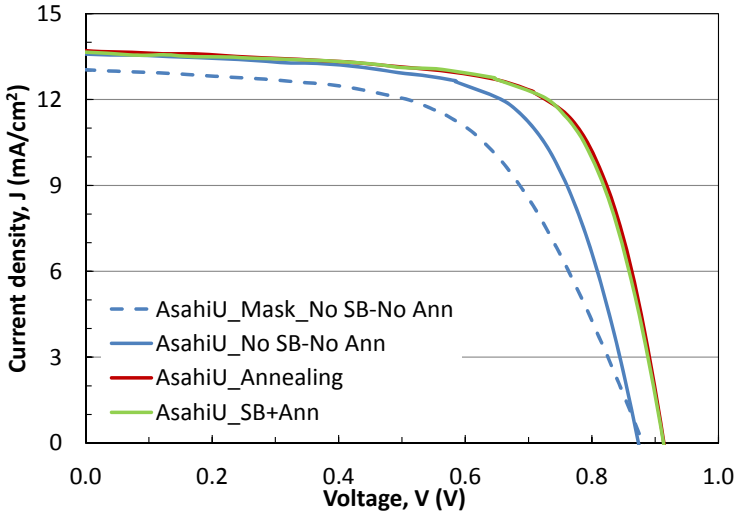


Figure 4.2: JV curves for solar cells on Asahi U TCO-glass. The blue dashed line is produced with mask without shunt busting and annealing. Continuous lines are produced through laser scribe onto the same panel without shunt busting and annealing (blue), with annealing (red) and with shunt busting and annealing (green).

Table 4.5: Electrical parameters for solar cells on Asahi U TCO-glass produced with different production methods and treatments. Results are the best cell/coupon.

TCO & Prod. Method	Treatment	η	Jsc	Jsc	Voc (mV)	FF	Rs (Ωcm^2)	Rsh (Ωcm^2)
			(mA/cm^2)_SR	(mA/cm^2)_SS				
AsahiU_8b_LSRscribe	NO	7.27%	13.11	13.45	840.5	64.3%	8.76	1329
AsahiU_8a_Mask	NO	6.57%	13.20	12.95	875.2	58.0%	14.85	2034
AsahiU_LSRscribe	NO	7.86%	-	13.45	873.2	66.9%	8.48	3127
AsahiU_LSRscribe	Ann.	8.73%	13.34	13.75	913.6	69.5%	6.68	1511
AsahiU_LSRscribe	SB+Ann.	8.72%	13.05	13.57	913.4	70.4%	7.20	2196

4.2 Preparation of samples with solar cells for shipments to project partners

In the frame of the European Project HELATHIS and other projects, T-Solar send periodically to its partners different types of samples. One of them consists of coupons 10 cm x 10 cm cut out of the panel with p-i-n layers deposited at the T-Solar facilities on AGC TCO-glass. Then, they were sent to, e.g. FZJ, UB or UU, to be finished with their back contact, producing 1 cm² solar cells. This methodology allows us to try new laboratory developments in the back contact for our own industrial solar cells. In this way we can evaluate the technical viability of the transfer from laboratory scale to industrial scale as well as the economical feasibility based on the investment needed in comparison to the decrease of the production cost (e.g. price per W_p).

4.2.1 First shipments to Research Centre Jülich

The two first samples' shipments that T-Solar did to FZJ were during the authors' internship in FZJ. One of the objectives of these shipments was to find and to analyse the possible problems for the production or transport of the samples since we did not have previous experience with this kind of tests produced in two different laboratories.

Experimental details

During the first shipment we sent coupons 10 cm x 10 cm with TCO-glass + p-i-n structure produced on 16/07/2009. However the cells did not work properly. The main problems we found, were oxidation of the p-i-n surface and shunts in the coupons. The oxidation was caused by the time in between the p-i-n deposition and the back contact deposition due to transport time. During this period a native oxide layer grows, resulting in silicon oxide (SiO₂)

formed at the interface n-layer/back contact. To avoid this problem we etched with hydrogen fluoride (HF) the coupons with TCO-glass + p-i-n layers to remove the SiO_2 layer but it did not improve the electrical performance. The native oxide layer problem results in JV curves with "S"-shape. "S"-shape curves result in low R_s and FF and appear when the contact at TCO/p-layer or n-layer/AZO interfaces is not good. The shunts were probably caused by sending the samples in CD paper envelopes and/or due to the way we cut the samples. At the beginning, we cut them by hand from the rear side, which could damage the deposited layers. With the experience of the following experiments, we decided to send the samples in plastic boxes (FZJ model) and to cut them by hand from the glass side.

To look for the root cause of the electrical problems in the coupons sent without the back contact layers, we organised the second shipment where we sent coupons from two different panels produced on 18/08/2009, one with TCO-glass + p-i-n structure and another one with TCO-glass + p-i-n + back contact to avoid the possible native oxide layer.

Solar cell results

To check if we could recover the samples of the first shipment, a shunt busting was done at -6 V (at this time we did not perform shunt busting as the usual procedure). We see in Table 4.6, Fig. 4.3 and Fig. 4.4 how the cells recover to acceptable values. Nevertheless, the FF is still a little bit low (it should be around 69% for solar cells produced with shadow mask at this period) and the series resistance is high (it should be around 6Ω). In Fig. 4.4 the high reduction of the ideality factor of the diode (n) and reverse saturation current density (J_0) due to the SB is shown. Hence, the main problem in this coupon was the shunts, but there is also a problem induced by the oxide created during the time between the a-Si:H deposition and the back contact sputtering.

Table 4.6: Average electrical parameter values before and after performing shunt busting for a coupon sent to FZJ without back contact (first shipment).

AVERAGE ALL THE CELLS	η	J_{sc} (mA/cm^2)_SR	J_{sc} (mA/cm^2)_SS	Voc (mV)	FF	R_s (Ωcm^2)	R_{sh} (Ωcm^2)
Initial State							
Before shunt busting	2.68%	-	12.55	571.0	33.6%	21.16	98
After shunt busting	7.59%	-	13.38	861.4	65.8%	9.57	1665
Δ	64.7%	-	6.3%	33.7%	48.9%	-121.1%	94.1%

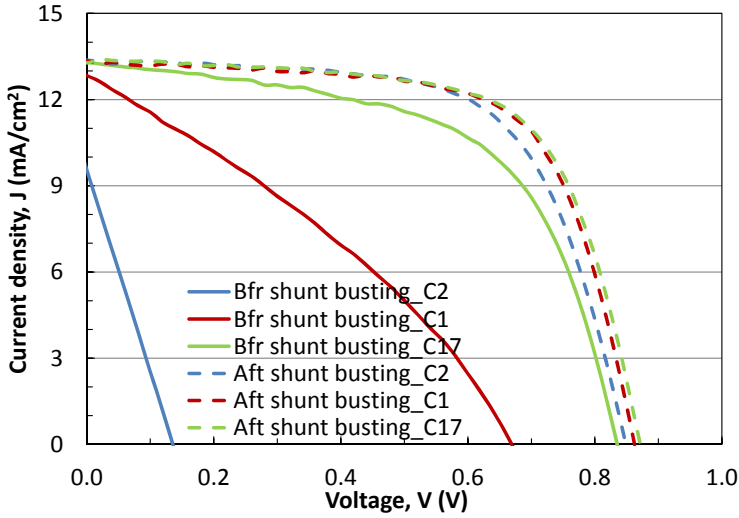


Figure 4.3: Illuminated JV curve for three cells before and after perform shunt busting for a coupon sent to FZJ without back contact (first shipment).

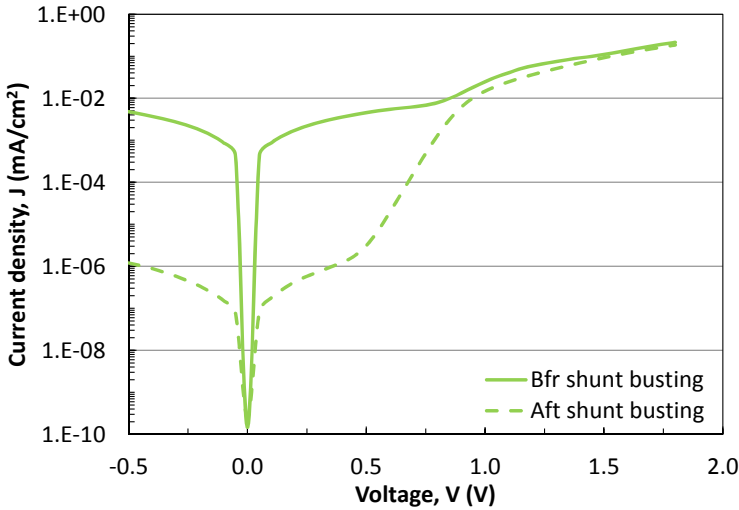


Figure 4.4: Dark JV curve for the best cell (C17) before and after performing shunt busting for a coupon sent to FZJ without back contact (first shipment).

4.2.2 Oxidation study

To exclude transport problems, two test panels were produced on 04/02/2010 in the T-Solar production line. We kept the samples for about 1 month in the laboratory. The task was to find out which is the best way to process the solar cells considering the influence of the native silicon oxide, which forms during the shipment.

Experimental details

The test panels had the following structure:

- TCO-glass + p-i-n
- TCO-glass + p-i-n + AZO

Samples were finished on 18/03/2010 in the T-Solar production line preparing 1 cm² solar cells using the next procedure:

1. Three samples with TCO-glass + p-i-n: we put shadow masks and we deposited directly the back contact (AZO + Al + NiV) on the p-i-n structure.
2. Two samples with TCO + p-i-n: we treated the p-i-n surface by HF etching (1 min, 5%) and then we placed shadow masks and sputtered the back contact (AZO + Al + NiV, together with samples from 1.
3. Five samples with TCO + p-i-n + AZO: we placed the masks, sputtered the Al and NiV and made HCl etching (10 s, 0.5%), which removes the ZnO film between solar cells for isolation.

Next, we present the results of spectral response measurements and JV curves. We have measured one coupon (8 solar cells, 12 for structure with HF etching) for each one of the three previous experiments.

Solar cell results

In Table 4.7 we compare the average electrical parameter values for all the cells/coupon in the three types of coupons (p-i-n, p-i-n + HF and p-i-n + AZO) produced on 04/02/2010 and finished on 18/03/2010. In Table 4.8 we compare the electrical parameter values for the best

cell (BC) of these three coupons, together with the average values for 1 cm² cells produced (with mask) with the T-Solar standard process.

Table 4.7: Average electrical parameter values for the measured solar cells in each experiment (p-i-n: 8 cells, p-i-n + HF: 12 cells, p-i-n + AZO: 8 cells). Right column indicates number of cells with FF > 62%.

AVERAGE ALL THE CELLS	η	Jsc (mA/cm ²)_SR	Jsc (mA/cm ²)_SS	Voc (mV)	FF	Rs (Ω cm ²)	Rsh (Ω cm ²)	Cells with FF>62%
Initial State								
p-i-n	6.31%	-	12.52	876.2	57.4%	13.04	612	3
p-i-n + HF etching	3.89%	-	12.53	691.9	41.3%	20.35	297	2
p-i-n + AZO (HCl etch.)	7.89%	-	12.52	914.8	68.9%	7.98	1359	8

The cells with p-i-n that were not treated with HF before the back contact deposition present poor electrical values and some of them do not work. The cells with p-i-n that were treated with HF present the worst statistic and the highest number of cells with poor performance. The HF etching has not improved the cell performance, cells are still shunted and many are even worse. In both types of samples R_s is high and R_{sh} is low, as a result, η and FF are bad, except J_{sc} , which is in a reasonable range. The number of good cells (FF > 62%) is only between 0 and 4 out of 18 per coupon. The electrical parameters of the best cell are only good for the structure p-i-n + AZO (see Fig. 4.5). This is more evident in the average values of all the cells (Table 4.7) since it is the only coupon presenting an acceptable yield. We can confirm this by comparing the results with our usual solar cells fabricated in one step without having the delay of one month for finishing the back contact (Table 4.8). We see that the values for the p-i-n + AZO structure are very close to the usual ones.

Table 4.8: Electrical parameter values of the best cell (BC) for the three experiments and average values for 1 cm² cells produced (with mask) with the T-Solar standard process.

BEST CELL	η	Jsc (mA/cm ²)_SR	Jsc (mA/cm ²)_SS	Voc (mV)	FF	Rs (Ω cm ²)	Rsh (Ω cm ²)
Initial State							
p-i-n	7.00%	12.02	12.48	898.9	62.4%	14.31	951
p-i-n + HF etching	7.91%	12.05	12.68	909.7	68.5%	7.47	1284
p-i-n + AZO (HCl etch.)	8.13%	12.10	12.59	917.3	70.4%	6.74	1687
Usual 1cm2 cell (mask)	8.16%	12.11	12.95	910.1	69.2%	7.99	1635

In addition, Fig. 4.6 presents the dark JV curve for two solar cells belonging to the second shipment, one sent with back contact and another one without it. We see that the solar cell sent without back contact has an n and a J_0 much higher than the other one.

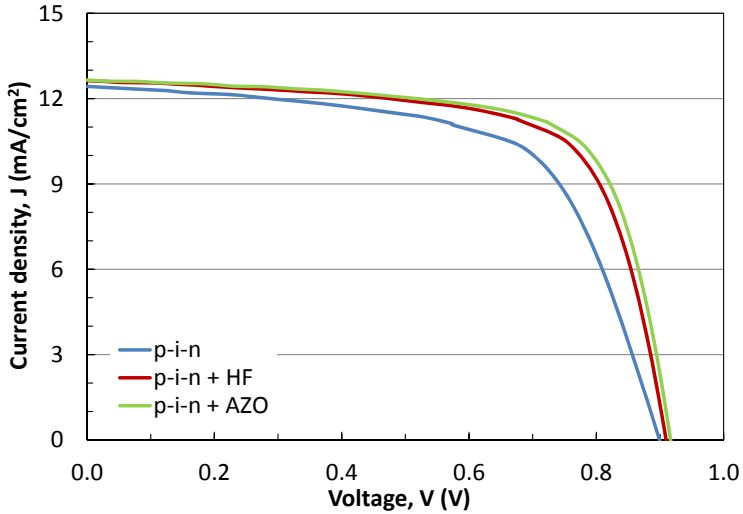


Figure 4.5: JV curve comparison for the best cells between the samples produced on 04/02/10 only with p-i-n, with back contact layers added on 18/03/10: p-i-n without any treatment (blue), p-i-n treated with HF etching (red) and p-i-n + AZO (green).

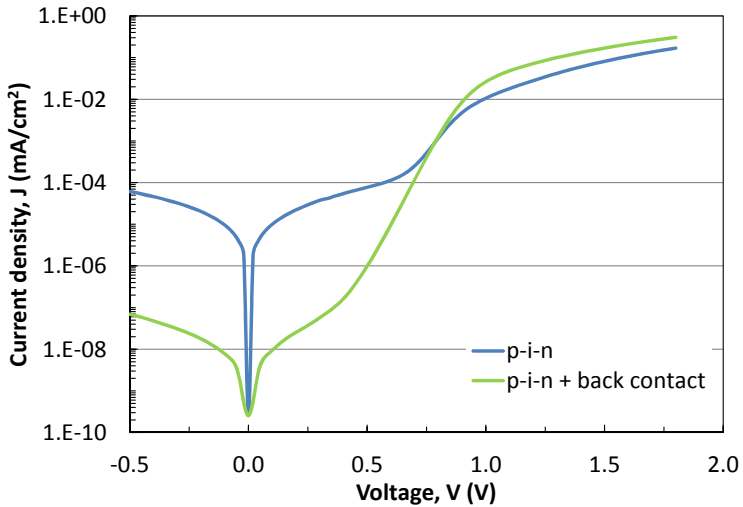


Figure 4.6: Dark JV curves for two solar cells. The blue line corresponds to a coupon sent with T-Solar back contact and the red line to a coupon sent without back contact (it was deposited later at FZJ). These coupons belong to the modules produced on 18/08/2009 for the second shipment.

The only electrical parameter that has similar values for all three experiments (p-i-n, p-i-n + HF and p-i-n + AZO) is the J_{sc} . Therefore, we can use EQE measurements to take information about J_{sc} . In Fig. 4.7 a comparison between the EQE of the three cases is presented. Short circuit current density values were calculated for the three cells from the spectral response and are presented in Fig. 4.7 and Table 4.8.

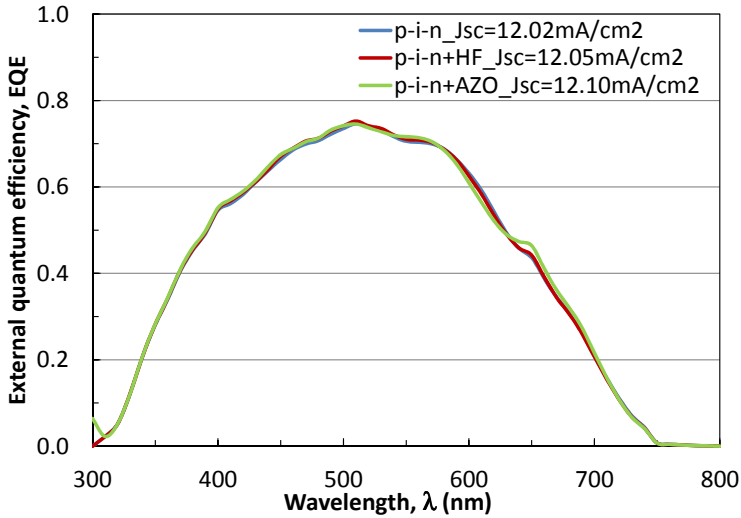


Figure 4.7: EQE comparison (for the best cell measured under J_{sc} conditions) between the samples produced on 04/02/10 with back contact layers deposited on 18/03/10: p-i-n without any treatment (blue), p-i-n treated with HF etching (red), p-i-n + AZO (green).

With samples of the first shipment we made an experiment using shunt busting to recover the cell's performance. Despite improving the cell's performance, the FF is still a little bit low (around 65% when should be around 69%) and the series resistance is high. Therefore we assume that there is a problem induced by the oxide created between the a-Si:H deposition and the back contact sputtering. To investigate in more detail the shunts we detected them with the thermocamera and the microscope, finding a lot of possible defects in the layers which could result in shunts. We have also looked for holes in the films using the transmission mode of the microscope. We have found around 200 holes/cm² in samples sent without back contact and about 5 holes/cm² in samples sent with back contact.

Therefore, samples with only TCO glass and p-i-n do not result in reliable results, the only way to get high efficient solar cells is to deposit a protective ZnO layer, at least a very thin one (e.g. 5 nm thick).

4.3 Front TCO layer and glass developments

The optical light confinement is a key point to increase the module's efficiency. The TCO-glass substrate presents the highest potential of improvement, therefore, the biggest efforts were focused on them. The optimization of the TCO layer properties at the front contact have to be achieved to, e.g. reduce reflectivity at the TCO/p-layer interface, increase the TCO layer transmission or to optimize its texture. Additionally, methods for the reduction of reflection losses at the front glass must be developed, at the same time an increase of the glass transmission must be achieved. Moreover, it must be possible to transfer the performed optimizations from laboratory scale to large area deposition.

4.3.1 Front TCO layer developments

During the HELATHIS project AGC has developed a new front TCO layer with enhanced carrier mobility (mobility enhanced (ME) type TCO), resulting in reduction of the optical and electrical losses in the TCO layer. In addition, they have optimised the layer thickness and the sheet resistance (R_{sq}). To find the best trade-off between electrical and optical properties, prototype TCO layers with different sheet resistance and thickness were fabricated by AGC. The impact on the efficiency was investigated in laboratory solar cells and large area modules, both at T-Solar. The here studied research was performed by producing four test panels with 1 cm² solar cells with different TCO prototypes (and one standard panel with AN10) on 24/01/11. Table 4.9 presents the main characteristics of the different TCO types.

Table 4.9: Summary of the main characteristics of the different TCO types. Standard is referred to the AN10 thickness.

TCO glass	Enhance carrier mobility	TCO layer thickness	R_{sq}
AN10	No	Standard	10.0
AN10 ME	Yes	Standard	10.0
AN10 Thin ME	Yes	Thinner	10.0
AN8.5 Thin ME	Yes	Thinner	8.5
AN7 Thin ME	Yes	Thinner	7.0

Optical Data

Table 4.10 presents the transmission and absorption of each TCO-glass type as well as their sheet resistance. The TCO glass AN10 Thin ME and AN8.5 Thin ME have the highest transmission and lowest absorption, whereas AN10 ME presents the worst values. A comparison of the five TCO-glass transmission curves is done in Fig. 4.8. The thinner TCO layer thickness affects the most in the range between 400 nm - 600 nm, being the most important change in terms of transmission. The ME TCO layers present a small loss in transmission in the range 700 nm - 800 nm. In Fig. 4.9 we see that J_{sc} of solar cells fabricated on these TCO-glasses correlates quite well with the absorption in the TCO-glass since the TCO-glasses with lower absorption are the ones with higher J_{sc} .

Table 4.10: Transmission, absorption and sheet resistance for five TCO-glass types with different carrier mobility, thickness and resistivity.

TCO	T_{TCO} (%)	A_{TCO} (%)	$Rs_{q\ TCO}$ (Ω/sq)
AN10	83.72	7.31	9.78
AN10 ME	83.37	7.66	8.57
AN10 Thin ME	84.26	6.77	8.54
AN8.5 Thin ME	84.27	6.60	8.85
AN7 Thin ME	83.90	7.21	6.95

Solar cell results

Table 4.11 presents the initial and stabilized electrical parameters of 1 cm² solar cells fabricated with the different ME-type TCO-glasses. As well, the LID coefficients are shown. Fig. 4.10 presents the JV characteristics in the stabilized state for the best cell coupons fabricated with the different ME-type samples and the standard AN10.

In the degraded state the overall best TCO within the ME TCOs is the AN8.5 Thin ME, due to high J_{sc} , relative high V_{oc} and FF and low degradation coefficients. AN8.5 Thin ME has the highest J_{sc} followed by AN10 Thin ME, whereas AN7 Thin ME and especially AN10 ME present the lowest J_{sc} . Furthermore, AN10 ME has the highest V_{oc} and AN10 Thin ME has the lowest V_{oc} (especially when degraded). Finally, AN10 ME presents a FF significantly higher than the rest of TCOs in the initial state. However, this difference almost disappears in the stabilized state.

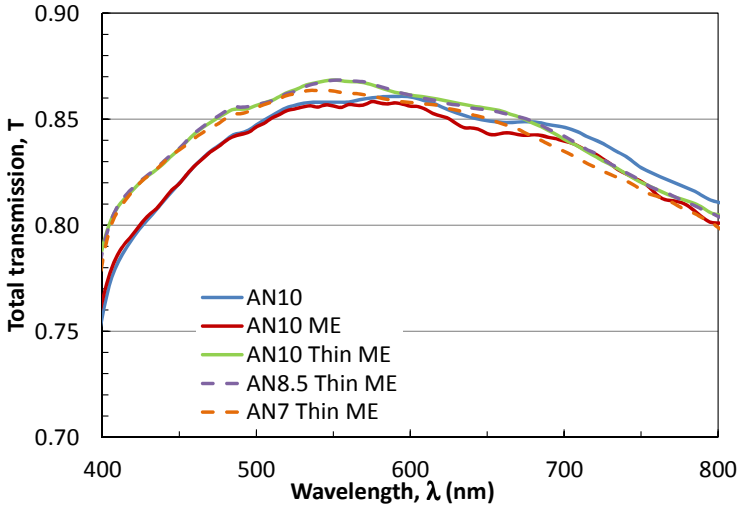


Figure 4.8: Total transmission for five TCO types with different carrier mobility, thickness and resistivity.

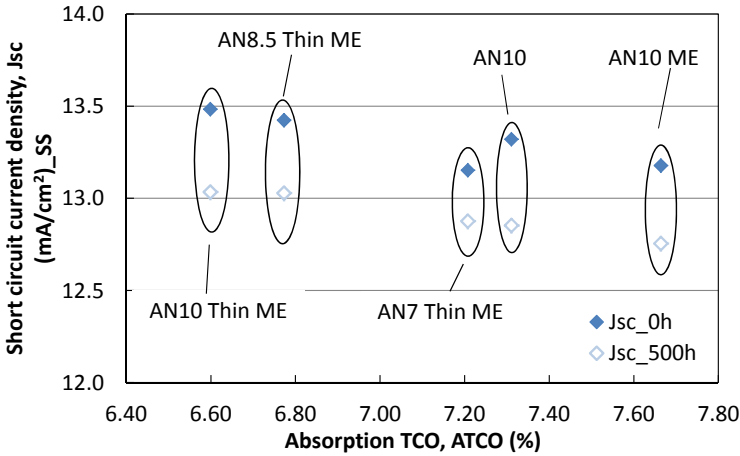


Figure 4.9: Correlation between J_{sc} measured in the SS and TCO-glass absorbance for five TCO-glass types with different carrier mobility, thickness and resistivity.

Fig. 4.11 plots the EQE of the five TCOs resulting in the highest J_{sc} for the AN8.5 Thin ME and AN10 Thin ME and the lowest for AN7 Thin ME. All the samples have a similar behaviour regarding the curve shape.

Table 4.11: Electrical parameters for five TCO types with different carrier mobility, thickness and resistivity. Top: Results in the initial and stabilized state (after 500 kWh/m² of light soaking). Bottom: LID for the five coupons. Results are the average of the best 5 cells/coupon for JV curves and the best cell/coupon for spectral response.

TCO	η	Jsc (mA/cm ²) _{SR}	Jsc (mA/cm ²) _{SS}	Voc (mV)	FF	Rs (Ω cm ²)	Rsh (Ω cm ²)
Initial State							
AN10	8.74%	12.22	13.32	914.2	71.7%	5.76	1680
AN10 ME	8.80%	12.31	13.18	913.7	73.1%	5.80	2348
AN10 Thin ME	8.78%	12.33	13.42	913.3	71.6%	5.78	1570
AN8.5 Thin ME	8.73%	12.38	13.48	909.2	71.2%	5.75	1586
AN7 Thin ME	8.58%	12.19	13.15	913.4	71.4%	5.49	1437
Stabilized State (500 kWh/m²)							
AN10	7.72%	11.92	12.85	896.8	67.0%	6.98	1341
AN10 ME	7.77%	11.82	12.75	903.3	67.4%	6.94	1696
AN10 Thin ME	7.76%	11.98	13.03	896.4	66.4%	7.03	1351
AN8.5 Thin ME	7.84%	11.99	13.03	898.7	67.0%	6.88	1410
AN7 Thin ME	7.70%	11.84	12.88	898.1	66.6%	6.63	1263
TCO	$\Delta \eta$	Δ Jsc _{SR}	Δ Jsc _{SS}	Δ Voc	Δ FF	Δ Rs	Δ Rsh
AN10	11.7%	2.5%	3.5%	1.9%	6.7%	-21.2%	20.2%
AN10 ME	11.7%	4.0%	3.2%	1.1%	7.7%	-19.8%	27.8%
AN10 Thin ME	11.7%	2.8%	2.9%	1.8%	7.3%	-21.7%	13.9%
AN8.5 Thin ME	10.1%	3.2%	3.3%	1.2%	5.9%	-19.6%	11.1%
AN7 Thin ME	10.2%	2.9%	2.1%	1.7%	6.7%	-20.8%	12.1%

In this solar cell test the best option results to be between AN10 Thin ME and AN8.5 Thin ME TCO. Both TCOs have the highest current, which is the parameter that presents the most outstanding improvement in the T-Solar solar cells and results in a significant reduction in TCO layer thickness with respective reduction in the production cost of the TCO layer. Therefore, the best adjustment resulted in keeping the usual sheet resistance, a little bit lower than 10 Ω /sq and to reduce the optical losses in the TCO layer by reducing the layer thickness.

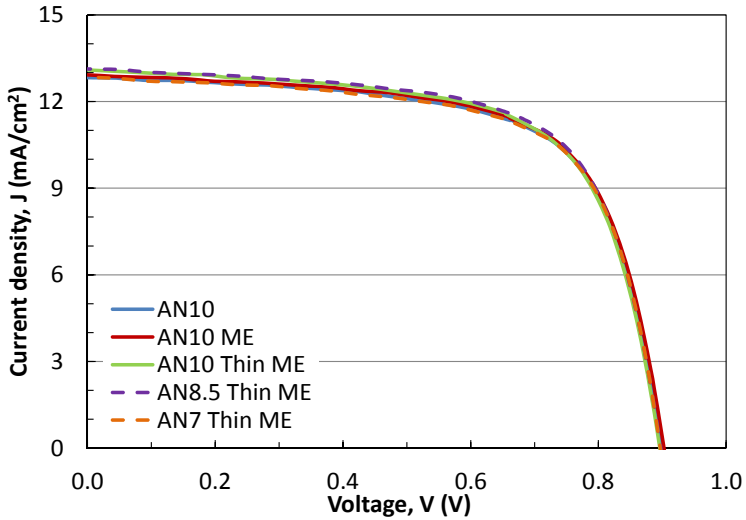


Figure 4.10: JV curve for five TCO types with different carrier mobility, thickness and resistivity. Curves are the best cell/coupon in stabilized state (after 500 kWh/m² of light soaking).

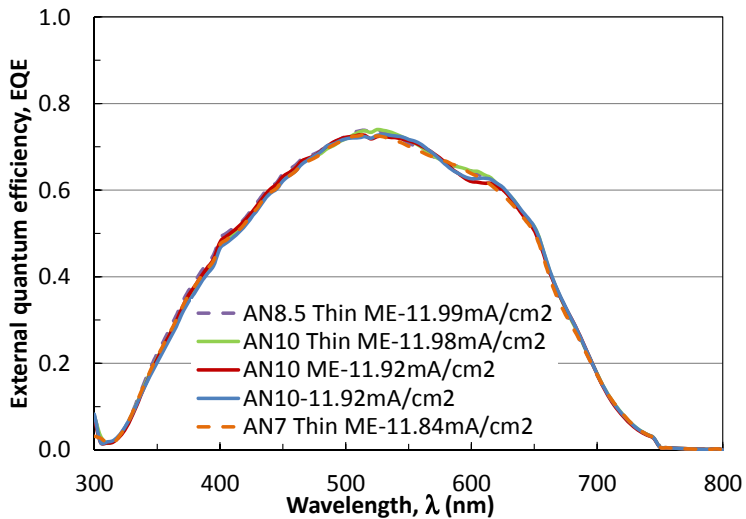


Figure 4.11: EQE curve for five TCO types with different carrier mobility, thickness and resistivity. Curves are the best cell/coupon in stabilized state (after 500 kWh/m² of light soaking). The measurements are done without bias light and reverse voltage in 1 cm² cells.

4.3.2 New generation TCO glasses

The last development of the TCO-glass by AGC introduced successfully into the T-Solar production line is the combination of the best ME-type TCO with low iron float glass (ANS10ME). Thus, we get more transmission through both, the low iron content in the substrate glass (see Fig. 4.12) and the thinner TCO layer (to notice that the before used "Thin" is note included in the new notation of TCO-glass).

Optical data of laboratory and industrial TCO-glasses

In Table 4.12 we compare the integrated total transmission in the range 400 nm - 800 nm for the laboratory TCO-glass Asahi U (not low iron content) and three industrial TCO-glasses from AGC. The industrial TCO-glass are the standard AGC TCO (AN10), the same TCO layer with low iron-content float glass (ANS10) and the improved TCO layer with low iron-content float glass (ANS10ME). The gain in the integrated total transmission respect to AN10 is also presented. We see that most of the gain is due to the low iron content float glass (2%). To compare the optical data of both, laboratory and industrial TCO-glasses, we have to keep in mind their different thickness. The first one has a higher transmission due to the thinner glass thickness of the substrate (1.0 mm), whereas the industrial float glass has a 3.2 mm thickness.

Table 4.12: Integrated total transmission in the range 400 nm - 800 nm for three industrial TCO-glasses and one laboratory TCO-glass (Asahi U) and their gain with respect to AN10.

TCO	T_{TCO} (%)	Δ to AN10
Asahi U	85.4	1.79%
AN10	83.9	0.00%
ANS10	85.6	2.03%
ANS10ME	86.1	2.62%

In Fig. 4.12 we compare the four TCO-glass transmissions curves. We see that the improvements due to changes in the TCO layer affect more in the range 400 nm - 700 nm. In contrast, the low iron content in the glass has more influence in the range 650 nm - 800 nm, where the J_{sc} of solar cells increases significantly due to the higher photon flux in the solar spectrum. ANS10ME TCO-glass presents the highest transmission, even higher than Asahi U (except in the range 400 nm - 475 nm, probably due to the different glass thickness).

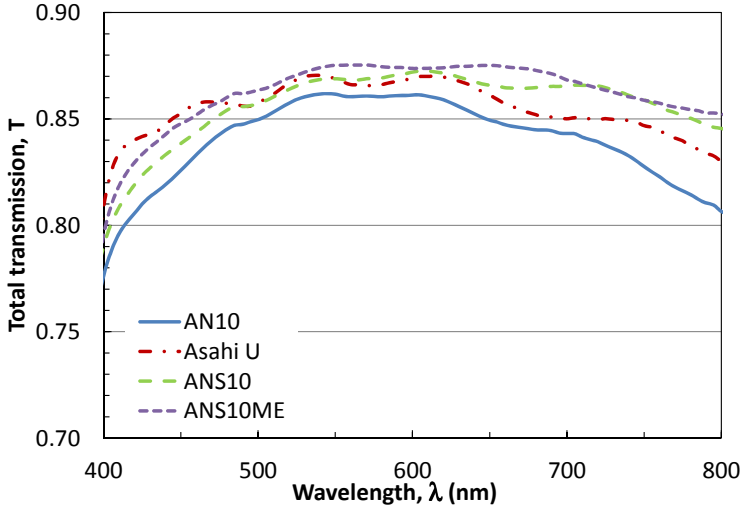


Figure 4.12: Total transmission for three industrial TCO-glasses and one laboratory TCO-glass (Asahi U).

Solar cell results

Table 4.13 presents electrical data of solar cells before and after light-soaking as well as their LID coefficients. The table compares the standard (AN10) and the new development (ANS10ME) of AGC TCO-glass. Fig. 4.13 shows the JV curves for the best cells of these coupons. The improvement in efficiency for ANS10ME respect to AN10 is about 3.4% in the initial state and 2.5% in the stabilized state. The gain is mainly a result of the increase in current due to the improved total transmission.

Fig. 4.14 shows the EQE for the AN10 and ANS10ME TCO-glass in the initial and stabilized state. The main difference is in the short wavelength range (300 nm - 350 nm) and in the range 575 nm - 625 nm due to the improvement in the transmission.

Table 4.13: Electrical parameters for two TCO-glass types with different total transmission, carrier mobility and thickness. Top: Results in the initial and stabilized state (after 300 kWh/m² of light soaking) with their corresponding gain (Δ). Bottom: LID for both coupons. Results are the average of the best 5 cells/coupon for JV curves and the best cell/coupon for spectral response.

TCO	η	Jsc (mA/cm ²)_SR	Jsc (mA/cm ²)_SS	Voc (mV)	FF	Rs (Ω cm ²)	Rsh (Ω cm ²)
Initial State							
AN10	8.69%	12.22	13.28	912.3	71.7%	5.73	1725
ANS10ME	8.98%	12.48	13.84	916.2	70.8%	6.40	1573
Δ	3.4%	2.1%	4.3%	0.4%	-1.3%	11.6%	-8.8%
Stabilized State (300 kWh/m²)							
AN10	7.66%	11.92	12.88	897.2	66.3%	7.03	1261
ANS10ME	7.85%	12.11	13.38	894.9	65.5%	7.83	1253
Δ	2.5%	1.6%	3.9%	-0.3%	-1.1%	11.4%	-0.6%

TCO	$\Delta \eta$	Δ Jsc_SR	Δ Jsc_SS	Δ Voc	Δ FF	Δ Rs	Δ Rsh
AN10	11.9%	2.5%	3.0%	1.7%	7.6%	-22.5%	26.9%
ANS10ME	12.7%	3.0%	3.4%	2.3%	7.5%	-22.3%	20.3%

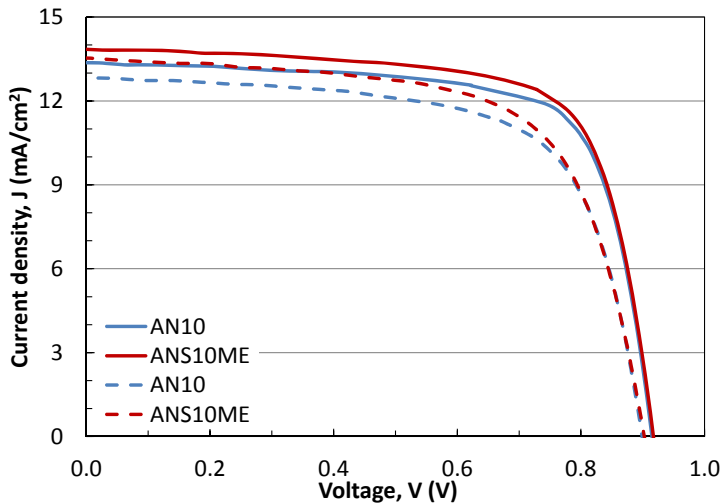


Figure 4.13: JV curve for two TCO-glass types with different total transmission, carrier mobility and thickness. Curves are the best cell/coupon in initial (continuous line) and stabilized state (dashed line, after 300 kWh/m² of light soaking).

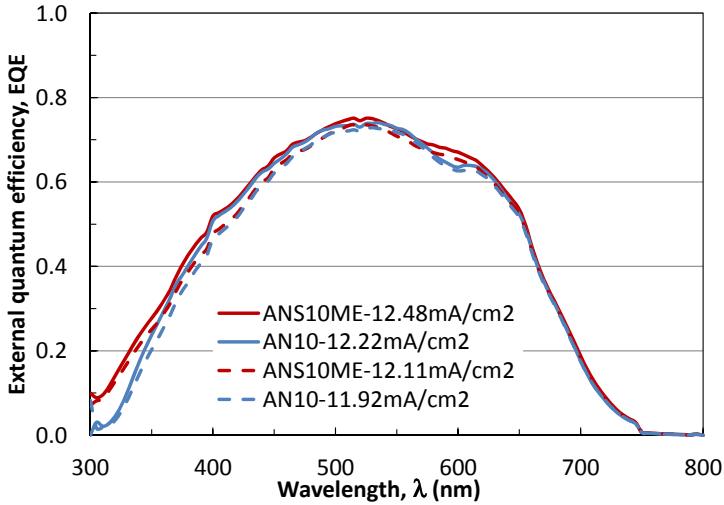


Figure 4.14: EQE curve for two TCO-glass types with different total transmission, carrier mobility and thickness. Curves are the best cell/coupon in initial (continuous line) and stabilized state (dashed line, after 300 kWh/m² of light soaking). The measurements are done without bias light and reverse voltage in 1 cm² cells.

4.3.3 Anti-reflection coating or interface layer

The refractive index (n) for the air is 1, for the glass is about 1.5, for the front SnO₂ TCO layer 2.0 and for the Si-layers 3.4. The difference in the refractive index leads to optical losses at the interfaces air/glass and TCO/p-layer since part of the light will be reflected. To reduce this effect, one could introduce anti-reflection coatings (ARCs) or interface layers (IFLs) in the interfaces air/TCO and TCO/p-layer (see Fig. 4.15) using materials with intermediate refractive index. These layers increase the transmitted light, which means more absorbed light in the device and, therefore, increase the current and the efficiency. We have studied the introduction of IFL (ARC2 in Fig. 4.15) in the interface TCO/p-layer. The most used material at this interface is titanium oxide (TiO₂), which has a n value of about 2.6.

Experimental details

The samples for the fabrication of solar cells with IFL layer were Asahi U front TCO-glass (deposited on substrate glass of 1 mm) with a Niobium pentoxide-doped titanium oxide, TiO₂ : Nb₂O₅ (NTO) interface layer deposited by sputtering at UB. The samples were sent

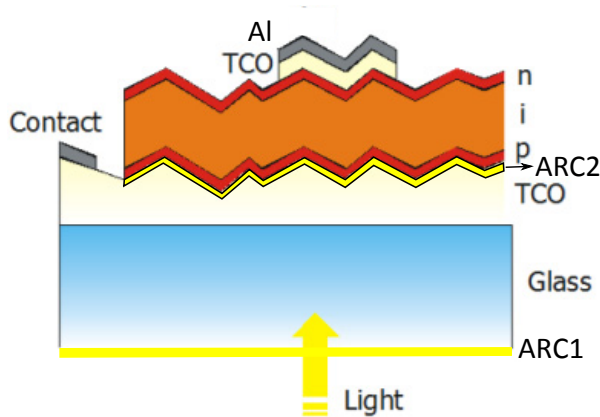


Figure 4.15: Structure of an a-Si:H solar cell including the placement of two ARC at interfaces air/glass and TCO/p-layer.

to T-Solar to be finished with the p-i-n structure and back contact layers using the laser scribe process. The samples were placed on the top of a TCO-glass in the production line in the position where the laser scribe solar cells are produced. Therefore, these samples will have slightly different layer thicknesses (measuring in the profilometer we have estimated about 2% less total p-i-n thickness).

UB sent samples with four different NTO layers on Asahi U TCO-glass. Their thickness and NTO sputter target composition with the doping percentage indicated in brackets is shown in Table 4.14. We used an Asahi U without NTO layer and the ANS10ME TCO-glass used in the production line as references.

Table 4.14: Thickness and doping conditions for four different interface layers of NTO deposited on Asahi U.

TCO	Thickness NTO (nm)	Composition NTO target
Asahi U + NTO1	20-25	TiO ₂ :Nb ₂ O ₅ (1%)
Asahi U + NTO2	30	TiO ₂ :Nb ₂ O ₅ (1%)
Asahi U + NTO3	35-40	TiO ₂ :Nb ₂ O ₅ (1%)
Asahi U + NTO4	25	TiO ₂ :Nb ₂ O ₅ (0.5%)

Solar cell results

In Table 4.15 the electrical parameters of the four samples with NTO and the two references are presented. Fig. 4.16 and 4.17 present the JV curves and EQE of the samples in Table 4.15.

Table 4.15: Electrical parameters (initial state) for two references and four solar cells with NTO interface layer with different thickness and doping concentration deposited on Asahi U TCO-glass. Results are the average of the best 5 cells/coupon for JV curves and the best cell/coupon for spectral response.

TCO	η	Jsc (mA/cm ²) _{SR}	Jsc (mA/cm ²) _{SS}	Voc (mV)	FF	Rs (Ω cm ²)	Rsh (Ω cm ²)
Ref ANS10ME	8.98%	12.86	13.45	922.7	72.4%	5.59	1752
Asahi U	9.03%	13.40	13.69	910.1	72.5%	5.71	1759
Asahi U + NTO1	7.52%	13.40	13.63	816.7	67.5%	7.55	1403
Asahi U + NTO2	8.53%	13.55	13.79	884.3	70.0%	7.49	1859
Asahi U + NTO3	7.19%	13.68	13.78	815.7	63.9%	10.33	4298
Asahi U + NTO4	8.03%	13.39	13.61	882.0	66.9%	11.00	1367

Fig. 4.16 shows that all the NTO conditions present a very poor V_{oc} and FF, which result in efficiency lower than the references. This problem is caused by the TiO₂ layers presenting contact difficulties with the p-layer. At the moment, we were not able to solve this inconvenience.

J_{sc} in NTO2 and NTO3 is higher than in references. J_{sc} in NTO1 and NTO4 is as in reference or slightly lower. NTO2 is the best condition with the best J_{sc} , V_{oc} and FF when comparing only NTO samples. It has better J_{sc} but less V_{oc} and FF than the references. So, it has fewer efficiency but not much less than references ($\eta_{NTO2} = 8.53\%$, $\eta_{AsahiU} = 9.03\%$).

Fig. 4.17 shows how the most important gain of current is produced in the range 330 nm - 525 nm. Most part of this gain is due to the use of Asahi U as front TCO but the use of TiO₂ layers is also remarkable (especially for NTO2).

Reflection curves presented in Fig. 4.18 show NTO2 coupon as the sample with the lowest reflection loss according with the J_{sc} obtained in the JV curve. ANS10ME presents less reflection than Asahi U.

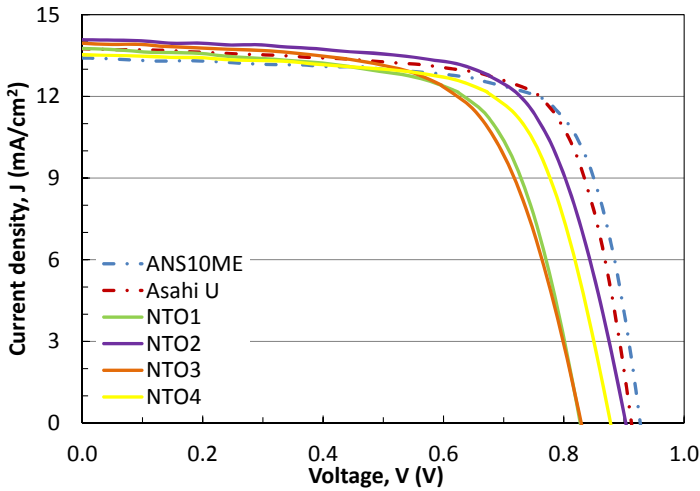


Figure 4.16: JV curve for four solar cells with NTO interface layer with different thickness and doping concentration deposited on Asahi U TCO-glass. There are two references, one Asahi U (laboratory reference) and one ANS10ME (industrial reference). Curves are the best cell/coupon in initial state.

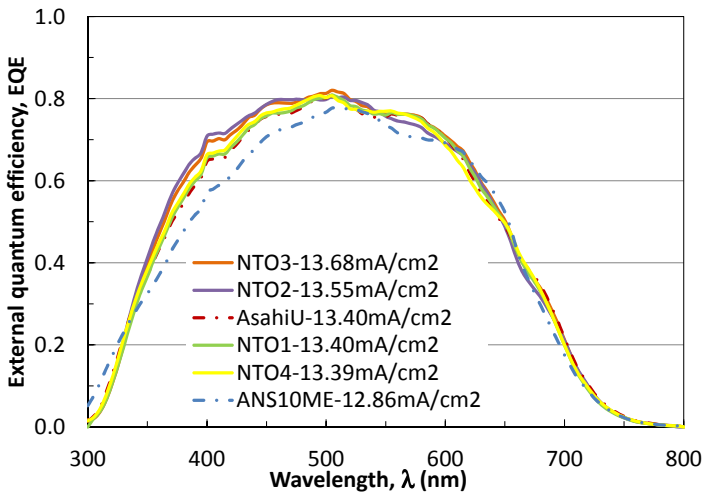


Figure 4.17: EQE curve for four solar cells with NTO interface layer with different thickness and doping concentration deposited on Asahi U TCO-glass. There are two references, one Asahi U (laboratory reference) and one ANS10ME (industrial reference). Curves are the best cell/coupon in initial state. The measurements are done without bias light and reverse voltage in 1 cm^2 cells.

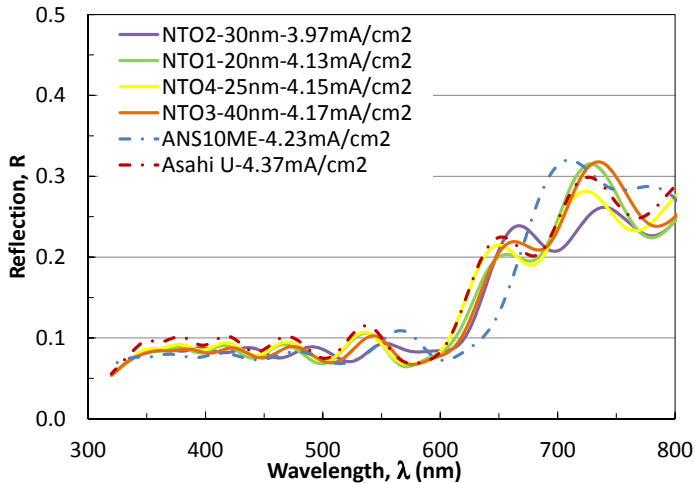


Figure 4.18: Reflection for four solar cells with NTO interface layer with different thickness and doping concentration deposited on Asahi U TCO-glass. There are two references, one Asahi U (laboratory reference) and one ANS10ME (industrial reference). The current densities, that would be generated if all the reflected light (300 nm - 800 nm) could be absorbed in the solar cell, are shown in the legend.

4.3.4 Study for new materials in the front TCO-layer (ZnO-TCO)

Our usual front TCO layer is a SnO_2 :F layer. The thoroughly known laboratory TCO-glass Asahi U is also made up of the same material. The alternative laboratory ZnO TCO layer has been developed in FZJ and tested in the T-Solar's production line with solar cells.

Optical data of ZnO TCO-layers

As indicated in Table 4.16 and shown in Fig. 4.19 and 4.20, ZnO TCO-glass has about 3% more integrated total transmission in the range 400 nm - 800 nm and much higher diffuse transmission (57% vs. 13%) and, therefore, following Eq.2.54, it has a much higher haze than tin oxide (SnO_2) TCO-glass.

Table 4.16: Material properties of a SnO_2 TCO deposited on float glass of 3.2 mm and a ZnO TCO deposited on Corning glass of 1.0 mm.

TCO	T (Glass+TCO)	Tdif (Glass+TCO)	Haze	A (Glass+TCO)	A (Glass)	Thickness (nm)	Rsq (Ω_{sq})
ZnO	88.64%	56.81%	64.40%	2.08%	0.00%	473	8.00
SnO_2	85.81%	12.92%	15.19%	5.14%	2.87%	1000	9.03

The difference in the total transmission of both TCO-glasses is due to the absorption in the glass. The substrate glass in the ZnO sample is Corning glass ($A \approx 0\%$) whereas the glass in the SnO₂ sample is low iron float glass ($A \approx 3\%$). Hence, the total transmission in the TCO layer is very similar for both materials but the way to transmit is totally different since in ZnO material the diffuse transmission is much higher. This occurs because the ZnO's texture presents a crater structure, whereas the SnO₂'s texture is pyramidal. Other characteristics to differentiate both TCO-glasses is that thickness and sheet resistance of ZnO are lower and its roughness higher.

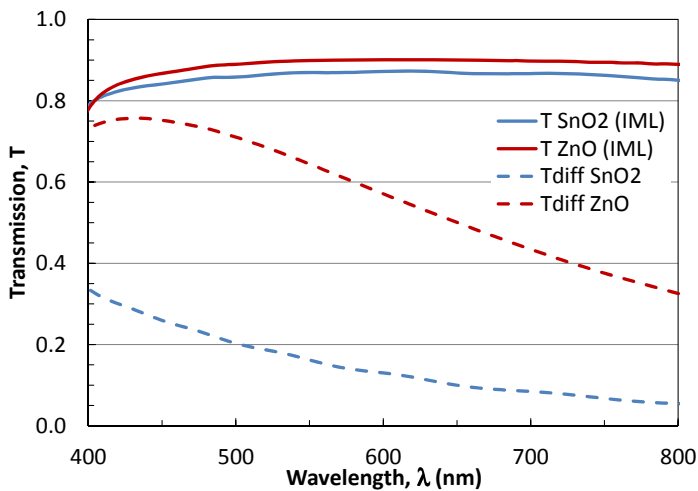


Figure 4.19: Total transmission (T) (measured with index matching liquid, IML) and diffuse transmission (T_{diff}) for a SnO₂ TCO deposited on float glass of 3.2 mm and a ZnO TCO deposited on Corning glass of 1.0 mm.

Solar cell results

Table 4.17 presents the electrical parameters of three different ZnO TCO-glasses (2a, 4a, 7a) on which we have fabricated solar cells. Samples 4a and 7a have 0.5% of Al-doping concentration and a sheet resistance of 5.99 Ω/sq and 5.95 Ω/sq, respectively. Sample 2a has 2.0% of doping concentration, 5.64 Ω/sq of sheet resistance and different ZnO layer thickness. Two references, an Asahi U TCO-glass (which has a similar substrate glass of 1.0 mm thickness as ZnO TCO-glasses) and an ANS10ME sample, are also in the table. All the solar cells, except the ones of ANS10ME, are fabricated with shadow masks since, at this

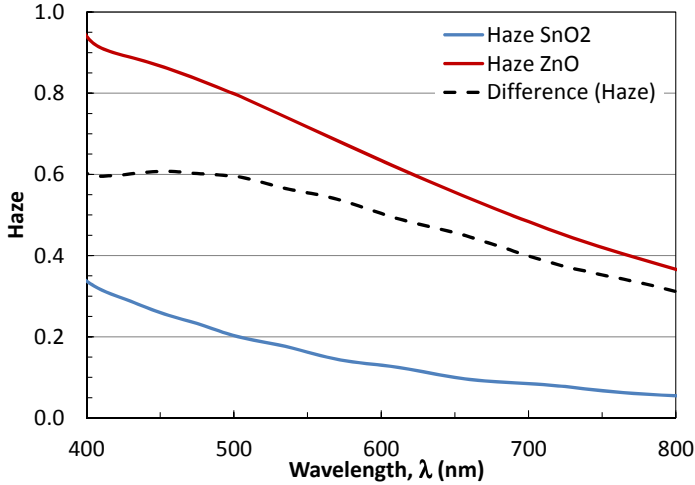


Figure 4.20: Haze for a SnO₂ TCO deposited on float glass of 3.2 mm and a ZnO TCO deposited on Corning glass of 1.0 mm.

period, we were not able to produce solar cells through laser scribe on substrate glass coupons placed on the TCO-glass in the production line. Coupons fabricated with shadow mask do not have shunt busting or annealing.

Table 4.17: Electrical parameters (initial state) for three solar cells with ZnO front TCO produced at FZJ with different doping concentration and deposition process. The rest of layers were deposited at T-Solar with shadow mask. There are two references, one Asahi U (laboratory reference, shadow mask) and one ANS10ME (industrial reference, laser scribe). Results are the average of the best 5 cells/coupon for JV curves and the best cell/coupon for spectral response.

TCO	η	Jsc (mA/cm ²) _{SR}	Jsc (mA/cm ²) _{SS}	Voc (mV)	FF	Rs (Ωcm ²)	Rsh (Ωcm ²)
Initial State							
ANS10ME(BKM21.2)	8.77%	12.78	13.27	907.7	72.8%	4.85	1690
AsahiU_8a (mask)	6.50%	13.20	13.19	868.3	56.7%	15.13	1352
ZnO-FZJ (2%)_2a (mask)	6.07%	12.28	12.67	877.0	54.6%	19.81	665
ZnO-FZJ_4a (mask)	5.86%	12.38	12.62	869.5	53.4%	36.79	852
ZnO-FZJ_7a (mask)	5.94%	12.24	12.91	871.6	52.8%	39.91	859

The JV curves for ZnO TCO samples with 0.5% doping concentration present high R_s values and a strong "S"-shape near to V_{oc}, indicating a contact problem at the ZnO/p-layer interface (see Fig. 4.21). The "S"-shape is slightly appreciated in ZnO TCO sample with 2.0% doping concentration and in Asahi U reference. Moreover, the FF is very low for the

four TCO-glasses. The ZnO-FZJ sample with the best performance in the solar cells is the one with higher doping concentration (2.0%), despite having less J_{sc} . However, it has less efficiency than Asahi U and ANS10ME references. The shadow mask production process with not well defined area and high distance to the front contact results in poor J_{sc} , R_s and FF values, as confirmed by the poor performance obtained with Asahi U reference.

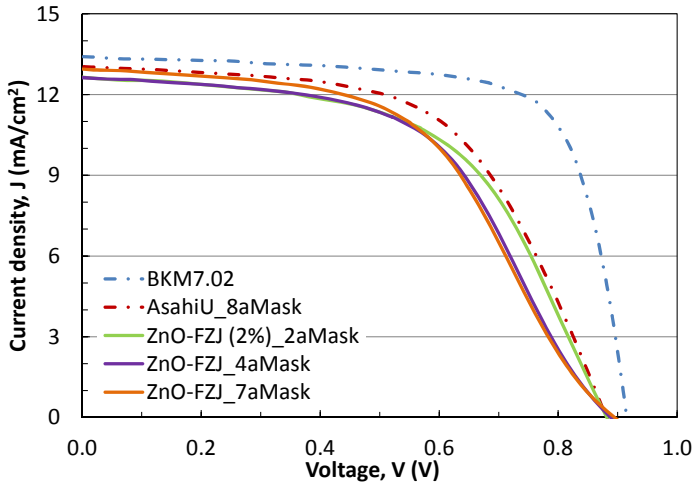


Figure 4.21: JV curve for three solar cells with ZnO front TCO produced at FZJ with different doping concentration and deposition process. The rest of layers were deposited at T-Solar with shadow mask. There are two references, one Asahi U (laboratory reference, shadow mask) and one ANS10ME (industrial reference, laser scribe). Curves are the best cell/coupon in initial state.

As we see in Fig. 4.22, the solar cells on ZnO TCO-glass present less J_{sc} than Asahi U along the whole spectrum. The most important difference is in the range 300 nm - 400 nm and 540 nm - 615 nm. The three solar cells with ZnO front TCO have similar EQE. All of them absorb less light than expected in the long wavelength range 540 nm - 615 nm, where the texture could have influence generating different interferences. This EQE shape agrees well with the reddish appearance shown by the ZnO front TCO solar cell coupons.

FZJ has optimized the ZnO TCO layer properties for tandem solar cells (a-Si:H/ μ c-Si:H). In this case, it is usual to deposit a μ c-Si:H p-layer in the a-Si:H top cell. With the objective to achieve a better cell performance with the ZnO TCO we have produced solar cells with 15 nm μ c-Si:H p-layer in a ZnO TCO and an Asahi U used as reference. These samples were produced through laser scribe but we did not perform shunt busting or annealing.

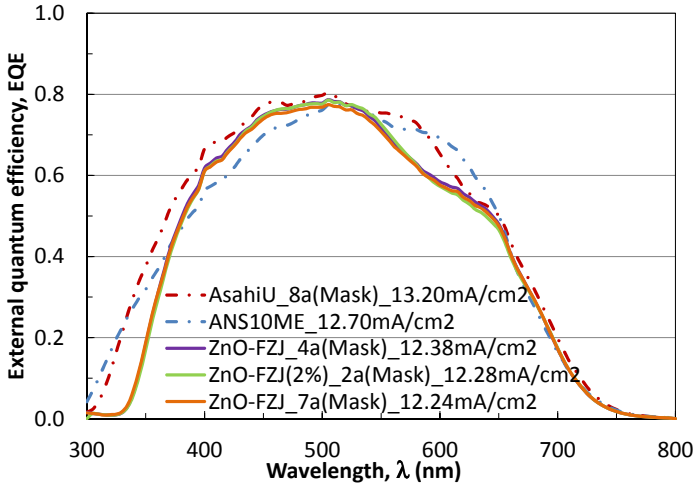


Figure 4.22: EQE curve for three solar cells with ZnO front TCO produced at FZJ with different doping concentration and deposition process. The rest of layers were deposited at T-Solar with shadow mask. There are two references, one Asahi U (laboratory reference, shadow mask) and one ANS10ME (industrial reference, laser scribe). Curves are the best cell/coupon in initial state. The measurements are done without bias light and reverse voltage in 1 cm² cells.

Table 4.18 shows the electrical parameters of these two samples and Fig. 4.23 their JV curves. Taking into account that solar cells were fabricated through laser scribe, we see how efficiency values are worse for both samples in reference to the results presented above with a-Si:H p-layer. J_{sc} is the most affected parameter by both TCOs. Moreover, ZnO TCO continues being worse than Asahi U, especially because Asahi U presents a FF much higher than ZnO TCO.

Table 4.18: Electrical parameters (initial state) for two solar cells with ZnO front TCO produced at FZJ and Asahi U (SnO₂) front TCO. Both samples have μc -Si:H p-layer. The solar cells were produced at T-Solar through laser scribe without shunt busting and annealing. Results are the average of the best 5 cells/coupon for JV curves and the best cell/coupon for spectral response.

TCO	η	J_{sc} (mA/cm ²) _{SR}	J_{sc} (mA/cm ²) _{SS}	Voc (mV)	FF	Rs (Ω cm ²)	Rsh (Ω cm ²)
Initial State							
ZnO-FZJ+p-ucSi=15nm	6.02%	11.34	11.64	863.2	59.9%	7.96	548
AsahiU+p-ucSi=15nm	7.17%	11.79	11.95	861.4	69.6%	6.58	1788

Fig. 4.24 shows that the difference in EQE at every wavelength between both TCOs is similar to the one with a-Si:H p-layer, despite the total generated currents have decreased for

both samples. If we compare the ZnO TCO with a-Si:H p-layer and the one with $\mu\text{c-Si:H}$ p-layer, one sees that the loss in current observed with the $\mu\text{c-Si:H}$ p-layer is produced in the range 330 nm - 550 nm.

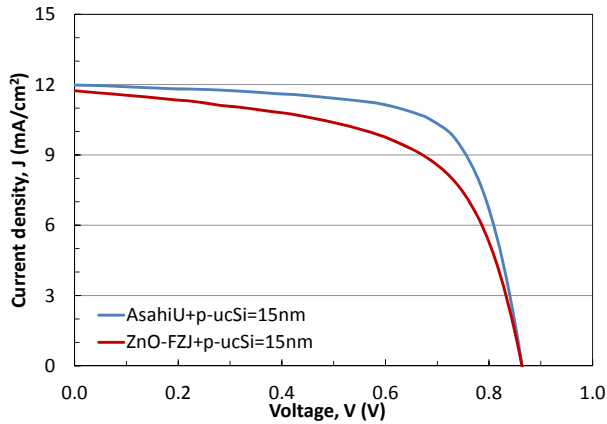


Figure 4.23: JV curve for two solar cells with ZnO front TCO produced at FZJ and Asahi U (SnO_2) front TCO. Both samples have $\mu\text{c-Si:H}$ p-layer. The solar cells were produced at T-Solar through laser scribe without shunt busting and annealing. Curves are the best cell/coupon in initial state.

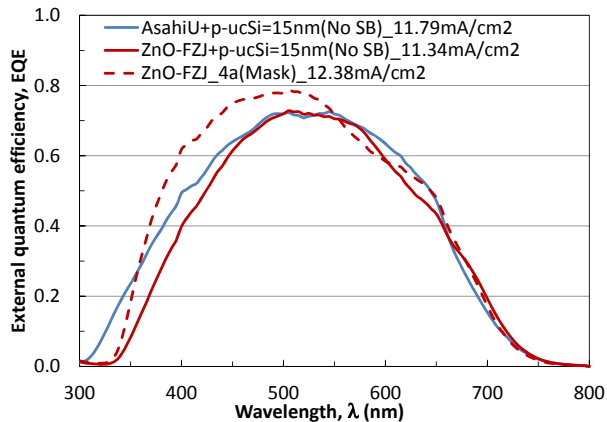


Figure 4.24: EQE curve for two solar cells with ZnO front TCO produced at FZJ and Asahi U (SnO_2) front TCO. Both samples have $\mu\text{c-Si:H}$ p-layer and are compared with a solar cell with ZnO front TCO with a-Si:H p-layer. The solar cells were produced at T-Solar through laser scribe without shunt busting and annealing. Curves are the best cell/coupon in initial state. The measurements are done without bias light and reverse voltage in 1 cm^2 cells.

4.4 p-i-n structure developments

The p-i-n structure is the key part of silicon thin film modules. To optimize the layers of the p-i-n structure it is crucial to improve the efficiency and to reduce the production costs. The efficiency can be improved, on one hand, by increasing the power of the modules in the initial state by process changes not affecting the degradation factors or, on the other hand, by process changes reducing the degradation factors. The reduction of costs results, e.g. from the increase of the factory throughput and efficiency, where the PECVD equipment is the most important machine and could be the bottleneck of the production line.

4.4.1 Uniformity of thin film properties along the panel

Fig. 4.25 presents a typical thickness mapping of a n-type control layer, showing a good uniformity of the layer thickness over the 5.72 m² area. The main characteristic of this mapping is that the profile has a slight inclination and the centre has the highest thickness. The mappings for the other layers deposited in the PECVD have similar characteristics. Hence, solar cells at the centre have p-i-n structures thicker than solar cells at the border. The uniformity of the a-Si:H layer thickness over a large area is critical to make highly efficient large-scale thin film a-Si:H solar modules. For the T-Solar layers, the thickness non-uniformity of the different a-Si:H layers over an area of 2.2 x 2.6 m² is less than 10% (calculated according to Eq. 3.17) if we consider an edge exclusion zone of 50 mm at the glass border. This is also valid for other material properties as e.g. the film conductivity or the optical absorption.

A different thickness could cause different generated current and voltage for solar cells placed in separated parts of the module. Nevertheless, thanks to such good uniformity of the a-Si:H layers' thickness, we have achieved very constant cell performance over the 5.72 m², a must to get highly efficient modules. In Fig. 4.26 the main electrical parameters in stabilized state of four coupons with solar cells placed along the panel diagonal is shown. The position of each coupon 10 cm x 10 cm in the panel is indicated with different colours. The average values for the four coupons placed throughout the large area, together with their standard deviation, variation coefficient and non-uniformity are presented in Table 4.19. All the parameters behave very similar, finding non-uniformities always lower than 1%.

In Fig. 4.27 we show the EQE of two solar cells, one placed in the centre (thickest p-i-n structure) and another one placed in the border (thinnest p-i-n structure). The thickest solar

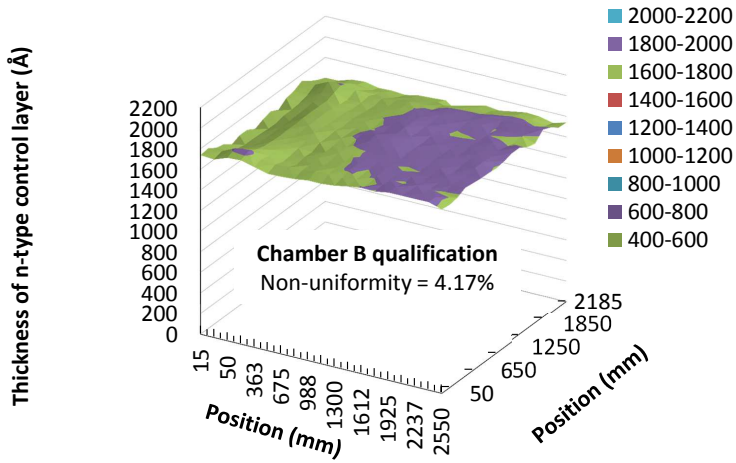


Figure 4.25: Typical thickness mapping of a n-type a-Si:H control layer [88].

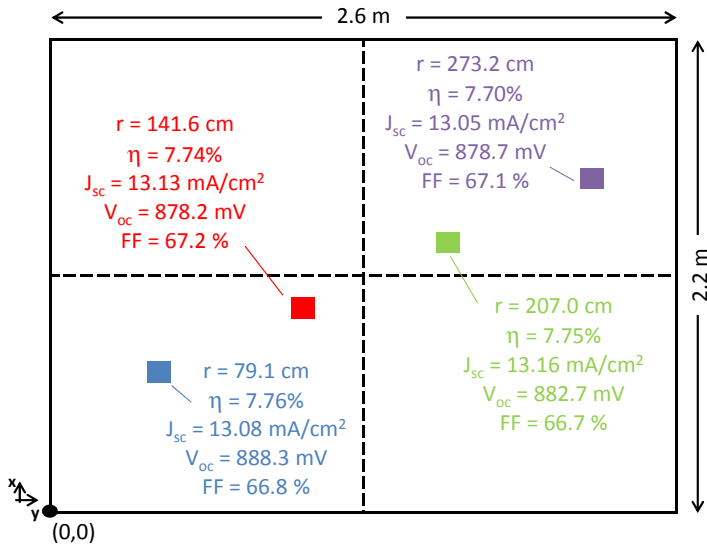
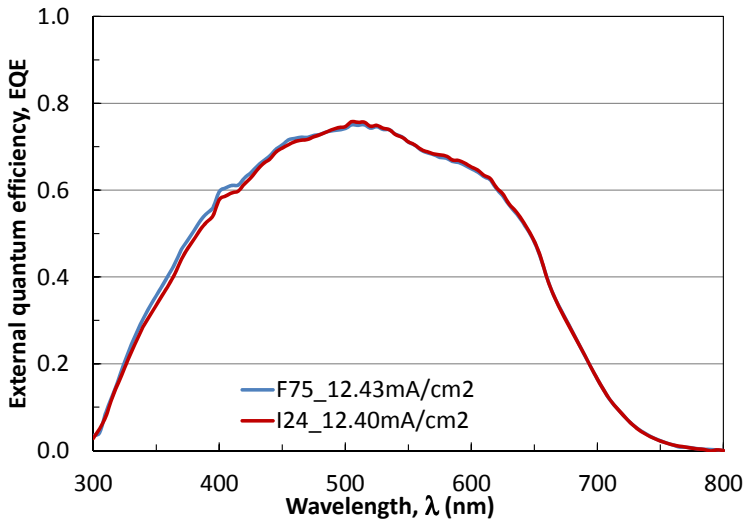


Figure 4.26: Variation of the main electrical parameters for four coupons placed along the diagonal F-I of the panel. Results are the average of the best 5 cells/coupon in stabilized state (after 300 kWh/m² of light soaking). r (cm) is the module of the coordinates, $r = \sqrt{x^2 + y^2}$.

Table 4.19: Electrical parameters statistics for four coupons of the same panel placed along the diagonal. Results in the initial and stabilized state (after 300 kWh/m² of light soaking).

	Average	Std. Dev.	Var. Coef.	Non-unif.
Initial State				
η	8.84%	0.05%	0.55%	0.64%
Jsc_SR (mA/cm ²)	12.85	0.10	0.77%	0.84%
Jsc_SS (mA/cm ²)	13.41	0.07	0.49%	0.54%
Voc (mV)	904.3	1.5	0.17%	0.18%
FF	72.97%	0.25%	0.34%	0.36%
Stabilized State (After 300 kWh/m² of light soaking)				
η	7.74%	0.03%	0.35%	0.39%
Jsc_SR (mA/cm ²)	12.44	0.07	0.54%	0.60%
Jsc_SS (mA/cm ²)	13.11	0.05	0.38%	0.42%
Voc (mV)	882.0	4.7	0.53%	0.57%
FF	66.96%	0.22%	0.32%	0.31%

cell has an EQE slightly lower in the short wavelength range (thicker p-layer absorbs more light at this range) and an EQE slightly higher in the long wavelength range (thicker i-layer absorbs more light at this range) than the thinner solar cell.

**Figure 4.27:** EQE curve for two coupons of the same panel, one placed in the centre (I24) and the other one in a corner (F75). Curves are the best cell/coupon in stabilized state (after 300 kWh/m² of light soaking). The measurements are done without bias light and reverse voltage in 1 cm² cells.

4.4.2 Electrical parameters variation with i-layer thickness

In order to investigate the impact of the p-i-n structure fabrication process, several benchmarking experiments have been done comparing the solar cell's performance with the processes of the different laboratories of the HELATHIS consortium on industrial TCO-glass. We have investigated, e.g., the dependence of i-layer thickness on solar cell efficiency and LID (see Table 4.20). Fig. 4.28 and 4.29 show how LID factors decrease significantly when reducing the i-layer thickness, resulting in very similar efficiencies of solar cells in the stabilized state. The electrical parameter presenting the highest degradation coefficients is the FF, followed by J_{sc} and, finally, V_{oc} . For the thinnest i-layers (≈ 200 nm or less) J_{sc} and V_{oc} degradation factors are very similar.

Fig. 4.30 shows the efficiency in the initial and stabilized state and the power degradation factors for quarter size modules (1.3 m x 1.1 m) fabricated with AGC AN10 TCO-glass and different i-layer thickness. The power LID-factor changes from about 9% at 140 nm i-layer thickness to about 17% at 260 nm i-layer thickness. The reduction of the i-layer thickness has a big impact on the throughput of the PECVD machine as shown in Fig. 4.31. Reducing the i-layer thickness from 260 nm to 140 nm, the PECVD throughput could be increased from 20 to 30 panels/h. This is equivalent to an upgrade of the annual factory production capacity from about 55 MW to 75 MW (36% more), when manufacturing modules of 400 W.

Table 4.20: LID (after 300 kWh/m² of light soaking) for thirteen coupons produced at different laboratories (2 at UU, 3 at FZJ and 8 at TS) with different i-layer thicknesses. In addition, the coupons have different TCOs, as indicated. Results are the average of the best 5 cells/coupon for JV curves and the best cell/coupon for spectral response.

PROD.PLACE	TCO	di (nm)	ΔJ_{sc_SR}	ΔV_{oc}	ΔFF
UU	AN10	300	7.9%	2.6%	12.9%
UU	ANS10	300	8.3%	2.7%	13.9%
FZJ	AN10	200	3.8%	1.6%	9.5%
FZJ	AN10	200	4.0%	1.8%	7.2%
FZJ	AN10 ME	200	2.7%	1.6%	4.1%
TS	AN10	260	4.6%	2.1%	9.8%
TS	AN10	220	3.7%	2.1%	8.4%
TS	AN10	200	3.0%	1.9%	7.6%
TS	AN10	200	3.6%	2.4%	9.5%
TS	ANS10ME	200	3.0%	2.3%	7.5%
TS	ANS10ME	180	2.2%	2.1%	5.0%
TS	ANS10ME	180	2.6%	2.1%	6.4%
TS	ANS10ME	220	3.0%	1.8%	6.7%

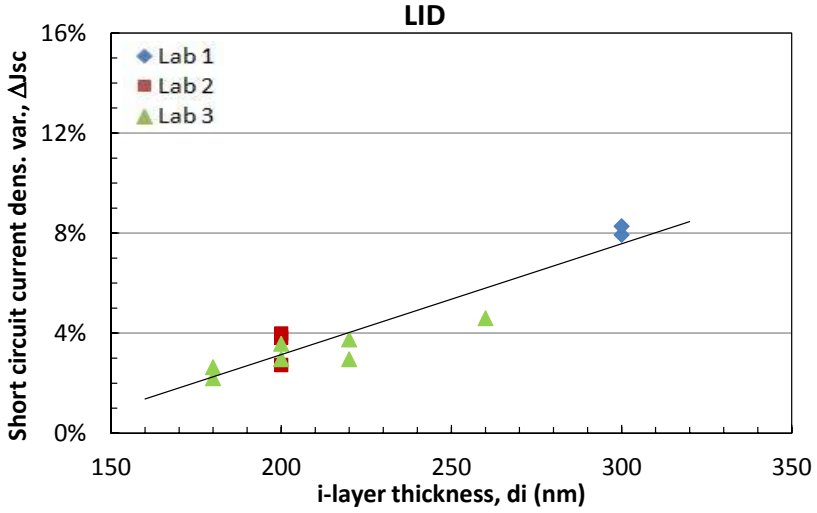


Figure 4.28: Degradation factors (after 300 kWh/m² of light soaking) of J_{sc} for solar cells prepared with different i-layer thicknesses in different laboratories.

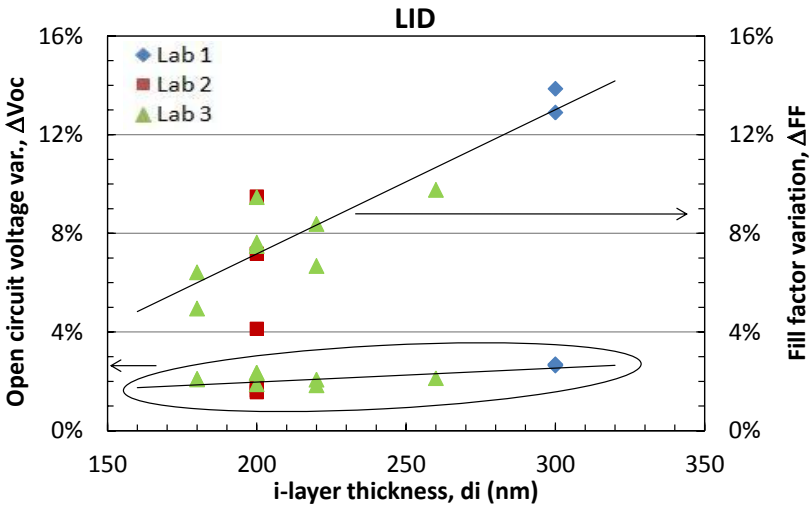


Figure 4.29: Degradation factors (after 300 kWh/m² of light soaking) of V_{oc} and FF for solar cells prepared with different i-layer thicknesses in different laboratories.

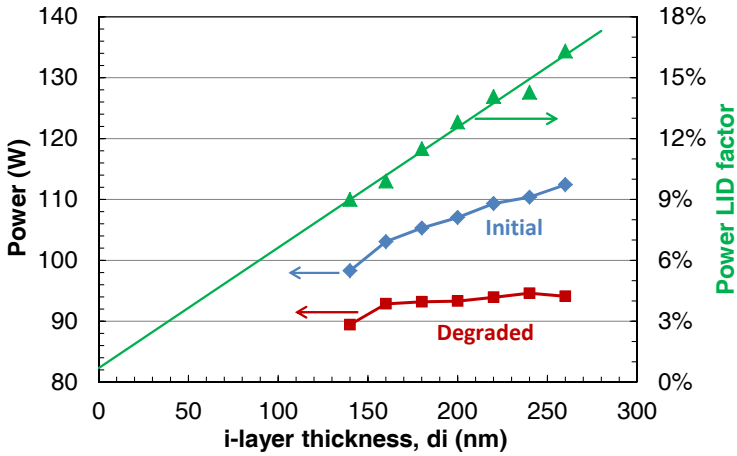


Figure 4.30: Efficiency of quarter size modules in the initial and stabilized state (after 300 kWh/m² of light soaking) and η degradation factors.

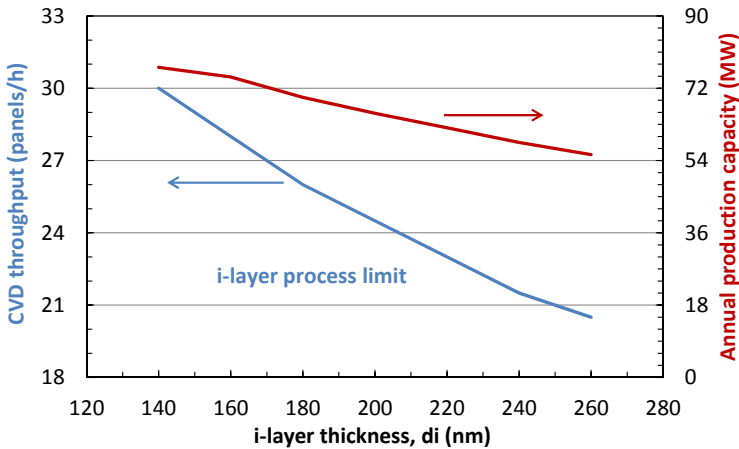


Figure 4.31: Relation between i-layer thickness reduction and throughput increase of the PECVD machine and extrapolation to the annual production capacity.

4.4.3 p-i-n structure evolution

During its lifetime, T-Solar has continuously improved its production process. To know which is the production process implemented at each moment, T-Solar uses as notation the initials BKM (best known method) followed by a number. In Table 4.21 the evolution of the

main BKM changes related to the PECVD process and a short description of the change is presented. The developments have followed three main improvement axes:

Table 4.21: Main BKM evolution related to the PECVD process since the T-Solar production start. Evolutions below dashed line are in the frame of the HELATHIS project.

Evolution No.	BKM	CVD BKM	Change description
1	0.0	0.00	AMAT BKM
2	3.0	1.00	i-layer with 25% of SiH ₄ flux
3	10.0	3.01	p-layer 10% thicker
4	15.0	5.01	Thinner i-layer & n-layer
5	17.1	5.04	Reduction of η dispersion I
6	20.1	7.02	pib-layer adjustments & Thinner p-layer
7	25.0	8.01	Reduction of η dispersion II & plasma H ₂
8	R&D prototype		Multiple p-layer + LDR + n- μ cSi

- **Increase the efficiency:** The main changes have been, first, to adjust the deposition of the p/i buffer (pib)-layer combined with a reduction in the p-layer thickness. Secondly, to introduce a H₂ plasma to improve interface properties. Finally, and only as prototype, we have developed a new recipe in which we have deposited graded multiple p-layers divided in several steps with different deposition conditions, an i-layer deposited with low deposition rate and a n-layer which is in part μ c-Si:H.
- **Increase the throughput:** The main action to increase the throughput was to reduce the i-layer thickness, followed by other less influential developments, such as the waiting time in the load lock, the speed of the transfer between chambers or the sputtering time.
- **Reduce the efficiency dispersion between different PECVD chambers:** This was done by changing the deposition process conditions and by modifying the distance between substrate and electrodes. Both changes have been done independently for each PECVD chamber trying to achieve in all of them the average efficiency of the best chamber.

Table 4.22 shows the electrical parameters of solar cells for five coupons which represent the five evolutions (corresponding with evolutions below dashed line in Table 4.21) performed at T-Solar during the three years of the HELATHIS project. The first evolution considered is the No. 4, which was produced at the beginning of the project on 31/05/2010 with AN10

TCO-glass and CVD recipe with thin i-layer and n-layer. The rest of development steps are implemented on ANS10ME TCO-glass and different evolutions of the p-i-n structure.

Table 4.22: Electrical parameters for five coupons with solar cells which represent the main five evolutions performed at T-Solar during the three years of the HELATHIS project. Top: Results in the initial and stabilized state (after 300 kWh/m² of light soaking). Bottom: LID for the coupons. Results are the average of the best 5 cells/coupon for JV curves and the best cell/coupon for spectral response.

Evolution No.	η	Jsc (mA/cm ²)_SR	Jsc (mA/cm ²)_SS	Voc (mV)	FF	Rs (Ω)	Rsh (Ω)
Initial State							
No.4	8.50%	12.29	12.97	911.8	71.9%	5.48	1724
No.5	8.77%	12.38	13.32	913.1	72.1%	5.58	1661
No.6	8.98%	12.96	13.55	906.9	73.0%	5.18	2115
No.7	9.12%	13.05	13.58	917.6	73.2%	5.27	2099
No.8 (R&D)	9.43%	13.40	13.99	926.6	72.8%	5.59	5668
Stabilized State (After 300 kWh/m² of light soaking)							
No.4	7.32%	11.85	12.64	890.3	65.1%	7.09	1229
No.5	7.70%	12.16	13.21	889.6	65.5%	6.95	1077
No.6	7.80%	12.68	13.32	879.5	66.6%	6.48	1407
No.7	7.97%	12.62	13.13	894.3	67.9%	6.40	1809
No.8 (R&D)	8.20%	13.10	13.63	897.3	67.0%	6.69	1890
LID							
Evol. No./LID	$\Delta \eta$	ΔJsc_SR	ΔJsc_SS	ΔVoc	ΔFF	ΔRs	ΔRsh
No.4	13.9%	3.6%	2.6%	2.4%	9.5%	-29.3%	28.7%
No.5	12.1%	1.8%	0.8%	2.6%	9.1%	-24.6%	35.1%
No.6	13.1%	2.2%	1.7%	3.0%	8.8%	-25.2%	33.5%
No.7	12.7%	3.3%	3.3%	2.5%	7.3%	-21.5%	13.8%
No.8 (R&D)	13.1%	2.2%	2.6%	3.2%	7.9%	-19.7%	66.7%

From the T-Solar's record solar cells (1 cm²) at the end of the project HELATHIS one can highlight:

- **Last evolution step in standard production solar cell:** 9.20% and 8.02% for the initial and stabilized efficiency, respectively.
- **R&D prototype solar cell:** 9.56% and 8.22% for the initial and stabilized efficiency, respectively.

Figs. 4.32 and 4.33 present the JV curves and EQE, respectively, for three of the five main evolutions performed during the HELATHIS project. Fig. 4.32 shows the improvement achieved in the T-Solar solar cells, especially through enhancement in the J_{sc}. In Fig. 4.33

one sees that the main enhancement in the current generation was done between 300 nm - 575 nm, especially in the short wavelength range 300 nm - 450 nm. Comparing the EQE of the T-Solar record cell on an industrial TCO-glass with the absolute world record solar cell of Oerlikon Solar-Lab S.A. (Oerlikon Solar-Lab) in Neuchâtel [89] we see the further potential to improve our device, especially optimizing the light confinement. The main differences of the Oerlikon Solar-Lab record cell are the implementation of a much thinner TCO-glass with ARC, an optimized TCO layer texturing, and a high reflective back reflector.

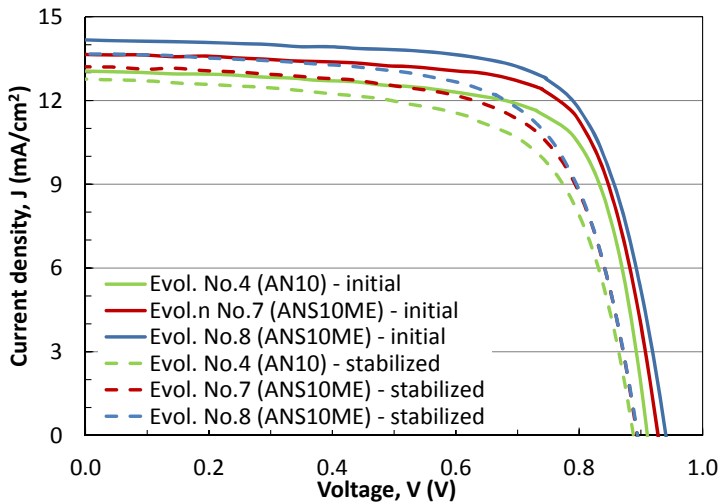


Figure 4.32: JV curve for three solar cells which represent the main three evolutions performed at T-Solar during the three years of the HELATHIS project. Curves are the best cell/coupon in initial and stabilized state (after 300 kWh/m² of light soaking).

Table 4.23 and Fig. 4.34 shows the continuous gain obtained for the last four evolution steps with respect to the step No. 4. We see that the efficiency gain with reference to step No. 4 is 8.8% for the last evolution step in production and 12.0% for the R&D prototype. The parameter that contributes the most to this increase is the current improvement, followed by the FF rise. The voltage does not vary too much because we already had a high value in comparison to the world record solar cell achieved by Oerlikon Solar-Lab (see Table 4.24), which results mainly from the different front TCO layer material (ZnO). V_{oc} and FF of the T-Solar record cell are 2% and 1% better respectively than the world record solar cell. However, the J_{sc} is 27% worse. This results in 23% less efficiency for the T-Solar record cell.

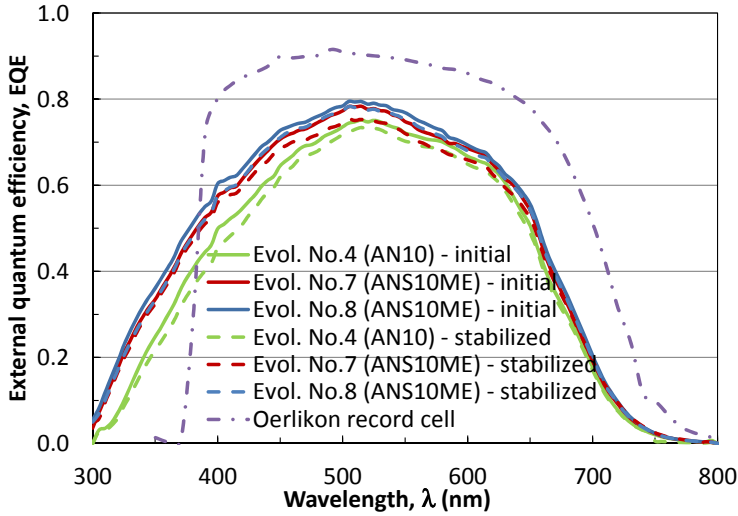


Figure 4.33: EQE curve for three coupons which represent the main three evolutions performed at T-Solar during the three years of the HELATHIS project. Curves are the best cell/coupon in initial and stabilized state (after 300 kWh/m² of light soaking). The measurements are done without bias light and reverse voltage in 1 cm² cells. The EQE for the world record solar cell of Oerlikon Solar-Lab is also presented [89].

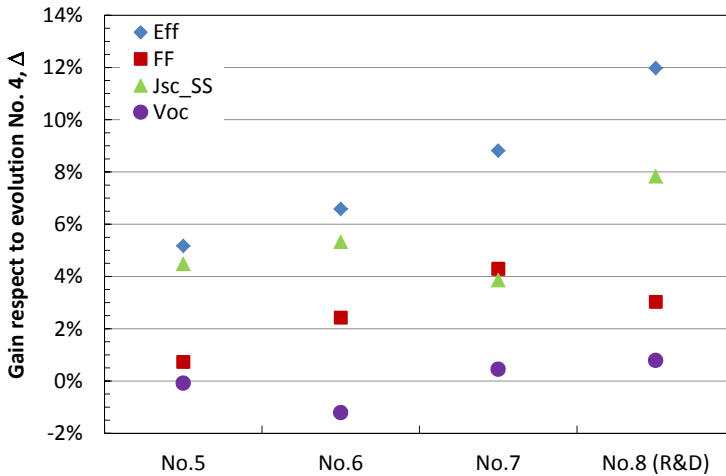


Figure 4.34: Gain of the main electrical parameters (in stabilized state) respect to evolution No. 4 for the main four evolutions performed at T-Solar during the three years of the HELATHIS project.

Table 4.23: Gain in the stabilized state respect to evolution No. 4.

Evol. No./Gain	$\Delta \eta$	ΔJ_{sc_SR}	ΔJ_{sc_SS}	ΔVoc	ΔFF	ΔR_s	ΔR_{sh}
No.5	5.2%	2.6%	4.5%	-0.1%	0.7%	-2.0%	-12.4%
No.6	6.6%	7.0%	5.3%	-1.2%	2.4%	-8.6%	14.4%
No.7	8.8%	6.5%	3.9%	0.4%	4.3%	-9.7%	47.2%
No.8 (R&D)	12.0%	10.5%	7.8%	0.8%	3.0%	-5.6%	53.7%

Table 4.24: Electrical parameters for the stabilized record T-Solar solar cell and world record solar cell of Oerlikon Solar-Lab [89].

	η	J_{sc} (mA/cm ²)	Voc (V)	FF
T-Solar record	8.20%	13.63	897	67.0%
Oerlikon Solar-Lab	10.09%	17.28	877	66.6%
Δ	23.1%	26.8%	-2.3%	-0.7%

4.5 Back contact developments

To improve the efficiency by modifying the back contact, the main study we have performed was to replace the Al-layer by a silver (Ag)-layer. We have done different experiments with Ag and/or Al back reflectors deposited with shadow mask at UB and UU in samples with p-i-n structure + AZO layer deposited in the TS production line. The deposition of Ag and Al was done by sputtering and evaporation, finding similar results.

Fig. 4.35 presents the EQE for a solar cell with Al back reflector and another one with Ag back reflector, both deposited by sputtering at UU. The Ag-layer shows a J_{sc} increase of 5.6% with respect to the Al-layer. The rise in the efficiency will be the same since the introduction of this layer does not affect electrically but only optically. Despite the important efficiency gain, the Ag back reflector has not been implemented in the industrial application. The main reason to not introduce the Ag back reflector was the cost calculation, since it showed that at the high 2011 - 2012 Ag's price, the implementation of silver as back reflector was not enough cost effective in comparison to the overall impact and implementation risk. One of the risk was the long-term reliability, since Ag-layer presents low adherence on the AZO layer and it could result in shorter lifetime of the module, which would have been necessary to investigate in detail.

To solve the difficulties found with the Ag back reflector, we have performed reliability tests achieving good results. In addition, to reduce the Ag cost we have designed an experiment combining Ag/Al-layers with different thickness to look for the minimum Ag

thickness that we could deposit without losing too much current. In Fig. 4.36 we see the reflection of test samples combining Ag/Al-layer, presenting a promising reflectance spectra that points to a good reflector, which improves the Al-layer reflectance using only a few nm of Ag-layer. Nevertheless, further experiments should be performed.

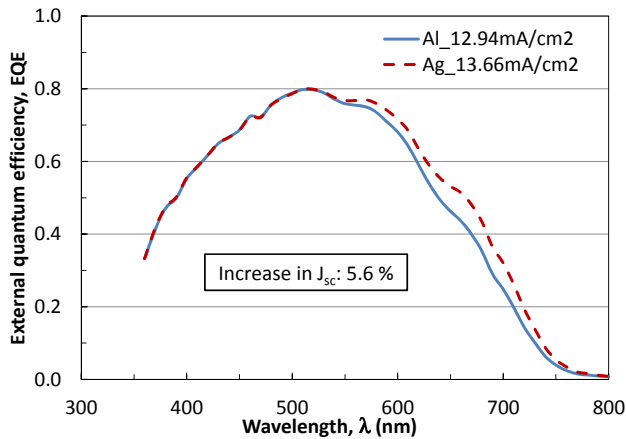


Figure 4.35: EQE curve for two solar cells, one with Al back contact and another one with Ag back contact, both deposited by sputtering at UU. Curves are the best cell/coupon in initial state. The measurements are done without bias light and reverse voltage in 1 cm^2 cells.

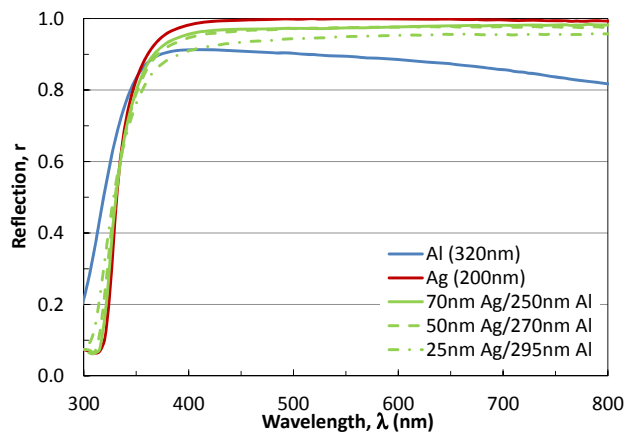


Figure 4.36: Reflectance for five different Ag and/or Al back reflectors. The samples were produced at T-Solar except the Ag and/or Al deposition which was done at UB by evaporation or sputtering.

4.6 Experimental results with the very fast spectral response equipment

To evaluate the capabilities and the accuracy of our VFSR equipment we have performed measurements on solar cells and mappings on 10 cm x 10 cm mini modules.

In Fig. 4.37, first to evaluate the accuracy of the VFSR equipment, we present the EQE comparison of two stabilized SJ solar cells (after 300 kWh/m² light-soaking) with different i-layer thicknesses (260 nm vs. 200 nm). Both cells were measured with our CSR equipment and the new VFSR equipment. The dots represent the average data of five repetitive measurements at each wavelength presenting an average relative error of about 0.2% within the five measurements. The variation of the SR of the two samples at about 600 nm is due to interferences caused by the different i-layer thickness.

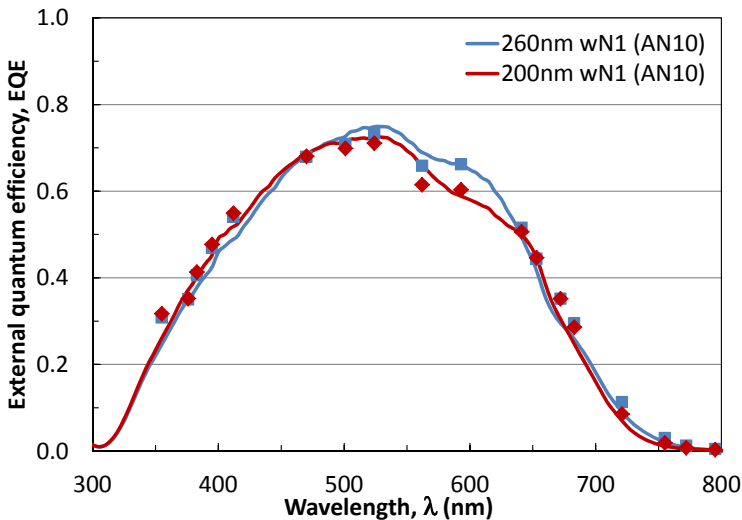


Figure 4.37: EQE of two SJ solar cells with different i-layer thickness, both measured with our CSR equipment (5 nm step width, continuous curves) and the new VFSR equipment (dots). The blue line and dots are the measurements of a solar cell with 260 nm i-layer thickness whereas the red line and dots are the measurements of a solar cell with 200 nm i-layer thickness.

The VFSR equipment reproduces properly the EQE curve, following the trend of the CSR equipment at every wavelength. Despite this, to achieve a more accurate SR measurement and to detect, e.g. small changes like the ones produced by the variation in the i-layer thickness, we would need to measure with higher resolution in the range from 500 nm to

650 nm. The difference in the integrated J_{sc} along the spectrum (355 nm – 800 nm) between both thicknesses is 3.2% and 3.7% for the CSR and the VFSR respectively (see Table 4.25). Moreover, the difference in the integrated J_{sc} for both equipments is 0.7% and 1.1% for the 260 nm and the 200 nm layers respectively.

Table 4.25: J_{sc} determined from SR with the VFSR and CSR equipments for solar cells with i-layer thickness (d_i) of 260 nm and 200 nm.

d_i (nm)	Jsc(CSR) (mA/cm ²)	Jsc(VFSR) (mA/cm ²)	Δ (CSR vs. VFSR)
260	11.78	11.70	0.7%
200	11.41	11.28	1.1%
Δ (260 vs. 200)	3.2%	3.7%	

Next, in Fig. 4.38 we present the EQE comparison of two stabilized SJ solar cells (after 300 kWh/m² light-soaking) with different BKM evolution steps (No. 4 vs. No. 8), both measured with our CSR equipment and the new VFSR equipment. The main variation of the SR between both samples is located in the range 350 nm - 500 nm. The VFSR equipment reproduces again properly the EQE curve. The difference in the integrated J_{sc} along the spectrum (355 nm – 800 nm) between both evolution steps is 3.4% and 2.5% for the CSR and the VFSR respectively (see Table 4.26). Moreover, the difference in the integrated J_{sc} for both equipments is 1.0% and 1.9% for the evolution No. 4 and the evolution No. 8, respectively.

Table 4.26: J_{sc} determined from SR with the VFSR and CSR equipment for solar cells with different BKM evolution steps (No.4 vs. No.8).

Evolution No.	Jsc(CSR) (mA/cm ²)	Jsc(VFSR) (mA/cm ²)	Δ (CSR vs. VFSR)
No. 4	12.50	12.37	1.0%
No. 8	12.93	12.69	1.9%
Δ (No.4 vs. No.8)	3.4%	2.5%	

One objective of the development of the VFSR equipment is the performance and analysis of J_{sc} mappings to better understand the current generation in modules.

In Fig. 3.9 one can observe a mini module design with 10 cm x 10 cm total area (6.0 cm x 7.1 cm active area) used to investigate J_{sc} mappings as presented in Fig. 4.39. The production of these MMs was explained in section 3.2. We have only modified the way to connect the cells. Here, every cell is connected individually with a buss (see Fig. 3.24), which enables us to perform the measurements connecting each cell directly or connecting the extremes of the MM as done in modules. Currently, we are investigating possible differences between both

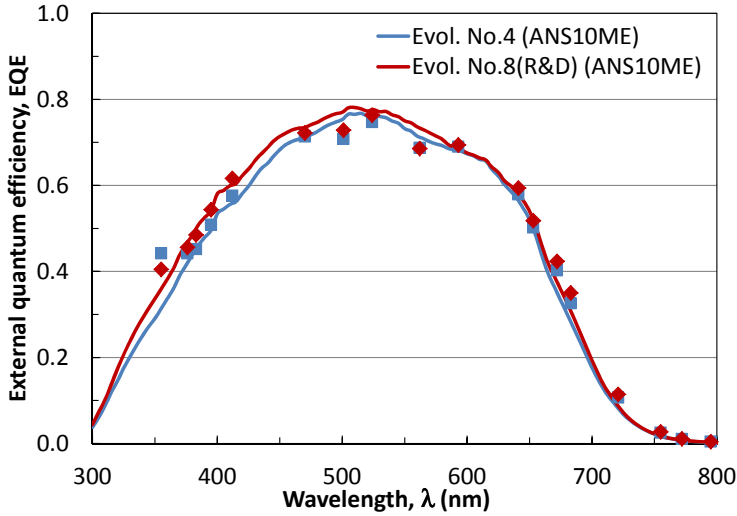


Figure 4.38: EQE of two SJ solar cells with different BKM evolutions (No.4 vs. No.8), both measured with the CSR (lines) and VFSR (dots) equipment.

types of current measurement for the determination of the SR. Here we report on results after measuring each cell connected individually.

In Fig. 4.39 we show the J_{sc} spatial mapping of 30 points over a $10 \times 10 \text{ cm}^2$ size mini module measured with the VFSR equipment. To perform this with the traditional equipment about 10 h are needed. In contrast, we only need about 1 h with the new equipment, which is mainly determined by displacing the VFSR equipment's measurement head. We have estimated that using an optimized xy displacement system to move the equipment we could perform the same mapping in about 2 minutes.

Table 4.27 summarizes the statistical parameters obtained from the mapping in Fig. 4.39, measured with the VFSR equipment, and the data measured with the CSR equipment. It shows a non-uniformity of 2.7% for the VFSR equipment and 0.5% for the CSR equipment. The higher non-uniformity (calculated according to Eq. 3.17) in the VFSR measurement is mainly attributed to the mechanical uncertainty and the nonequal illumination of the 1 cm wide solar cells when moving the measurement head, which is a target of future optimization.

Table 4.27: Statistical parameters obtained from the mapping in Fig. 4.39 (VFSR equipment) and the same mapping obtained with the CSR equipment.

	J_{sc} (avg) (mA/cm^2)	Rel. error	Non-unif
CSR	12.20 ± 0.03	0.27%	0.47%
VFSR	12.46 ± 0.19	1.55%	2.73%

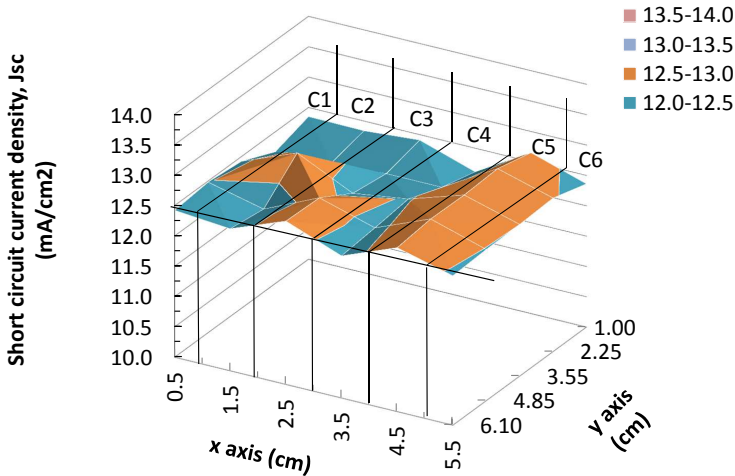


Figure 4.39: J_{sc} spatial mapping along a $10 \times 10 \text{ cm}^2$ size mini module measured with the VFSR equipment.

4.7 Simulation results

Next, simulation data of the electrical performance of a-Si:H thin film solar cells using the software package Sentaurus TCAD (Synopsys Inc.) are presented. Within this work, the Sentaurus software, a standard software for electronic device simulation widely used in the semiconductor industry, has been configured with standard theoretical models describing, among others, the density of states in the mobility gap of a-Si:H, generation/recombination statistics, optical data of a-Si:H thin films, etc. The aim is to calculate dark and illuminated JV curves and the respective spectral response for the initial and degraded state of the solar cell.

4.7.1 Study on theoretical electrical performance of the p-i-n structure

In the next figures, the variation of J_{sc} and V_{oc} (Fig. 4.40) and η and FF (Fig. 4.41) as function of i-layer thickness for three different p-layer thicknesses are presented. The optimum i-layer thickness for the studied values of the p-layer thicknesses is located between 200 nm and 250 nm (looking at the efficiency). In this region, J_{sc} decreases and V_{oc} increases with the p-layer thickness. This is because with thicker p-layers less light is absorbed in the i-layer (short wavelengths). However, a higher electric field is created at the p/i interface. The FF is quite close together in the three cases, being slightly higher for 10 nm. These characteristics result in a higher efficiency for 10 nm, reaching around 7.83% at the maximum point (see Fig. 4.41).

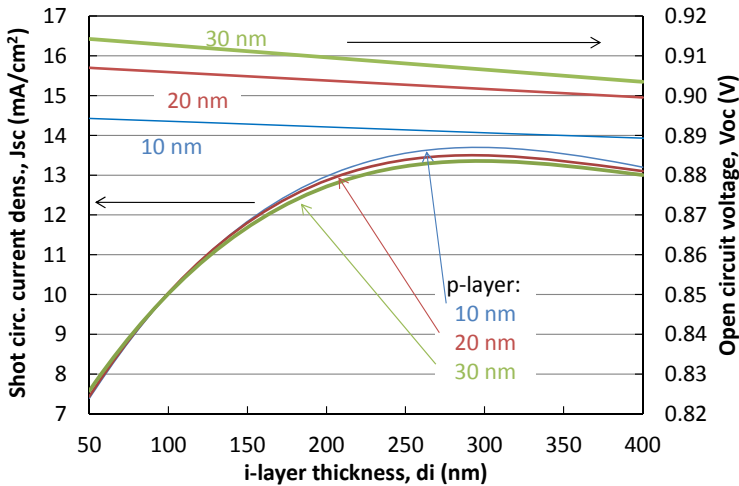


Figure 4.40: Variation of short circuit current density and open circuit voltage with the i-layer thickness for three different p-layer thicknesses (doping concentration $3 \times 10^{18} \text{ cm}^{-3}$).

Figs. 4.42 and 4.43 show the variations of J_{sc} and V_{oc} , and η and FF respectively as function of i-layer thickness for three different p-layer doping concentrations. For simplicity, first a constant doping profile was chosen about $N_A \approx 1 \times 10^{18} \text{ cm}^{-3}$, a doping level that can easily be achieved for a-SiC:H layers [44]. Increasing the doping concentration, on one hand increases the built-in voltage, as well as the electric field. On the other hand the recombination rate and the absorption coefficient of the p-layer increase, both reducing the generated current.

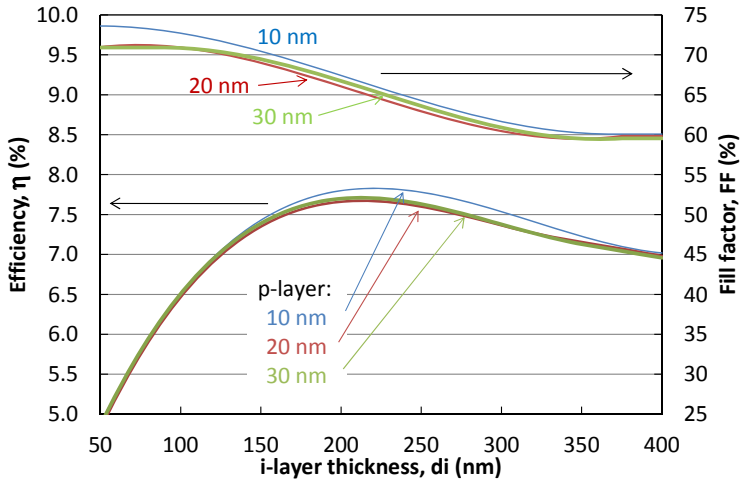


Figure 4.41: Variation of efficiency and fill factor with the i-layer thickness for three different p-layer thicknesses (doping concentration $3 \times 10^{18} \text{ cm}^{-3}$).

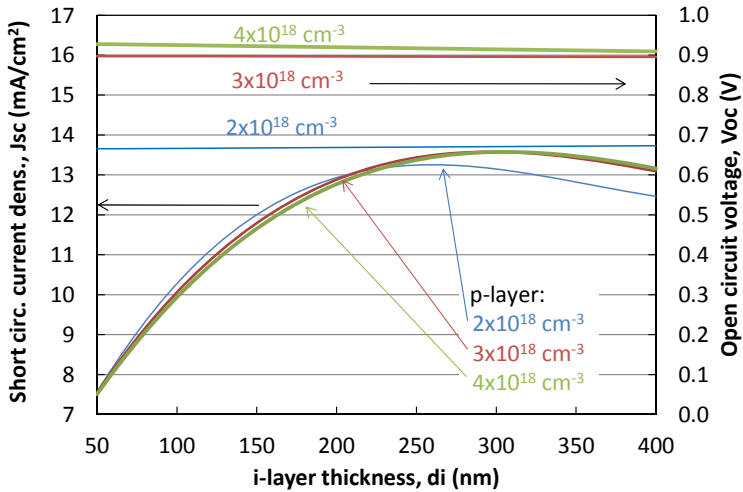


Figure 4.42: Variation of short circuit current density and open circuit voltage with the i-layer thickness for three different p-layer doping concentrations (p-layer thickness 15 nm).

The optimum i-layer thickness is still placed between 200 nm and 250 nm. For doping concentrations lower than $N_A = 3 \times 10^{18} \text{ cm}^{-3}$ (e.g. $N_A = 2 \times 10^{18} \text{ cm}^{-3}$) the V_{oc} and FF drop

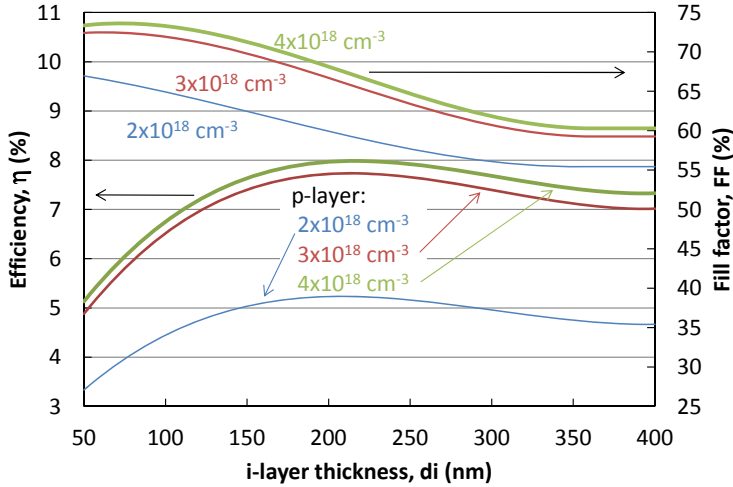


Figure 4.43: Variation of efficiency and fill factor with the i-layer thickness for three different p-layer doping concentrations (p-layer thickness 15 nm).

strongly, resulting in low efficiencies. In addition, we observe a reduction in current for the thickest i-layers, despite the lower absorption coefficients. This is because of the reduction of the electric field at the interface p/i, resulting in a reduction in the i-layer current collection.

We have to look for a trade-off between high acceptor concentration level and low optical absorption coefficients. At doping concentrations higher than $N_A = 4 \times 10^{18} \text{ cm}^{-3}$ the V_{oc} trends to saturate, on the other hand the absorption will continue to increase.

As can be seen in Figs. 4.41 and 4.43 the efficiency in the stabilized state presents a maximum around 200 nm - 300 nm i-layer thickness, dropping strongly for thinner absorber layers. The maximum efficiency results from the trade-off between increasing the J_{sc} , due to larger absorber thickness, and decreasing the degradation factors, due to thinner i-layers. The first 20 nm of the p-i-n cell structure have a crucial influence on the overall solar cell performance. The p-layer is situated at the front side of the solar cell ($d \approx 10 \text{ nm} - 30 \text{ nm}$), hence its importance. The difficulty is to achieve a high active doping concentration and low optical absorption at the same time, since the p-layer usually presents a high defect density and therefore, does not contribute to the current generation.

Results showed in this section present relatively low efficiencies since we were simulating here the T-Solar solar cell structure produced at the end of 2010, which is identified with

evolution step No. 4 and applying a simple simulation model in reference to the light trapping properties. In the next section, an improved simulation model will be presented, as well as its application to one of the latest solar cell developments.

4.7.2 Study on the front TCO layer texture

To improve the simulation accuracy shown in the previous section we have added in this development the implementation of a textured front TCO layer and the modelling of layers with graded doping concentration. The structure simulated here corresponds with evolution step No. 6.

The surface texturing is implemented to improve the simulation of the light trapping in thin film solar cells. This helps to reduce light reflections from solar cell surfaces and to increase the light scattering, improving the photon absorption in the i-layer and, therefore, the electron–hole pairs generation. The roughness of the layers enhances the amount of light reflected at the AZO/Al interface [90]. As a result, the light trapping in the i-layer of the cell improves. Consequently, the optical path length increases in this layer [45] as shown in Fig. 4.44.

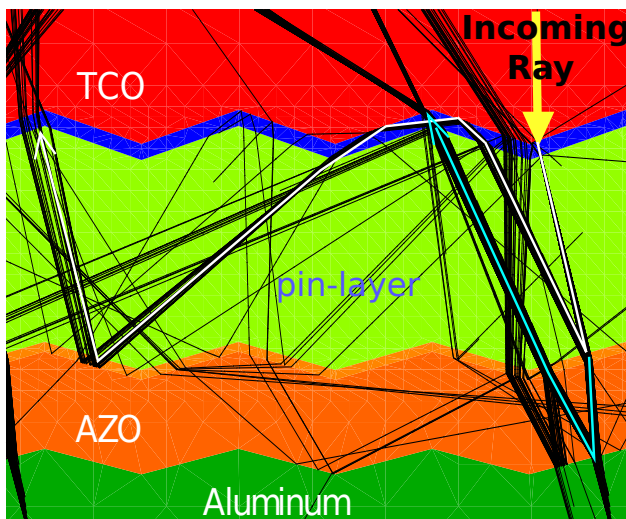


Figure 4.44: Light trapping in the active layer (i-layer) of an a-Si:H solar cell.

Different TCO textures have been simulated in order to find the optimal roughness to know if the texture of our industrial TCO could be further optimized. As shown in Fig. 2.16 the SnO₂ AGC TCO has a pyramidal-shaped texture. To simulate the 3D pyramidal-shaped texture, we use 2D triangular profiles as a representation. As presented in Fig. 4.45 we have considered a constant base of 200 nm and we have varied the β angle (angle between the edge of the triangular profile and the segment which joins its projection with the horizontal axis) and, as consequence, the height of the triangles.

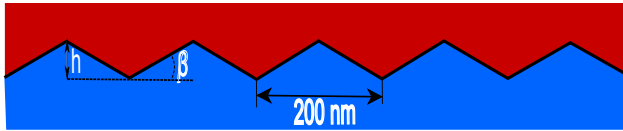


Figure 4.45: Representation of the texture interface parameters. To find the optimal texture conditions we kept constant the base in 200 nm and we vary the β angle and, as consequence, the height (h) of the triangles.

Textures with different angles, including $\beta = 0^\circ$, which is a flat interface, have been simulated to compare their performance. Fig. 4.46 presents the JV curves for four different textures and the flat case, considering in all cases the degraded state. This figure shows that J_{sc} increases with the angle β reaching its maximum at $\beta = 20^\circ$, where the J_{sc} saturates. For higher values of β ($\beta = 30^\circ$), J_{sc} decreases.

Table 4.28 shows the simulated electrical parameters for a solar cell with different textures as function of the β angle in detail. J_{sc} and η increase with β up to $\beta = 20^\circ$, whereas V_{oc} and FF does not suffer important changes. For angles higher than 40° the values of η , J_{sc} and V_{oc} drop strongly, becoming lower than the flat case. Therefore, a value of $\beta \approx 20^\circ$ presents the best electrical parameters which agrees very well with the β angle of our industrial TCO, which is about 22° as determined from AFM measurement.

The EQE for four different textured interfaces and the flat case is presented in Fig. 4.47. Textured interfaces significantly improve the performance of the solar cell in the long wavelength range, for wavelengths higher than 550 nm, up to $\beta = 20^\circ$. In the short wavelength range the values of EQE are very close, with the exception of $\beta = 30^\circ$ which is slightly higher than the rest.

According the experimental data of AFM measurements of ANS10ME TCO texture (RMS roughness, $\delta \approx 40$ nm and peak to peak distance about 200 nm), the estimated value of β is about 22° which has been considered to simulate the roughness of the manufactured

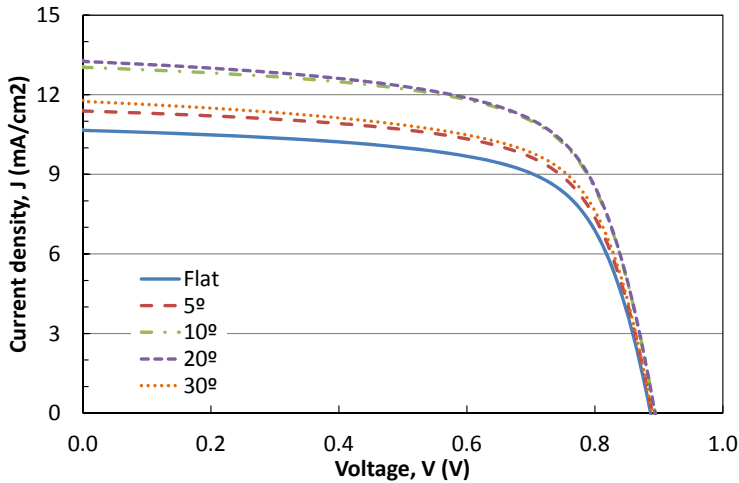


Figure 4.46: Simulated JV curves for flat and textured interfaces with different heights. All textured interfaces have a common period of 200 nm.

solar cells. Table 4.29 shows a comparison of electrical parameters between simulated and experimental results in both, initial and stabilized state. According to the table, simulation data is in good agreement with experimental results, finding a difference lower than 1% for all the electrical parameters in both, initial and stabilized states.

Fig. 4.48 plots experimental and simulated JV curves for the initial and degraded states. In this figure, a very good agreement between results from the simulation and experimental data is achieved. The consistency between experimental and simulated results indicates that

Table 4.28: Simulated electrical parameters depending on the β angle in the degraded state.

β	η	J_{sc} (mA/cm ²)	V_{oc} (mV)	FF
Flat	6.35%	10.66	887.1	67.2%
5	6.77%	11.39	889.6	66.9%
10	7.74%	13.03	894.2	66.4%
20	7.78%	13.26	893.9	65.6%
30	6.91%	11.75	889.4	66.2%
40	5.85%	9.91	882.8	66.9%
50	5.00%	8.25	875.6	69.2%

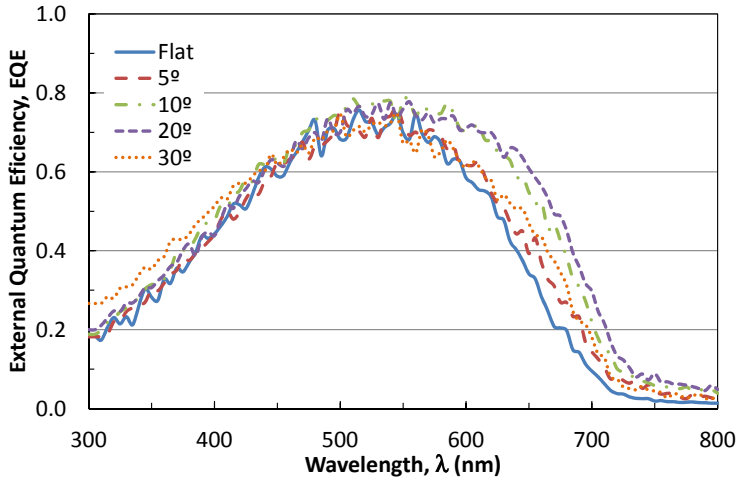


Figure 4.47: Simulated EQE for flat and textured interfaces with different heights. All textured interfaces have a common period of 200 nm.

the model to simulate textured interfaces works correctly. In addition, we observe how the simulation reproduces adequately the variation between initial and stabilized states.

Fig. 4.49 shows the experimental and simulated results of the EQE for the initial and degraded states. In general trend, the simulated and experimental data agree. However, further optimization should be performed, since a slightly overestimation is observed at wavelengths lower than 350 nm and higher than 550 nm. In contrast, a slightly underestimation is seen in the wavelength range 375 nm - 475 nm. The optical effects around 600 nm, resulting from the interference in the i-layer, are especially not well reproduced.

Table 4.29: Electrical parameters for an experimental and simulated solar cell in the initial and degraded state.

	η	J_{sc} (mA/cm ²)	V_{oc} (mV)	FF
Initial State				
Experimental	8.97%	13.60	907.4	72.7%
Simulated	9.02%	13.61	909.3	72.9%
Δ (Sim-Exp)	0.54%	0.04%	0.21%	0.27%
Stabilized State				
Experimental	7.80%	13.12	893.5	65.6%
Simulated	7.80%	13.16	894.5	66.3%
Δ (Sim-Exp)	-0.08%	0.30%	0.12%	1.07%

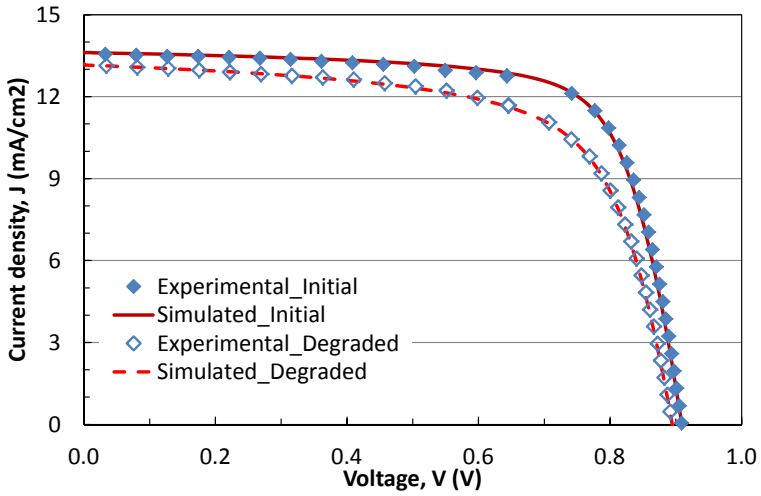


Figure 4.48: Experimental and simulated JV curve in the initial and degraded state.

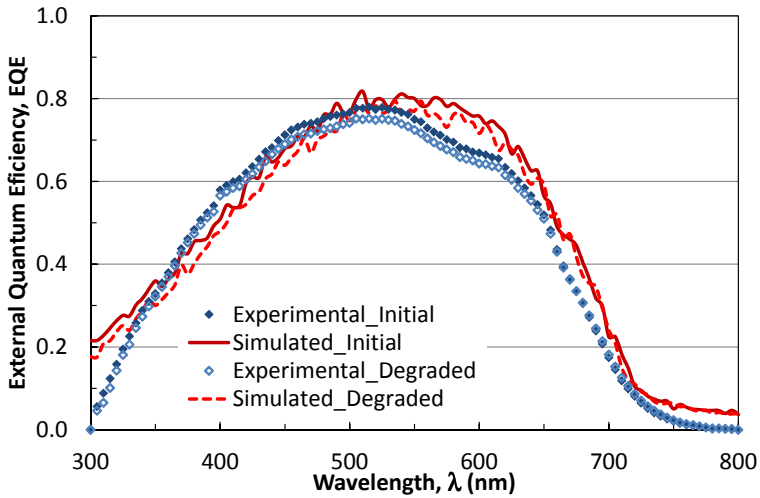


Figure 4.49: Experimental and simulated EQE in the initial and degraded state.

4.8 Improvements in the industrial production line of T-Solar

During its lifetime, T-Solar has continuously increased the annualized production capacity and reduced the price per W_p of the modules which is its main aim. To achieve this reduction, in the factory production line, we focused on the next improvements:

- Increase of efficiency: New materials, new deposition process conditions, etc.
- Increase of throughput: Optimization of production process.
- Increase of factory availability: Reduction of corrective and preventive maintenance.
- Reduction of material costs: Decrease of scrap, increase of reliability and decrease of raw material cost.

The efficiency evolution during the last four years (since the beginning of the factory in July 2008 and until the second half of 2012) is presented in Fig. 4.50. The first modules had an efficiency of about 6% using the BKM provided by AMAT. The last production modules from July 2012 have an efficiency of about 7.5% (25% improvement). The last R&D development in modules presents a stabilized efficiency of 7.95% or 455 W_p . The most important evolution steps indicated in Table 4.21 are labelled in the figure.

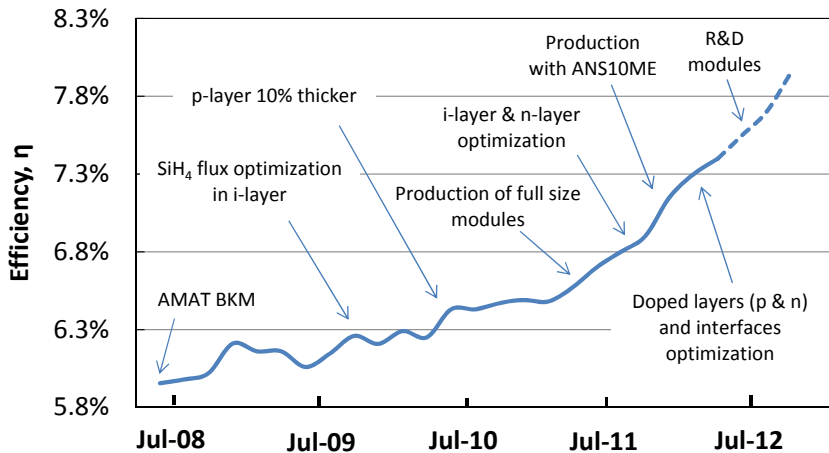


Figure 4.50: Efficiency evolution in modules in the last four years.

In Table 4.21 we saw that two of the evolutions were performed to reduce the efficiency dispersion. We reach that aim by changing the deposition process conditions and by modifying the distance between substrate and electrodes for each PECVD chamber individually. Thus, one gets the efficiency of all the modules very close to the ones from the best PECVD chamber, which does the average efficiency higher. Fig. 4.51 compares that dispersion and the module efficiency for the years 2009, 2011 and 2012. One sees that for the year 2012 the most of modules were inside the same power class, the TS410 (power between $410 W_p$ - $430 W_p$ and efficiency between 7.2% - 7.5%) whereas in 2009 they were shared in two classes.

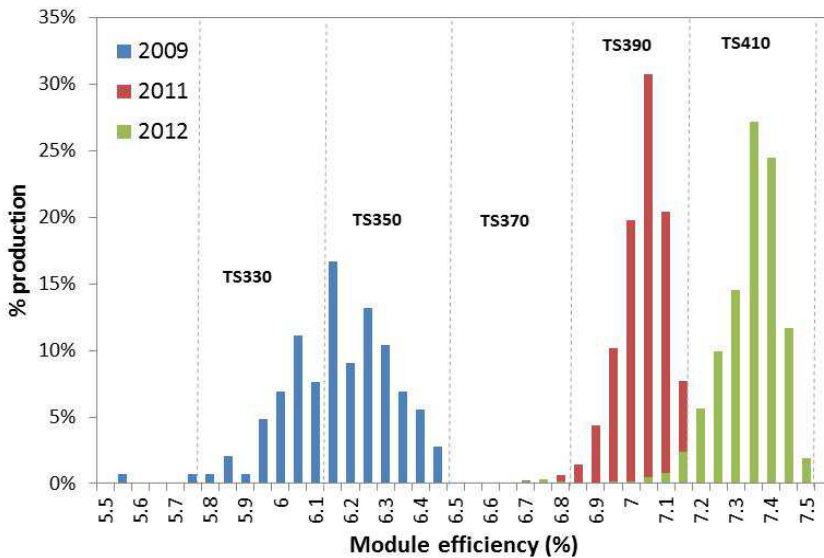


Figure 4.51: Efficiency histogram for similar production periods of 5.72 m² a-Si:H modules from 2009 to 2012.

Another important factor of improvement is the throughput, which was increased from 17 panels per hour (pph) in 2009 to 22 pph in 2012 (29% improvement), as shown in Fig. 4.52. In addition, the factory availability was increased by about 50% in the same period of time, mainly due to reduction in the number of corrective maintenances and reduction of hours to perform preventive maintenances.

Combining the increase in efficiency, throughput and factory availability with the reduction of scrap modules, one sees that the annualized production capacity of the factory has increased from 33 MW in 2009 to 72 MW in 2012 which represents a 118% of improvement.

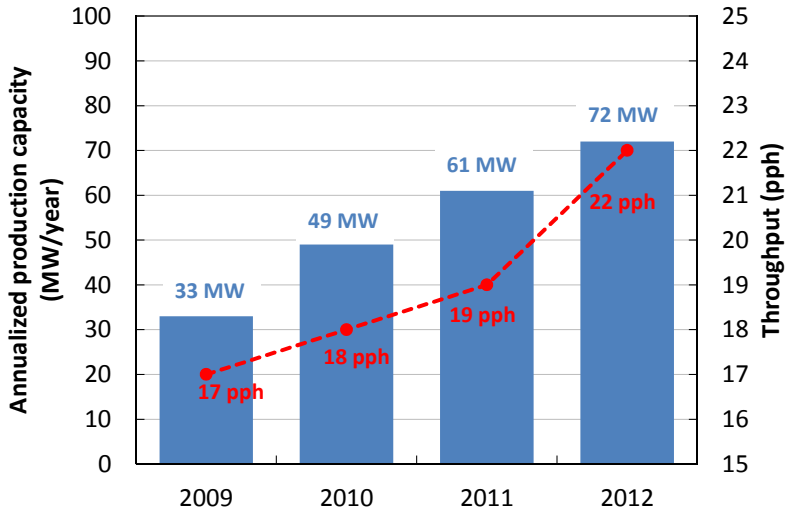


Figure 4.52: Evolution of the T-Solar production capacity and throughput during the period 2009 - 2012.

Conclusions

Photovoltaic sector is becoming a mainstream player in the renewable energy sector and has a promising future being nowadays a very competitive and well established energy source. PV installations will continue to grow in the coming years accelerating its consolidation. The results of the PV installation capacity of 2012 bear this out. But they also reveal that a shift is taking place in PV markets – from one driven mostly by Europe to one that also depends on countries world-wide, especially China.

Despite the expected growth, the possibility to have a low PV market in Europe in 2013 due to its economic situation will most likely prolong the imbalance between supply and demand of PV components, making 2013 a difficult year for industrial PV companies. But under even the most pessimistic scenario, PV will continue to increase its share of the energy mix in Europe and around the world, becoming a reliable source of clean, safe and infinite renewable energy. In the long-term, growth rates for photovoltaics will continue to be high, even if economic frame conditions vary and can lead to a short-term slow-down.

Concerning the PV industry, it has changed dramatically over the last few years. China has become the major manufacturing place followed by Taiwan, Germany and Japan. Amongst the 20 biggest PV manufacturers in 2011, only three had production facilities in Europe and all of them have an uncertain future to continue producing there.

Since 1990, PV production has increased by about 2.5 orders of magnitude, from 129 MW to about 70 GW in 2012. The introduction of new technologies much faster than expected (thin film, CPV) together with dramatic price decline of solar modules of more than 50% over the last two years caused by the overcapacity has put enormous pressure on a large number of companies and is accelerating the consolidation of the industry. For the next years the forecast is to continue the expansion to an economy of scale changing from a MW size industry into a mass-producing industry aiming for multi GW production.

Further cost reduction of PV electricity now depends no longer only on the PV system components itself, but increasingly on the integration costs into the existing infrastructure. Therefore, to make PV-generated electricity a major source of the world-wide electricity supply for the next decade, more effort has to be focussed on optimising the non-PV costs and public support, especially on regulatory measures.

The IEA's "Energy Technology Perspectives 2010" stated that for their current Baseline Scenario, the overall investments in energy supply and use, for the period between 2010 and 2050, totals € 208 trillion (IEA Baseline scenario) [20]. To limit the concentration of Greenhouse Gases at 450 ppm, it is necessary an additional financing of € 35.4 trillion (BLUE-Map scenario), but at the same time the cumulative fuel savings of this scenario compared to the Baseline would be € 86.2 trillion, or more than twice the investment cost. This clearly indicates the huge societal benefit of a more aggressive climate change approach.

In the frame of this work, results for two dimensional computer simulation of a-Si:H p-i-n structures were presented using a basic configuration of the Sentaurus simulation tool. We have implemented the standard models for the DOS distribution and the generation/recombination process used in a-Si:H. As well, we have modelled layers with graded doping concentration. A model to simulate the texture of the front TCO layer and light trapping effects in a-Si:H solar cells has been implemented. The simulation reproduces well the current-voltage characteristics and spectral response of typical T-Solar a-Si:H solar cells. The simulations show the importance of the optimization of the p-layer properties and give a guide how its thickness and doping concentration affect on the electrical parameters of the solar cell.

Three measurement equipment were developed in the laboratory related to this PhD thesis, a conventional spectral response and a very fast spectral response equipment, which are used to determine the external quantum efficiency (EQE) curves, and a solar simulator equipment with its current-voltage (IV) curves tracer to measure illuminated or dark IV curves. In Chapter 4 we have shown the importance not only of the conventional spectral response equipment but also of the solar simulator equipment with its current-voltage (IV) tracer. However, the most innovative tool is the very fast spectral response equipment, reason why we are going to focus in the main aims achieved with this equipment and its future developments.

The very fast spectral response equipment is capable of measuring the SR of a-Si:H SJ solar cells in a few seconds. To that end, we have characterized LEDs in the range from 300 nm to 800 nm. In addition, to measure TJ solar cells in a near future, we have

analysed LEDs in the range from 800 nm to 1000 nm. The equipment reproduces properly the behaviour of different solar cells with, e.g. different i-layer thicknesses or different BKM evolutions. We have also performed J_{sc} mappings in mini modules of 10 cm x 10 cm size. It is noteworthy that the VFSSR equipment only spends 1 h against the 10 h needed to perform the mapping with our traditional equipment.

Nowadays we use 18 LEDs to measure SJ solar cells and we intent to use 24 LEDs to measure TJ solar cells. However, it is difficult to find in the market commercial LEDs fulfilling the criteria for, e.g., the spectral width and intensity. To achieve an accurate SR measurement and to detect e.g. changes like variation in the i-layer thickness, we would need to measure with higher resolution in the range from 500 nm to 650 nm. Furthermore, a mechanically robust optical coupling system is under development. The mechanical uncertainty and the non-equal illumination when moving the measurement head are still producing the main measurement error of the equipment.

The fabrication of highly efficient and reliable a-Si:H test solar cells in the industrial environment of T-Solar was achieved by using laser scribe process and shunt busting in combination with annealing (145 °C, 30 min). With this procedure, we achieve highly efficient cells, low dispersion and high yield. In addition, we have automated the production of test panels, so we know exactly where the cells are placed in the full size panel and we spend less time for their production. As well, we are able to send samples with TCO-glass, p-i-n and a protective ZnO layer to manufacture high efficient solar cells in another laboratories.

During this PhD thesis we have performed several developments and tests to improve the T-Solar solar cells and modules (improvement of efficiency, throughput, reliability, material cost, etc.). Some of these developments have already been implemented, others have not still reach the desired technical conditions and others are not economically competitive at this moment. Taking into account the previously presented results for 1 cm² solar cells and the same results obtained with modules one calculates the potential for efficiency improvement of a-Si:H single junction solar cells and modules achieved with all the commented developments:

- **Front TCO layer and glass developments:** The carrier mobility of the TCO layer was increased resulting in thinner and more transparent TCO layers. As well, it was combined with float glass with low iron content, increasing again the transmission. The resulting TCO-glass is the ANS10ME. The gain in efficiency due to the ME-type layer is about 1% - 1.5% relative, for the low iron-content glass is about 2% - 3% relative. Both of them have been implemented in the T-Solar production line.

In addition, a IFL was introduced at the interface TCO/p-layer to decrease the reflected light at this interface. The IFL should improve the efficiency up to 5% relative (due to the increase in current) but it is not implemented since a drop in the voltage is produced due to an unspecified problem at the interface TCO/p-layer which is caused by the TiO₂ interface layer.

Moreover, new materials in the front TCO layer were tested, specifically a ZnO TCO layer developed in FZJ. The main difference was that the ZnO TCO layer presented much higher diffuse transmission than our usual SnO₂ TCO-glass (57% vs. 13%). Nevertheless, the JV curves for ZnO TCO samples presented "S"-shape near to V_{oc} indicating a contact problem at the ZnO/p-layer interface.

- **p-i-n structure developments:** For the T-Solar layers, the thickness non-uniformity of the different a-Si:H layers over an area of 2.2 x 2.6 m² is less than 10%. Thanks to such good uniformity of a-Si:H layers thickness, we have achieved very constant cell performance over the 5.72 m², a must to get highly efficient modules. Thus, the average values for the electrical parameters of four coupons with solar cells placed along the panel diagonal present non-uniformities always lower than 1%.

The investigation of light-induced degradation in function of the i-layer thickness presents very similar stabilized efficiency in the i-layer thickness range between 140 nm to 260 nm. Reduction of i-layer thickness allows to increase the PECVD throughput from 20 panels/h to 30 panels/h and therefore, the factory production capacity could be increased from about 55 MW/year to 75 MW/year, when producing modules of 400 W.

The optimization of the p-i-n structure on the TCO-glass resulted in a further improvement of the electrical and optical properties in solar cells. The gain in efficiency resulting from the optimization of the p-i-n structure achieves about 4% - 5% relative efficiency gain. The main changes we have done are the introduction of graded layers and the reduction of defects at the p/i interface. With the last R&D prototype we have achieved an additional 3% of potential efficiency improvement. Finally, to reduce the efficiency dispersion between different PECVD chambers maximizing the efficiency we changed the deposition process conditions.

- **Back contact developments:** Ag back reflector showed a 5.7% relative efficiency improvement. However, nowadays it has not been implemented due to possible

adherence problems and, especially, economical reasons since at 2011 - 2012 Ag price level its implementation as back reflector was not cost effective.

- **Developments through increase of the active area:** The death area produced between two consecutive cells due to the distance between the P1 laser scribe and P3 laser scribe was about 350 μm and it was reduced to about 250 μm . The optimization of the laser scribe process reducing the death area improved the efficiency about 1.5% - 2% relative. This development only affects to modules.

Collecting all the results from the HELATHIS project period, one fixes the total potential of improvement of a-Si:H single junction modules efficiency in about 25% relative. We have implemented in our factory approximately 10% relative of the total improvements, by combining AGC's ME-type TCO layer with low iron substrate glass and with an industrial feasible p-i-n structure. With the last BKM in production in 2012 we have achieved stabilized 1 cm^2 solar cell efficiency of 8.00% and stabilized module efficiency of 7.48% (428 W) for full 5.72 m^2 size modules. With the last R&D prototype we have gotten record 1 cm^2 solar cells of 8.22% and full size modules of 7.95% (455 W), both in stabilized state. If we extrapolate the remaining potential of improvement of 12%, we would get an efficiency of 9.21% for solar cells and 8.90% (510 W) for full size modules, both in stabilized state.

Between the different PV technologies, the silicon thin film technology has been presented as a competitive alternative to the majority c-Si technology, especially thanks to its lower temperature coefficients and better behaviour under diffuse radiation, which usually make higher its performance ratio (kWh generated per kW_p). In addition, the silicon thin film technology presents less energy payback time and less price per W_p . Furthermore, we have shown the dramatic evolution of the main productivity parameters during the T-Solar production line lifetime, such as the module efficiency, the factory throughput or the factory availability. These improvements resulted in an impressive increase in the annualized production capacity from 33 MW in 2009 to 72 MW in 2012.

Resumen de la tesis

Actualmente, la mayor parte de la energía consumida en el mundo proviene de combustibles fósiles como petróleo, gas natural o carbón. Sin embargo, en los últimos años, las políticas energéticas a nivel mundial están cambiando, haciendo que las energías renovables incrementen rápidamente su cuota en el mix energético. Las principales razones para esta modificación son que el precio de los combustibles fósiles está en alza debido a la reducción de la oferta, que los países consumidores son energéticamente dependientes de los países productores y que el uso masivo de estos combustibles está produciendo el cambio climático.

Los objetivos climáticos y energéticos de la Unión Europea (EU), conocidos como los objetivos "20-20-20", fijan tres propósitos para 2020 [1]: un 20% de reducción de las emisiones de gases de efecto invernadero con respecto al nivel de 1990 (para volver al rango 450 ppm - 550 ppm), aumentar al 20% el porcentaje de consumo energético que proviene de recursos renovables y mejorar un 20% la eficiencia energética.

La energía renovable más prometedora es la energía solar fotovoltaica (PV), ya que reúne condiciones óptimas como que la luz solar es un recurso ilimitado (el sol proporciona 1000 veces más energía que el consumo energético mundial) o que es una energía limpia y segura. En 2011, por segundo año consecutivo, atrajo la mayor parte de la inversión realizada en energías renovables en todo el mundo (98,5 billones de euros), monopolizando el 49% del total e incrementándose un 44% con respecto al 2010 [2]. Como resultado, sólo en 2012 se ha instalado la cifra récord de 31 GW de energía fotovoltaica en todo el mundo, alcanzando un total de 102 GW instalados.

Hoy en día, la energía solar fotovoltaica es una fuente de energía muy competitiva y bien establecida que ofrece un producto fiable. Además, durante los próximos años, se va a acelerar su consolidación, ya que va a continuar registrando altas tasas de crecimiento. Los resultados

de capacidad PV instalada en 2012 confirman esto, pero también revelan un cambio en el mercado PV de instalaciones, desde uno impulsado principalmente por Europa a uno global a nivel mundial, donde China tendrá una gran importancia.

Con respecto a la industria PV, ésta ha cambiado radicalmente en los últimos años. China se ha convertido en el mayor fabricante del mundo seguido por Taiwán, Alemania y Japón. Entre los 20 mayores fabricantes PV en 2011, solo tres empresas tenían instalaciones en Europa y las tres tienen un futuro incierto para seguir produciendo aquí.

Desde 1990, la producción PV se ha incrementado aproximadamente unos 2,5 órdenes de magnitud, desde 129 MW a 70 GW en 2012. La inserción de nuevas tecnologías mucho más rápido de lo esperado (lámina delgada, concentración PV), sumado a la drástica caída de precios de los módulos solares del 50% en los últimos dos años debido al exceso de oferta, ha puesto una presión enorme en un gran número de empresas y está acelerando la consolidación de la industria. La previsión para los próximos años es continuar la expansión del sector hacia una economía de escala, pasando de una industria de tamaño de 10 MW - 100 MW a una de producción de varios GW.

Actualmente, continuar reduciendo el coste de la electricidad PV ya no depende únicamente de los componentes del sistema PV, sino también de los costes de integración en la infraestructura existente. Por lo tanto, para hacer de la electricidad PV una gran fuente de suministro de energía a nivel mundial en la próxima década, se deben centrar más esfuerzos tanto en optimizar los costes no PV como en el apoyo público, especialmente en medidas regulatorias.

Las "Perspectivas para la Tecnología de la Energía en 2010", realizado por la Agencia Internacional de la Energía (IEA) manifiesta que en su actual escenario de referencia, la inversión global en suministro y uso de energía, para el período 2010 - 2050, asciende a 208 trillones de euros (escenario de referencia) [20]. Limitar la concentración de gases de efecto invernadero a 450 ppm, tiene una necesidad de financiamiento adicional de 35,4 trillones de euros (escenario *BLUE-Map*), pero al mismo tiempo, el ahorro en consumo de energías fósiles de este escenario comparado con el escenario de referencia sería de 86,2 trillones de euros, es decir, más del doble del coste de la inversión adicional. Esto indica claramente, el enorme beneficio social que proporcionaría una estrategia más agresiva para combatir el cambio climático.

Como se ha comentado previamente, el desarrollo y reciente crecimiento de la industria PV ha provocado que haya un exceso de oferta de módulos y, con ello, una rápida bajada de

precios en los últimos años. Esto ha obligado a todos los actores del sector PV a aumentar su inversión en I+D para poder seguir siendo competitivos. En este marco se han realizado las investigaciones de esta tesis doctoral que ha sido financiada por el proyecto europeo "High Efficient very LArge area THIn film Silicon photovoltaic modules"(HELATHIS) y el programa nacional "Torres Quevedo". La actividad ha involucrado al Departamento de Tecnología e I+D de la empresa T-Solar Global S.A. (T-Solar), donde se ha realizado la mayor parte del trabajo, y al Departamento de Electrónica e Computación de la Universidad de Santiago de Compostela.

T-Solar es una empresa dedicada a la fabricación de módulos PV de silicio amorfo hidrogenado (a-Si:H). Forma parte del Grupo T-Solar que a su vez es una filial de la multinacional Isolux. Sus primeros módulos fueron fabricados en julio de 2008.

T-Solar ha implementado en su línea de producción la tecnología SunFab de la compañía estadounidense Applied Materials Inc. (AMAT), siendo su segundo cliente. Además, su fábrica fue la primera en construirse en Europa. El proceso de fabricación de sus módulos de lámina delgada fue un proyecto innovador a nivel mundial debido al bajo coste del proceso de producción y al enorme tamaño de los módulos, de dimensiones 2,2 m x 2,6 m (módulos *full*) y una potencia máxima de unos 430 W_p (eficiencia de 7,52%). La capacidad anual de producción de la fábrica es de unos 72 MW_p.

El proceso de fabricación de los módulos de T-Solar se basa en la deposición de diferentes capas en un sustrato de vidrio de dimensiones 2,6 m x 2,2 m, alternado por el proceso de grabado láser de las citadas capas finas. Así, se obtienen células separadas e interconexión monolítica entre las mismas para coleccionar la corriente. Mediante la deposición secuencial de capas y el grabado láser se logra una conexión en serie de 216 células de 1 cm x 257 cm. El electrodo positivo (que contacta la primera célula de la conexión en serie) y el electrodo negativo (conectado a la última célula) están conectados a la caja de conexiones, que está situada en la parte trasera del módulo, a través de una cinta metálica. Una vez que el módulo está fabricado eléctricamente, se encapsula con otro sustrato de vidrio. Entre ambos vidrios se interpone una lámina de polímero polivinil butiral (PVB). De esta manera las capas están protegidas de la humedad y la fricción mecánica.

Centrándonos en la parte eléctrica del proceso de producción, cabe destacar que la primera capa que se deposita sobre el vidrio es un óxido transparente conductivo (TCO) que actúa como contacto frontal. El conjunto vidrio-TCO es suministrado por la empresa AGC Flat Glass Europe S.A. (AGC), por lo tanto es el material de entrada en la línea de producción

de T-Solar. El TCO es una capa texturizada de SnO_2 dopada con flúor ($\text{SnO}_2:\text{F}$). Tiene la función de transmitir y dispersar la luz, así como conducir la corriente generada en las capas de a-Si:H. Posteriormente se deposita una unión p-i-n de a-Si:H mediante deposición química en fase vapor activado por plasma (PECVD). Las capas dopadas (p y n) tienen la función de generar un campo eléctrico a través de la capa intrínseca (i, que es la que genera la corriente) y proporcionar un contacto eléctrico a los terminales. La capa i tiene las funciones de absorber la luz y transportar los portadores fotogenerados. Por último, se deposita el contacto trasero que consta de tres capas: TCO trasero, Al y NiV. El TCO trasero es una capa de ZnO dopado con aluminio (AZO) que actúa como contacto y como capa dieléctrica para mejorar la reflexión. La capa de metal de Al se usa como reflector y la de NiV tiene una función protectora y facilita el proceso de soldadura [24].

Esta tesis doctoral se basa en la caracterización óptica y eléctrica de células solares en tecnología de a-Si:H con capas fabricadas con diferentes materiales o condiciones del proceso de deposición. Asimismo, se lleva a cabo la optimización y modelado de estas células y sus capas. También se han desarrollado diferentes equipos de metrología.

En lo que se refiere a las simulaciones, se han obtenido resultados en dos dimensiones de estructuras p-i-n de a-Si:H. Para ello se ha usado una configuración básica de la herramienta de simulación Sentaurus (Synopsys Inc.). A mayores hemos implementado los modelos estándar reportados en la literatura para la distribución de la densidad de estados (DOS) y para las estadísticas de generación/recombinación del a-Si:H. Asimismo, hemos modelado capas con concentración gradual de dopado y degradación inducida por iluminación (LID), que el a-Si:H sufre debido al efecto Staebler-Wronski (SWE). También se ha implementado un modelo para simular la textura de la capa de TCO frontal y la cantidad de luz que es atrapada en células solares de a-Si:H. La simulación reproduce bien las curvas de corriente-voltaje (IV) y respuesta espectral de células solares de T-Solar. Los resultados muestran la importancia de la optimización de las propiedades de la capa p, cuyo espesor y concentración de dopado afectan especialmente a los parámetros eléctricos de la célula solar.

En el laboratorio de T-Solar se han desarrollado tres equipos de medida que están relacionados con esta tesis. Dos equipos son para determinar la eficiencia cuántica externa (EQE): uno es el equipo convencional de respuesta espectral (CSR) y el otro el equipo rápido de respuesta espectral (VFSR). Por último, está el equipo del simulador solar (SS) con su trazador de curvas IV tanto de iluminación como de oscuridad. Sin duda, el más innovador es

el equipo VFSR, por tanto nos centraremos en los objetivos principales conseguidos con este equipo y en su desarrollo futuro.

El equipo VFSR permite medir la respuesta espectral (SR) de células solares de a-Si:H (unión simple, SJ) en unos segundos. Para ello, se han caracterizado diodos de emisión de luz (LEDs) en el rango de 300 nm a 800 nm. Además, para medir células solares de unión tándem (TJ) en un futuro próximo, también se han analizado LEDs en el rango de 800 nm a 1000 nm. El equipo reproduce correctamente el comportamiento de células solares diferentes, por ejemplo, diferentes espesores de capa i o diferentes evoluciones tecnológicas. También hemos realizado mapeados espaciales de la densidad de corriente de cortocircuito (J_{sc}) en mini módulos de tamaño 10 cm x 10 cm. Cabe destacar que el equipo VFSR solo emplea 1 h para realizar el mapeado, frente a las 10 h que se necesitan con el equipo tradicional.

En la actualidad se usan 18 LEDs para medir células solares de SJ y pretendemos utilizar 24 LEDs para medir células solares de TJ. Sin embargo, es difícil encontrar en el mercado LEDs comerciales que cumplan los criterios deseados en parámetros como el ancho espectral o la intensidad luminosa. Para conseguir una medida más precisa de la SR necesitaríamos medir con mayor resolución en el rango de 500 nm a 650 nm. Así podremos detectar con mayor facilidad, por ejemplo, cambios en el espesor de la capa i. Actualmente, la incertidumbre mecánica y la diferente iluminación que se produce al mover el cabezal de medición están produciendo el error principal de medida del equipo. Por ello, un sistema de acoplamiento óptico mecánicamente más robusto está desarrollándose.

La fabricación de células solares de test de a-Si:H, con alta eficiencia y fiabilidad, producidas en el entorno industrial de T-Solar se ha conseguido usando el proceso de grabado láser y *shunt busting* en combinación con *annealing* (145 °C, 30 min). Con este procedimiento, conseguimos células solares altamente eficientes y un gran número de células operativas por muestra que presentan poca dispersión en sus parámetros eléctricos. Igualmente, hemos automatizado la producción de paneles de test, por lo que consumimos menos tiempo en su fabricación y conocemos la posición exacta de las muestras con células solares en el panel tamaño *full*. Asimismo, somos capaces de enviar muestras con vidrio-TCO, p-i-n y una capa protectora de ZnO para, posteriormente, fabricar células solares altamente eficientes en otros laboratorios.

Durante esta tesis se han realizado varios desarrollos y test con el objetivo de optimizar las células solares y módulos de T-Solar. Se persigue mejorar parámetros como la eficiencia, el *throughput* (rendimiento de producción, se mide en paneles por hora, pph), la fiabilidad o el

coste de materiales. Algunos de esos desarrollos ya han sido implementados, otros aún no han alcanzado las condiciones técnicas deseadas y otros no son económicamente competitivos en estos momentos. A través de las mejoras individuales obtenidas en los prototipos que se han fabricado para células solares de 1 cm^2 y módulos de unión simple de a-Si:H, se puede calcular su potencial de mejora en eficiencia. A continuación se explican los desarrollos realizados, la mejora que se consigue con cada uno de ellos y su nivel de implementación en la línea de producción de T-Solar.

- **Desarrollos en la capa de TCO frontal y en el vidrio:** La movilidad de portadores de la capa de TCO se ha incrementado resultando en una capa más delgada y transparente. Esta nueva capa de TCO se denomina movilidad mejorada (ME). Por otra parte, esta mejora se ha combinado con vidrio flotante de bajo contenido en hierro, lo cual incrementa de nuevo la transmisión. El vidrio-TCO resultante es el ANS10ME. La ganancia en eficiencia es alrededor de 1% - 1,5% en valor relativo debido a la capa tipo ME, y aproximadamente 2% - 3% relativo para el vidrio con bajo contenido en hierro. Ambos avances han sido implementados en la línea de producción de T-Solar.

Además, se ha introducido una capa interfaz (IFL) de TiO_2 en la interfaz TCO/capa p con el objetivo de disminuir la cantidad de luz reflejada debido al abrupto cambio en el índice de refracción. La IFL debería mejorar la eficiencia hasta en un 5% relativo (debido al mismo incremento en corriente). Sin embargo, no ha sido implementada ya que en las pruebas realizadas se produce una caída del voltaje debido a algún problema sin especificar en la interfaz TCO/capa p, el cuál es causado por la IFL de TiO_2 .

También han sido probados nuevos materiales para la capa de TCO frontal. Concretamente, una capa de TCO de ZnO desarrollada en el Centro de Investigación de Jülich (FZJ). La principal diferencia con respecto al TCO de SnO_2 utilizado es que el primero presenta una transmisión difusa integrada (300 nm - 800 nm) mucho mayor que el segundo (57% vs. 13%). Sin embargo, las curvas JV del TCO de ZnO presentaban forma de "S" en la región de V_{oc} , lo cual indica un problema de contacto en la interfaz ZnO/capa p.

- **Desarrollos en la estructura p-i-n:** La no-uniformidad de las diferentes capas de a-Si:H de T-Solar en un área de $2,2 \times 2,6 \text{ m}^2$ es menor al 10%. Gracias a la buena uniformidad en el espesor de las capas de a-Si:H, hemos logrado un comportamiento muy similar de las propiedades eléctricas (de células solares) en los $5,72 \text{ m}^2$ de

superficie. Esto es un factor clave para obtener módulos de alta eficiencia. Así, los parámetros eléctricos promedio de cuatro muestras con células solares localizadas a lo largo de la diagonal del panel presentan una no-uniformidad menor al 1%.

La investigación de la degradación inducida por iluminación (LID) en función del espesor de la capa *i* presenta una eficiencia estabilizada muy similar para el rango de espesores entre 140 nm y 260 nm. La reducción del espesor de la capa *i* permitiría incrementar el *throughput* del PECVD de 20 pph a 30 pph y por lo tanto, la capacidad de producción de la fábrica de unos 55 MW/año a 75 MW/año, en el caso de producir módulos de 400 W.

La optimización de la estructura p-i-n, adaptándola al nuevo vidrio-TCO ha resultado en una gran mejora de las propiedades ópticas y eléctricas de las células solares. La optimización de la estructura p-i-n da como resultado una ganancia en eficiencia de aproximadamente un 4% - 5% en valor relativo. Los cambios principales que hemos realizado son la introducción de capas graduales y la reducción de defectos en la interfaz capa *p*/capa *i*. Con el último prototipo de investigación hemos obtenido un 3% adicional de mejora. Por último, se redujo la dispersión en eficiencia entre las diferentes cámaras del PECVD. Para ello, cambiamos, de forma individual para cada cámara, las condiciones del proceso de deposición. Así, conseguimos maximizar la eficiencia promedio, acercándola a la de la mejor cámara.

- **Desarrollos en el contacto trasero:** El reflector trasero de plata (Ag) presentó una mejora en eficiencia del 5,7% en valor relativo. A pesar de ello, actualmente no ha sido implementado debido a posibles problemas de adherencia y, especialmente, motivos económicos ya que su implementación como reflector trasero no era viable al precio de la Ag en 2011- 2012.
- **Desarrollos incrementando el área activa:** El área muerta existente entre dos células consecutivas debido a la distancia entre los grabados láser P1 y P3 era de unas 350 μm y ha sido reducida a unas 250 μm . La optimización del proceso de grabado láser, reduciendo el área muerta, ha incrementado la eficiencia entre 1,5% - 2% en valor relativo. Este desarrollo sólo afecta a módulos.

Recopilando todos los resultados de los tres años de duración del proyecto HELATHIS, se fija el potencial total de mejora de la eficiencia de módulos de unión simple de a-Si:H en

aproximadamente un 25 % relativo. En la fábrica se ha implementado sobre un 10 % relativo combinando la capa de TCO de AGC del tipo ME con el sustrato de vidrio con bajo contenido en hierro y con una estructura p-i-n industrialmente viable. Con la última receta de fabricación que estaba en producción en 2012 se ha conseguido una eficiencia estabilizada de 8,00 % para células solares de 1 cm² y de 7,48 % (428 W) para módulos *full* de 5,72 m². Con el último prototipo de investigación hemos obtenido récords con una eficiencia estabilizada de 8,22 % para células solares de 1 cm² y de 7,95 % (455 W) para módulos *full*. Si extrapolamos el potencial restante de mejora del 12 %, se llegaría a una eficiencia estabilizada de 9,21 % para células solares y 8,90 % (510 W) para módulos *full*.

Entre las tecnologías PV existentes, el silicio de lámina delgada se presenta como una alternativa competitiva frente al mayoritario silicio cristalino (c-Si). Las principales ventajas del silicio de lámina delgada son sus bajos coeficientes de temperatura y su mejor comportamiento ante radiación difusa, los cuales provocan que, normalmente, su parámetro de prestaciones (kWh generados por kW_p) sea mayor. Además, la tecnología de silicio de lámina delgada cuenta con un menor tiempo de retorno energético y menor precio por W_p.

En el caso concreto de la fábrica de T-Solar, todos estas ventajas se han visto mejoradas gracias a la espectacular evolución de los principales parámetros de productividad durante la vida de la línea de producción. Los parámetros de productividad con mayor influencia son la eficiencia de los módulos, el *throughput* de la fábrica y la disponibilidad de la fábrica (número de horas con disponibilidad para producir). La evolución de la eficiencia durante los últimos cuatro años (desde la apertura de la fábrica en julio de 2008 hasta julio de 2012) ha pasado desde el 6 %, usando la receta de fabricación suministrada por AMAT, al 7,5 % (módulos de producción récord). Esto supone un 25 % de mejora en la eficiencia estabilizada de los módulos. Además, se ha reducido la dispersión en la eficiencia de los módulos según la cámara de PECVD que se use, aumentando así la eficiencia promedio. Por su parte, el *throughput* ha pasado de 17 pph en 2009 a 22 pph en 2012 (29 % de mejora). La disponibilidad de la fábrica se ha incrementado sobre un 50 % en ese mismo período de tiempo, principalmente debido a la reducción del número de mantenimientos correctivos y a la reducción de horas en las que se realizan los mantenimientos preventivos. Combinando el aumento en eficiencia, *throughput* y disponibilidad de la fábrica con la reducción en módulos que se desechan, se obtiene un impresionante incremento de la capacidad de producción anualizada de la fábrica, pasando de 33 MW en 2009 a 72 MW en 2012.

Bibliography

- [1] European Commission. Climate action policies. 2020 targets.
- [2] Joint Research Centre (JRC). PV status report 2012. Technical report, 2012.
- [3] International Renewable Energy Agency (IRENA). Solar photovoltaics. Technical Report 4, 2012.
- [4] European Photovoltaic Industry Association (EPIA). Photovoltaic energy. Electricity from the sun. Technical report, 2009.
- [5] European Photovoltaic Industry Association (EPIA). Global market outlook for photovoltaics 2013-2017. Technical report, 2013.
- [6] M. A. Green, K. Emery, Y. Hishikawa, W. Warta, and E. D. Dunlop. Solar cell efficiency tables (version 41). *Progress in Photovoltaics: Research and Applications*, pages 1–11, 2013.
- [7] P. Jackson, D. Hariskos, E. Lotter, S. Paetel, R. Wuerz, R. Menner, W. Wischmann, and M. Powalla. New world record efficiency for Cu(In,Ga)Se₂ thin-film solar cells beyond 20%. *Progress in Photovoltaics: Research and Applications*, 19(7):894–897, November 2011.
- [8] M. A. Green. Solar cell efficiency tables (version 37). *Progress in Photovoltaics Research and Applications*, 19:84–92, 2011.
- [9] International Energy Agency (IEA). PV technology roadmap. Technical report, 2010.
- [10] OrgaPVnet. Technology roadmap towards stable & low-cost organic based solar cells. Technical report, Brussels, 2009.

- [11] A. Nozik. Multiple exciton generation in colloidal quantum dots, singlet fission in molecules, quantum dot arrays, quantum dot solar cells, and effects of solar concentration. In *Proceedings of MRS. Symposium B: Third-Generation and Emerging Solar-Cell Technologies*, San Francisco, California, 2011.
- [12] R. P. Rafaelle. Next generation photovoltaics. In *Proceedings of MRS. Symposium B: Third-Generation and Emerging Solar-Cell Technologies*, San Francisco, California, 2011.
- [13] Energy Research Centre of the Netherlands (ECN). Annual Report 2012. Technical report, 2012.
- [14] Issolsa. Projet BIPV - Gare TGV de Perpignan. Technical report, 2011.
- [15] M. Giesecking. BIPV. Technical report, 2011.
- [16] European Photovoltaic Industry Association (EPIA). Global market outlook for photovoltaics until 2016. Technical report, 2012.
- [17] European Commission. Directorate-General for Energy. Photovoltaics in 2010. Technical report, 1996.
- [18] Bloomberg New Energy Finance. PV market outlook Q3 2012. Technical report.
- [19] International Energy Agency (IEA). World energy outlook. Technical report, 2011.
- [20] International Energy Agency (IEA). Energy technology perspectives - Scenarios and strategies to 2050. Technical report, 2010.
- [21] Fraunhofer institute for solar energy systems (ISE). Photovoltaics report. Technical report, 2012.
- [22] M. Fonrodona, S. Santos, C. Mata, M. Vetter, and J. Andreu. Performance and productivity improvements in very large area amorphous silicon modules. In *Proceedings of 25th European Photovoltaic Solar Energy Conference and Exhibition (EUPVSEC)*, Valencia, 2010.
- [23] J. Merten, J. M. Asensi, C. Voz, A. V. Shah, R. Platz, and J. Andreu. Improved equivalent circuit and analytical model for amorphous silicon solar cells and modules. *IEEE Transactions on Electron Devices*, 45(2):423–429, 1998.

- [24] R. E. I. Schropp and M. Zeman. New developments in amorphous thin-film silicon solar cells. *IEEE Transactions on Electron Devices*, 46(10):2086–2092, 1999.
- [25] R. E. I. Schropp and M. Zeman. *Amorphous and microcrystalline silicon solar cells: Modelling, materials and device technology*. Kluwer Academic, Norwell, Massachusetts, 1998.
- [26] R. F. Pierret. *Semiconductor fundamentals*. Addison-Wesley, Delaware, 2nd edition, 1988.
- [27] S. M. Sze. *Physics of semiconductor devices*. John Wiley & Sons, Inc., New Jersey, 3rd edition, 1981.
- [28] W. Shockley and W. T. Read. Statistics of the recombinations of holes and electrons. *Physical Review*, 87(5):835–842, 1952.
- [29] C. T. Sah and W. Shockley. Electron-hole recombination statistics in semiconductors through flaws with many charge conditions. *Physical Review*, 109(4):1103–1115, 1958.
- [30] R. N. Hall. Germanium rectifier characteristics. *Physical Review*, 83:228, 1951.
- [31] R. N. Hall. Electron-hole recombination in Germanium. *Physical Review*, 87:387, 1952.
- [32] H. Okamoto, H. Kida, and Y. Hamakawa. Steady-state photoconductivity in amorphous semiconductors containing correlated defects. *Philosophical Magazine Part B*, 49(3):231–247, 1984.
- [33] Y. Tawada, H. Okamoto, and Y. Hamakawa. a-SiC:H/a-Si:H heterojunction solar cell having more than 7.1% efficiency. *Applied Physics Letters*, 39:237–239, 1981.
- [34] R. R. Arya, A. Catalano, and R. S. Oswald. Amorphous silicon p-i-n solar cells with graded interface. *Applied Physics Letters*, 49:1089–1091, 1986.
- [35] S. Yamanaka, S. Kawamura, M. Konagai, and K. Takahashi. Yamanaka, S. Kawamura, S. Konagai, M. Takahashi, K. In *Technical Digest of the 3rd International PVSEC*, pages 709–712, Tokyo, Japan, 1987.
- [36] Synopsys. *Sentaurus device user*. 2010.

- [37] W. Bludau, A. Onton, and W. Heinke. Temperature dependence of the band gap in silicon. *Journal of Applied Physics*, 45(4):1846–1848, 1974.
- [38] R. A. Street. *Hydrogenated amorphous silicon*. Cambridge University Press, New York, 2005.
- [39] D. L. Staebler and C. R. Wronski. Reversible conductivity changes in discharge-produced amorphous Si. *Applied Physics Letters*, 31:292–294, 1977.
- [40] D. L. Staebler and C. R. Wronski. Optically induced conductivity changes in discharge-produced hydrogenated amorphous silicon. *Journal of Applied Physics*, 51(6):3262–3268, 1980.
- [41] V. L. Dalal and G. Baldwin. Design and fabrication of graded bandgap solar cells in amorphous silicon and alloys. In *Proceedings of Materials Research Society Symp.*, volume 297, pages 833–838, Hawaii, 1993.
- [42] D. Fischer, N. Wyrsh, C. M. Fortmann, and A. V. Shah. Amorphous silicon solar cells with graded low-level doped i-layers characterised by bifacial measurements. In *Proceedings of 23rd IEEE Photovoltaic Specialists Conference (PVSC)*, pages 878–884, Louisville, 1993.
- [43] B. Von Roedern. Innovative optimization procedures for solar cells based on a unique model for junction optimization. In *Proceedings of 12th European Photovoltaic Solar Energy Conference (EUPVSEC)*, pages 1354–1358, Amsterdam, 1994.
- [44] Y. Kazama, K. Seki, W. Kim, S. Yamanaka, M. Konagai, and K. Takahashi. High efficiency amorphous silicon solar cells with "Delta-doped" p-layer. *Japanese Journal of Applied Physics*, 28(7):1160–1164, July 1989.
- [45] S. S. Hegedus and R. Kaplan. Analysis of quantum efficiency and optical enhancement in amorphous Si p-i-n solar cells. *Progress in Photovoltaics: Research and Applications*, 10(4):257–269, June 2002.
- [46] M. Vetter, J. Andreu, J. P. Borrajo, A. Martin, J. A. Rodriguez, O. Agustsson, J. Schotsaert, K. Bittkau, R. Carius, A. Gordijn, A. Hoffmann, I. M. Macedo, J. K. Rath, R. E. I. Schropp, A. Antony, J. Bertomeu, and F. Kail. Development of high performance industrial TCO glass for very large area a-Si:H PV modules. In *Proceedings of 26th*

- European Photovoltaic Solar Energy Conference and Exhibition (EUPVSEC)*, pages 2676–2679, Hamburg, 2011.
- [47] C. Lin, W. Liu, and C. Hsieh. Scalar scattering model of highly textured transparent conducting oxide. *Journal of Applied Physics*, 109(1):014508, 2011.
- [48] K. Jäger, O. Isabella, L. Zhao, and M. Zeman. Light scattering properties of surface-textured substrates. *Physica status solidi (c)*, January 2010.
- [49] M. Zeman, R. A. C. M. M. Van Swaaij, and J. W. Metselaar. Optical modeling of a-Si:H solar cells with rough interfaces: Effect of back contact and interface roughness. *Journal of Applied Physics*, 88(11):11–13, 2000.
- [50] K. Jager and M. Zeman. A scattering model for surface-textured thin films. *Applied Physics Letters*, 95(17):171108, 2009.
- [51] National Renewable Energy Laboratory (NREL). Reference solar spectral irradiance: Air Mass 1.5. Technical report.
- [52] International Electrotechnical Commission (IEC). Photovoltaic devices- Part 8: Measurement of the spectral response of a photovoltaic (PV) device. Technical report, 1998.
- [53] C. Lee, H. Efstathiadis, J. E. Reynolds, and P. Haldar. Two-dimensional computer modeling of single junction a-Si:H solar cells. In *Proceedings of 34th IEEE Photovoltaic Specialists Conference (PVSC)*, pages 1118–1122, Philadelphia, June 2009.
- [54] C. M. Snowden. Semiconductor device modelling. *IEE Materials and Devices*, 5, 1988.
- [55] D. L. Scharfetter and H. K. Gummel. Large-signal analysis of a silicon read diode oscillator. *IEEE Transactions on Electron Devices*, pages 64–77, 1969.
- [56] J. J. Barnes and R. J. Lomax. Finite-element methods in semiconductor device simulation. *IEEE Transactions on Electron Devices*, 24(8):1082–1089, 1977.
- [57] S. E. Laux and R. J. Lomax. Numerical investigation of mesh size convergence rate of the finite element method in MESFET simulation. *Solid State Electronics*, 24:485–493, 1981.

- [58] J. M. López González. *Contribución al estudio de los transistores bipolares de heterounión*. PhD thesis, Universitat Politècnica de Catalunya, 1994.
- [59] A. J. García Loureiro. *BIPS3D: Un simulador 3D paralelo de dispositivos bipolares BJT y HBT*. PhD thesis, Universidade de Santiago de Compostela, 1999.
- [60] S. Selberherr. *Analysis and simulation of semiconductor devices*. Springer-Verlag, Austria, 1984.
- [61] J. M. Ortega and W. C. Rheinboldt. Iterative solution of nonlinear equation in several variables. *Academic Press inc.*, 1970.
- [62] M. A. Aldegunde Rodríguez. *Desarrollo de herramientas para la simulación de transistores MOSFET*. PhD thesis, Universidade de Santiago de Compostela, 2009.
- [63] C. S. Rafferty, M. R. Pinto, and R. W. Dutton. Iterative methods in semiconductor device simulation. *IEEE Transactions on Computer-Aided Design*, 4(4):462–471, 1985.
- [64] H. K. Gummel. A self-consistent iterative scheme for one-dimensional steady state transistors calculations. *IEEE Transactions on Electron Devices*, 11:455–465, 1964.
- [65] H. Meiling. *Deposition of amorphous silicon thin films and solar cells*. PhD thesis, Utrecht University, 1991.
- [66] J. Perrin. *Plasma deposition of amorphous-based materials*. Academic Press Inc., San Diego, CA, 1995.
- [67] W. Beyer, J. Hupkes, and H. Stiebig. Transparent conducting oxide films for thin film silicon photovoltaics. *Thin Solid Films*, 516(2-4):147–154, December 2007.
- [68] Fraunhofer Institut Solare Energiesysteme (FHG-ISE). Measurement report WPVS cell. Technical report, 2008.
- [69] H. Field. Solar cell spectral response measurement errors related to spectral band width and chopped light waveform. In *Proceedings of 26th IEEE Photovoltaic Specialists Conference (PVSC)*, California, 1997. NREL / CP-530-22969 UC Category: 1250.
- [70] P.A. Basore. Extended spectral analysis of internal quantum efficiency. In *Proceedings of 23rd IEEE Photovoltaic Specialists Conference (PVSC)*, pages 147–152, Louisville, 1993.

- [71] J. Sinkkonen, A. Hovinen, T. Siirtola, E. Tuominen, and M. Acerbis. Interpretation of the spectral response of a solar cell in terms of the spatial collection efficiency. In *Proceedings of 25th IEEE Photovoltaic Specialists Conference (PVSC)*, pages 561–564, Washington, 1996.
- [72] S. Winter. Survey of optical metrology for solid state solar energy conversion. In *Proceedings of 10th International Conference on New Developments and Applications in Optical Radiometry (NEWRAD)*, Daejeon, Korea, 2008.
- [73] J. Metzdorf. Calibration of solar cells. 1: The differential spectral responsivity method. *Applied Optics*, 26:1701–1708, 1987.
- [74] J. A. Rodríguez, M. Fortes, C. Alberte, M. Vetter, and J. Andreu. Development of a very fast spectral response measurement system for analysis of hydrogenated amorphous silicon solar cells and modules. *Materials Science and Engineering: B*, 178(1):94–98, January 2013.
- [75] D. L. Young, S. Pinegar, and P. Stradins. New real-time quantum efficiency measurement system. In *Proceedings of 33rd IEEE Photovoltaic Specialists Conference (PVSC)*, San Diego, California., 2008.
- [76] W. Reetz, D. Erdweg, W. Hilgers, P. Kaienburg, A. Gerber, B. Pieters, and U. Rau. A novel high speed spectral response measurement system based on LED light sources. In *Proceedings of 26th European Photovoltaic Solar Energy Conference and Exhibition (EUPVSEC)*, pages 113–116, Hamburg, 2011.
- [77] B. H. Hamadani, J. Roller, B. Dougherty, and H. W. Yoon. Versatile light-emitting-diode-based spectral response measurement system for photovoltaic device characterization. *Applied optics*, 51(19):4469–76, July 2012.
- [78] G. Zaid, S. Park, and L. Dong-Hoon. Differential spectral responsivity measurement of photovoltaic detectors with a light-emitting-diode-based integrating sphere source. *Applied Optics*, 49(35):6772–6783, 2010.
- [79] S. Kohraku and K. Kurokawa. New methods for solar cells measurement by LED solar simulator. In *Proceedings of 3rd World Conference on Photovoltaic Energy Conversion*, pages 1977–1980, Osaka, 2003.

- [80] R. H. Bishop. *Learning with LabVIEW 8*. Pearson, P. Hall, Upper Saddle River, New Jersey, 2007.
- [81] J. A. Rodriguez, M. Vetter, M. Fortes, C. Alberte, and P. Otero. Development of a very fast spectral response measurement system for silicon thin film modules. In *Proceedings of 9th Spanish Conference on Electron Devices (CDE)*, Valladolid, 2013.
- [82] M. A. Green. *Silicon solar sells: advanced principles & practice*. Centre for Photovoltaic Devices and Systems, University of New South Wales, Australia, 1995.
- [83] M. Alonso Abellá. Capítulo 3: Módulos y generadores fotovoltaicos. In *Sistemas Fotovoltaicos. Introducción al diseño y dimensionado de instalaciones solares fotovoltaicas*. 2005.
- [84] M. Vetter, J. P. Borrajo, M. Fonrodona, P. Otero, J. A. Rodríguez, J. Andreu, O. Agustsson, J. Schotsaert, R. Carius, K. Bittkau, E. Bunte, A. Hoffmann, R. E. I. Schropp, J. K. Rath, and I. M. Macedo. High efficient very large thin film silicon photovoltaic modules (HELATHIS). In *Proceedings of 25th European Photovoltaic Solar Energy Conference and Exhibition (EUPVSEC)*, pages 5–8, Valencia, 2010.
- [85] J. A. Rodriguez, P. Otero, M. Vetter, J. Andreu, E. Comesana, and A. J. Garcia-Loureiro. Simulation of the effect of p-layer properties on the electrical behaviour of a-Si: H thin film solar cells. In *Proceedings of 8th Spanish Conference on Electron Devices (CDE)*, Palma de Mallorca, 2011.
- [86] P. Otero, J. A. Rodriguez, M. Vetter, J. Andreu, E. Comesana, and A. J. Garcia-Loureiro. Simulation of the temperature dependence of a-Si: H solar cell current-voltage characteristics. In *Proceedings of 8th Spanish Conference on Electron Devices (CDE)*, Palma de Mallorca, 2011.
- [87] M. Vetter, J. Andreu, J. P. Borrajo, M. Fonrodona, P. Otero, J. A. Rodríguez, O. Agustsson, J. Schotsaert, K. Bittkau, R. Carius, A. Gordijn, J. Hüpkens, G. Jost, O. M. Moustapha, J. K. Rath, R.E.I. Schropp, A. Antony, J. Bertomeu, P. Carreras, and F. Kail. Optimization of the solar cell structure for the industrial implementation in very large area a-Si:H PV modules. In *Proceedings of 27th European Photovoltaic Solar Energy Conference and Exhibition (EUPVSEC)*, pages 8–11, Frankfurt, 2012.

- [88] P. Otero, I. Quelle, M. Fonrodona, S. Santos, J. A. Rodríguez, E. Grande, C. Mata, M. Vetter, and J. Andreu. Improvement of very large area (5.7m²) a-Si:H PV module manufacturing by PECVD process control. In *Proceedings of 27th European Photovoltaic Solar Energy Conference and Exhibition (EUPVSEC)*, pages 2109–2112, Frankfurt, 2012.
- [89] S. Benagli, D. Borrello, E. Vallar-Sauvain, J. Meier, U. Kroll, J. Hoetzel, J. Bailat, J. Steinhauser, M. Marmelo, G. Monteduro, and L. Castens. High-efficiency amorphous silicon devices on LPCVD-ZnO TCO prepared in industrial KAI-M R&D reactor. In *Proceedings of 24th European Photovoltaic Solar Energy Conference (EUPVSEC)*, pages 21–25, Hamburg, 2009.
- [90] J. Müller, B. Rech, J. Springer, and M. Vanecek. TCO and light trapping in silicon thin film solar cells. *Solar Energy*, 77(6):917–930, December 2004.

